

Elasticity Mapping for Breast Cancer Diagnosis Using Tactile Imaging and Auxiliary Sensor Fusion

Rory Hampson

Department of Electronic and Electrical Engineering

University of Strathclyde

A thesis submitted for the degree of

Doctor of Philosophy

March 2021

Copyright

This thesis is the result of the author's original research. It has been composed by the author and has not been previously submitted for examination which has led to the award of a degree.

The copyright of this thesis belongs to the author under the terms of the United Kingdom Copyright Acts as qualified by University of Strathclyde Regulation 3.50. Due acknowledgement must always be made of the use of any material contained in, or derived from, this thesis.

Signed: Rory Hampson

Date:31/03/2021

Abstract

Tactile Imaging (TI) is a technology utilising capacitive pressure sensors to image elasticity distributions within soft tissues such as the breast for cancer screening. TI aims to solve critical problems in the cancer screening pathway, particularly: low sensitivity of manual palpation, patient discomfort during X-ray mammography, and the poor quality of breast cancer referral forms between primary and secondary care facilities. TI is effective in identifying ‘non-palpable’, early-stage tumours, with basic differential ability that reduced unnecessary biopsies by 21% in repeated clinical studies. TI has its limitations, particularly: the measured hardness of a lesion is relative to the background hardness, and lesion location estimates are subjective and prone to operator error. TI can achieve more than simple visualisation of lesions and can act as an accurate differentiator and material analysis tool with further metric development and acknowledgement of error sensitivities when transferring from phantom to clinical trials.

This thesis explores and develops two methods, specifically inertial measurement and IR vein imaging, for determining the breast background elasticity, and registering tactile maps for lesion localisation, based on fusion of tactile and auxiliary sensors. These sensors enhance the capabilities of TI, with background tissue elasticity determined with MAE < 4% over tissues in the range 9 kPa – 90 kPa and probe trajectory across the breast measured with an error ratio < 0.3%, independent of applied

load, validated on silicone phantoms. A basic TI error model is also proposed, maintaining tactile sensor stability and accuracy with 1% settling times $< 1.5\text{s}$ over a range of realistic operating conditions. These developments are designed to be easily implemented into commercial systems, through appropriate design, to maximise impact, providing a stable platform for accurate tissue measurements. This will allow clinical TI to further reduce benign referral rates in a cost-effective manner, by elasticity differentiation and lesion classification.in future works.

Acknowledgements

I acknowledge the support of Dr. Jae Son of PPS Inc. and David Ables of Sure Inc. for providing this project with sensor technology, documents pertaining to clinical systems, and permission for use of media.

I also acknowledge and thank Dr. Gordon Dobie and Dr. Graeme West, from the university of Strathclyde for their invaluable advice and support executing the project., and lab mates Robert Anderson and Alistair Lawley for their clinical expertise without which any developed technology would lack substance.

Finally, I gratefully thank my partner Natasha for putting up with late working nights, my fretting about progress, and generally supporting the research through excellent tea making and being an open ear to ideas and issues. Thank you, without your support this work would have been very difficult indeed.

Contents

Contents	vi
List of Figures	xiv
List of Tables	xix
Abbreviations	xx
1. Introduction.....	1
1.1. Chapter Summary.....	1
1.2. Introduction to Tactile Sensing	2
1.2.1. Introduction to Tactile Breast Imaging	7
1.2.2. Research Questions and Objectives	9
1.2.3. Research Trajectory and Defined Scope	10
1.3. Knowledge Contribution	11
1.3.1. Formal Contribution to Knowledge	11
1.3.2. Other Research Outputs.....	12
1.4. Publications	12
1.4.1. Accepted Journal Publications	13
1.4.2. Note on Published Material Re-use.....	13
1.4.3. Works Under Review/ In Preparation	14
1.5. Thesis Structure and Chapter Summary	14

- 2. Literature Review17**
- 2.1. Introduction 17
- 2.2. Clinical Breast Imaging Using Tactile Sensors..... 18
 - 2.2.1. Clinical Breast Cancer Screening in the UK..... 18
 - 2.2.2. Issues in Clinical Reporting 22
 - 2.2.3. General Breast Cancer Screening Globally..... 25
 - 2.2.4. Tactile Imaging Use in Current Breast Screening..... 27
- 2.3. Other Medical Applications of TI 32
- 2.4. Other Breast Tactile Imaging Systems 35
 - 2.4.1. Commercial Systems 35
 - 2.4.2. Academic Systems 36
- 2.5. Detail on Current Common Screening Technology 38
 - 2.5.1. Mammography by X-Ray..... 38
 - 2.5.2. Ultrasound Imaging..... 40
 - 2.5.3. Ultrasound based Elastography 43
 - 2.5.4. Computer Aided Tomography (CT)..... 45
 - 2.5.5. Magnetic Resonance Imaging (MRI) 46
 - 2.5.6. Comparative Note on Different Use Cases 48
- 2.6. Metrics for Automated Diagnosis 50
 - 2.6.1. Elasticity and Disease..... 54
- 2.7. Automated Decision Making..... 56
- 2.8. Summary of Current Tactile Imaging Capabilities 60

2.8.1.	Commercial Implementations of Tactile Imaging.....	60
2.8.2.	Problems in Current Commercial System Use.....	61
2.8.3.	Academic Capabilities not in Commercial Use	62
2.9.	Priority Areas and Justification of Scope	66
3.	Inertial Guidance in Elasticity Imaging.....	69
3.1.	Introduction	69
3.2.	Tactile Elasticity Measurement Systems.....	70
3.3.	Inertial/Orientation Sensors in Medical Applications	72
3.4.	Application to Elasticity Measurement	75
3.4.1.	Displacement in the Context of Elasticity	75
3.4.2.	Hardware Description.....	76
3.4.3.	Theory of Operation	78
3.4.4.	Test Methodology.....	85
3.4.5.	Results	86
3.4.6.	Results Discussion.....	91
3.4.7.	Error Sources and Limitations.....	92
3.4.8.	Range Compared to Typical Breast Tissues.....	94
3.5.	Clinical Practicality	95
3.6.	Application in Production of Tactile Maps	96
3.6.1.	Displacement Context and Measurement Problems.....	96
3.6.2.	Test Methodology.....	98
3.6.3.	Results	99

3.6.4.	Discussion	102
3.7.	Conclusions from Inertial Elasticity Mapping	104
3.7.1.	MARG Based Elasticity Mapping Practicality	104
3.7.2.	Summary and Next Steps	106
4.	Optical and Tactile Breast Imaging	108
4.1.	Introduction	108
4.2.	Opto-Tactile Breast Imaging Systems.....	109
4.3.	Breast Background Elasticity Measurement	114
4.3.1.	Hardware Description.....	114
4.3.2.	Theory of Operation	118
4.3.3.	Practical Validation	134
4.3.4.	Discussion	141
4.4.	Application in Improved Tactile Mapping	144
4.4.1.	Introduction	144
4.4.2.	Image Affine Deformation Reduction.....	146
4.4.3.	Estimation of Material Constant ‘k’	148
4.4.4.	Producing Vein Maps by Mosaicking.....	150
4.4.5.	Discussion	154
4.5.	Conclusion from Optical Tactile Mapping.....	157
4.5.1.	Prototype Optical Based System Practicality	157
4.5.2.	Summary and Next Steps	158
5.	Prototype System Development and Testing.....	160

5.1.	Introduction	160
5.2.	Integration into Commercial Footprints	161
5.2.1.	System Design.....	161
5.2.2.	Minor Algorithm Changes for New Geometry	166
5.3.	Automatic Calibration in Use.....	168
5.3.1.	Normalisation of Tactile Array	168
5.3.2.	Initial Load and Orientation Sensor Calibration	170
5.3.3.	Dynamic Material Property Estimation.....	172
5.4.	Registration of Tactile Images onto Vein Structure	175
5.4.1.	Interfacing Tactile and IR Images	175
5.4.2.	Tactile Image Registration Method.....	178
5.4.3.	Deviation in Project Hardware	181
5.4.4.	Registered Tactile Images using Proposed Prototype	185
5.5.	Test Strategy and Methodology	187
5.5.1.	Test Materials	188
5.5.2.	Test Strategy and Validation	191
5.5.3.	Test Controls	192
5.5.4.	Testing Limitations.....	193
5.6.	Imaging Matching Vs. Load and Tilt Angle	195
5.7.	Probe Tracking Vs. Load and Tilt Angle	198
5.8.	Performance Vs. Elasticity Vs. Feature Density	202
5.8.1.	Elasticity Measurement	202

5.8.2. Probe Position Tracking	204
5.9. Discussion	207
5.10. Conclusion to Prototype System Development.....	209
5.10.1. Developed Prototype System Practicality	209
5.10.2. Suitability for Purpose and Engineering Limitations	209
5.10.3. Summary and Next Steps	211
6. Tactile Sensor Error Modelling.....	213
6.1. Introduction	213
6.2. Tactile Sensor Error Analysis and Modelling	214
6.3. Tactile Imaging Sensor Error Sensitivities.....	216
6.3.1. Thermal Analysis	221
6.3.2. Effect of Thermal Sensitivity on Tactile Images.....	225
6.3.3. Short Term Creep Analysis	230
6.3.4. Effect of Short-Term Creep on Tactile Images	233
6.3.5. Hysteresis	235
6.3.6. Effect of Hysteresis on Tactile Images.....	237
6.3.7. Element Cross Coupling.....	239
6.3.8. Effect of Element Cross Coupling.....	241
6.4. Error Summary and Relative Effect Discussion.....	242
6.5. Reverse Error Model	244
6.6. Error Model Validation	249
6.6.1. Thermal Model Validation	249

6.6.2. Mechanical Model Validation	251
6.7. Discussion	254
6.7.1. Results	254
6.7.2. Limitations in Testing	255
6.7.3. Implementation Practicality	255
6.8. Conclusion from Sensor Error Modelling	256
6.8.1. Applications and Significance	256
6.8.2. Summary and Next Steps	257
7. Conclusion	260
7.1. General Summary	260
7.2. Thesis Impact	263
7.3. Future Development and Work	264
7.4. Additional Applications of This Work	265
References	267
Appendix A	279
A.1. Description of Referral Forms	279
A.2. Referral Forms from Various NHS Trusts	280
Appendix B	285
B.1. Calibration Apparatus	285
B.2. Pressure Sensor Normal Calibration	287
B.3. Scanner Tilt Angle Calibration	289
B.4. Tactile Array Normalisation.....	290

Appendix C	291
C.1. Temperature Analysis and Apparatus	291
C.2. Creep/Hysteresis Analysis and Apparatus	293
C.3. Cross Coupling Analysis and Apparatus.....	295

List of Figures

Figure 1.1 - Parallel plate capacitor basic diagram.....	3
Figure 1.2 - Diagram of Hooke's law.....	4
Figure 1.3 - Illustration of a Capacitive tactile array.....	5
Figure 1.4 - Example Tactile Images.....	6
Figure 2.1 - Breast cancer screening process in the UK..	19
Figure 2.2 - Divide of mammography, breast cancer deaths, and population	25
Figure 2.3 - Tactile breast exam performed at GP equivalent surgery	29
Figure 2.4 - Example of Tactile Images of suspicious breast conditions.....	29
Figure 2.5 - SureTouch Output Report..	30
Figure 2.6 - Prostate Mechanical Imaging using TI.....	33
Figure 2.7 - Transvaginal Tactile Imaging.....	33
Figure 2.8 – iBreastExam™ device and graphical output	35
Figure 2.9 - Hyperspectral TIS device and graphical output	36
Figure 2.10 - Opto-Mechanical tactile sensor and graphical output	37
Figure 2.11 – X-ray Mammography and Output Image	39
Figure 2.12 - Ultrasonic Breast Imaging and Output Image	41
Figure 2.13 - CT Breast Imaging and Output Image	45
Figure 2.14 - MRI Breast Imaging with Output Image.....	47
Figure 2.15 - Comparison of MRI and CT images of palpable lesions	49

Figure 2.16 - Anatomical representation of the breast.....	53
Figure 3.1 - Definition of probe motions and basic concepts in TI.	74
Figure 3.2 - Graphical representation of device usage.....	75
Figure 3.3 - Handheld elastometer hardware implementation.	77
Figure 3.4 - MARG sensor algorithm flow diagram.....	81
Figure 3.5 - Graphical representation of integrator start and stop conditions.....	82
Figure 3.6 - Example of the sensor guard invalidating measurements	82
Figure 3.7 - Representations of data rejection situations	84
Figure 3.8 - Representation of full experimental results.....	87
Figure 3.9 - Systemic Error Vs. Measured Elasticity.....	89
Figure 3.10 - Intraexperimental scatter Vs. Elasticity.....	89
Figure 3.11 - Comparison between 6 compressions per test and 10.....	90
Figure 3.12 - Error and repeatability plots	93
Figure 3.13 – Illustrative graphic of MARG accuracy and repeatability.....	100
Figure 4.1 - Illustrative example of waveguide deformation.....	113
Figure 4.2 - Example thermogram of breast tissue	113
Figure 4.3 - Breast scanner simple prototype design	116
Figure 4.4 - Prototype scanner assembly	116
Figure 4.5 - System Block Diagram of proposed system.	117
Figure 4.6 – Effect of increased normal load on image view plane.....	120
Figure 4.7 – Effect of increasing affine tilt on image view plane.....	122
Figure 4.8 – Application of a binary mask to raw images of phantom tissue.....	126
Figure 4.9 – SIFT point matching between normal load variant images.....	126

Figure 4.10 -Illustrative example of finite load discretisation.	128
Figure 4.11 - Validation material construction diagram.	135
Figure 4.12 – dR shown as a linear function of R.....	138
Figure 4.13 – Stress Vs. Strain plot for the validation material.....	139
Figure 4.14 – Single compression elasticity measurement statistics.	140
Figure 4.15 - Projection of loaded tissue images to the unloaded viewpoint.	152
Figure 4.16 – Mosaicking of affine corrected images.....	153
Figure 4.17 - Comparison of the force-based feature matching function vs. SIFT.	155
Figure 5.1 - Developed prototype system internal view..	162
Figure 5.2 - Developed prototype system underside view.....	162
Figure 5.3 - Prototype System Block Diagram.	163
Figure 5.4 – Prototype system completed view in use.....	165
Figure 5.5 - Method of normalisation of the SureTouch™ tactile array	169
Figure 5.6 - Illustrative prototype calibration/normalisation process..	171
Figure 5.7 - General flowchart of automatic material property estimation.....	173
Figure 5.8 - Tactile and IR Image Re-scaling Stages.....	176
Figure 5.9 - Superimposed Tactile and IR Vein Images.....	177
Figure 5.10 - Mosaicked Tactile Data using IR Vein Images on silicone phantoms.....	179
Figure 5.11 - Positioning of PN5420 Tactile Array.....	182
Figure 5.12 - Superimposed Tactile and IR Vein Images.....	182
Figure 5.13 - Implementation of PN5420 in the Prototype Scanner.....	184
Figure 5.14 - Registered Tactile Images from Prototype System.	185
Figure 5.15 - Silicone phantom material construction.	189

Figure 5.16 - Image Matching Vs. Load and Tilt Angle using SIFT	196
Figure 5.17 - Normalised Feature Matching Vs. Applied Load and Tilt Angle.	196
Figure 5.18 – Typical sample scan position estimation..	199
Figure 5.19 – Rate of error accumulation sensitivity to load and tilt angle.	199
Figure 5.20 - Normalised Error Rate Vs. Applied Load and Tilt Angle.....	201
Figure 5.21 - Elasticity measurement error sensitivity to sample parameters.	203
Figure 5.22 - Position tracking RMS error sensitivity to sample parameters.	205
Figure 5.23 - Path distance measurement sensitivity to sample parameters.	205
Figure 6.1 - Effect of thermal expansion on capacitive plate pressure sensors.	218
Figure 6.2 - Effect of viscoelastic creep on capacitive plate pressure sensors.	218
Figure 6.3 - Effect of hysteresis on capacitive plate pressure sensors.	219
Figure 6.4 - Effect of cross coupling on capacitive pressure sensor arrays.	219
Figure 6.5 - Effect of error in the dielectric distribution on capacitive sensor arrays....	220
Figure 6.6 - Effect of electrode misalignment on capacitive sensor arrays.	220
Figure 6.7 - Modelling of capacitive force sensors.....	222
Figure 6.8 – Results of temperature sensitivity analysis.....	224
Figure 6.9 - Effect of temperature on tactile pressure distributions.....	226
Figure 6.10 - Effect of realistic temperature changes between scans.	229
Figure 6.11 - Illustration of creepage in capacitive pressure sensors.	232
Figure 6.12 - Results of creep parameter analysis.	232
Figure 6.13 - Effect of creep on tactile pressure distributions.	234
Figure 6.14 - Illustration of the coupling between creep and hysteresis.....	236
Figure 6.15 - Results of hysteresis analysis..	236

Figure 6.16 - Effect of hysteresis on tactile pressure distributions.	238
Figure 6.17 - Results of cross coupling analysis.....	240
Figure 6.18 - Effect of cross coupling on tactile pressure distributions.....	241
Figure 6.19 - Reverse error model hierarchy diagram.	244
Figure 6.20 - Thermal compensation model.	246
Figure 6.21 - Viscous creep compensation model.	246
Figure 6.22 - Linearised hysteresis compensation model.	248
Figure 6.23 - Cross Coupling correction model.....	248
Figure 6.24 - Temperature model time series plot.	250
Figure 6.25 – Thermal model error vs. temperature..	250
Figure 6.26 - Mechanical model time series plot.....	253
Figure 6.27 – Mechanical model error vs. time and cycles.	253
Appendix Figure B.1 - Calibration and test apparatus.....	286
Appendix Figure B.2 – SingleTact™ array normal loading calibration setup..	288
Appendix Figure B.3 - Tilt angle calibration setup.....	289
Appendix Figure B.4 – Example SureTouch™ surface calibrated response.....	290
Appendix Figure C.1 – General schematic for a thermal control chamber.	292
Appendix Figure C.2 – Mechanical Creep/Hysteresis test apparatus.	294
Appendix Figure C.3 - Method for measuring interelement cross coupling.....	295

List of Tables

Table 2.1 - Diagnostic metrics used in breast cancer diagnosis studies.....58

Table 3.1 - Material compositions with measured elasticity.....88

Table 3.2 - Results for repeated tests of 50 runs of 0.15m with the MARG probe 100

Table 4.1 – Material compositions for the validation sample..... 135

Table 4.2 - Total camera position error comparison. 155

Table 5.1 - Material compositions for silicone phantom testing..... 190

Table 5.2 – Comparison of positioning error200

Table 5.3 – Proposed system elasticity measurement results. 203

Table 6.1 - Summary of tactile array error terms.....242

Abbreviations

2D	2 Dimensional
3D	3 Dimensional
APAC	Asia-Pacific Countries
ARNN	Adaptive Recurrent Neural Network
A-SIFT	Affine SIFT
BI-RADS	Breast Imaging-Reporting and Data System
BMI	Breast Mechanical Imaging
BSE / SBE	Self Breast Exam
CAT / CT	Computer Aided Tomography
CBE	Clinical Breast Exam
DDSM	Digital Database for Screening Mammography
DOF	Degrees of Freedom
EEMEA	Eastern Europe, Middle East, and Africa
F/R NN	Fully Recurrent Neural Network
FDA	Food and Drug Administration
FPS	Frames Per Second
GONN	Genetically Optimised Neural Network
GP	General Practitioner
GUI	Graphical User Interface
HRPE	High Resolution Pressure Elastography
IMU	Inertial Measurement Unit
IR	Infra-Red
JPN	Japan
K-SVM	K means Support Vector Machine
LA	Latin America
LED	Light Emitting Diode

LEDC	Less Economically Developed Countries
LVDT	Linear Variable Differential Transformer
MARG	Magnetic, Angular Rate, and Gravity
MEDC	More Economically Developed Countries
MI	Mechanical Imaging
MP	Mega Pixels
MRI	Magnetic Resonance Imaging
MTBF	Mean Time Between Failure
NA	North America
NB	Naïve Bayes
NFIR	Near Field Infra-Red
PDMS	Polydimethylsiloxane
QALY	Quality Adjusted Life Year
RANSAC	Random Sample Consensus
SCBDL	Soft Clustered Basic Direct Learning
SIFT	Scale Invariant Feature Transform
SNR	Signal to Noise Ratio
SVM	Support Vector Machine
TI	Tactile Imaging
TRL	Technology Readiness Level
USD	United States Dollar
w.r.t	With Respect To
WBCD	Wisconsin Breast Cancer Database
WE	Western Europe

Chapter 1

Introduction

1.1. Chapter Summary

This thesis explores techniques and technologies to continue the long-term development of tactile imaging (TI), a process of measuring mechanical stress distributions using a spatially distributed array of pressure sensors, particularly in medical applications. Tactile imaging technologies, based on capacitive pressure sensors, have been used for decades as a medical imaging tool, particularly for: breast cancer screening (Egorov et al., 2009), internal imaging of the pelvic floor (Egorov et al., 2019) and prostate (Egorov et al., 2006), and prevention of foot ulcers (Tao et al., 2020). In these applications, medical conditions are commonly identified by ‘hard’ lumps that can be detected by measuring stress distribution often before they are palpable by a clinician. This thesis, focussing on the field of breast cancer screening and diagnosis, explores the requirements for developing TI from a basic screening tool into a high accuracy tool for differentiating benign and malignant breast conditions and providing diagnostic metrics for use in later stages of the cancer treatment process. This chapter shall introduce TI and how it works in a medical context and define the project scope, with the requirements for development explored, and fully justified, in Chapter 2.

1.2. Introduction to Tactile Sensing

Tactile sensing in general is a technique for quantifying the sensation of touch using force or pressure sensors. In the same way that a person may press or touch a material and learn about the material from the reaction forces and deformation of the material, so too can a machine view the material properties. The key difference being, when a person does this there is only a qualitative assessment of the interaction, however when tactile sensors are used there is a quantitative assessment of the interaction which allows for further analysis and characterisation of it. This is expanded to tactile imaging when multiple tactile sensors are arrayed together, or individual measurements are spatially related, to form an ‘image’ of physical reaction stress in response to load stimuli. This is commonly used to measure the reaction forces between people and common objects, particularly for: anthropological studies and better product design, or measuring hardness differences in soft materials for medical condition screening.

Relating the above to the topic of this thesis, the interaction in question shall be the palpation of breast tissue for the identification of hard nodules related to breast cancer, which shall be discussed in detail later on in Chapter 2. Although TI can refer to the use of any force sensor array, including strain gauges, resistive, and piezoelectric force sensors; from this point forward in this thesis, TI shall refer to the use of an array of capacitive sensor elements for differentiating soft tissues.

Capacitive tactile sensors can be thought of as simple parallel plate capacitors, which themselves are devices that stores electrical energy, which change their

capacitance in response to an applied force. There are other arrangements and topologies, however the parallel plate capacitor is the simplest and exhibits the same basic properties as more complex architectures. The capacitance is the value that controls the energy storage capability of a capacitor at fixed voltage and is expressed in terms of the physical properties of the capacitor as shown in Equation 1.1. ϵ_0 is the permittivity of free space, the ability of a vacuum to propagate electric fields; ϵ_R is the relative permittivity of the dielectric material, the material placed between the capacitor plates to improve the electric field propagation; A is the overlapping area of the two capacitive plates; d is the separation between the capacitive plates or the thickness of the dielectric.

$$C = \frac{\epsilon_0 \epsilon_R A}{d} \tag{1.1}$$

From equation 1.1, it is clear that capacitance increases as the plate separation decreases. This results in a variable capacitor that can respond to a change in plate separation as shown in Figure 1.1.

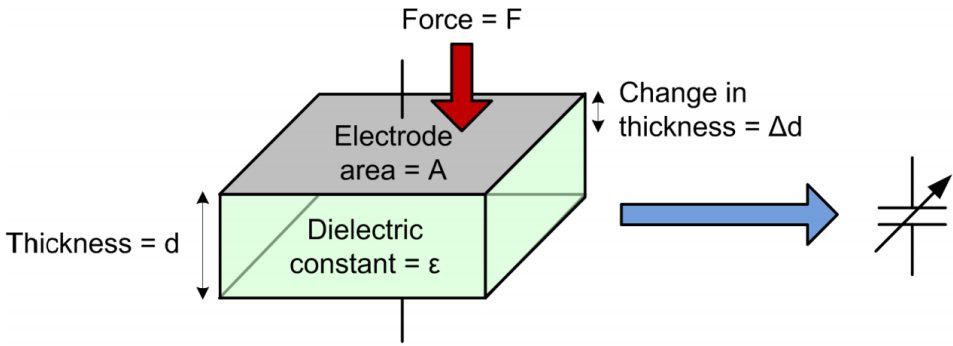


Figure 1.1 - Parallel plate capacitor basic diagram. The capacitance changes with the plate separation, d , resulting in a variable capacitor that measures the plate separation. (Yip et al., 2009)

If the dielectric material is made from a springy, elastic, material such that the capacitor can be compressed linearly in response to an applied force, then Hooke's law can be applied to describe the compression, or change in plate separation, in response to a force (F) in terms of a spring constant (k). This is shown in Equation 1.2 and illustrated in Figure 1.2. The change in an object's length in response to a load can also be described using the material Young's modulus, which is an extension of Hooke's law. By combining equation 1.1 with equation 1.2, an expression for the basic operation of a parallel plate capacitive force sensor can be derived, as described in equation 1.3.

$$\Delta d = -\frac{F}{k} \quad (1.2)$$

$$C = \frac{\epsilon_0 \epsilon_R A}{d_0 - F/k} \quad (1.3)$$

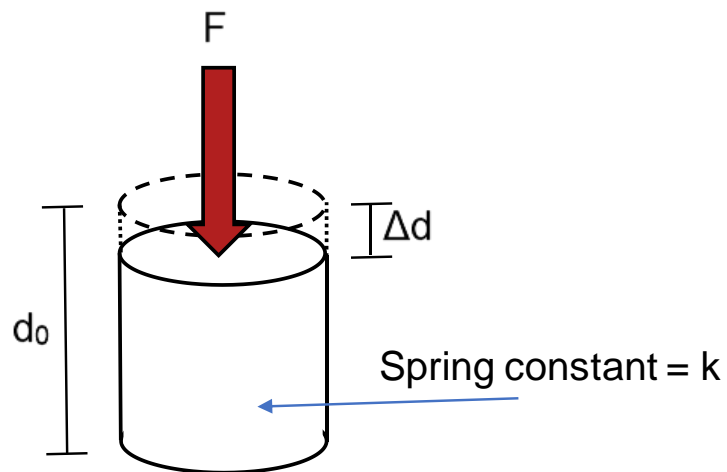


Figure 1.2 - Diagram of Hooke's law. Applying a force, F , to an object causes a deformation proportional to the applied load, controlled by the spring constant or stiffness, k , of the material.

The capacitance of the plate sensor can be measured using a capacitance to digital converter (CDC), for recording on a PC. Equation 1.3 can be used in reverse to determine the applied load from the capacitance as shown in equation 1.4.

$$F = k(d_0 - \frac{\epsilon_0 \epsilon_R A}{C}) \quad (1.4)$$

Several capacitive plate sensors can be combined into an array, as shown in Figure 1.3. Here, rows and column electrodes are layered with the springy dielectric in between them to form a matrix of elements that are read sequentially by a multiplexed CDC. This is done by scanning each row and switching in each column sequentially.

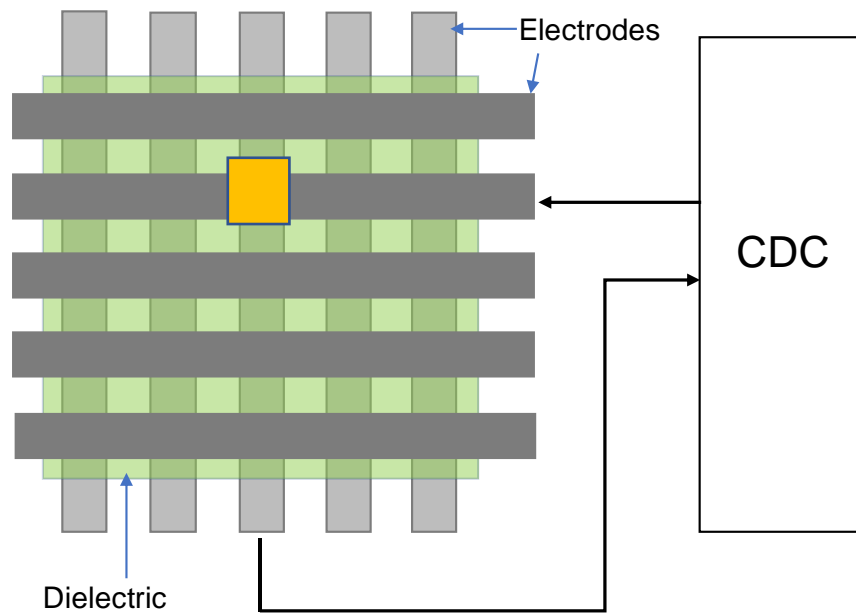


Figure 1.3 - Illustration of a Capacitive tactile array. The capacitance to digital converter (CDC) is connected using an internal multiplexer (MUX) to each row and reads elements sequentially by scanning each row and column. On this 5x5 element illustration, the CDC would read from element [3,4], highlighted.

The basic tactile array is mounted onto a rigid backing, the shape of which is dependent on the required application, additionally, the number and size of the elements is variable depending on the application. Data from the tactile array, read by the CDC, can be combined into a pressure map, which displays the pressure distributions across the array. This pressure map can then be analysed to design comfortable products or to make medical decisions depending on the application. For example, if a person was to stand barefoot on a flat array, the pressure map would show the contact points, potentially showing things like flatfoot or over pressure that can lead to ulcers as shown in Figure 1.4. If a tactile array is pressed into breast tissue, the resultant pressure map can indicate hard spots within the breast that may not even be palpable to a clinician, as shown in Figure 1.4. These applications shall be discussed in detail later in this thesis.

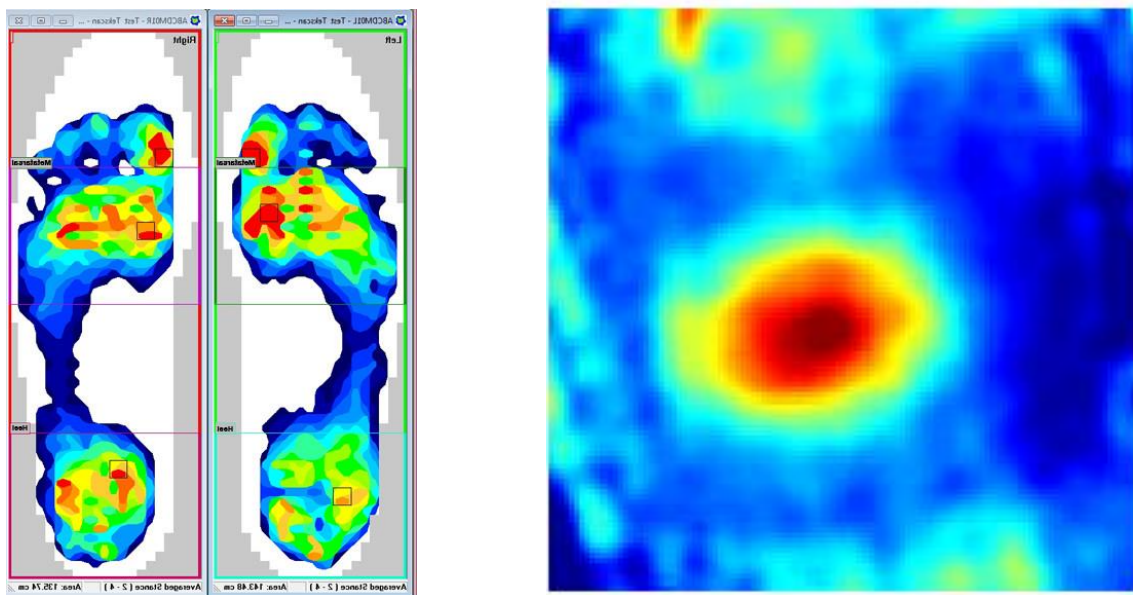


Figure 1.4 - Example Tactile Images. Left) Foot contact pressure map used to visualise contact stress for designing comfortable footwear and reducing ulcers (Tekscan. Inc., US) Right) Tactile image of an embedded breast lesion, used to screen for malignant breast conditions (Wellman et al., 1999b).

1.2.1. Introduction to Tactile Breast Imaging

Manual palpation has long been a staple tool in clinical diagnosis, from feeling for: a broken limb, bloating of the stomach, or lumps in the breast; with clinical experience allowing for correlation of the sensation with a diagnosis. In breast cancer diagnosis, but similar for other conditions, the link between the elasticity, or stiffness, of a breast lesion is known to be correlated to histological diagnosis (Woods et al., 2011).

The most common methods of initially detecting breast lesions are the clinical breast exam (CBE) or self-breast exam (SBE), where the breast is palpated manually to detect lumps or pain, but, since people are unable to quantify the elasticity of a suspected lesion or even agree on a qualitative description (Farrugia et al., 2015) this almost always requires a secondary care referral for a mammogram, the standard screening method, for diagnosis. The number of benign referrals generally is close to 90% (McCain et al., 2011), which gives a good indication on the relatively high sensitivity, and poor specificity, of the CBE or SBE.

This is where tactile imaging comes in; introduced as a method of quantifying touch, an obvious application for it is in medical palpation. TI is used clinically in several countries including US, India, Saudi Arabia and Mexico, but is not generally considered to be standard practice by national health boards. The earliest form of tactile imaging applied to breast imaging was called full breast mammobarography (Gentle, 1988). This did not have any advantages over mammography, other than the lack of radiation, and so it was quickly adapted into a handheld system for patient comfort (Wellman et al., 1999b) able to produce localised images of suspicious lesions. These

handheld systems were capable of forming local images under the probe, but the whole breast view was largely lost, or made impractical in clinical use.

Following continued academic and private development (Egorov and Sarvazyan, 2008), TI was proven to be effective in reducing unnecessary biopsies by 21% by successfully classifying lesions as benign or malignant based on the contents of the tactile images (Egorov et al., 2009), later independently validated (Tasoulis et al., 2014). In these studies, the authors say the classification of benign and malignant conditions could be improved with more detailed diagnostic metrics including but not limited to, the absolute elasticity of the tissue and spatial information on the lesion such as the location and relation to other breast structures.

Despite the advances in breast TI, the technology is not considered standard clinical screening practice in most countries, although the technology is gaining traction in countries such as India, Saudi Arabia, and Mexico where x-ray mammography is not commonplace as it is in the US and UK (Sarvazyan et al., 2008). The need for cost effective screening has led to the introduction of TI in these countries, where median incomes are low and cancer rates are high. In the US and UK, TI is used as a hassle free tool in private clinics for screening however this always requires referral to a hospital for mammography to be sure as it is not considered clinical practice in the UK. Patients may be spared a stressful trip to a hospital in the US using breast TI, following a negative result, where the use of such devices is more accepted. It is important to improve and demonstrate the reliability of TI to ensure adoption in developed countries, and to develop safe, reliable, and cost-effective screening tools for less developed countries.

1.2.2. Research Questions and Objectives

The ultimate goal of this thesis, and related future works, is to move towards answering: to what extent can the classification accuracy of breast condition using TI be improved by new/improved diagnostic metrics? This is in line with a void in the literature following the works of (Egorov et al., 2009) and (Tasoulis et al., 2014), where improved metrics were postulated to be able to reduce the benign biopsy rate by up to 80%. Due to constraints on available technology, budget, and logistical issues during the period of this work it is impossible to fully realise this goal, however the steps required to achieve the ultimate goal can be explored in greater detail, trading breadth of scope found in other theses (Wellman, 1999) for detail and practical use considerations for generating maximum clinical impact. The preceding questions leading towards the ultimate goal are: What metrics are required to improve tactile imaging performance, compared with what is currently available from TI? And: What are the fundamental requirements for deliverance these metrics, and what technologies can be leveraged to deliver them? Answering these questions shall form the theme for an extensive literature review, delivered in Chapter 2. During the literature review, key metrics are identified and ranked for priority allowing for technology for delivering metrics to be determined, that will be addressed in subsequent chapters.

A pressing point in the medical TI literature is the lack of acknowledgement of tactile sensor error sources, which limits the usefulness of current TI to simple visualisation. Understanding and mitigating these error sources is critical to developing practical systems that function outside of laboratory conditions, and to linking early

stage phantom research with live clinical results helping to explain differences in performance. To this end we must answer: what error sources affect the output from a tactile image and what are the clinical implications of this?

1.2.3. Research Trajectory and Defined Scope

It is known that with additional diagnostic information, the clinical performance of TI will improve and become more accepted in the clinical environment, and with additional burden of proof and proven reliability can become accepted by national health boards. It is unlikely that TI will take the place of mammography in developed countries with structured healthcare systems such as the UK where mammography is the standard for screening, however there is scope for development in less developed countries where a cost effective mass screening tool is needed due to the lack of mammography in such environments. As such, the trajectory of breast TI in future is towards a high accuracy, cost effective screening tool for widespread use in LEDCs (Broach et al., 2016), and a hassle free differentiator for MEDCs to save patient exposure to uncomfortable mammography and to improve on the subjective reporting of lesions by overstretched clinicians (Lefemine et al., 2012).

It is not feasible to fully realise this goal during the course of this PhD due to the current state of clinical TI, resources required and resources/logistic arrangements available during this project. The scope of the project is subsequently limited to the development of support technology to improve the diagnostic capability of TI, and characterisation of the technology in phantom trials to provide a stable technological platform for future clinical and societal trials to continue the clinical development of TI.

1.3. Knowledge Contribution

This project has led to a number of valuable research outcomes and contributions to knowledge to the benefit of both academia and commercial partners. These contributions are both technological and analytical in nature, filling gaps in the literature.

1.3.1. Formal Contribution to Knowledge

This thesis presents the following formal contributions to knowledge, in the form of publications (P) and/or as thesis chapters (TC), expected to become publications:

1. Novel elasticity measurement technique using single element tactile sensors fused with inertial and orientation sensors (P).
2. Novel material strain measurement technique using double integration of compression acceleration data, with application specific error management (P).
3. Novel vascular mapping technique based on non-rigid image registration using IR cameras and tactile sensors (P).
4. Novel image rectification technique to rectify local camera/scanner induced deformation of the breast using tactile sensors (P).
5. Novel breast background elasticity measurement from SIFT point tracking in camera/scanner palpation images (P).
6. Novel tactile image mosaicking technique, independent of applied load, based on the use of auxiliary IR camera systems (P).
7. Error analysis of medical tactile imaging systems used in breast cancer imaging, with investigation into the effect of error sources in practical use cases (TC).

1.3.2. Other Research Outputs

This thesis presents the following additional research outcomes that, whilst not necessarily academically novel, were important to the success of the project, or will become important for future works in this area. These outcomes are largely ‘housekeeping’ research outcomes, or to increase commercial impact, however the lack of acknowledgement of such things in the literature validates their worth as valuable research outcomes.

1. IR camera and tactile mapping system integrated into commercial tactile imaging system footprint, to ease implementation and increase TRL.
2. Method for normalising mounted tactile arrays, useful for manufacturers.
3. Mechanical error analysis of real material dielectric capacitive pressure transducers, with low budget methodology.
4. Inverse error model for parallel plate pressure transducers, with commentary on the requirements for implementation, useful for operators of tactile sensors

1.4. Publications

A number of academic works have been published, or engaged in, either directly through the PhD project or through contacts gained during the process in related fields. The accepted journal publications are used as material for this thesis in Chapters 3 and 4 respectively. Additional publications are in the pipeline or under review at the time of thesis submission, based on the works of Chapters 5 and 6.

1.4.1. Accepted Journal Publications

R. Hampson, G. Dobie and G. West, "Elasticity Measurement of Soft Tissues Using Hybrid Tactile and MARG-Based Displacement Sensor Systems," in IEEE Sensors Journal, vol. 19, no. 22, pp. 10262-10270, 15 Nov.15, 2019, doi: 10.1109/JSEN.2019.2930207.

S. Rana, R. Hampson and G. Dobie, "Breast Cancer: Model Reconstruction and Image Registration from Segmented Deformed Image Using Visual and Force Based Analysis," in IEEE Transactions on Medical Imaging, vol. 39, no. 5, pp. 1295-1305, May 2020, doi: 10.1109/TMI.2019.2946629.

1.4.2. Note on Published Material Re-use

Chapter 3 of this thesis is entirely derived from the former paper, exploring the use of inertial sensors in tactile sensing and elasticity imaging applications. The work presented in the paper is entirely my own and copyright permissions have been granted for this case.

Chapter 4 of this thesis is based in part on the latter paper, exploring the use of tactile sensor and IR cameras to produce tactile maps of the breast. The work presented in the paper is only partly that of my own, specifically sections relating to hardware design, elasticity measurement, calibration, and experimental procedure were the work of myself and shall be developed in this thesis. Suitable author differentiation and credit is given in the relevant chapter subsections in this thesis. Copyright, and other author, permissions have been granted for material use in this case.

1.4.3. Works Under Review/ In Preparation

R. Hampson, G. West, and G. Dobie, “Non-rigid registration of tactile images onto the breast vascular network using infra-red vein imaging”, IEEE Transactions on Medical Imaging. (In preparation) Based on Chapter 5 of this thesis.

R. Hampson, R. Matthews, R. Pratico, and G. Dobie, “Effect of environmental influence and sensor error on static and dynamic tactile imaging in clinical applications”, in IEEE Sensors Journal. (Under Review) Based on Chapter 6 of this thesis.

1.5. Thesis Structure and Chapter Summary

Chapter 1 of this thesis introduced the problem and formally defined both the project goals, with limitations on scope, and the outputs in terms of knowledge contributions and published papers. Chapter 2 shall expand on these problems, by defining the requirements for successful breast cancer diagnosis and by defining what the current capability is, both commercially and academically, for delivering the required metrics using TI. This chapter shall answer the question of “what needs done?” based on a comprehensive literature review of this and related fields, before offering the range of activities to be undertaken. Naturally not every avenue can be explored, so priority tasks shall be highlighted, and the remainder shall form the basis of future work in this area. Specifically, for this thesis, these areas will be elasticity measurement of background breast tissue, and non-subjective lesion localisation on the breast through mosaicking of tactile images.

Following the definition of requirements from Chapter 2, Chapter 3 shall begin solving the problem of measuring the background elasticity of breast tissue which is known to be difficult with currently available TI systems. This is done by integrating inertial and orientation sensors into TI, allowing for the simultaneous measurement of stress and strain, and assessing the system accuracy and reliability over a range of realistic breast phantom materials. While this technique shall prove effective in measuring the breast elasticity, it is found to be unsuited by itself in producing tactile maps of the breast. This, coupled with the practicality of such a system in clinical use, shall lead to the abandonment of this technology in favour of technologies capable of simultaneous elasticity measurement and mapping.

Chapter 4 shall develop lesion localisation technology based on the fusion of IR cameras and tactile sensors. This technology shall be shown to be effective in both measuring the background elasticity of soft materials and producing tactile maps. Lesion tracking between cancer screening sessions is important for assessing malignancy and so accurate and patient specific localisation of a lesion, with transferable and time trackable location markers, is a must for any next generation screening and diagnosis technology.

Chapter 5 shall explore the changes required to use the developed technology from Chapter 4 on live breast tissues and integration with commercial TI systems, specifically miniaturising the technology of Chapter 4 into a commercial footprint. This provides a working prototype system capable of measuring elasticity and spatially relating tactile images, which will lead on to recommendations for implementation in future works. These developments will raise the system technology readiness level (TRL)

from TRL1 to TRL4 (NASA, 2012). Engineering and supply problems during the course of the project limited the scale of integration and subsequent development to TRL5. This chapter also shows parametric testing of system performance vs simulated breast tissue and scanning conditions to validate this proof of concept system. In this trial the tactile mapping accuracy of the system, in terms of the reconstructed scanning path, is tested vs. material background elasticity and vs. the number of available tracking points. The measurement accuracy of the background elasticity is similarly tested vs. the true elasticity vs. the visual feature density. The results are compared against professional, commercially available, reference standards for analysis.

Chapter 6 shall develop the system prototype further by investigating tactile sensor error sources applicable to this application and exploring their effects on measurements of tactile objects. This leads into an inverse error model being proposed and tested for key error sources. This provides a stable foundation for which to do detailed material testing in future works, and an expectation of performance when transferring between phantom testing and clinical trials.

Finally, Chapter 7 shall conclude the thesis with a discussion on the efficacy of the developed systems in delivering the desired metrics, as well as a discussion on the practicality of such systems for use in the clinical environment. This will be followed up with recommendations for future work in this line of research.

Chapter 2

Literature Review

2.1. Introduction

This chapter summarises the UK breast cancer screening pathway, with discussion on how tactile sensor systems fit into this pathway worldwide, acknowledging that TI is not current clinical practice in the UK.

Following a detailed review of the clinical significance and performance of TI in breast cancer diagnostics, and a general overview of other breast cancer imaging modalities and devices, this chapter presents a review of clinical differential metrics for breast cancer diagnostics. This allows for a critique of the historical performance of TI in automated diagnosis, with comparison with automated detection from other modalities in a corresponding time frame. This analysis allows for the project scope to be defined, addressing limitations and opportunities presented in the critical review of TI, addressing gaps in the literature and commercial landscape towards the goal of developing the capabilities and reliability of TI in automated breast cancer diagnosis.

2.2. Clinical Breast Imaging Using Tactile Sensors

2.2.1. Clinical Breast Cancer Screening in the UK

Referring to Figure 2.1: A simplified flowchart of the current screening process derived from the UK National Institute for Health and Care Excellence (NICE) guidelines NG101 (NICE, 2018), and discussions with clinical professionals, surgeons, and oncologists; a patient's view of the process from start to classification is shown. The flowchart is an over-simplification of a complex and variable screening process implemented by clinicians following the NICE cancer referral pathways (NICE, 2020a), distilled down to the basic pathway for imaging technology that a patient or member of the public would see. Current breast cancer screening is split into 3 primary imaging steps, each increasing in both severity and invasiveness, of which the first step in the screening process is manual palpation performed in the clinical breast exam (CBE). The following steps of mammography (X-ray) and other additional imaging techniques are usually performed if there is not enough information for a differentiation, or as part of controlled screening in the case of mammography. Note that many technologies are not listed, as they are not commonly used for screening and early detection (NICE, 2018), and inclusion of all available technologies is not conducive to easily understandable diagrams (Public Health England, 2018).

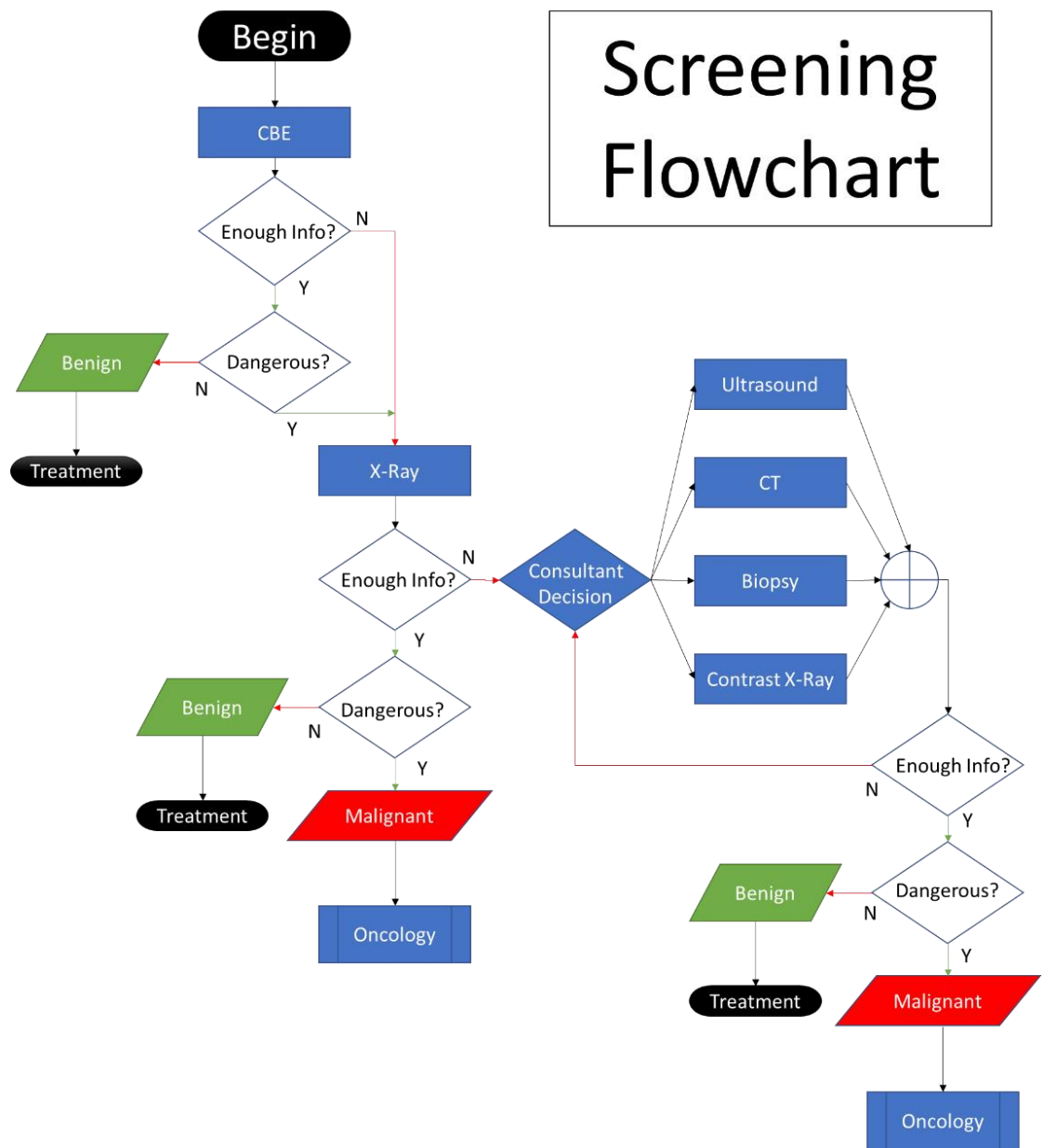


Figure 2.1 - Breast cancer screening process in the UK. Progress to the next stage of the imaging process is based on whether there is adequate information from the current stage for discrimination of malignant/benign. Benign conditions would then be passed into regular treatment processes, malignant conditions would then be passed to oncology. The consultant decision phase is largely based on what is available at the local hospital, as many rural hospitals do not have CT equipment.

The rules or guidelines governing the process and the passage of patients through the process are complex and vary depending on patient parameters. For example, according to NICE guidelines NG12 (NICE, 2020b), a patient in the UK screening program aged 50-70 with an inversion or texture change in the nipple, or patients aged over 30 with an unexplained lump would receive priority referrals to the next screening stage within 2 weeks. Other patients with skin changes related to breast cancer, or aged 30+ with lump in the axilla, may receive priority referrals. Patients aged <30 with an unexplained lump will not be given urgent referrals (within 2 weeks) to the next stage, unless exhibiting other symptoms on the skin or nipple (Public Health England, 2018). These rules make it difficult to relay the full process to the public in a simple diagram, without causing alarm, and so Figure 2.1 only shows the technological pathway, rather than the detailed process leading from one technology to another. The basic process for breast cancer screening, starting with the CBE at a GP surgery, is outlined below.

CBE is the process of manually palpating the breast to detect hard or tender areas. Formal CBE is typically done by a general practitioner (GP) at a GP surgery and can be precipitated either through the UK breast cancer screening program for women aged 50-71 or, more commonly, by women performing the self-breast exam at home. It is difficult to obtain accurate estimates for the voluntary screening program, or for use of self-breast exam (BSE), but it is well documented that people go to their GP when they exhibit 1 or more of the 5 indicators of breast conditions: A palpable lump which may be visible, a change in breast skin texture, a change in nipple appearance, nipple discharge, redness or rash around the nipple (Public Health England, 2018).

The purpose of the CBE is mainly to collect information for referral to the second stage, X-ray mammography, however it is often possible to differentiate benign conditions at this stage and recommend a regular treatment program for the condition. If there is not enough information at the CBE stage, which is common, or a differentiation can be made where the outcome is likely malignant, then the GP will make a referral for X-ray mammography (NICE, 2020a). Most patients in screening programs are sent directly for mammography due to the current low cost, approximately £150/exam, differential ability and sensitivity compared with CBE. Physicians will typically use risk to determine their recommendations for treatment or further testing, and so will nearly always refer the patient for mammography (>95%) from the CBE. If there is not enough information from mammography to differentiate the condition, then the patient will be invited back for more scans or assessments which will typically be selected based on the availability of local facilities such as: Ultrasound, Computer aided Tomography (CT/CAT), Surgical Biopsy, Contrast X-ray, and MRI. Benign conditions diagnosed from these methods will be referred to regular treatment programs and malignant conditions will be referred to oncology which will perform their own tests typically with MRI or CT. It is estimated that 1/25 patients will be invited back for further scans after X-ray mammography, due either to genuine conditions or from inconclusive results, with ¼ of these patients having genuine cancers (NHS, 2018). The screening process is fairly robust, with the false negative result rate estimated at 1/2500. The system may be oversensitive, or not specific enough in diagnosis, as 3/200 women screened every 3 years from age 50-70 are diagnosed with cancer that would not have become life threatening. This oversensitivity results in patients receiving unnecessary treatment,

increasing the risk to the patient and the burden on the health system. However, as the primary purpose of the screening process is to detect cancers whether life threatening or not, this problem is low on the priority spectrum, particularly as it is not well understood whether the cancer will become life threatening later. The final determinant of breast cancer, and gold standard for diagnosis, is surgical biopsy and subsequent analysis by a pathologist. Mammography, and the other screening methods or diagnostic methods if instigated by symptoms, serve to sort critical patients for diagnosis via biopsy. Sending known benign conditions away for regular treatment reduces the number of patients subjected to unnecessary biopsies, which does have the risk of complications just like any other surgery, and so the use of screening and diagnostic imaging is important for reducing patient stress and healthcare burden.

2.2.2. Issues in Clinical Reporting

One of the biggest problems faced by overstretched physicians and GPs is the quality of reporting during the referral between CBE and X-ray mammography. The current process requires a form be filled out detailing the reasons for referral, where a typically concise statement would be ‘lump in left breast’. This is not so much a problem in facilities that have X-ray machines where the scan is performed/examined by the same physician within a short period of time, where the area of interest on the breast can be remembered. This becomes an issue when dealing with separate facilities, or separate practitioners, particularly if it is not immediately clear from the X-ray where a suspected condition may be on the breast. This results in many delays, with patients sent home, or repeated testing on a patient that is unnecessary. After X-ray, in later stages of the

process, this reporting is less of a problem as there are images and reporting schemes such as BI-RADS (American College of Radiology, 2013) that allow for quantisation, or discretisation, of subjective measurements. Modern NHS breast cancer referral forms, examples of which can be found in Appendix A, go a long way to alleviating the reporting issues experienced by physicians of the 1980s and 1990s as the forms typically include diagrams that assist with locating the lesion and various fields to provide descriptions from the CBE. These forms have been shown to reduce unnecessary referrals (Lefemine et al., 2012) when properly filled out. The improvement is limited by a lack of physician cooperation, with 25% of referrals still dictated or handwritten (Lefemine et al., 2012), and by a lack of widespread standardisation between NHS trusts. This is clear from the differences between the forms in Appendix A, where both the level of detail and length of the forms vary greatly between trusts in England. There are two primary limitations in these forms. Firstly, the information detailed is subjective and prone to errors and omissions. Secondly, the increasingly detailed forms developed in recent years take increasing amounts of time to complete, which has reduced the number of fully completed forms from 83% in 2005 to 58% in 2010 in a random audit (Lefemine et al., 2012). The most common omission in the audit was the differential diagnosis, indicating whether breast cancer was suspected, which could be reasonably described as a valuable piece of information. This could be down to subjectivity, or that the forms are still too cumbersome for accurate use.

The problem of subjectivity is widely acknowledged and has led to the introduction of standardised forms for breast cancer referral, which in theory helps with

the reporting of issues, but not with the subjectivity in what is detected (Lefemine et al., 2012). The reason for this comes down to physicians often describing breast conditions and breast size using fruit similes (Wellman, 1999), which is obviously not conducive to detail measurements of tissue properties for cancer diagnosis. It is these issues that handheld TI aimed to solve, and it was successful to a reasonable extent (Egorov et al., 2009), but more remains to be done to allow TI to compete with mammography and other methods in diagnosis and become standard practice. To advance current clinical TI the system must be given the ability to view the whole breast similar to mammography (Woods et al., 2011), get a global view of the elasticity of the breast and variation therein, and be able to spatially locate lesions within the breast without subjectivity for later tracking, whilst maintaining the cost effectiveness of the system to a level at least that of mammography (Mandrik et al., 2019). The other way of improving cost effectiveness is to greatly reduce the costs of the systems by reducing complexity, rather than improving diagnostic capabilities, which is the strategy of more recent researchers (Broach et al., 2016).

It is widely acknowledged that there is a balancing act to be done between the rigid bureaucracy of detailed forms, and the need for GPs to process patients quickly and keep up with ever increasing workloads. It is known that standardised forms are effective in reducing rejected referrals, and so the GPs and the public will benefit from any system implemented to facilitate easy form completion. This could come from either: automatic computer form completion, or from improved differential diagnosis ability to remove the subjectivity and fill out this complex form field.

2.2.3. General Breast Cancer Screening Globally

Looking more generally at breast cancer screening, the rates for cancer deaths and screening by mammography vary drastically with geographic and political location globally. The research of (Sarvazyan et al., 2008) summarises this divide using data for 2005 in Figure 2.2, where it is shown that ~80% of the female population aged 25-70 live in less economically developed countries (LEDCs), constituting ~70% of global breast cancer deaths, whilst only having access to <10% of global mammograms (Liang et al., 2003) when compared with more economically developed countries (MEDCs). This divide was found to still be relevant in recent times (Mandrik et al., 2019). This is directly related to the prevalence and cost of mammography in these economic areas.

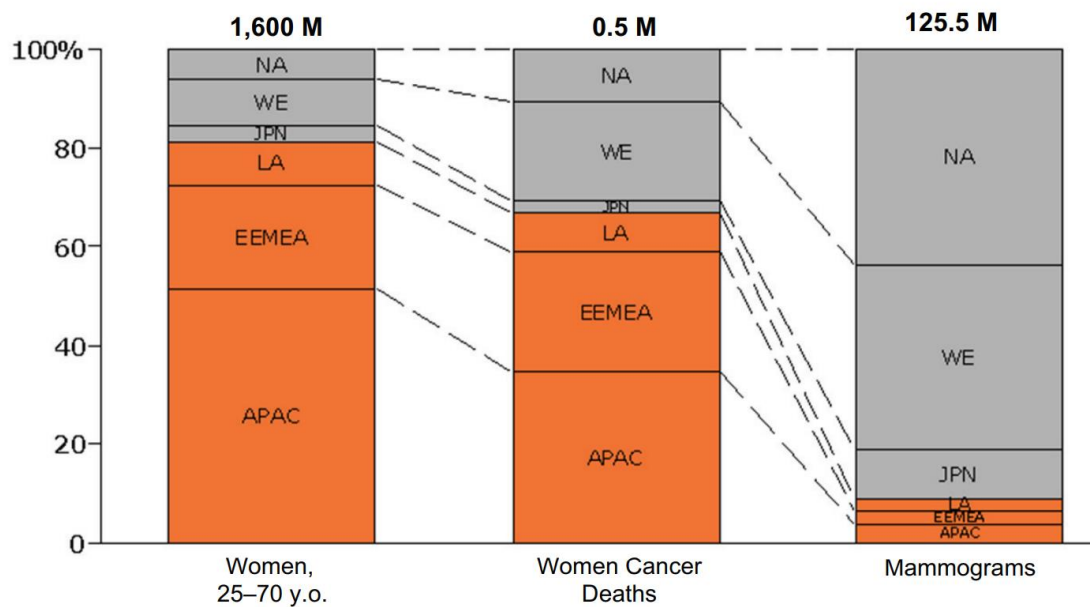


Figure 2.2 - Divide of mammography, breast cancer deaths, and population across geographic areas from (Sarvazyan et al., 2008) for 2005. The result shows clearly that the MEDCs have fewer deaths and more mammograms compared with LEDCs, correlating lower access to advanced diagnostic and screening techniques with higher fatality rates.

In MEDC areas, it is easy to simply opt for a mammogram as they are available and relatively inexpensive however in LEDC areas it is not feasible or often even possible to perform mammography as a default option. In these areas there is a much greater reliance on the CBE (Anderson et al., 2006). As such, there has been drives both commercially and in the literature to make breast cancer screening more affordable, or cost effective, in these economic areas by either reducing the cost of mammography or by developing new technologies to improve the diagnostic and differential capability of the CBE without the excessive cost of the X-ray mammogram.

There are numerous alternative methods to mammography including: ultrasound, MRI, ultrasound/MRI elasticity imaging, biopsy, and tactile imaging, although none of these methods are direct replacements. Ultrasound and MRI are not feasible for mass screening in LEDCs, as these machines are rarer than X-ray machines, and it is both impractical and dangerous to biopsy everyone, so a remaining option is tactile imaging. Tactile imaging, applied to breast cancer screening has been projected to cost 5 USD/exam in LEDCs and 50 USD/exam in MEDCs (Sarvazyan et al., 2008) (Sure Inc., US) when screening is performed by a physician's assistant. This translates to a projected cost effectiveness of 162 USD/QALY compared with 1846 USD/QALY for film mammography in LEDCs (India) (Laxminarayan et al., 2006) (Mandrik et al., 2019). This is only a projection, and there is not enough data from tactile imaging to form accurate cost effectiveness figures, as it is not part of standard screening processes in most countries; it presents a feel for current screening trajectory. Although much of the literature on diagnosis focuses on continuing to develop mammography, as that is

here to stay, there is growing attention being paid to developing cheaper and less invasive technologies, including tactile imaging (Sarvazyan and Egorov, 2012).

The key point here is that a national screening program based on advanced technologies such as mammography or CT, though effective in MEDC areas, is not practical in LEDC areas where the majority of the global population resides. These populations require lower cost screening methods, more effective than simple CBE at differentiating benign and malignant conditions; Tactile Imaging being one such option (Wellman et al., 1999b) (Egorov et al., 2009) (Broach et al., 2016), although these are not yet considered to be standard practice.

2.2.4. Tactile Imaging Use in Current Breast Screening

Tactile imaging (TI) for breast cancer screening, sometimes referred to as breast mechanical imaging (BMI), mechanical imaging (MI), differential stress imaging (DSI), or high resolution pressure elastography (HRPE); is a method of identifying, quantifying, and reporting breast conditions by measuring the apparent hardness of a breast lesion using tactile pressure sensors (Sarvazyan and Egorov, 2009). TI, on the screening flowchart in Figure 2.1, would take the place of CBE in developed countries where X-ray mammography is the de-facto standard (Sarvazyan and Egorov, 2012) and is used instead of CBE and often in place of mammography in LEDCs, where available (Broach et al., 2016). It is important to note, for the sake of clarity, that TI is not used as part of the standard clinical screening/diagnostic process in any country except Mexico where the technology is being adopted. In the US and UK, TI is a commercial tool used in GP (equivalent) clinics for patient screening, replacing CBE where available, but still

requiring referral to a hospital upon a suspected detection, where the patient would then follow the countries national screening pathway as previously described.

TI, in this case SureTouch™ (Sure Inc., US), is an FDA approved non-invasive breast elastography tool, used to quantify the sensation of touch and remove the subjectivity inherent in the CBE, improve the reporting quality during subsequent referrals whilst reducing the burden on the GP/physician. This has been shown reduce the rate of benign referrals of approximately 21% in clinical studies (Egorov et al., 2009), meaning the rate of unnecessary biopsies and X-rays are reduced, alleviating some of the burden on the healthcare system which is beneficial to the patient, where lower stress improves recovery times (Levkovich et al., 2015).

A patient would attend a participating TI practice where a GP (or equivalent), or an orderly (US), would perform a tactile scan in place of CBE. The patient is laid in a supine position on an examination bed and the tactile imaging system, after calibration, is scanned gently over the breast surface including the armpit as shown in Figure 2.3. This process will highlight areas of higher ‘hardness’ than others that will then receive a second pass. The second pass images the area of interest in more detail, allowing for estimates to be made of the lesion shape and size as shown in Figure 2.4.

The 12x16 capacitive pressure sensor array on SureTouch, compacted into a 40mm x 50mm area, is capable of resolving multinodular lesion and estimate the size of a lesion with greater sensitivity than CBE or ultrasound (Wellman et al., 1999b), with 15 times the spatial resolution of similar TI systems such as iBreastExam (UCLifeSciences – IN).



Figure 2.3 - Tactile breast exam performed at GP equivalent surgery (US). The physician scans the breast using the tactile imaging system (SureTouch – Sure Inc., US) using gentle pressure. The tactile imaging system quantifies the sensation of the CBE.

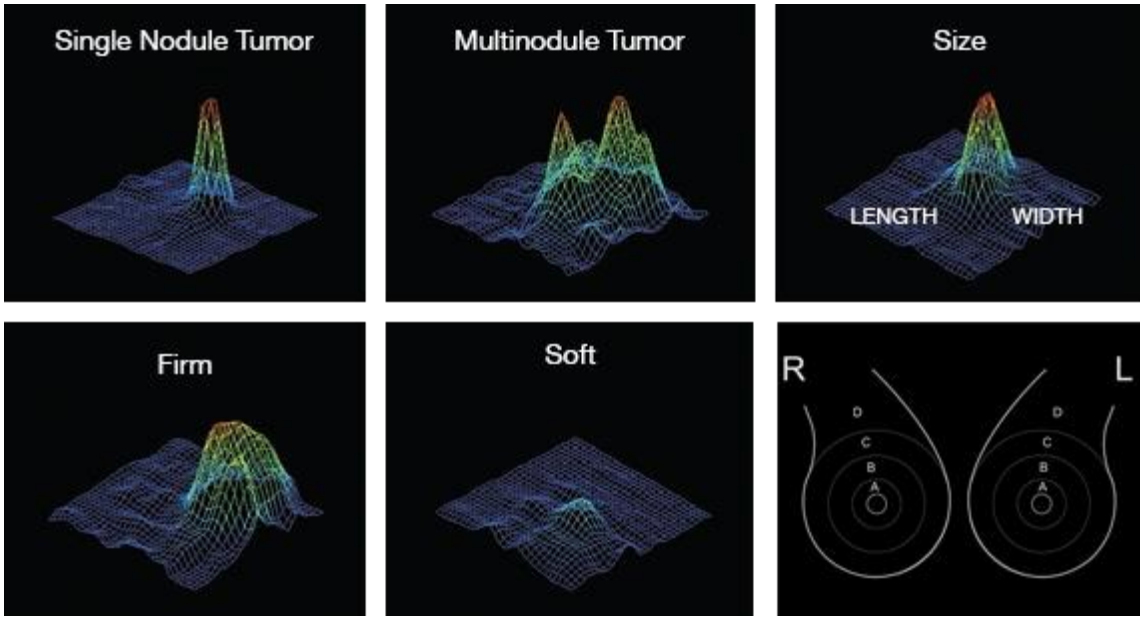


Figure 2.4 - Example of Tactile Images of suspicious breast conditions. Tactile imaging uses high spatial resolution to detect complex lesion shapes and differentiate between hard and soft features using differential stress on the image. The cross section of the lesion can also be determined. The lesion location is then indicated on the 2D topography plot (bottom right) for reporting.

On completion of the 15 minute scanning process, an output report is automatically generated as shown in Figure 2.5, similar to the referral forms in Appendix A. The report contains details of the patient, and separate outputs for each breast consisting of: A lesion location on the breast highlighted by a cursor point, a heatmap and stress plot of the lesion with load condition for inter scan comparison, a lesion size estimate, and a relative hardness estimate. This report is then analysed by the physician to determine the appropriate action, and will form the basis of a well structured referral note if required, providing the subsequent screening physician high quality information on the nature of the patients condition. This output report fills in all of the important fields in the NHS referral forms, but in a simple digital format.

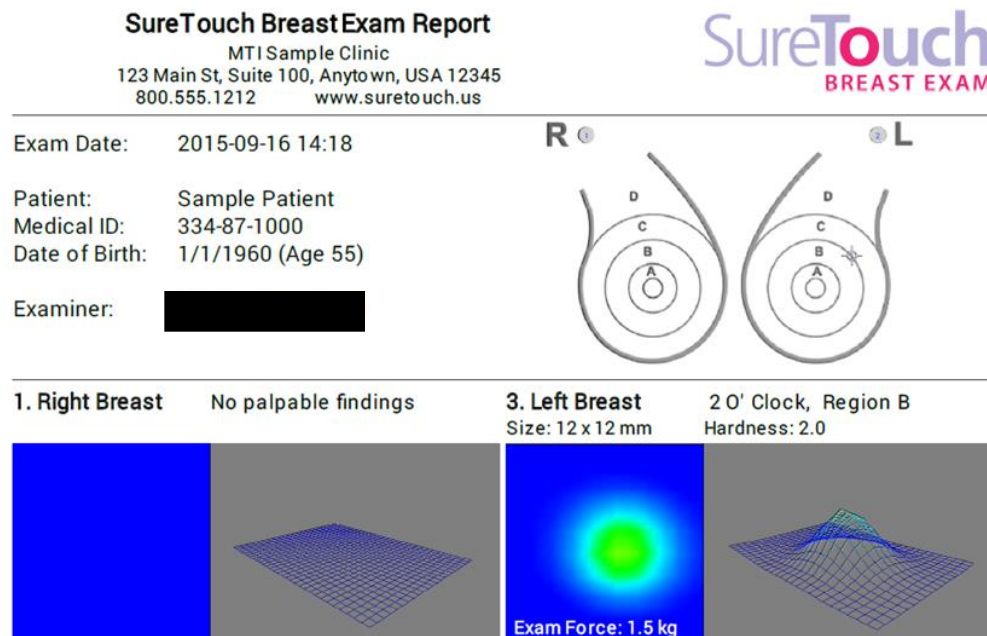


Figure 2.5 - SureTouch Output Report. The output report from the SureTouch tactile imaging system gives patient details, and separate findings for each breast. In this, a lesion position is indicated, with a relative hardness value, estimated size, and the exam load used for comparison between scans. The tactile image given for each breast is a differential stress image over a suspicious area of the breast.

There has been several attempts in academic literature to improve the abilities of TI, by creating large composite tactile maps of the whole breast using a scanner position tracking system (Wellman, 1999), creating tactile maps of the breast using tactile image mosaicking by tactile feature tracking (Egorov and Sarvazyan, 2008), and automatically differentiating benign and malignant conditions from tactile images (Egorov et al., 2009). These developments have not yet been implemented into current clinical TI systems. The first method is not implemented as it requires a >\$100000 magnetic position sensor system, making the system not economically viable. The second is not implemented as there is no clinical requirement for such a tactile map in the current screening role of TI, to provide information for referral to mammography. Additionally, the tactile maps produced by this method are not registered to a fixed location on the breast, there is no identifying location metric other than the original SureTouch output report. The third method is not implemented as this would change the products FDA classification, and there have been insufficient studies done to determine the accuracy of such diagnostic methods on large populations.

If TI is to be used in lieu of mammography however, particularly in LEDCs as mammography is well cemented into clinical procedure in MEDCs, then it must have the ability to differentiate between malignant and benign conditions without referral for mammography (or other methods), and output results with feature detail comparable to mammography. New methods of collating tactile data and evaluating diagnostic metrics must be developed for this to be successful and adopted in this use case.

2.3. Other Medical Applications of TI

Traditional TI systems, that is capacitive sensor arrays, have been applied to other cancer screening applications such as prostate imaging and transvaginal pelvic floor imaging, there are many other applications, but these are the most relevant. As expected, these are common historic uses for manual palpation in clinical diagnosis. Developed in parallel with breast tactile imaging (Sarvazyan, 1997), the prostate and transvaginal imagers deployed similar tactile technology to the breast imaging system, but compacted into a smaller array for comfortable use as shown in Figure 2.6 and Figure 2.7, these are used to detect prostate cancer and pelvic organ prolapse (POP) respectively.

The method of forming tactile images, and measuring tissue properties is similar for breast, prostate, and vaginal imaging, however a key difference is that prostate and vaginal systems are easily able to form compound tactile images of the full structure in a manner not dependent on the applied load. This is done using an insertion depth sensor and an orientation sensor that determines the depth and angle from the sphincter/opening to the tactile array. This allows the tactile array to be spatially located on the prostate or vaginal wall. This is an important distinction from breast tactile imaging, as this approach is not possible on the breast as there is no ‘opening’ for position to be measured with respect to. Additionally, the relatively constrained nature of the prostate in terms of size, shape, and location meant that tactile images can be fit to a pre-generated model of the prostate for better visualisation.

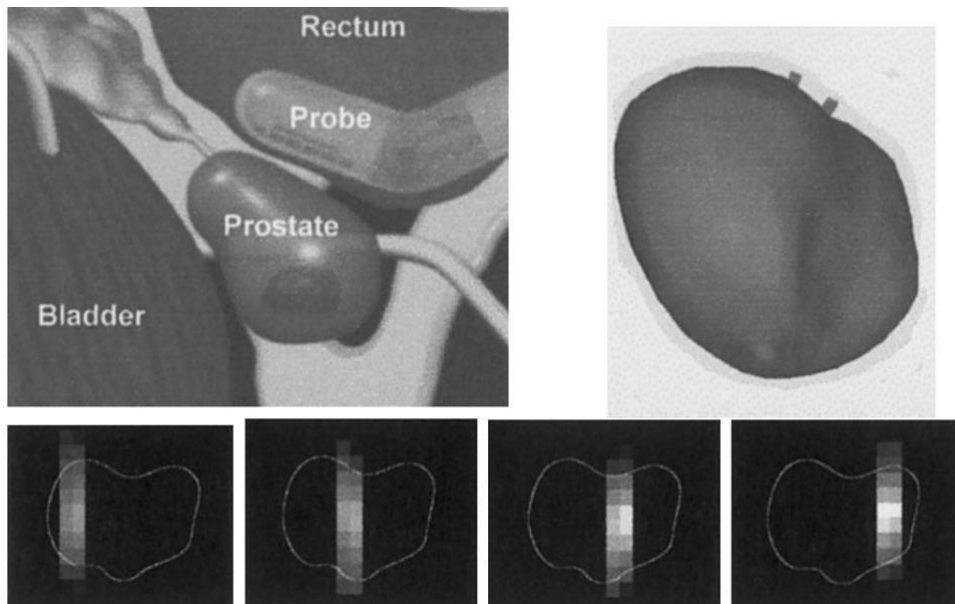


Figure 2.6 - Prostate Mechanical Imaging using TI (Sarvazyan, 1998). The tactile array gives a ‘slice’ of the prostate, which are then mosaicked together using spatial relation information obtained from probe depth and orientation sensors on the probe handle. This is typically used for detection of prostate cancer.

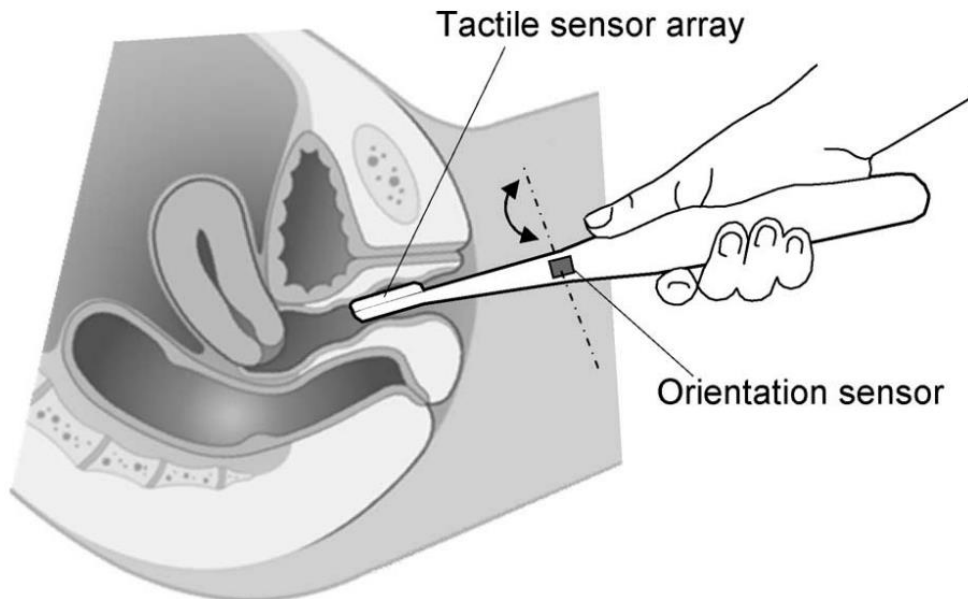


Figure 2.7 - Transvaginal Tactile Imaging (Egorov et al., 2010). Similar to the prostate imaging system, the tactile array gives a slice of the vagina wall, with a composite image being created from spatial relations obtained from insertion depth and probe orientation. This is typically used for detection of pelvic organ prolapse (POP).

The authors admit that this makes prostate imaging much simpler than breast imaging, mainly due to the hugely variable nature of breast sizes and shapes, as well as the pendulous nature of the organ making registration of tactile images onto an area of the breast difficult (Sarvazyan and Egorov, 2012).

Tactile images of breast tissues have been mosaicked into larger tactile maps using additional sensors before, however these required major infrastructure and were reliant on the patient remaining still (Wellman, 1999) or were not well registered to static patient body structures (Egorov and Sarvazyan, 2008).

The integration of additional simple sensors, such as the depth and orientation sensors, coupled with the relatively well constrained nature of the prostate and vagina wall has led to this technology being in active development to this day (Egorov et al., 2019) (Brandt et al., 2020) through clinical product design and clinical trials. This indicates an emerging trend in tactile imaging, which is increasing the capabilities through integration with other sensor types.

2.4. Other Breast Tactile Imaging Systems

2.4.1. Commercial Systems

Another primary commercial breast screening tool using tactile imaging is the iBreastExam™ (UELifeSciences Inc., IND), shown in Figure 2.8. This device uses a 4x4 array of micro-palpating piezo-resistive force sensors to measure hardness variations beneath the scanner. This has been shown to be effective in classifying malignant and benign conditions in clinical trials (Broach et al., 2016). The low spatial resolution of the tactile array makes this system unsuitable for detailed lesion characterisation like that of SureTouch™, however it is still effective at screening for lesions and its simplicity makes it ideal for low income countries like India where this product is commonly used in breast screening due to the low mammography availability.

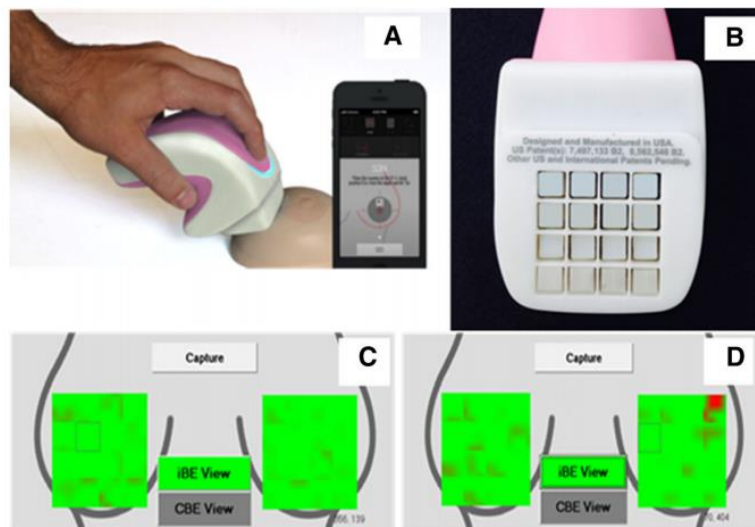


Figure 2.8 – iBreastExam™ device and graphical output (Broach et al., 2016). The low resolution array is effective at detecting tactile lumps, but cannot resolve lesion size of shape. This is suitable for screening indications and not detailed lesion characterisation.

2.4.2. Academic Systems

2.4.2.1. Mature Systems

A mature system that has reached clinical trials in academia, but has not been introduced as a clinical product is the hyperspectral tactile imaging system (TIS) (Oleksyuk et al., 2016). This system uses a deformable waveguide to indirectly image tactile inclusions as shown in Figure 2.9. The elasticity and size of the tactile inclusion is determined from the rate of change of image size with respect to the applied load. This method has excellent resolution for convex inclusion geometries, but is limited by the stiffness of the waveguide in measurements of complex concave lesion shapes that static TI can measure. This method has been shown in clinical trials to have similar lesion classification accuracy as other TI systems, however this technology is still a long way off commercialisation due to lack of integrated product development from the authors.

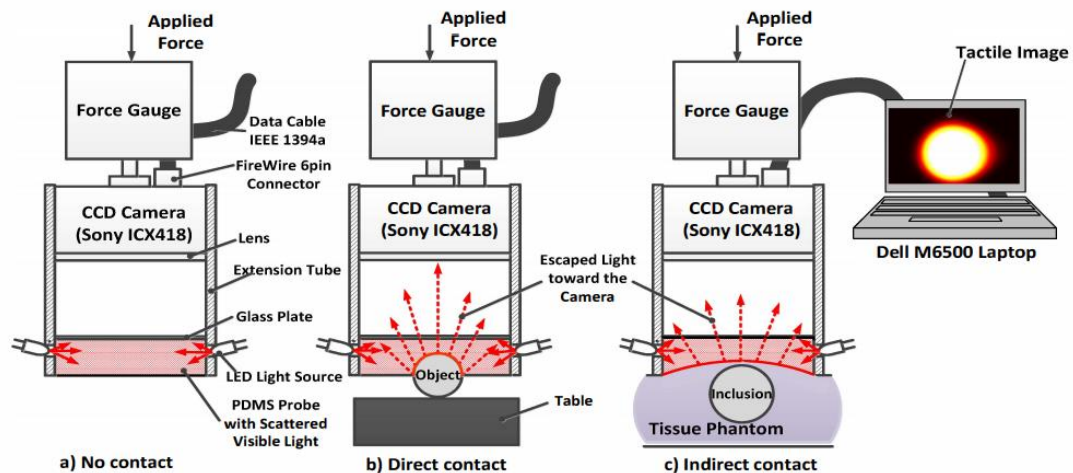


Figure 2.9 - Hyperspectral TIS device and graphical output (Oleksyuk et al., 2015). The deformation of a PDMS waveguide allows light to escape and reach the camera. The size and gradient of the image is related to the material elasticity and applied force.

2.4.2.2. Early Stage Systems

An immature tactile sensor system that has not reached clinical trials is the opto-mechanical tactile sensor (Ayyildiz, 2011) shown in Figure 2.10. This complicated system uses contour pins to couple surface stress to a deformable rubber membrane. The deformation of the membrane is detected using IR reflective sensors, with the intensity proportional to the applied stress, to produce a 10x10 tactile image of the material interaction. This system is interesting as the sensing elements are well isolated from the material under test, however the spatial resolution is limited by the stiffness of the rubber membrane similar to the hyperspectral TIS described previously. This system was shown to be effective at measuring lesion hardness and size in phantom trials, but has not advanced beyond this initial prototype and work in the literature.

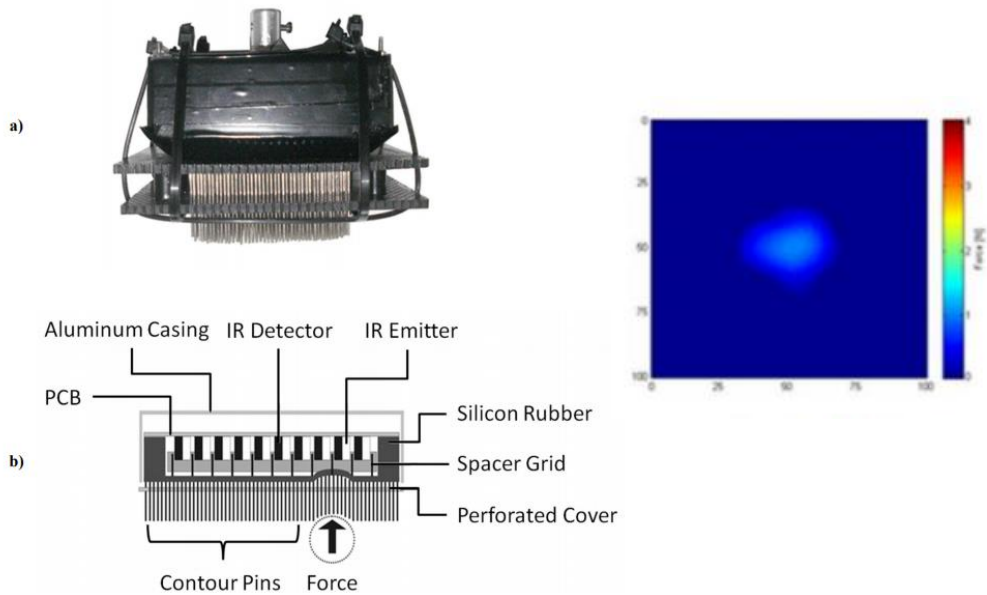


Figure 2.10 - Opto-Mechanical tactile sensor and graphical output (Ayyildiz, 2011). The applied stress on a tactile inclusion causes differential strain to actuate contour pins on the device. These pins deform a rubber diaphragm, which is detected using IR reflective sensors to produce a tactile image of the deformation.

2.5. Detail on Current Common Screening Technology

2.5.1. Mammography by X-Ray

X-Ray mammography is by far the most ubiquitous breast cancer screening method in current clinical practice. It regularly constitutes the front line of breast cancer screening programs worldwide. Although there are many different makes and models for mammography machines, one typical version is shown in Figure 2.11. The output image, also shown in Figure 2.11, is a 2D photograph of the internal density distribution of the breast, with lighter areas indicating areas of high density and thus X-Ray absorption. It is well known that density, and hardness, of breast tissue is highly correlated with histological diagnosis (Woods et al., 2011), and so X-ray mammography is well suited for detection of cancers. This technique has been consistently shown, since its conception in the early 20th century to today, to be effective in highlighting unpalpable cancers and differentiating malignant/benign conditions (Richard H. Gold et al., 1990) (Mandrik et al., 2019) as well as being useful in other medical and industrial fields.

X-ray mammography uses low levels of ionizing radiation to image the breast, approximately 13% of natural annual background radiation, which does carry some risk to the patient, however it is widely acknowledged that this risk is minor (Public Health England, 2018). This risk, coupled with the need for a firm breast compression between rigid plates, makes traditional X-ray mammography an unpopular choice for many patients, despite its obvious selling point of detecting unpalpable cancers.

X-ray mammography can struggle to differentiate cancers in naturally dense breast tissue, where the contrast between dense cancerous tissue and the background is not well defined. Additionally, fluidic lesions such as cysts cannot be easily identified on mammography and so further tests using other screening techniques such as ultrasound may be required (Public Health England, 2018). 2D planar mammography views all breast material stacked together, and so cannot easily be used to locate a lesion in 3D space without multiple views, which also hides cancers beneath other dense tissues. Despite these issues, X-Ray mammography remains the most common screening method in the world with 126 million mammograms performed annually worldwide (Sarvazyan et al., 2008) due to its effectiveness, prevalence, and low cost (Mandrik et al., 2019).

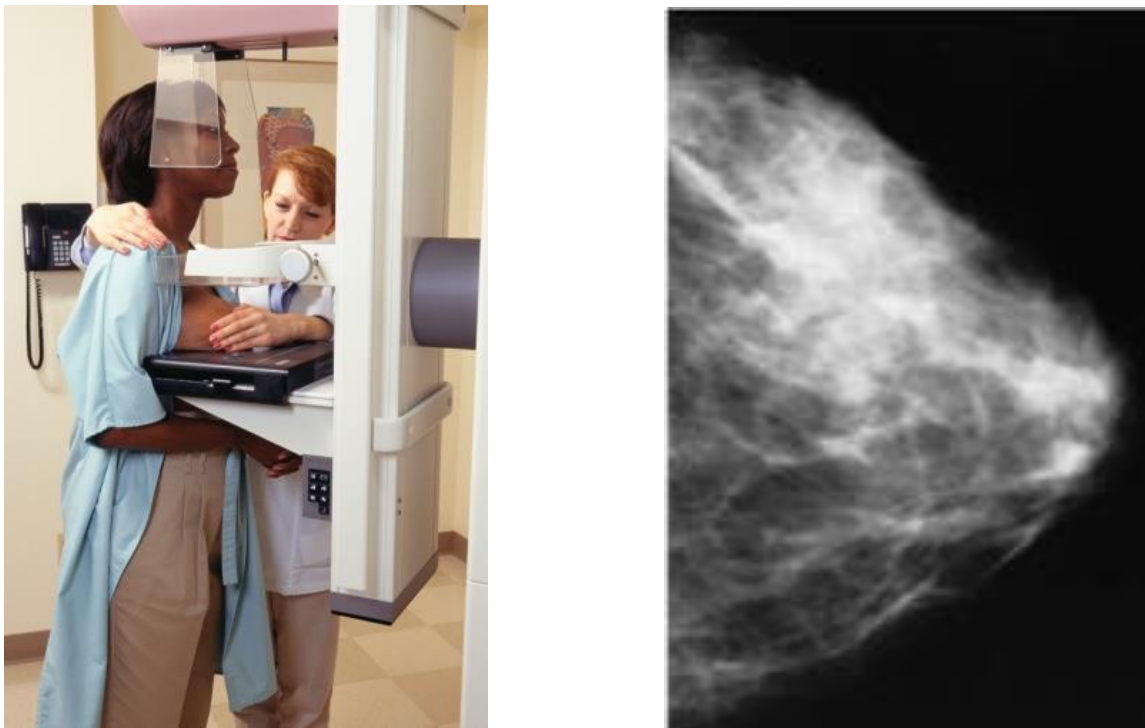


Figure 2.11 – X-ray Mammography (left) and Output Image (right) (CDC, 2020). The breast is flattened, often uncomfortably, and photographed using X-Rays. The output image shows a 2D representation of the 3D tissue density distribution within the breast.

2.5.2. Ultrasound Imaging

Ultrasonic mammography, or sonography, is a breast cancer imaging modality based on ultrasound where high frequency ‘ultrasonic’ sound waves are directed into the breast, and an image is formed from the reflections. Areas with differing elasticities and viscosities affect the local speed of sound, allowing for tissues to be differentiated effectively as shown in Figure 2.12. This method uses sound waves that are inaudible and is non-invasive, and so there are no known clinical risks associated with external ultrasonic imaging.

Traditional sonograms take a 2D ‘slice’ view through the breast tissue, and so can resolve objects hidden behind other objects, as shown in Figure 2.12. This is in contrast with X-ray mammography, which takes a whole breast image but does not resolve stacked objects, as sonograms resolve stacked objects but are limited in their field of view to tissue directly below the probe. More advanced machines can form 3D views, either using complex scan probes, or using superposition of sequential 2D slices, however these are less commonplace in breast cancer screening as they are in other fields such as imaging unborn babies in the womb.

Ultrasound, due to its relative comfort and low risk compared with X-ray mammography, is a popular method amongst patients, however it is mainly used in characterisation of lesions identified during mammography, to investigate suspicious areas for differentiation, or on patients with naturally dense breast tissue (Sarvazyan et al., 2008). This is largely due to the labour-intensive nature of imaging the whole breast, limiting its usefulness in a large-scale screening role.

The scanning method used in sonography, where a probe is gently pressed onto the breast surface and scanned over the breast using a coupling gel to reduce friction, as well as to improve ultrasonic coupling, is very similar to how TI is used. There is a high degree of similarity between TI, from Figure 2.3 and sonography, from Figure 2.12, which helps conceptualise the use case of each. Other forms of sonography, particularly transvaginal sonography, share similarities with other applications of TI in clinical use.

The use of ultrasound in screening is limited, particularly as there is little literature on the use of ultrasound as an adjunct to mammography, with some studies showing its use in screening leading to higher false positives than X-ray mammography (Lee et al., 2019). However, it is a straightforward and simple characterisation method for pre-identified lesions, similar to MRI but with greatly lower imaging cost.

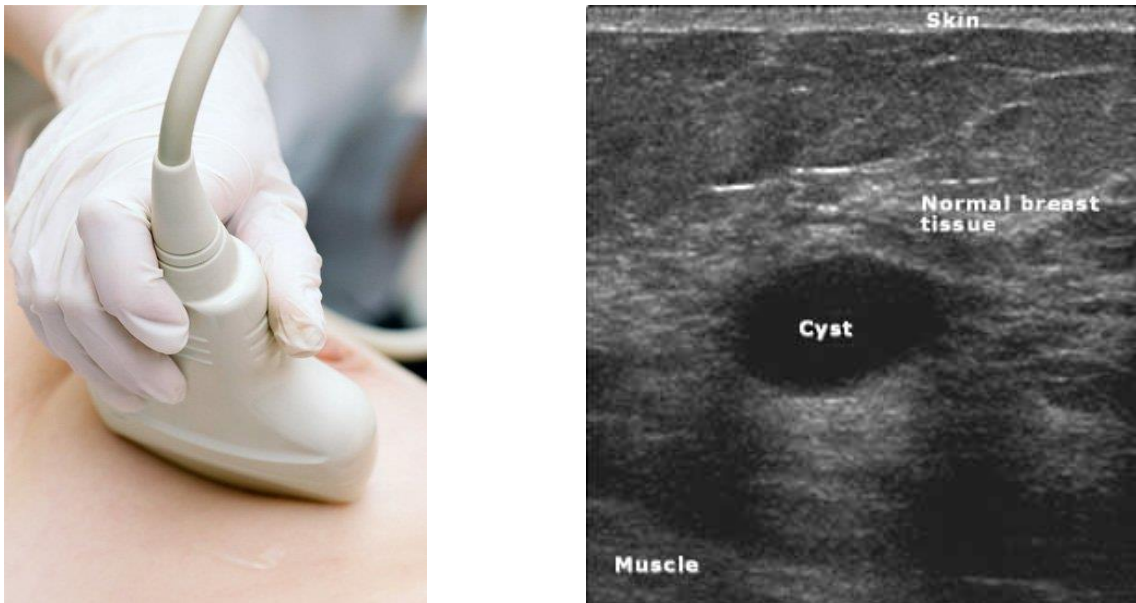


Figure 2.12 - Ultrasonic Breast Imaging (left) (BHI Houston, 2020) and Output Image (right). The scanner contacts a small area of the breast and images a 2D 'slice' of the breast using phased array ultrasound, where the y axis of the output image represents depth into the breast. Pressure is light and friction is reduced with coupling gel.

Medical ultrasound is a broad and rapidly expanding field in the literature, with applications ranging from targeted drug delivery (Frazier et al., 2019) to 3D visualisation of a foetus, even focussing on breast cancer imaging it is impossible to do the field full justice in this thesis. Although ultrasound is not common in current screening, its use in the clinical environment generally is widespread (Barr et al., 2015) and regularly used in clinical laboratory research on tumours (Elyas et al., 2017) and skin variation in response to tumours (Coutts et al., 2016), as well as general material characterisation.

Ultrasound is perhaps the most direct competitor to TI in terms of material characterisation and lesion measurement, and has been trialled competitively early on in the development of TI (Wellman et al., 1999b). TI was shown to be superior in terms of in-vivo lesion size estimation with mean absolute errors (MAE) 3 times less than for ultrasound in a limited clinical trial. TI at this time produced an output similar to the young's modulus image from supersonic shear imaging (Cao et al., 2013). This result led to further development of TI, described previously in this thesis, as this was compelling at the time. Lesion size estimation studies using TI (Egorov and Sarvazyan, 2008) and ultrasound (Brusseau et al., 2013) have been conducted since the early work of Wellman, however there has not been a repeat study directly comparing current TI and ultrasound in a like-for-like trial. Going forward in this thesis the assumption will be that TI is superior to ultrasound in lesion characterisation, in applicable fields, with the understanding that further comparative study is required to accurately determine the place of current TI with respect to current state-of-the-art ultrasound imaging.

2.5.3. Ultrasound based Elastography

Ultrasound elastography, or sonoelastography, is an application of ultrasonic imaging where complex wavemodes are used to non-invasively ‘agitate’ the tissues of the breast, where the resultant microscopic motion of the tissues can be measured and translated into the elasticity to the material. There are two main types: strain elastography, and shear wave elastography (Youk et al., 2017). Similar to simple ultrasound imaging, it is impossible to cover this topic fully, and is included here to highlight methods in general breast imaging.

Strain elastography is the simplest of the two, utilising the compressive force of the scanner to palpate the tissues which, through the actions of the Youngs modulus (stiffness) of the material, will exhibit a strain in the material which can be measured by comparing characteristics of the ultrasonic beam before and after compression. This method does not return the absolute elasticity of the tissues, but a relative measurement compared with the surrounding tissue as the applied stress is unknown, and so is useful for detecting tissue anomalies but does not quantitatively characterise them in terms of elasticity. This method has a dependence on the contact mechanics between the probe and tissue, requiring uniform stress distributions during scans, and is not used to diagnose breast conditions by itself, instead being used to support other ultrasonic imaging techniques (Dietrich et al., 2017). The method is being superseded in clinical development of breast cancer imaging and diagnosis by shear wave elastography (SWE).

Shear wave elastography is an advanced ultrasonic imaging technique that utilises high frequency ultrasound to micropalpate the tissues under investigation. This

process induces shear waves in the tissues, the speed of which can be measured by high speed detectors (Park and Kang, 2021). As the speed of shear waves, and the speed of sound, through a material is related to the elasticity of the material, this method is able to quantify the elasticity of the material in question (Bian et al., 2021). The results from SWE have been consistently shown to have high inter and intra-observer repeatability, overcoming the limitations of strain elastography (Tian et al., 2017) (Jia et al., 2021).

The link between elasticity measurements from SWE and the differentiation of malignant and benign conditions is well known in the literature (Yang et al., 2020), so much of the research in the recent literature focusses on sensitivities and error control (Chino and Takahashi, 2018), and evaluation of the boundary conditions of a lesion (Liu et al., 2019) which is known to be related to lesion malignancy (Verma et al., 2010). Similarly, the literature has introduced new parameters available from SWE other than the elasticity and lesion boundary characteristics such as the mass characteristic frequency which has been shown to improve differentiation when utilised with other metrics from SWE (Gu et al., 2021). One of the key points that SWE offers clinicians is the ability to characterise supporting tissues such as axillary lymph nodes, the status of which is important in management and prognosis of high likelihood malignancies (BIRADS 4 and 5) (Elmesidy et al., 2021).

SWE offers clinicians valuable information on known diagnostic metrics such as lymphatic status, lesion elasticity, and boundary characteristics, but it also provides the potential to offer more metrics than are currently used in clinical diagnosis. This makes SWE a rapidly developing field, both technically and clinically.

2.5.4. Computer Aided Tomography (CT)

Computer aided tomography, abbreviated to CAT or CT, scans are an advanced form of X-ray mammography designed to form a 3D view of the internal breast density distribution. This requires a large and expensive machine, and so would not be done as part of initial screening, except where a patient attends a properly equipped hospital or has multiple palpable lesions. The patient lies in the prone position, face down, allowing the breast under examinations to hang freely in a cavity in the machine, shown in Figure 2.13. A mobile X-ray scanner then revolves around the breast taking multiple images at different heights and angles, allowing for the creation of a 3D image of the breast. This technology carries the same patient risks as traditional X-ray mammography in terms of radiation exposure (Public Health England, 2018) and so is not commonly used in screening. The output metrics are identical to that of mammography, but with the added ability to estimate size and shape in 3D space, view hidden structures, and glean invasiveness information from localisation.



Figure 2.13 - CT Breast Imaging (left) and Output Image (right) (UC Davies Health, 2020). The patient is supine, with the breast hanging freely in a cavity about which a mobile X-ray scanner revolves. This produces a 3D breast density image, viewable in 2D slices. This allows for viewing of stacked structures invisible to traditional 2D X-ray.

2.5.5. Magnetic Resonance Imaging (MRI)

Magnetic resonance imaging, MRI, is an advanced general purpose body imaging technique, applied to breast cancer imaging. This is the most expensive of the imaging modalities noted in this literature review, coming in at approximately 8 times that of screening X-ray mammography from average US Medicare data from 2005, however it is the most detailed imaging technique in terms of resolution and tissue differentiation.

This technique is vastly different in its method of operation to other methods detailed in that it operates by exposing the patient to a targeted oscillating magnetic field, which polarises the spin of hydrogen atoms in the tissue molecules. The relaxation of the hydrogen atoms to their original state releases a radio signal that can be detected and triangulated its emission location in the breast. Materials with different hydrogen concentrations, such as lipids (fats) and water react differently to the nuclear excitation and so can be differentiated. The physics involved is complex and outside the scope of this review, but from the point of view of the patient, the requirements are that they remain stationary within the MRI machine, shown in Figure 2.14 for the duration of the scan and may need a sedative to do this.

Although there is little risk of harm from NMRI itself, with the ‘nuclear’ part removed to form MRI to better public perception, the machine is loud and claustrophobic (American Cancer Society, 2019a) and the scan times are long. This, coupled with its high false positive rate when compared with X-ray mammography (Kuhl et al., 2018), means that MRI is not recommended for screening by itself. That

being said, MRI can detect cancers not visible to X-ray mammography, as shown in Figure 2.15, although it also detects things that are not cancers causing the costs of unnecessary biopsies and tests outweighing the benefits of the clear images in a screening context. MRI is not used preoperatively on patients, except those at very high risk of breast cancer, and always in conjunction with mammography (NICE, 2018), it is also not suitable for patients with metallic implants. MRI is particularly useful in characterising cancers already identified by other methods for size, shape, and location. This is important for operative intervention, particularly with the namesake MRI guided breast biopsy, as well as for continued monitoring of post-operative recovery to ensure that the cancer was successfully extracted. The accurate position information obtained from MRI, and other methods combined is crucial for reducing collateral damage to peripheral tissues during surgical extraction of a cancerous lesion.

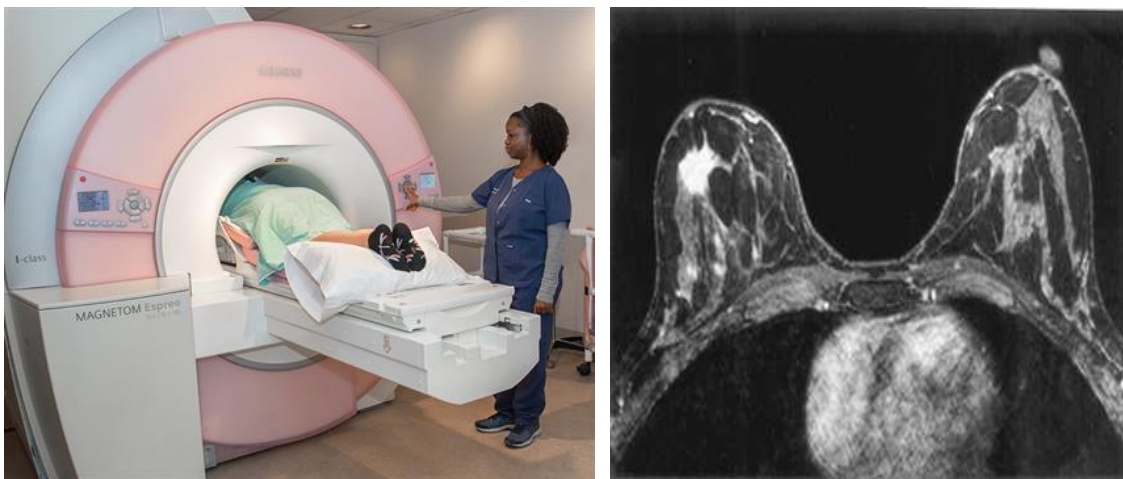


Figure 2.14 - MRI Breast Imaging (left) (Cleveland Clinic, 2019) with Output Image (right) (Robert J Miller, 2020a). The patient must remain perfectly still during the MRI scan, and may be given a sedative to help with this. The scan produces 2D slices of the breast, and other tissues, that are sequenced to form a 3D image for estimating size, shape, and location of the lesion. This displays both breasts at once.

2.5.6. Comparative Note on Different Use Cases

This section of the literature review has provided some general background information on the most common screening/breast imaging technologies in current clinical practice. There are of course other technologies (American Cancer Society, 2019b) such as scintimammography, a form of nuclear imaging, and positron emission mammography, a form of PET scan, to name a few however it exceeds the scope of this review to detail each one. This leads to a justification of the screening flowchart presented in Figure 2.1, as a simplification of a complex web of ‘what ifs’ and ‘it depends’ conditions for the use of each technology. As it is largely unimportant how certain imaging techniques work for this review, it is important to understand what is gleaned from each one for the purpose of developing novel technology to replicate the diagnostic/screening capability of existing systems.

It should be clear that X-ray mammography is the defined standard technique for screening and cancer diagnosis, as it is able to image tissue density in a simple and efficient manner. This success is largely based on its ability to image the full breast in one scan, making X-ray the regular choice over other methods such as ultrasound in most cases. Additionally, there is an important distinction between a mass screening tool and a diagnostic tool. X-ray mammography is an excellent screening tool for early detection; however, diagnosis often requires more advanced imaging and tissue differentiation methods. From this, a new screening tool would need to be able to image the full breast either directly as with X-ray, or compositely as with MRI. However, a diagnostic tool only needs to survey a pre-identified suspicious site like with ultrasound.

With respect to the theme of this thesis, reducing the false positive rate and thus increasing the positive predictive value of a screening/diagnostic system is important in improving the cost effectiveness of that system or process. From the examples of MRI vs. CT/X-ray (Robert J Miller, 2020b), highlighted in Figure 2.15, there is clearly a balancing act to be played with when it comes to a suitable sensitivity for large scale screening and sufficient specificity to keep the false positive rate at a manageable level. From this, the goal of any proposed/developed system should not be to simply increase the sensitivity of the screening process, but to simultaneously improve the specificity of the system to keep both the false positive and false negative rates low through proper use of diagnostic metrics (Kuhl et al., 2018). This reduces the rate of unnecessary procedures (reducing patient stress), and the number of missed cancers respectively.

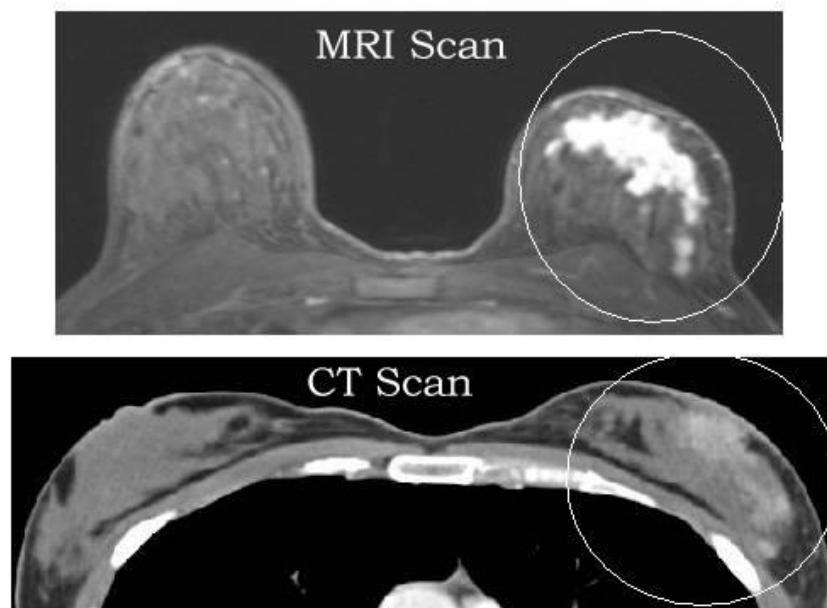


Figure 2.15 - Comparison of MRI and CT images of palpable lesions (Robert J Miller, 2020b). These were taken on a patient with known cancer measured at 5.1cm after mastectomy. CT does not show this clearly, in contrast to MRI, although the mass was flagged as 'suspicious' during screening.

2.6. Metrics for Automated Diagnosis

Before any decision or diagnosis can be made, it is vital to understand the information, or metrics, that are used to make a decision. In breast cancer diagnostics the metrics for diagnostics are features of a suspicious lesion and surrounding tissues, as well as risk factors relating to the patient although the value of many of these are not well documented in the literature.

One of the most valuable metrics for breast cancer diagnostics is the relative density of a lesion compared with background tissue. Lesion density/hardness can come from a variety of sources depending on the screening methods available. The most common of these is the mammographic breast density, indicative of the proportion of breast fat (Woods et al., 2011), which has been standardised in recent years to use the breast imaging reporting and data system (BIRADS) (American College of Radiology, 2013). The breast and lesion densities can also come from manual palpation, although this is difficult to quantise (C.D Haagensen, 1986), ultrasound, and increasingly commonly tactile imaging (Wellman et al., 1999b).

As Haagensen points out, the lesion size and shape are other important metrics when examining for breast cancer although it is still noted that these are difficult to quantise using manual palpation. More advanced screening methods such as mammography, ultrasound, and tactile imaging can provide this information as presented by Wellman et al. These metrics are expanded upon by defining the importance of acutance, that is the nature of the lesion boundary conditions, and its

relation to malignancy (Rangayyan et al., 1997). The authors presented the observation that benign tumours generally are well defined with sharp boundaries between them and the surrounding tissues, as opposed to malignant tumours which are generally blended with the surrounding tissues due to the tumours need for nutrients and blood flow.

The discussion was furthered by showing that 4 discrete measures of shape – Round, oval, lobulated, and irregular; with 5 classes of acutance – circumscribed, micro-lobulated, obscured, ill defined, and spiculated; can be used for the classification of malignancy or benign lesions (Verma et al., 2010). The authors presented a thorough literature review, summarising nearly a decade of advancements in the classification of breast lesions. This improves the confidence in the statement of the metrics used for classification.

The summary of benign breast diseases (Guray and Sahin, 2006) is a useful tool for the classification activities presented by other authors. They present the idea that because benign lesions are far more common than malignant lesions in western countries, it is important that physicians recognise benign lesions confidently to reduce the need for surgical biopsy. This will reduce the unnecessary surgical biopsy rate, reducing the suffering and rate of complications amongst screening patients. Being able to accurately diagnose benign conditions is as important as diagnosing malignant condition during the screening process, and the detailed description of benign lesion features presented can lead to accurate subclass classification along the lines of that predicted by Egorov and Sarvazyan (Egorov et al., 2009). In this paper, the importance of lesion mobility is discussed, as well as the difficulties in measuring lesion

mobility. The authors show that malignant lesions typically exhibit restricted mobility due to lesion bonding with local tissues and blood vessels. This indicates that a highly mobile lesion is likely to be benign and based on their research will be easier to detect than a restricted lesion.

The primary metrics presented above that are used for clinical diagnostics are:

- Breast density
- Lesion density and elasticity
- Growth / fluctuation rate
- Lesion size, shape, and boundary conditions including blood invasion
- Lesion mobility

There are other secondary metrics that are publicly considered to be ‘risk factors’ but are not considered to be diagnostic features in the literature. These include:

- Previous history
- Patient weight / body fat percentage
- Ethnicity
- Breast or other related pain
- Whether the patient smokes or uses narcotics
- Early beginning to periods
- Late menopause

Information on risk factors can be found everywhere, with varying levels of credibility, with some being stuck in the public consciousness despite limited academic acceptance. The anecdotal difference between causality and correlation often plays a role here. The risk factors presented are from the British charity ‘Breast Cancer Care’ (2015), a popular and informative institution in the UK. Combining these secondary

metrics with primary diagnostic metrics obtained through tactile imaging or other means can lead to a better estimation of the confidence in a classification of lesion malignancy. Certainly, the secondary metrics should not be used directly for a diagnosis, but they can be used to indicate the reliability of a diagnosis. The example is a diagnosis of benign from primary metrics, combined with an absence of risk factors, leads to a higher confidence in the diagnosis. Similarly, a suspicious condition diagnosis may be initially weighted towards malignancy if the patient exhibits several risk factors.

One of the important but understated determinants of breast cancer, or specifically differentiation of breast cancer types, is location within the breast. A diagram of the breast is shown in Figure 2.16. The location of a lesion within the breast largely governs the type of cancer that it can be, if it is indeed cancer.

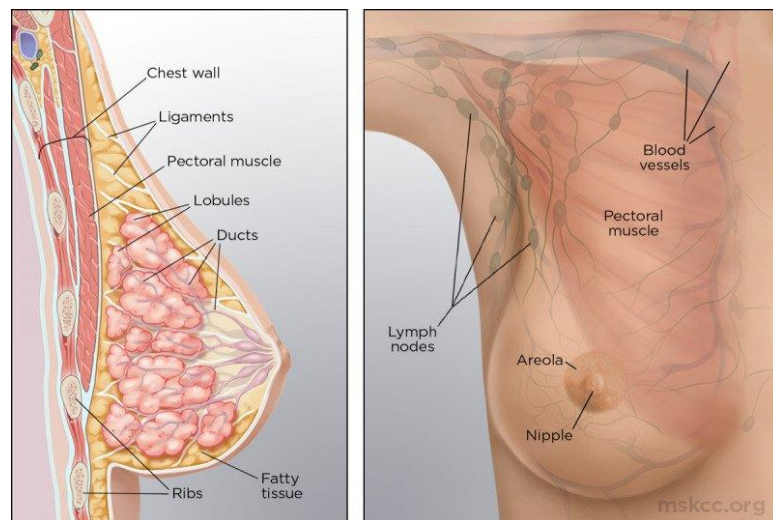


Figure 2.16 - Anatomical representation of the breast. Reproduced from: (Memorial Sloan Kettering Cancer Centre, 2021). The distribution of tissues within the breast is different for each person, and largely dictates the types of cancers that are possible, similarly providing markers for disease that can be detected.

Specific cancers are unique to certain locations in the breast, for example lobular carcinomas can only occur in lobules (milk producing tissues) and ductal carcinoma in situ can only occur in ducts (milk pipes), similarly fibroadenomas and fat necrosis are benign conditions that occur on fibrous and fatty tissues respectively. Knowledge of lymph node locations is also important, as swollen lymph nodes in conjunction with other symptoms is an indicator of cancer. This means that a breast scan should include the axillary region, where swollen (in this case stiffened) lymph nodes would be important to diagnosis. In addition to this, a full breast view gives the relation between lymphatic tissue and other suspicious tissues, which can help differentiate one from another. For lymphatic and cancerous tissues, stiffness is highly correlated with the severity of the conditions.

2.6.1. Elasticity and Disease

It is well known, and almost anecdotal, that the stiffness of tissue, or rather a change in stiffness from normal, is related to problems of multiple kinds including: cancer, inflammation, gaseous build-up, scarring, muscle injury, and many more. The ubiquitous lump that commonly denotes cancer in many parts of the body, is detectable through manual palpation only because its stiffness differs from that of the surrounding tissue, and so clearly stiffness is related to the condition. The properties of healthy and diseased breast tissue have been characterised by many authors, each focussing on specific areas such as temperature dependence, strain rate dependence, and strain dependence of the Young's modulus of various tissues. There is agreement on the general ranges of certain tissues, despite the differences in measurement methods between

authors and time periods, with ‘normal’ breast tissue consisting of fatty tissue and fibrous glandular tissue being 3-22kPa (9-15kPa typical) and 3-17kPa (6-17kPa typical) respectively, although some estimates went to the extreme of 0.2-40kPa each. ‘Diseased’ tissues have markedly higher elasticities, but also more variable, depending on the condition in question, with more severe conditions having higher elasticities. (Samani et al., 2007) (Matsumura et al., 2009) (Rzymiski et al., 2011) (Yang et al., 2020). To mark this point, conditions such as Ductal Carcinoma in Situ could have elasticities in the range of 3-2100kPa depending on the loading conditions.

The key issue with making diagnostic decisions based on elasticity alone is that there is such variability, and subsequent overlap in the elasticity ranges of different conditions, and even between healthy and diseased tissues in the literature. This problem is compounded by variability even within an individual, with a typical heterogeneity of 6kPa being quoted for normal breast tissue (Matsumura et al., 2009). This makes it impossible to reliably say ‘this object is 19kPa, it must be DCIS (for example)’, because it very much depends on the loading conditions and the patient in question. Unless the elasticity of a suspicious tissue is far above that of normal tissue, >50kPa, then determining the nature of the condition would require comparison with that patients normal breast elasticity. The example is for a patient with 4kPa typical breasts, with 6kPa heterogeneity, a measurement of 30kPa could be considered abnormal and worth of investigation, although this difference would not be detectable by hand.

As yet, there is no way to diagnose a condition based on elasticity alone, unless it is extreme, with other metrics being required for diagnosis as stated in this thesis.

However elasticity is related to breast cancer diagnosis despite the difficulty in the clinical literature in pinning specific numbers on it, as it is commonly used to detect and assess severity prior to detailed diagnosis via biopsy. This does not stop researchers developing elasticity measurement devices for breast cancer detection, as there may be a method for directly utilising the information found in the future, to pin down the relation between elasticity and diagnosis definitively. Pinning a number down on the lesion elasticity also helps track the lesion growth over time, all valiant reasons for continuing with elastography research, and provides justification for pursuing elastography research.

2.7. Automated Decision Making

Academics and professionals alike have attempted to remove some of the subjectivity and human error from the diagnosis process at all stages using machine learning, from initial screening to diagnosis and clinical management. By digitally quantifying lesion and patient parameters, machine learning methods can be applied to the data for either: simple benign/malignant screening, or complex sub-class diagnosis (Nahid and Kong, 2017)

There is a growing popularity for neural networks and deep learning in academic medical imaging, with several high profile papers published in Nature over the last few years (Shen et al., 2019) (Hu et al., 2020). Despite the success of such systems on recognised datasets such as Wisconsin Breast Cancer Diagnosis dataset (WBCD) and the Digital Database for Screening Mammography (DDSM), there is very limited commercial or clinical adoption of such systems. This is partly due to the maturity of the

stated systems, but even on neural network systems that are decades old (Karabatak and Ince, 2009) there is limited commercial adoption. This is because, as Rudin (Rudin, 2019) points out, neural networks lack the accountability and human interpretability of simpler methods such as Bayesian classifiers and logistic regression; shown to have comparable results with neural networks in many cases (Ng and Jordan, 2002).

The point that Rudin makes in regards to medical decision making is: when a physician or registrar is asked why a patient was recommended a mastectomy, they cannot just say ‘because the machine said so’; they must have a clear decision pathway such as a decision tree, or a probability table, or some combination of the two (Jiang et al., 2012) (de Campos et al., 2016). This would be more in line with how decision making is made by physicians currently, where a list of indicators and risk factors are compiled and assessed to determine the proper course of action.

Naturally, there are some cancer indicators that are more important than others in identifying malignant conditions or differentiating between conditions for proper treatment. By accepting that the results from the machine learning authors in the literature are correct and comparable, because they are tested on the same WBCD datasets; the diagnostic metrics used, or prioritised, in each method can be tabulated to determine the most significant indicators overall. This is shown in Table 2.1, where a range of machine learning techniques from different authors have been compared. The authors and works listed in the table have been selected to give a broad range of differing techniques applied to the same datasets, as well as the authors have explicitly stated in their works what metrics they have used or prioritised with explanations.

It is important to note that the works are not current, but are presented to compare the performance of historic TI with other automated analysis works of the period as ML applied to TI from ~2010 is not going to be competitive with a 2020 neural network.

Table 2.1 - Diagnostic metrics used in automated breast cancer diagnosis studies using machine learning. The metrics/features are shown for several prominent lesion classifier architectures, using similar datasets for comparison. The datasets and stated accuracy results for each author is shown.

COMPARISON OF METRICS USED FOR AUTOMATED BREAST CANCER DIAGNOSIS USING MACHINE LEARNING											
Researcher	Diagnostic Metrics / Features									Media Dataset	Result (%)
	Year	Lesion Shape	Lesion Size	Margin Adhesion and Acutance	Cell Size	Lesion Density and Hardness	Patient Age	Lesion Texture	Other BIRADS		
(Classifier)											
Akay 2009 (SVM)	0	0	0	0	0			0		WBCD	99.51
Bhardwaj et al. 2015 (GONN)	0	0	0		0	0		0		WBCD	98.24
Verma et al. 2009 (SCBDL)	0		0		0	0		0	0	Mammography DDSM Patient Data	97.50
Zheng et al. 2013 (K-SVM)	0	0	0		0	0	0			WBCD	97.38
Karabatak et al. 2008 (ARNN)	0		0	0	0		0	0		WBCD	95.60
Balamurugan et al. 2010 (NB)	0		0		0	0		0		WBCD	98.10
Onan 2015 (F/R NN)	0	0	0	0	0					WBCD	99.72
Egorov et al. 2009 (NB)	0	0			~	0	0			TI Patient Data	86.10
Tasoulis et al. 2014 (NB)	0	0			~	0	0			TI Patient Data	88.2

In the table several classifications of lesion metrics have been grouped together, such as: lesion density and hardness, and margin adhesion and boundary acutance; this is because they are similar concepts and are often determined using the same methods. On the other hand, some metrics have been separated, such as: lesion shape, and lesion size; this allows for a better comparison and takes into account the authors notes on the matter.

The works presented in the table cover a range of machine learning techniques, from the deterministic support vector machines (SVM) (Akay, 2009) (Zheng et al., 2014) to the abstracted neural networks (NN) (Bhardwaj and Tiwari, 2015) (Onan, 2015). These works highlighted that although the accuracies of each method were approximately equivalent (>95%), the diagnostic metrics used and prioritised changed between each one. This allows for the priority metrics to be determined.

When ranked, the priority diagnostic metrics used in machine learning in breast cancer care, based on use rates from the selected works, are:

1. Lesion shape, Lesion density and hardness.
2. Margin adhesion and acutance.
3. Lesion size, patient age.
4. Other reporting metrics from BI-RADS, including mammography image features, and lesion location w.r.t. blood vessels.
5. Lesion texture.
6. Cell size.
7. Other metrics and indicators, including subtlety value.

The tactile imaging with automated decision outcomes trials (Egorov et al., 2009) (Tasoulis et al., 2014) are included to link back to tactile imaging; they do not use the standard databases for classifier testing, instead using tactile images taken independently. The slightly lower accuracies of the tactile imaging Bayesian classifiers (NB) compared with a similar Bayesian approach applied to the WCBD (Balamurugan et al., 2011) is correlated with the differences in the diagnostic metrics used.

2.8. Summary of Current Tactile Imaging Capabilities

2.8.1. Commercial Implementations of Tactile Imaging

Current commercial and clinically used implementations of TI for breast cancer imaging, based mainly on SureTouch™ and iBreastExam™, have the following capabilities, though to differing degrees:

1. Both systems output a differential stress based quantified ‘hardness’ value for a suspected lesion.
2. Both systems can display and record suspected lesion location on the breast using operator input, with similar GUIs to allow reporting to secondary screening methods.
3. SureTouch can accurately determine lesion shape and size, and resolve multinodular and clustered lesions, iBreastExam lacks the spatial resolution to do this to the same degree (Wellman et al., 1999b).
4. Both systems can interpolate between sensor elements for artificially increased spatial resolution (Egorov and Sarvazyan, 2008).

5. Both systems have been shown to be effective in their current screening role compared with CBE (Egorov et al., 2009) (Broach et al., 2016).

Each system caters to a different market, with SureTouch (the more advanced and expensive system) in operation in typically MEDC areas, and iBreastExam (less advanced, but considerably cheaper) serves markets in typically LEDC areas. Each system is effective in their own environments, compared with CBE, as is their purpose.

2.8.2. Problems in Current Commercial System Use

TI has been shown consistently to be effective in screening, in either commercial implementation, when compared with CBE. Additionally, the well documented reports generated by TI systems addresses the clinical problem faced by GPs when referring patients for further screening. TI is not without its limitations, however, both in its current screening role and more generally in developing a standalone diagnostic tool.

The ‘hardness’ estimate from commercial TI systems is relative to the background and is measured using differential stress between the lesion and the surrounding tissue as described in Equation 2.1. E_L and E_0 are the elasticities of the lesion and background tissue respectively, P_L and P_0 are the measured pressure values over the lesion and background tissue respectively. This method allows for an indication of the elasticity of the lesion without quantifying a true value for it, limiting the systems future expansion into diagnosis which requires direct measurements of the lesion.

$$\frac{E_L}{E_0} \propto \frac{P_L}{P_0} \quad (2.1)$$

The lesion location estimate provided in the TI system report is entirely subjective and is fully reliant on the operator manually selecting the correct region on the breast. The breast template given in the report, in Figure 2.5, is also an ‘idealised’ representation of a typical breast in a specific orientation and so may not fit well for women with irregular or uneven breasts, a large degree of ptosis, very large or very small breasts. This limits the effectiveness of the system as a reporting and referral tool, although this is a minor issue due to the tactile image itself being the important differentiator, as there is well known operator subjectivity in estimation of locations on the breast (Hansson et al., 2014) that can be removed (or reduced) by automated methods (Quieregatto et al., 2014). The bigger issue is that without accurate lesion position estimates, particularly w.r.t. other breast features such as blood vessels and ducts, the diagnostic capability of TI is limited as implied in Table 2.1. TI is not able to resolve blood vessels and other soft features and lesions simultaneously, due to the vastly different scales, and so TI cannot estimate invasiveness by itself.

2.8.3. Academic Capabilities not in Commercial Use

The discussed problems with TI have been prevalent since the 1990’s, when TI took its current form as a handheld non-invasive imaging system (Sarvazyan, 1997). Incidentally, before this point tactile imaging was very similar to mammography in that it compressed the whole breast at once and measured resultant stress distributions in a process called ‘mammobarography’ (Gentle, 1988), and so did not have the same localisation issue as the more modern handheld implementations. Authors in the literature have attempted to address the problems in elasticity measurement, lesion

localisation, and lesion circumspection, amongst others over the years. These capabilities are summarised below.

The work of (Wellman, 1999) initially addressed the problem of elasticity using complex empirical mechanical modelling of the pressure distribution from the tactile array. Though the method was effective in limited trials, the approach showed high sensitivity to lesion size and depth, the latter of which could not be well separated from the effect of elasticity on the pressure distribution.

This work additionally implemented a tactile mapping system based on tracking the scanner in absolute space using magnetic trackers and superimposing the tactile images onto a best fit plane of the breast. This was effective, but highly impractical due to the high cost of the position trackers, and that the patient position is not tracked over time, meaning the patient must remain perfectly still for the mapping process to be effective.

The elasticity estimation of the embedded lesion was further simplified by (Egorov and Sarvazyan, 2008), where an approximation of the background elasticity was made using the pressure distribution of ‘normal’ tissue, allowing for lesion elasticity to be determined by differential measurement. This was effective, and much simpler than earlier works, however it had one fundamental limitation in that the method required a tactile image of normal tissue and a separate image with a lesion in order to work. Firstly, this assumes that the tissue in the ‘normal’ image is the same as that surrounding the lesion, which is known to be highly variable depending on where the image is taken (Woods et al., 2011) and thus unreliable in practice. Secondly, there is no spatial

information on the relationship between the ‘normal’ tissue and the lesion image, unless they are taken in a single continuous scan as there is no ‘global’ tactile map.

The authors were able to produce a ‘local’ tactile map of tactile images based on the correlation between adjacent tactile images allowing for spatial registration of lesions with respect to each other. This represented a great leap forward when compared with earlier work, as it removed the need for the complex and expensive 3D magnetic tracking system, relying only on the tactile images themselves. The limitation of this approach was that there was still no information, from the TI hardware, indicating where on the breast the tactile map is located, except where the tactile map covers a feature on the breast that is visible and is palpable such as the nipple. This limited the usefulness of the tactile map as it needed to be registered onto the breast, using the nipple, manually.

The same authors later added additional functionality without addressing the earlier limitations (Egorov et al., 2009), although they are acknowledged in the experimental limitations (Sarvazyan and Egorov, 2009). This functionality included an estimate of lesion mobility within the breast tissue, accomplished by observing the change in apparent lesion size and position over time using the curvature of the tactile array. The authors did not go into detail on the efficacy of this method, as it was used as a feature for lesion classification which was the true topic of the paper.

This point represents the terminus of research on tactile imaging, specifically pure tactile imaging based on an array of pressure sensors. Later works by these authors and others have either been reviews on tactile imaging in general (Sarvazyan and Egorov, 2012) or independent repeat experiments of the lesion classification study (Tasoulis et

al., 2014) and did not add anything new. To summarise, the current academic capability in breast tactile imaging is:

- Lesion elasticity can be determined if a suitable estimate of background elasticity can be made. (Egorov and Sarvazyan, 2008),
- Large tactile maps can be made from sequential spatially overlapping tactile images, with global registration on the breast in some cases. (Egorov and Sarvazyan, 2008),
- Size and shape can be easily measured from individual or composite tactile images (Wellman et al., 1999b),
- Lesion acutance and boundary margin can be estimated from tactile image pressure gradient, though this has not been separately published (Sarvazyan and Egorov, 2012),
- Lesion mobility can be determined for observing lesion changes over time (a few seconds) on tactile images (Egorov et al., 2009).

The difference between what is possible in the literature and what is implemented in commercial systems comes down to 2 key points: Firstly, the academic implementations often have subtle limitations, are tested in limited situations not representative of real use or are dependent on special processes that cannot be guaranteed in general use. Secondly, the clinical demand in most MEDCs where this research is typically carried out is not for a diagnostic system, as mammography is the de-facto method, but for a screening method and reporting system. There was no real commercial need to implement such techniques, however this represents a limitation in

research scope as it has been shown that the requirements in LEDCs, where mammography is less common, is different (Sarvazyan et al., 2008) (Broach et al., 2016). Thus, there is a global demand for breast cancer screening and diagnostic tools, and thus the implementation of these advanced academic technologies in commercial systems.

2.9. Priority Areas and Justification of Scope

From this literature review the scope of the project can be defined, or rather justified from the project introduction in Chapter 1. It is important to note that the project direction, and scope, is defined by a combination of: The strategic direction of the supporting industrial partners, the needs of the clinical professionals, the availability of resources for the project (both manpower and materials), and the personal interests of the researcher.

The iBreastExam is marketed as an advanced screening system for low resource environments, particularly based in India and APAC areas, where health services lack resources to purchase the advanced features of SureTouch that have been shown to be valuable in early detection and classification. From this, it can be argued that there is two important directions for the development of general tactile imaging in breast cancer diagnosis and screening: Improve the ‘cost effectiveness’ of advanced systems like SureTouch, where the benefits of improved diagnostic capability outweighs the financial cost in the eyes of national or local health services in LEDCs; or improve the technology on less advanced systems that are more financially viable in these areas with clever engineering so as to not significantly increase their cost whilst maximising their

screening potential. The latter is also equivalent to simplifying and reducing the cost of advanced systems to make them affordable to LEDC customers.

As this project is supported by the manufacturer of SureTouch, and the manufacturer of the tactile sensor, in that their sensors are available for use on this project, that shall set the direction for the project. The company strategic direction, at the start of the project, was to improve the diagnostic capability of the system for later automated diagnosis research as such the project shall focus on upgrading the capabilities of tactile imaging to deliver key diagnostic metrics identified during this review. These metrics and objectives are:

- Elasticity (E_0) of the background tissue, allowing the lesion elasticity to be determined from Equation 2.1 by differential measurement.
- Compound tactile maps, giving spatial information on the lesion surroundings and view of the whole breast.
- Automatically localised lesion positions, allowing for better reporting free from subjectivity, and inference of lesion invasiveness.

These features have been identified as the most important, through literature review and discussion with professionals in order to improve the current capabilities in screening and to develop the diagnostic capability of TI.

Throughout this research, and into the future, careful consideration will be made on developing 'appropriate technology'. Based on the demographics and economic conditions relating to breast cancer screening, Figure 2.2, appropriate technology serves

the purpose without gratuitous expense or unnecessary features. The anecdotal example of this is: it is fine to make a proof of concept with multi-thousand-pound metrology equipment, but this will not be viable in the target market and will limit impact, so the methods/technology/algorithms must be similarly shown to work on simpler (more appropriate) technology and sensor systems. Additionally, in order to increase the commercial viability and subsequent impact of the research, the technology developed must be compatible and complementary to current commercial tactile imaging. The fewer modifications required to current commercial systems will increase the speed at which research innovations are adopted in industry.

Chapter 3

Inertial Guidance in Elasticity Imaging

3.1. Introduction

This chapter explores the development of a handheld breast elasticity mapping technology based on inertial guidance, an interesting, low cost, and commonplace technology found in all manner of devices, that can be used to support TI and enhance its functionality leading into further clinical testing of TI with the developed technology.

The chapter presents the design of custom system hardware, using a single tactile element as a proof of concept, featuring a detailed method of operation highlighting understanding of displacement measurement using inertial dead reckoning and its limitations, with testing on calibrated elastic phantom material. The device proves effective in controlled laboratory conditions with MAE $<4\%$ over a range of material stiffnesses, however the lateral mapping capability is found to be unsuited for measuring translation across the phantom breast surface. The chapter is split into 2 parts detailing elasticity and translational measurement using the technology respectively. The chapter concludes with a discussion on the significance of the results, concluding that this technology not be developed further in the thesis due to practicality issues on real tissues.

3.2. Tactile Elasticity Measurement Systems

This chapter addresses the problems of estimating the background elasticity of breast tissue and spatially relating tactile images simultaneously through sensor fusion between tactile sensors and inertial/orientation sensors, applications of which is a developing area of research in the literature.

Given that absolute elasticity measurement, and material characterisation, can be generalised to a force variation with respect to a compressive, or tensile, displacement variation, the conventional methods of applying and measuring displacement are applied to portable handheld systems in the literature and in industry. These devices can typically be broken down into two main components: a force or pressure transducer, and a sensor for measuring resultant strain. In some cases, this can be the other way around, where a strain is applied and resultant stress is measured, but the effect is the same.

Typical load transducers include strain-gauge based load cells, capacitive sensors, or even the humble spring; the bread and butter of many undergraduate engineering projects, though each present their own unique design challenges. Measurement of resultant or applied strain is more varied in terms of approaches, with a wide assortment of both simple and advanced technologies being employed. Simple methods have included: linear potentiometers, linearly variable differential transformers (LVDT), fixed actuation using mechanical cams, and piezo crystal deformation.

Optical and hyperspectral camera based techniques have been developed (Sahu et al., 2014) measuring transverse stretching of a lesion for an applied load but, as the

camera presents clinical privacy issues this method may face pushback from clinicians and patients when moved from academia to industry.

More traditional methods of measuring elasticity using mechanically driven palpating elements (Broach et al., 2016) show more promise in terms of public acceptance however, the limitation of the 4x4 mobile tactile element array reduces the available spatial resolution compared with the fixed element implementation (Egorov and Sarvazyan, 2008) with a 12x16 fixed element array in a similar area. This means that though an absolute elasticity value is obtained, size and shape information is lost which are each important diagnostic metrics (Rangayyan et al., 1997).

With these issues in mind, this chapter develops a method of measuring tissue compression, without cameras or palpation guide rails, that can be applied to fixed element tactile arrays, characterising elasticity whilst maintaining the spatial resolution they enjoy. To that end, this chapter presents a novel sensor displacement measurement technique based on the double integration of compression acceleration, utilising Magnetic, Angular Rate and Gravity (MARG) sensors.

3.3. Inertial/Orientation Sensors in Medical Applications

The measurement of displacement using MARG sensors has been attempted by several eminent authors to varying degrees of success. The primary concern addressed in the literature is the mitigation of the quadratic drift typical of double integration, required to determine displacement from acceleration. The second is the accurate estimation of sensor orientation, required to separate the motion acceleration vector from the static freefall acceleration (gravity) vector.

Rahni and Yahya in 2007 showed that the orientation estimate obtained using a simple 6 degree of freedom (DOF) integrated accelerometer and gyroscope, or inertial measurement unit (IMU), was insufficient to reliably measure displacement. This was due to the limitations in response time and noise rejection from early complementary filters and Kalman filters, compounded with the reliance on a drifting gyroscope alone to measure orientation. From this point onward a 9 DOF, that is 3 DOF accelerometers with aligned 3 DOF gyroscopes and magnetometers, MARG is typically used for displacement measurements, as the orientation estimate has been repeatedly shown to be drift free and resilient to motion noise (Valenti et al., 2015) (Fan et al., 2017) (Madgwick et al., 2011).

Without an accurate estimation of orientation, it is difficult to differentiate the acceleration due to gravity and the acceleration due to motion, but with accurate orientation information the gravity vector can be separated from the measured acceleration vector to yield a linear acceleration vector related to motion.

Mitigation of the quadratic drift from double integration is ultimately achieved using expert knowledge concerning the type of motion being measured, namely: knowledge on when either velocity or displacement is equal to a known value.

In the field of human gait tracking, knowing that between steps the velocity of the sensor is zero, the integral drift can be determined and corrected for, allowing for reduction in displacement error shown by Yun et al., 2007, where an uncorrected displacement error of 33.3% can be reduced to 0.3% by applying the velocity constrained drift correction.

Similarly, in the application of Cardiac motion measurement, Krogh et al., 2017, shows that by knowing that the motion of the cardiac wall is cyclic, the displacement between cycles is zero and thus the displacement drift can be measured and corrected for. This type of assumption is more difficult to correct for, in terms of accuracy, relative to the velocity drift compensation as the error source is not restricted to the acceleration integral alone (Neto et al., 2013).

With these examples in mind, this chapter will introduce a novel 9 DOF MARG displacement algorithm tailored for the specific motion type experienced by an indenter insertion and lateral translation of a tactile probe across the breast as shown in Figure 3.1. Concisely, for compression this is the situation where, during an insertion cycle, the velocity, when displacement is maximal, is zero. This means that both displacement and velocity-based compensation methods are utilized simultaneously, and a full description of this situation and the algorithm is presented in the following sections and applied to elasticity measurement of soft tissues through sensor fusion with tactile sensors.

The basic operation of a tactile mapping system is recalled in Figure 3.1, that allows visualisation of the two distinct motions being measured, and why they are needed. A compressive motion into the tissue generates a reaction force from the material under test, varying throughout the material depending on the elasticity of the material at a particular point. This elasticity can be measured by measuring the load as a function of the compression depth using a tactile sensor and a depth measurement, from the proposed MARG algorithm in this case. These individual tactile measurements can then be spatially referenced by tracking motion in lateral directions to form a tactile map.

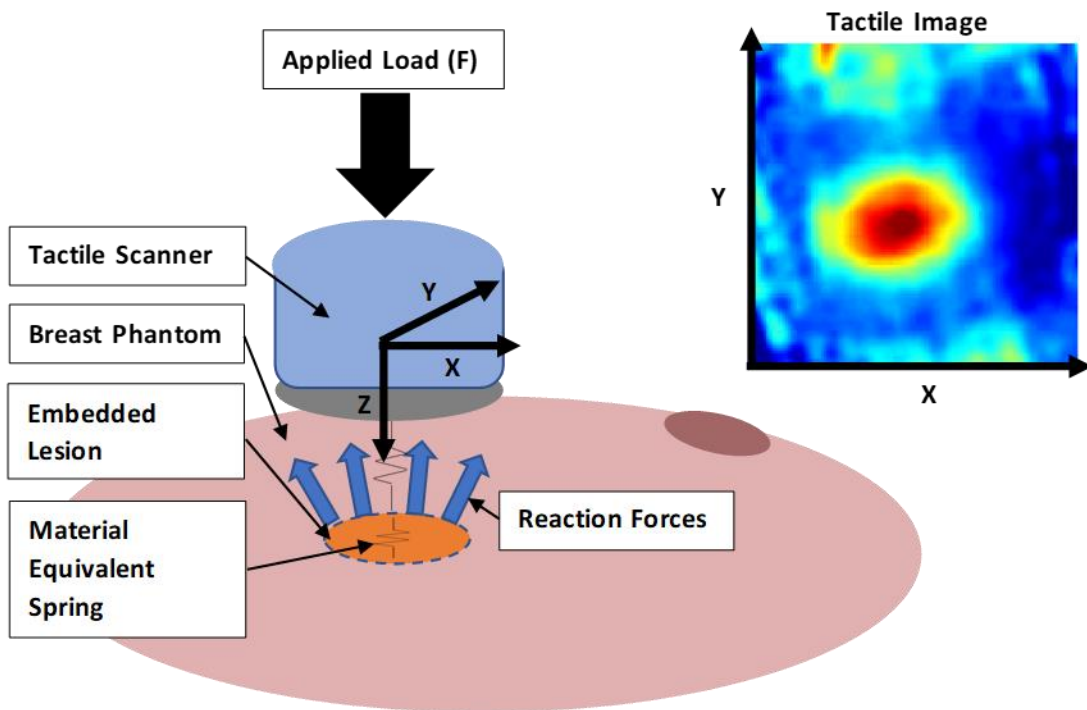


Figure 3.1 - Definition of probe motions and basic concepts in TI. The movement of the probe into the breast tissue along the Z axis compresses the material and generates a reaction force from Hooke's law in a linear case that can be measured using tactile sensors. Lateral motion in x and y axes are used to spatially related tactile measurements to form a large composite tactile map as shown.

3.4. Application to Elasticity Measurement

3.4.1. Displacement in the Context of Elasticity

The proposed device measures the force vs. displacement relationship of an unknown soft material, with the proposed MARG integration algorithm providing the displacement measurement. The displacement of interest is the displacement covered by the device from the point of first contact to the point of maximum force, as this will be the point of maximum displacement into the test material during the compression phase. Figure 3.2 shows the four principal phases of device operation, the device pictured was fabricated for this purpose as detailed in the following sections. The approach period is where the device approaches the test sample linearly along the principal measurement axis, and the compression period contains the displacement required for material characterisation, from the first indenter contact to the point of maximum force.

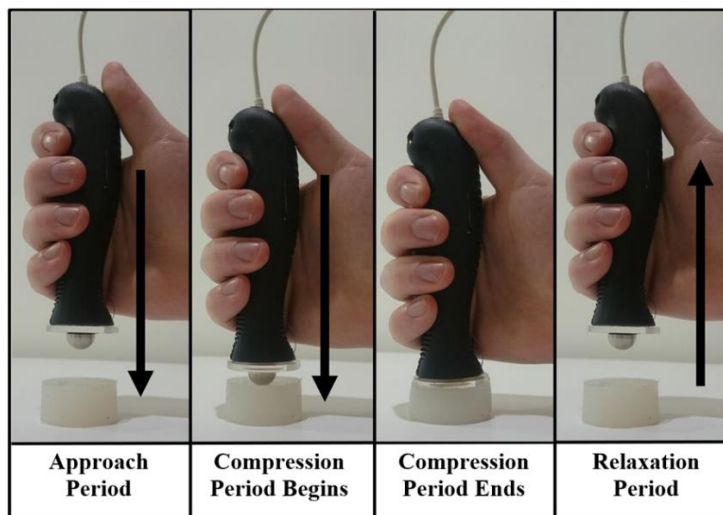


Figure 3.2 - Graphical representation of device usage, indicating the direction of compression and the need to apply the device perpendicular to the surface of the test material.

3.4.2. Hardware Description

The proposed algorithm is implemented in hardware using a SingleTact™ 15mm 45N rated capacitive pressure sensor (Pressure Profile Systems, US-CA), with <1% repeatability and <2% linearity, is coupled between a 15mm diameter hemispherical aluminium indenter and a 15mm diameter aluminium probe shaft. The sensor is fixed to the indenter tip and shaft using 3M 300LSE double sided tape (3M Company, US-MN). A 38mm diameter acrylic guard is used to protect the sensor from excessive load by decoupling the excess load, when depth is greater than 7.5mm, from the sensor and transferring it directly to the shaft. An ergonomic handle is applied to the end of the probe shaft, in which the MARG sensor and interfacing microcontroller are housed. The MARG sensor used is a BNO055 (Robert Bosch GmbH, DE), connected to an ATmega32U4 microcontroller (Microchip Technology Inc., US-AZ) running at 16 MHz. These sensors are commercially available and communicate via I2C. They each implement proprietary filters to output their respective variables. The constructed device is shown in Figure 3.3.

Power is supplied via the Universal Serial Bus (USB) port, also used to interface the measurement system to an external computer running the proposed algorithm. Data is requested from the BNO055 and SingleTact™ sensors at 100 Hz and transmitted to the computer immediately without buffering. The SingleTact™ interface board converts the capacitance change of the sensor into force and performs internal lowpass filtering. The BNO055 MARG sensor is configured to output the absolute orientation quaternion

as well as the linear acceleration vector. Its internal fusion algorithm filters the effect of intermittent magnetic fields with the gyroscopes.

Although the handle shape is largely unimportant, what is important is its effect on any elasticity measurement. The elasticity, or stiffness, of the handle and sensor must be very high with respect to the materials under test such that the elasticity of the handle does not significantly corrupt the elasticity measurement of the material under test. The deformation of the pressure sensor and adhesive tape is very low ($<20\mu\text{m}$) at the rated load, and thus its elasticity is very high ($>500\text{MPa}$), w.r.t. the material under test (in the order of $10\text{-}100\text{kPa}$ as described later) which will be deforming $\sim 10\text{mm}$.

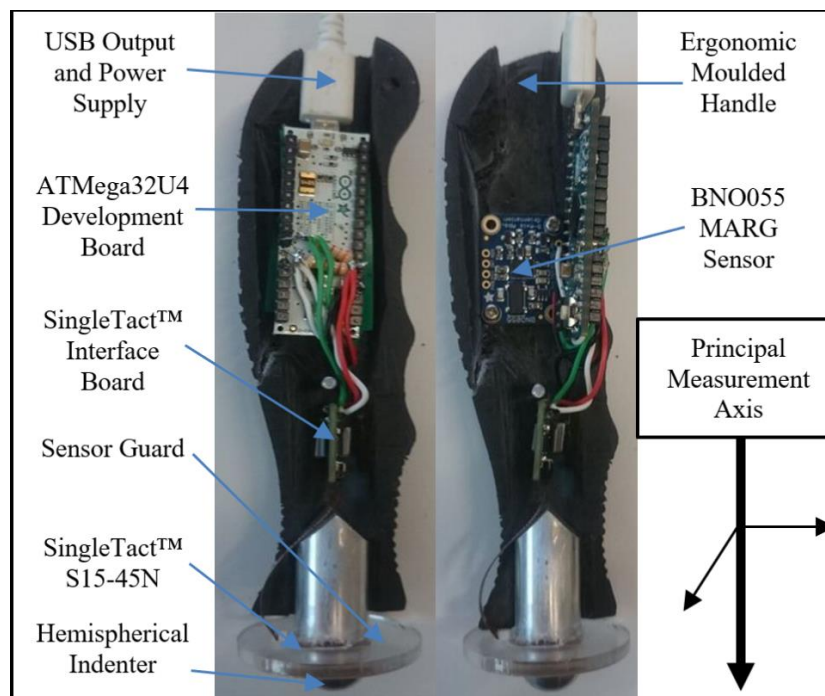


Figure 3.3 - Handheld elastometer hardware implementation. The BNO055 sensor has an axis aligned parallel to the normal axis of the SingleTact™ force sensor. The axes are radially offset, but this is unimportant to the design and does not affect performance.

3.4.3. Theory of Operation

3.4.3.1. Elasticity Specific Algorithm

The proposed sensor algorithm is shown in Figure 3.4. A 9 DOF MARG orientation fusion algorithm based on a gradient descent method (Madgwick et al., 2011) is implemented using the BNO055. This fuses the magnetic field (B), angular rotation rate (\dot{Q}), and the acceleration vector (a), to determine the orientation of the sensor with respect to the gravity vector. This allows for the gravity vector to be separated from the acceleration vector to produce the linear acceleration vector associated with the expected linear motion.

The force (F) measurement is used to trigger and stop the linear acceleration integrator. The force measurement is not subject to the free space vibration noise that the accelerometer is subject to, and so a sharp rise in force is indicative of the start of material compression. Similarly, the turning point of the force measurement indicates material relaxation, and thus triggers the integrator to stop. The accumulated acceleration data between the start and stop periods will then only be associated with the compression of the material.

The force and linear acceleration data for one measurement cycle is shown in Figure 3.5, highlighting the meaning of the start/stop conditions. Acceleration magnitude is too small during the relaxation period to reliably measure the material relaxation. The approach period, where the sensors are travelling towards the test material through air, will result in an unknown initial contact velocity. The acceleration data corresponding to

the compression period is integrated to yield velocity (V). The initial velocity parameter is estimated by knowing that the end velocity (V_{stop}) is ideally zero, the estimated velocity can then be offset using this V_{stop} value to give the true velocity during the compression cycle ($V_{\text{corrected}}$).

The error in $V_{\text{corrected}}$ is estimated and eliminated by examining the integral displacement (S) with the knowledge that the derivative of displacement, S , must be zero at the end of the compression cycle. Should there be an offset error on $V_{\text{corrected}}$, the subsequent displacement gradient after integration, which is V_{error} , can be removed from $V_{\text{corrected}}$ and integrated to yield the final displacement estimate (x) that is free from integral drift caused by the estimation of initial velocity.

The displacement vs. time, in the direction of the force sensor principal axis, is then used in conjunction with the force vs. time relationship to determine the material characteristic curve denoted by force vs. displacement. This relationship is then combined with the sensing area and material dimensions to determine the requisite stress vs. strain relationship, characteristic of individual material samples. The material characteristic curve, the force vs. displacement relationship describing bulk material elastic properties, is generated using a quadratic best fit line to the measured force vs. displacement data from the MARG based device. The quadratic is suitable for representing Hookean and neo-Hookean materials, typically modelled using exponential functions, and provides some resilience to noise (Jerison and Burgiel, 2010).

3.4.3.2. Calculation of Elasticity from Hemispherical Geometry

For a hemispherical indenter with radius, r , the cross-sectional contact area, A , is a nonlinear function of the displacement depth, x , as shown in equation 3.1.

$$A = \pi(2rx - x^2) \quad (3.1)$$

Thus, from the general equation for elasticity shown in equation 3.2, the final equation for elasticity using a hemispherical indenter is formed in equation 3.3, which considers the contact area changes in the estimation of applied stress. In this case the original size of the sample, L , is required and known. In (3.3), the term $E(x)$ is used to allow for conditions where E is not a constant, and is a function of x .

$$E = \frac{F/A}{\Delta x/L} \quad (3.2)$$

$$E(x) = \frac{F(x)/\pi(2rx - x^2)}{x/L} \quad (3.3)$$

3.4.3.3. Hardware Limit Considerations

As a result of the sensor guard, force measurements at compression depths greater than 7.5mm do not follow the expected Hookean or neo-Hookean response as the applied load is no longer being correctly coupled into the sensor and therefore will produce erratic results beyond this point as shown in Figure 3.6. Results with depths greater than 7.5mm are discounted from the calculation of the quadratic best fit line and

estimation material characteristic curve. The decoupling effect of the sensor guard manifests as a plateau, followed by a sharp spike as the probe compresses the material to the point where the backing dominates the signal.

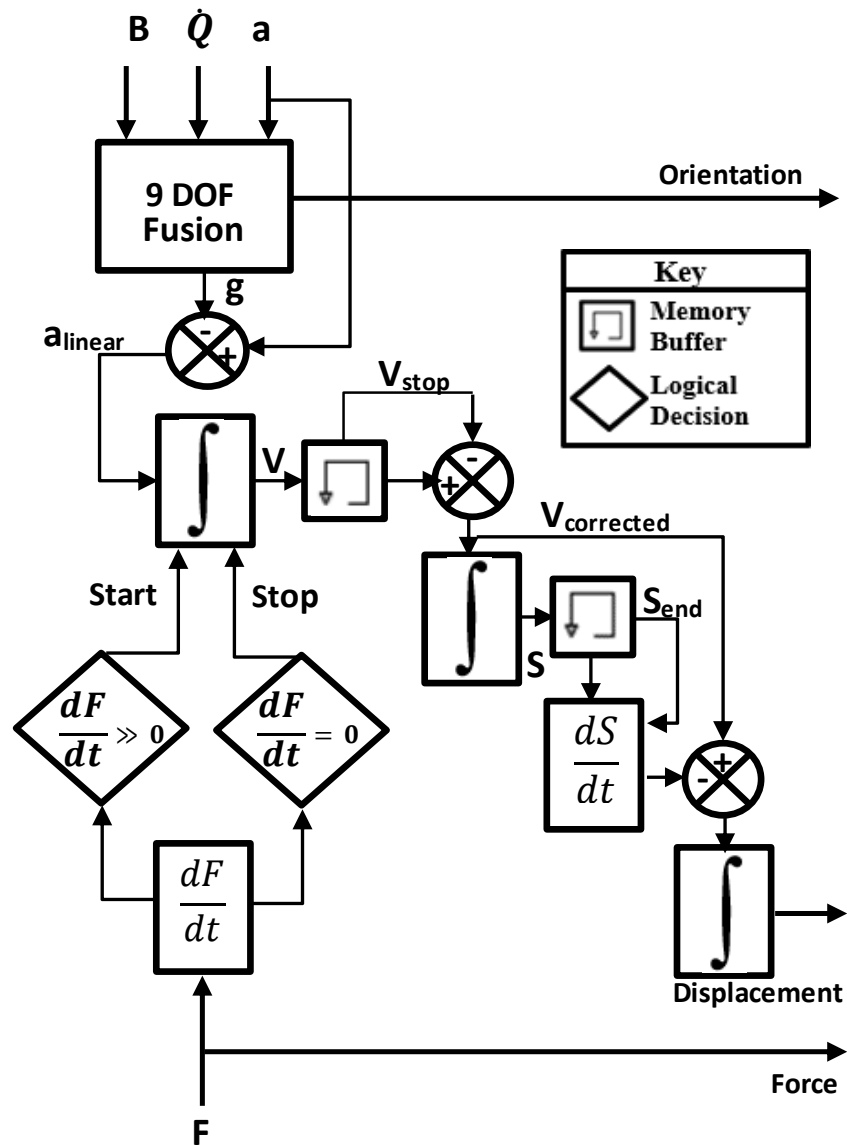


Figure 3.4 - MARG sensor algorithm flow diagram. Both velocity and displacement compensation methods are used to estimate the indenter compression depth. Force and displacement are plotted against each other. Orientation is output to assist with valid measurement criteria.

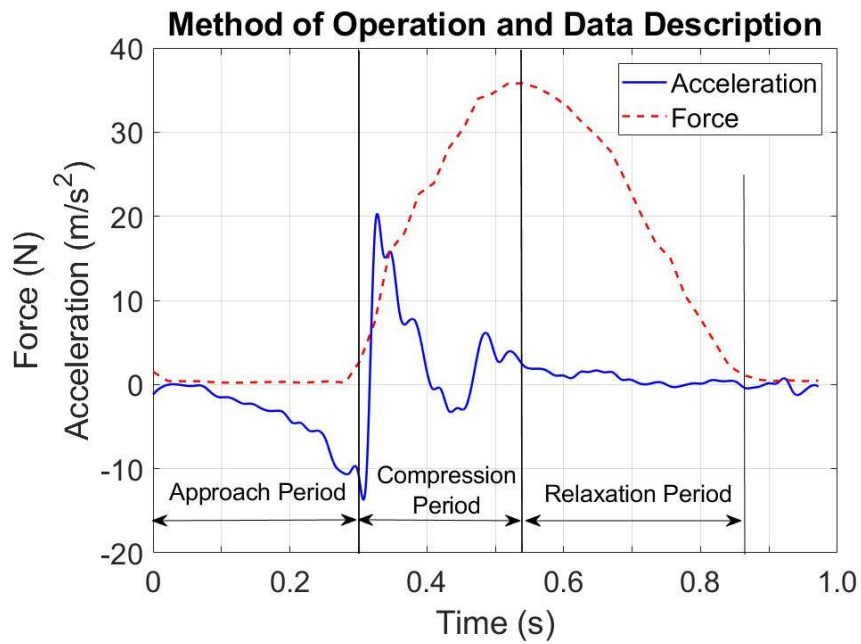


Figure 3.5 - Graphical representation of integrator start and stop conditions showing force and acceleration signals for one full measurement cycle. The acceleration on the advancement period will result in the compression beginning with unknown initial velocity.

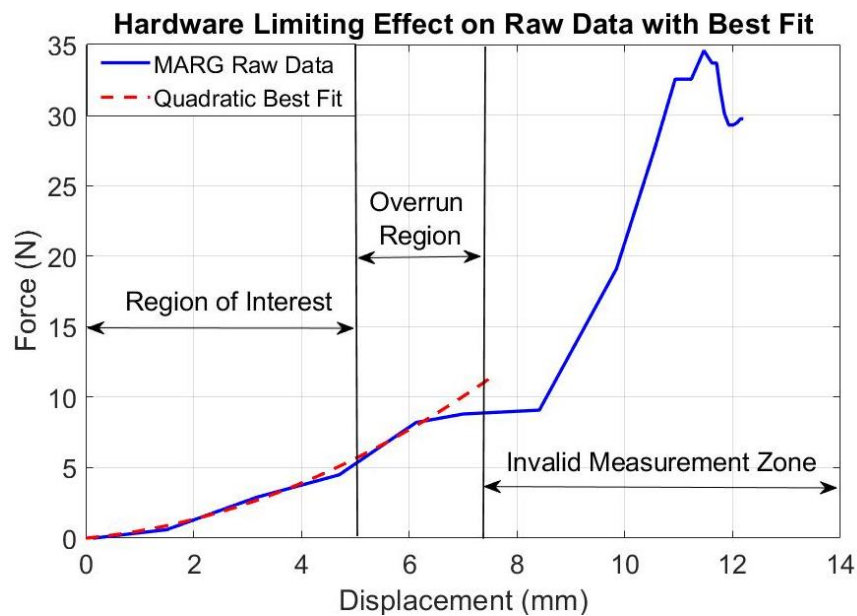


Figure 3.6 - Example of the sensor guard invalidating measurements at depths > 7.5mm. The invalid measurement stems from the change in force vs. displacement direction and rapid change in gradient.

3.4.3.4. Valid Measurement Criteria

Data cleansing is performed in two stages: pre-processing raw data based, and post-processing calculated data based.

Data pre-process cleansing involves immediately rejecting compression data that has a peak acceleration vector component parallel to the principal axis less than 10m/s^2 , approximately freefall. At values below this threshold, quantisation in time and quantisation in acceleration compound to produce unreliable displacement measurements. The maximum acceptable acceleration is 160m/s^2 , about 8g, to avoid saturating the accelerometer. Additionally, data where the displacement vector direction during compression deviates from the principal axis by more than 5° is immediately rejected. Beyond this point, the capacitive pressure transducer is experiencing a shear component that it is not designed for. Ideally this constraint would be 0° , but as this is a manually operated device some deviation is inevitable, and 5° keeps the cosine error within 0.5%. Data post-process cleansing removes force, F , vs. displacement, x , best fit curves that do not conform to Hookean or neo-Hookean models that typically describe biological tissues. Such models can be approximated, over a limited range, by a quadratic in the form of equation 3.4 as it is known that although biological tissues typically exhibit exponential responses (Wellman et al., 1999a), exponentials can be approximated over a limited range by a quadratic (Jerison and Burgiel, 2010).

$$F(x) = ax^2 + bx - c, \quad \{a \ b \ c\} \geq 0 \quad (3.4)$$

The implications of this are that viscoelastic materials will not be considered, as the test materials can be considered to be neo-Hookean or Hookean. A graphical representation of the data processing measurement rejection conditions is shown in Figure 3.7. In this situation, any solution that conforms to (3.4), has a direction vector within 5° of the principal measurement axes, and an initial impact acceleration greater than 10m/s^2 shall be considered in the calculation of the mean response.

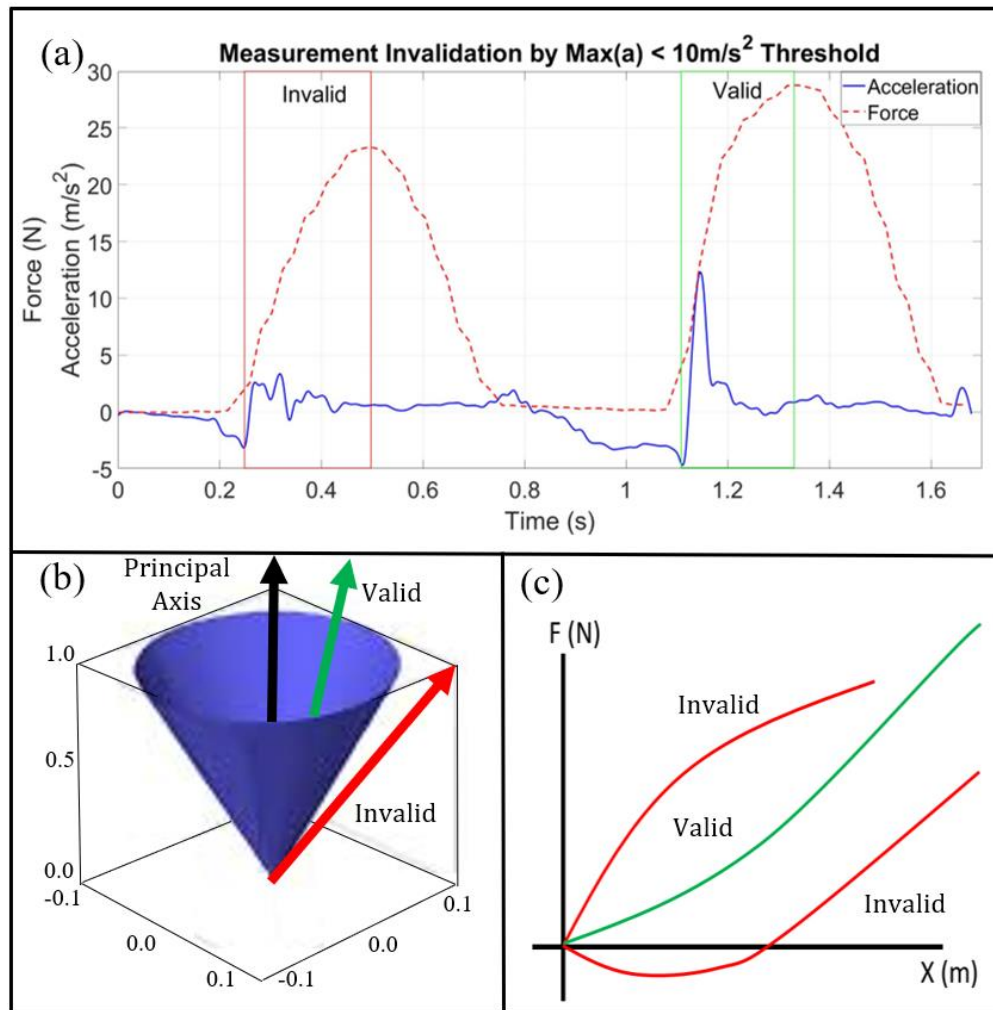


Figure 3.7 - Representations of data rejection situations: a) Acceleration magnitude threshold of 10m/s^2 . b) Compression angle deviation threshold of 5° , valid solutions within the cone. c) Equation form as Hookean or neo-Hookean as in (3.4).

3.4.4. Test Methodology

3.4.4.1. Sample Materials

The device is designed to compress the material under test in a linear direction, parallel to the pressure sensor principal axis. The device is pressed into the test material in a fashion akin to a gentle prod, repetitively, in order to be able to generate a range of force vs. displacement solutions whose mean will converge on the true value as the repetitions increase. These force vs. displacement solutions, in themselves are the material stiffness, (k), can then be used to calculate the material elasticity, (E).

Applying the MARG sensor and pressure sensor to elasticity measurements requires soft materials representative of breast tissue to test the system. The test materials used in this trial were made from Ecoflex™, 000-35, 00-10, and 00-30 rated Polydimethylsiloxane (PDMS) two-part elastomer (Smooth-on, Inc., US-PA) with differing A:B mixture ratios and additive thinning agents, Silicone Thinner™ (Smooth-on, Inc., US-PA) to give a range of materials that can approximate human tissues. These materials are listed in Table 3.1. The silicone elastomer samples were cast into uniform cylindrical billets with a diameter of 38mm and a height, L , of 20mm.

3.4.4.2. Test Strategy

Validation of the calculated characteristic material curve for each material sample is performed by comparing the response from the MARG and pressure sensor system with the response from an Instron® 3342 universal testing machine (Instron Engineering Corp., UK), fitted with a 2519-102 (50N) loadcell. This is a common

validation method for elasticity measurement techniques (Ozdemir et al., 2018) (Ettelaei et al., 2019) (Matsumura et al., 2009). The Instron® 3342 has a stated accuracy of 0.5% and compresses the sample using the same 7.5mm hemispherical indenter as the handheld MARG based system. Compression range is restricted to 5mm, or 25% strain, rather than the full 7.5mm, or 37.5% strain, as at high strains, $\epsilon > 0.33$, thin materials cannot be relied upon to exhibit bulk properties (Egorov et al., 2008). Similarly the load rate is set to 17mm/s, representative of the average load rate of the handheld probe.

Repeat measurements, for each sample, from the Instron®, and the MARG and pressure sensor system are performed, and mean values are used to compare the material characterisation ability of each method. The spread of results, from the repeat measurements, are presented to show the accuracy of any single measurement and compared to show the reliability of the MARG based system vs. the Instron® standard. Control of the average loading rate was done manually by rejecting data where the time taken to reach the 7.5mm plateau region is outside the range 0.4-0.5s. This keeps values representative and comparable

3.4.5. Results

The results of sequential compressions of 10 silicone samples by the MARG based system and the Instron® standard are shown in Table 3.1. The elasticities for each material are calculated using the linear region of (3.3) and are logged as the mean response with the interexperimental variability indicated separately as outsider range. The mean error in the MARG based estimation of elasticity is taken as the total error between the mean elasticity estimations from the Instron® using 4 trials per sample and

MARG using 10 trials per sample. These results are presented in graphical form in Figure 3.8 which shows the samples were well spaced over the range of 5kPa – 100kPa.

The results show that the MARG based elasticity estimate successfully tracks the ground truth from the Instron® test machine, and that the mean error and intraexperimental ranges are sufficiently small as to allow one material to be differentiated from another even when there is a greater than 2kPa change between materials. The differentiation breaks down on sample 4, which cannot be distinguished from sample 3 based on MARG elasticity estimate alone, though the Instron® shows they are slightly different. With many malignant tissues often having elasticities of 1:100 (Wellman et al., 1999a) when compared with healthy tissue, differentiating within 2kPa is likely not to be a problem in practice.

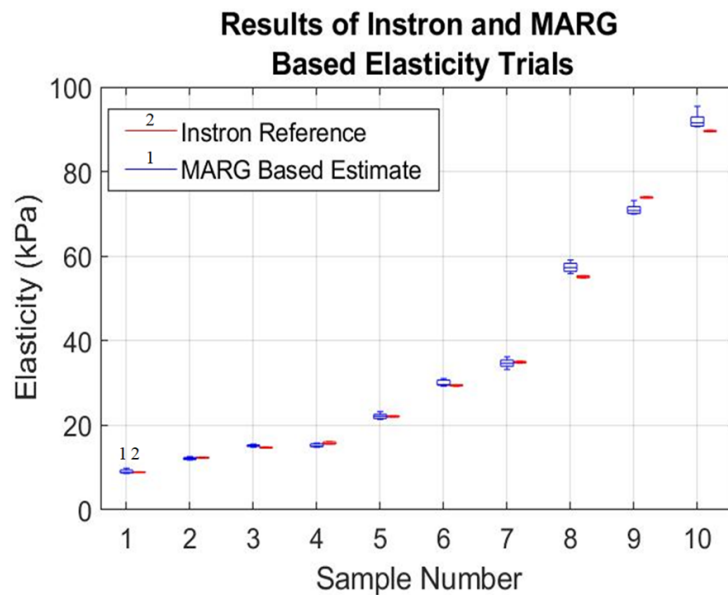


Figure 3.8 - Representation of full experimental results, showing the range of elasticities covered, the relative spread of each measurement and the agreement between the MARG system and Instron. The samples have been ranked for clarity, no correlation between samples is implied.

Table 3.1 - Material compositions with measured elasticity. Elasticity is taken as the mean of repeated cycles, with spread indicated.

MATERIAL COMPOSITIONS FOR ELASTICITY MEASUREMENT TRIAL					
Sample	Material A:B Ratio	Thinner By Mass	E_{Ref} (kPa)	E_{MARG} (kPa)	Mean Error (%)
1	000-35 1:1	+10%	8.9 +0.1 - 0.1	9.1 +0.9 - 0.5	2.24
2	000-35 1:2	+20%	12.3 +0.2 - 0.1	12.1 +0.6 - 0.4	-1.62
3	00-10 1:1	+10%	14.7 +0.2 - 0.1	15.1 +0.5 - 0.2	2.72
4	00-10 1:2	+0%	15.7 +0.5 - 0.3	15.2 +0.7 - 0.3	-3.18
5	00-10 2:1	+10%	22.1 +0.2 - 0.2	22.1 +1.0 - 0.5	-0.11
6	00-10 2:1	+20%	29.5 +0.1 - 0.3	30.1 +1.1 - 0.9	2.03
7	00-10 1:3	+0%	34.9 +0.3 - 0.2	34.7 +1.9 - 1.0	-0.57
8	00-30 1:1	+0%	55.2 +0.2 - 0.4	57.3 +1.8 - 1.5	3.80
9	00-30 2:1	+10%	73.8 +0.3 - 0.1	71.1 +2.5 - 1.6	-3.65
10	00-30 1:3	+0%	89.6 +0.2 - 0.2	92.4 +2.9 - 2.1	3.12

3.4.5.1. MARG Based System Performance Analysis

From the results in Table 3.1 the sensitivity of the MARG based system to errors borne from elasticity related effects of the material under test is shown in Figure 3.9. Additionally, the total intraexperimental scatter, for 10 repeated MARG trials per sample, is shown in Figure 3.10. These graphs are required to characterise the response of the MARG based system over its operational range.

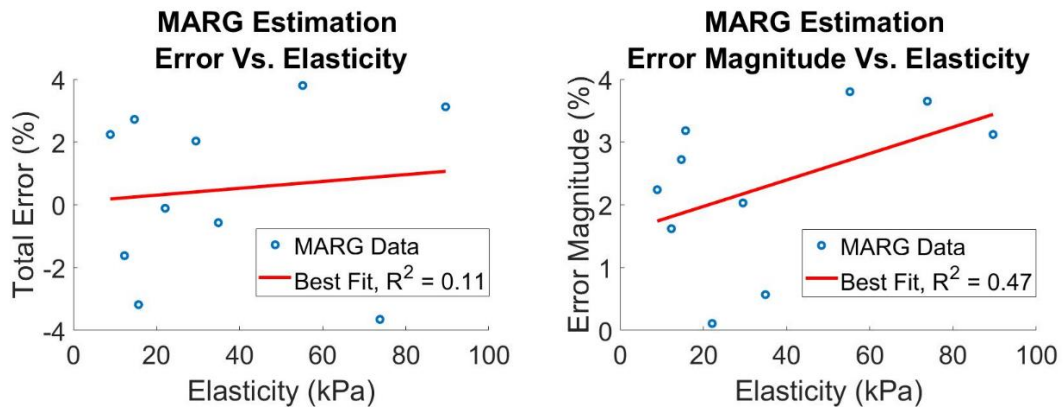


Figure 3.9 - Systemic Error Vs. Measured Elasticity, Left) Total Error Vs. Elasticity, showing a very weak correlation. Right) Error Magnitude Vs. Elasticity, showing a stronger correlation, but still weak.

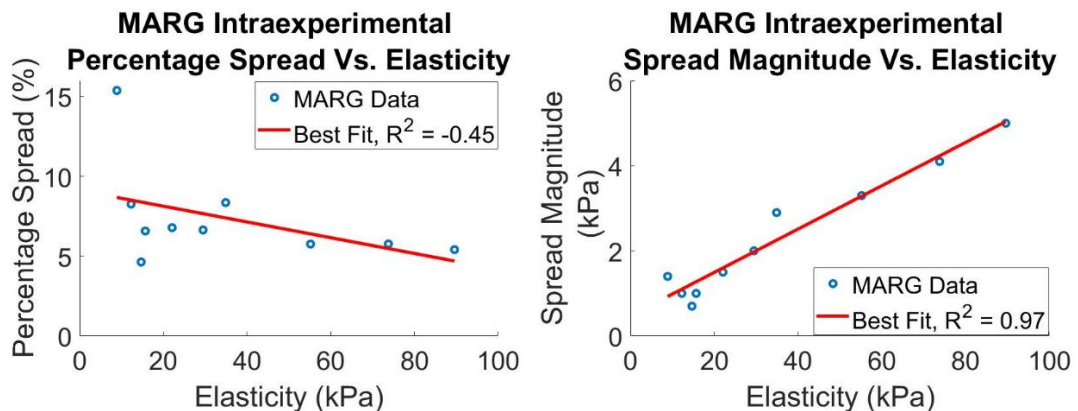


Figure 3.10 - Intraexperimental scatter Vs. Elasticity, Left) Spread as a percentage of measured Elasticity showing a weak negative correlation. Right) Spread magnitude, showing a very strong positive correlation.

The results of repeatability testing on sample 3, chosen at random, is shown in Figure 3.11. It can be seen that utilising a 10 compression cycle measurement regime rather than a 6 cycle regime significantly reduces the overall estimation spread. This is expected as statistical outliers are easier to identify with higher population numbers.

Additionally, it is shown that 3 repeated 10 cycle measurements produce excellent repeatability over the full compression range. This provides good confidence in the measurement technique as we are able to achieve repeatability on the raw force vs. displacement response even before statistical outlier rejection is applied. This single sample repeatability is typical of the global system repeatability and, when mean responses are considered, results in mean repeatability within 1.5%.

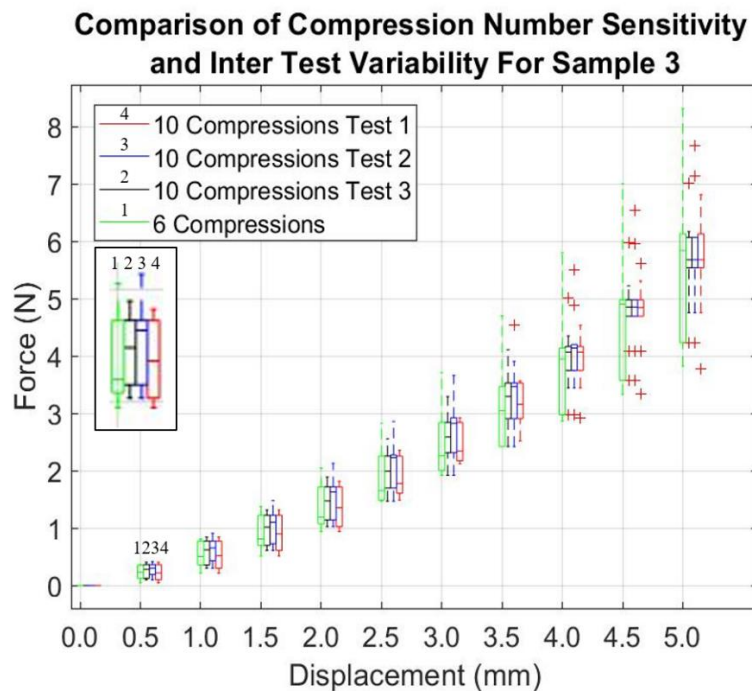


Figure 3.11 - Comparison between 6 compressions per test and 10, showing overall scatter decreases with compression number, and multiple sequential tests with constant compression numbers yield repeatable interexperimental results within 1.5%.

3.4.6. Results Discussion

The better than 4% measurement accuracy of the proposed system, shown in Table 3.1 and Figure 3.8 is achieved by taking the mean response of 10 repeated compression cycles and comparing this with the mean response of the Instron®. This is appropriate, as even the Instron® uses internal averaging, but the Instron® can achieve this in one compression. If any single compression cycle were taken as being representative of the material under test the accuracy would be considerably worse, up to 50% as indicated in Figure 3.11. Additionally, if fewer compression cycles are taken, say 6 for example, outliers cannot be easily identified and so the accuracy of any single compression used to calculate the mean response will also be up to 50%. However, by taking 10 cycles, outliers can be identified and rejected from the mean calculation resulting in the error of any single compression used to calculate the mean typically being between 5% and 10% as shown in Figure 3.10.

If any single full measurement of a tissue, defined as 10 compression cycles, is used to characterise a tissue then the accuracy becomes better than 4% when compared with the Instron®. Using a higher number of cycles, say 30 does not significantly improve the accuracy compared with going from 6 to 10 cycles. In order to facilitate a timely measurement, 10 cycles are used for each measurement as this gives acceptable accuracy in a reasonable timeframe (<10s). This balances the response time and accuracy, a common problem in medical device design.

3.4.7. Error Sources and Limitations

There are 2 primary sources of error in the proposed system. The first is error arising from the measurement of applied stress. One of the key requirements of this technique is that the probe compresses normally to the surface and have a direction vector within 5° of the sensor axes. This angle is used as an inexperienced operator can be expected to achieve a successful compression 95% of the time. Ideally this would be 0° , but people cannot move linearly without guidance due to the hinging nature of the elbow. Consequently, if the angle is not 0° the stress measurement will not correlate with the strain measurement but, as the angle is low, the shear force is low. The parasitic effects of the capacitive sensor in contact with biological tissues is not a significant source of error as the sensors are fully shielded. Figure 3.12 shows the effect of touching the sensor on the noise floor of the force measurement, where the noise can be characterised as Gaussian white noise and so can be mitigated in the mean filtering process. The effect of the temperature coefficient, $<0.2\%/^\circ\text{C}$, is negligible, particularly on the test data where the temperature was carefully controlled.

The second is error arising from the measurement of strain. As this is done by the double integration of acceleration, this is certainly the dominant source of error, despite the effect of the MARG fusion algorithm in reducing the effect of integral drift. The measurement of strain is most affected by vibration, as the direction is filtered using magnetometers and gyroscopes, but the strain is only determined by the acceleration, as such the measurement of strain is resistant to intermittent magnetic field variation, though this is difficult to validate in practice without special test equipment.

Figure 3.12 shows the validation of the displacement measurement vs. a Leica® AT403 Absolute Tracking system (Hexagon Metrology Ltd. UK) with accuracy $\pm 15\mu\text{m}$ over 120 manual repetitions on sample 3. These were at a range of depths between 8mm and 15mm. This shows the effect of the valid measurement criteria on error reduction. The increase in elasticity spread magnitude vs. elasticity, shown in Figure 3.10, suggests that the vibration gets worse as the materials stiffen. This is expected as the probe compresses the material harder, the stability of the hand reduces and so shakes the sensor. This results in variation in the strain measurement by constructive or destructive addition of the acceleration vectors although it has been shown through the results that this variation, when controlled using tactile sensor fusion, can produce acceptable mean errors comparable with a static soft tissue elastometer (Egorov et al., 2008).

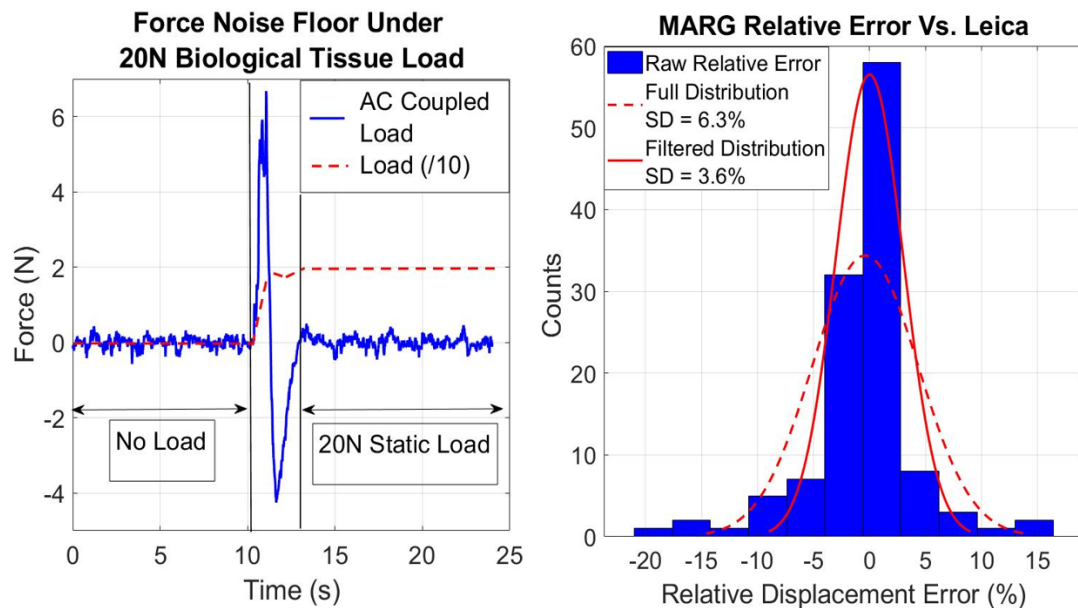


Figure 3.12 - Error and repeatability plots, Left) Force sensor noise does not noticeably increase near biological tissues, so is immune to parasitic effects. Right) Comparison of MARG displacement vs. Leica Tracker, showing that the overall error is reduced by applying the valid measurement criteria.

3.4.8. Range Compared to Typical Breast Tissues

As the proposed system is capable of measuring elasticity in the range 9kPa to 90kPa with accuracy within 4%, up to 115kPa based on the tactile sensor rating, it is possible to characterise the elasticity of a broad range of breast tissues directly including several malignant conditions such as Phyllodes Tumours and Papilloma (Samani et al., 2007). Given the tactile sensors can be operated up to 2 times their rating with recalibration, the range increases to 250kPa. This allows for measurements of ex-vivo samples of malignant tissues such as Lobular Carcinoma and Fibroadenoma at $\epsilon < 0.1$.

The intended future application of this system is as a support method for larger tactile imaging systems, where this method would be used to measure the background breast elasticity, allowing for characterisation of in-vivo lesions by differential measurement (Egorov and Sarvazyan, 2008). Consequently the system would be typically used on normal tissue and soft benign tissues (Guray and Sahin, 2006), with elasticities of approximately 10kPa and 88kPa for fatty tissue and glandular tissues respectively. This is within the characterised operational range of the proposed system.

The major limitation of this type of system in measuring real breast tissues is the assumption of elasticity, and subsequent omission of viscoelastic analysis amongst other things. The practicality of this system in real use will be limited to the need to define the average loading rate that the sample was measured at, as well as the need to take many more measurements than is done currently in order to control and vary the average loading rate. This is not considered to be a useful thing to do, as the loading rates here are considerably faster than calibrated values seen in the literature (Samani et al., 2007).

3.5. Clinical Practicality

The application of this technology is in fixed array tactile imaging, allowing for breast and lesion elasticity to be reliably determined together in a non-invasive manner, where this technology provides the background breast elasticity. This is an important step towards tactile imaging performing on the spot diagnosis of lesions, as commercial tactile imaging provides only the relative elasticity of a lesion currently.

The clinical significance of measuring elasticity of breast tissues is clear in that the material elasticity is correlated with histological diagnosis and identification of a tissue. The operating range of the proposed system covers the elasticity ranges of fatty tissue, glandular tissue, and several malignant tumours and carcinomas. This means that, although this technique is intended to support and supplement more established tactile imaging methods by measuring background tissue elasticity, which allows for in-vivo characterisation of lesions, the proposed system is fully capable of stand-alone usage as an elastometer for pathologists in the clinical environment, although this would be in ex-vivo conditions.

Despite the demonstrated functionality of the proposed system, the method proved to be a little impractical for live clinical use. The method of operation, taking at least 10 compression cycles per elasticity measurement, is awkward for the practitioner and for the proposed patients. That being said, the proposed system and algorithm achieves its intended purpose in that it is capable of determining the elasticity of soft elastic materials using the double integration of acceleration. With a ready solution to

the problem of elasticity measurement at hand, the next task is spatially registering tactile measurements. The MARG based displacement measurements investigated in this chapter have shown promise and represent an efficient reuse of technology if used for the purpose of measuring lateral translation as well as indenter compression depths.

3.6. Application in Production of Tactile Maps

3.6.1. Displacement Context and Measurement Problems

Producing a tactile map based on inertial dead reckoning alone is highly impractical due to the type of motion required to get reliable displacement information from acceleration double integration. The typical breast scan performed using tactile imaging, in the manner of (Egorov and Sarvazyan, 2008) and current clinical usage of SureTouch™, scans across the breast tissue with a relatively constant speed in the order of 0.05m/s. This presents a primary problem in that the only signals available for displacement estimation would occur at the start and end of the scan stroke, with a quadratic error building on residual error of the initial acceleration over a few seconds.

The second problem is that the accelerations at the start and end of a scan stroke would be very small indeed, in the order of 0.5m/s^2 , which would be lost in the noise floor of typical low-cost accelerometers. An ideal accelerometer, with no noise profile capable of measuring very low accelerations, would not even solve this issue as the ‘relatively’ constant scan speed is rarely truly constant. Inconsistencies in surface friction, the scan head catching on the skin, vibration of the hand, vibration of the patient,

and rolling of the scan head produce accelerations that dwarf the acceleration due to linear motion. A simple slip produces accelerations 10x the desired linear acceleration.

Displacement sensing using acceleration integration has been shown to be effective over long distances and long time frames (Yun et al., 2007) (Neto et al., 2013) even being effective at measuring the perimeter length of a football field with acceptable accuracies (~4%) after a distance of 350m at an average speed of 1.56m/s (3.5mph) when applied to gait tracking. This is a long time for errors to accumulate from double integration... so why does the proposed system face difficulty in mapping the breast?

The answer comes down to scale...

In gait tracking the great distances are broken down into manageable chunks, the steps themselves. These have easily definable start and end points which are used to estimate and control the integral drift. The proposed system has already demonstrated the effectiveness of this technique when it comes to material strain measurement. They are also short in comparison to the total distance being measured, effectively stopping to control the total integral drift 350 times during the total distance measurement (assuming 1m steps over 350m total). Finally, the steps are the dominant source of both acceleration and displacement, with each step being a smooth and natural motion with a very high SNR. It is these final two points where the proposed system, with a tactile array, fails to produce tactile surface maps. The proposed system would need to measure the full path distance in one step, with only the end point to control the integral error and would need to do this with a very low SNR which can make defining the end point difficult. It should be noted that when used in material strain measurement, the distances

and time are very short which precludes the need to sub sample the distance (though that would be impossible to achieve anyway), and the linear acceleration of the compression stroke is the dominant source of acceleration which provides a good SNR. This is combined with clearly defined start and end points from the tactile sensor, resulting in acceptable accuracy comparable with the gait tracking authors and fixed elastometers.

To highlight the problem that the contact between the material under test and the tactile scanner has on the measurement of sensor displacement across the material surface, needed to produce a tactile map of the surface, a simple experiment shall be performed to compare the displacement measurement of the proposed system when actuated in free air to that of the proposed system being dragged over an elastic surface.

3.6.2. Test Methodology

The proposed system is actuated over a distance of approximately 15cm horizontally, a reasonable figure for a single pass tactile breast scan, parallel to the surface of an elastic flat breast phantom material, both in free air (not in contact with the material), and in contact with the material with a target load of 5N, to determine the effect of contact on the accuracy of the displacement measurement. This is in the x/y dimension when considering Figure 3.1. Additionally, the effect of stroke speed on displacement measurement accuracy will be determined by actuating the proposed system slowly at first, at an average rate of about 0.05m/s in line with typical tactile imaging, then quickly, at around 0.8m/s in line with the gait tracking examples. A Leica® AT403 Absolute Tracking system (Hexagon Metrology Ltd. UK) with accuracy $\pm 15\mu\text{m}$ is used to provide a reference ground truth to the displacements and average

stroke speeds over 50 actuations of the system for each load and speed case. The target load is maintained using a household electronic weighing scale, 5kg rated, and visual feedback to the operator to attempt to control the average applied load. The proposed system will use a modified form of the gait tracking displacement algorithm developed by (Pierleoni et al., 2019) for estimation of displacement as this is more applicable to this type of motion than the material strain algorithm presented in this chapter. This algorithm additionally uses a sudden jerk, as well as a low acceleration, to signify the start and stop conditions at the beginning and end of travel, and assumes the velocity is zero at these points. Using this assumption, the integral drift can be estimated and removed to yield a useful result.

The mean difference error, and the sample standard deviation of differences, between the ground truth displacement and the MARG algorithm estimate will be presented for each load and speed case. This will show the accuracy and, perhaps more importantly, the reliability of current MARG based displacement measurement algorithms when in constant contact with the measurement surface and moving slowly, currently a requirement for tactile imaging of the breast.

3.6.3. Results

The results of 50 repeated 0.15m motions, with varying load states and stroke rates, are shown in Table 3.2 in terms of mean difference error and standard deviation from the Leica® ground truth. These errors, and the relationship between them, are shown graphically in Figure 3.13, where a categoric view of loading state and stroke rate is used as a continuous sweep of accuracy vs. velocity is impossible in this context.

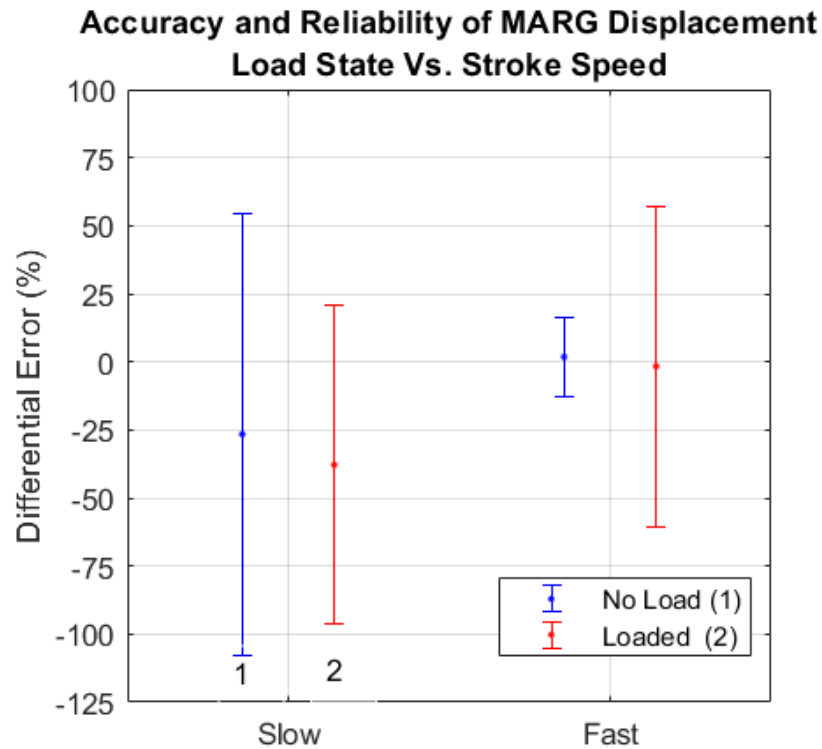


Figure 3.13 – Illustrative graphic of MARG accuracy and repeatability vs. Load vs. Stroke Rate. The results show that scanning slowly in any load state is detrimental to the accuracy and repeatability, and that loading when scanning quickly does not affect the accuracy over 50 trials but severely impacts the repeatability of a single motion.

Table 3.2 - Results for repeated tests of 50 runs of 0.15m with the MARG probe, with varying average stroke speeds and surface loading conditions.

ACCURACY AND RELIABILITY OF MARG DISPLACEMENT VS. GROUND TRUTH COMPARING LOAD AND STROKE RATE				
Test	Stroke Rate	Load	Mean Error	Standard Deviation
	(m/s)	(N)	(m)	(m)
1	0.05	0	-0.0399	0.1216
	(Slow)	(No Load)	-26.581 %	81.061 %
2	0.05	5	-0.0568	0.0880
	(Slow)	(Loaded)	-37.868 %	58.653 %
3	0.8	0	0.0027	0.0219
	(Fast)	(No Load)	1.7776 %	14.631 %
4	0.8	5	-0.0025	0.0882
	(Fast)	(Loaded)	-1.6601 %	58.7715 %

The results show that scanning slowly has a massive impact on the mean difference error, regardless of load state, when compared with scanning quickly. When scanning quickly, either loaded or unloaded, the mean difference error is within 2% of the reference values, but when the load state is changed to 'loaded' then the standard deviation jumps from 14% to 58% as the inconsistency in contact conditions affects the reliability. When scanning slowly, the MARG estimation is in the order of 30% under the reference on average, but when loaded the mean error increases from -26% to -37% despite the standard deviation dropping from 81% to 58%.

An expected result is that mean error and standard deviation deteriorate when the stroke rate is reduced with no load, and this is seen in the data, but a surprising result is that the standard deviation of the loaded cases does not depend on the stroke rate which would reasonably be expected to deteriorate similarly to the unloaded cases.

Finally, the results show that the MARG displacement estimation is effective over repeated similar motions, with mean errors $< 2\%$ when the motion is fast, but that the reliability of each individual motion measurement deteriorates significantly when the scanner is in contact with the material surface. When the stroke rate is reduced to a practical level for tactile imaging, then the mean error becomes untenable at -37% when in contact with the material surface. This, and the poor standard deviations of all trials, shows that the MARG based positioning system is suitable for situations where a total distance travelled value is required after multiple steps, rather than in applications where a single step/motion distance is required from only one scan motion as is the case in current tactile imaging.

3.6.4. Discussion

The difference in mean error sensitivity to loading state between fast scanning and slow scanning, with negligible change whilst fast and 11% change when slow, shows that the effect of stroke rate dominates the effect of loading on the mean difference error. When the two effects, loading and slow scanning, are combined then the worst result of all is obtained.

The term ‘worst’ refers to the mean difference error, which cannot be removed reliably by taking successive measurements as the effect of standard deviation can. The mean error in this situation cannot simply be compensated for, as in other applications, by characterising the mean error and subtracting it from the final result, as the mean error is dependent on both the stroke rate and the loading condition which would each need to be parametrically characterised. This sort of activity exceeds the scope of this project as the stroke rate and applied load are exceptionally difficult to control manually in a dynamic system like this and using a robotic manipulator would not accurately simulate the jitter of a hand or the reactions of a human operator. The target loads and speeds provide some measure of control., but they cannot be controlled tightly enough by manual actuation of the system to obtain a parametric sweep. As such the experiment used load and stroke rate values with an order of magnitude difference to obtain a categorical relationship sufficient to determine whether the proposed system could indeed work in a practical tactile mapping system as opposed to the elasticity imaging system application previously demonstrated.

The difference in standard deviation between fast and slow unloaded trials, and similar lack of change between fast and slow loaded trials is down to the range of motion in each case. Moving a probe slowly through the air requires constant feedback between the operator's eyes and the hand resulting in servo vibration, the effects of which compound over time and are not repeatable. Similarly, moving the probe across the breast surface constrains the motion and rotation of the probe, especially when the scan is slow, and so results in a better standard deviation when loaded and scanning slowly than when unloaded. The low standard deviation in the fast unloaded case is caused by a lack of operator servo control in the movement of the probe (it's a more natural and fluid motion), and so is largely immune to the vibration and rotation artefacts that affect the slow scans despite being unconstrained, with the artefacts that are present being small and having little time for the error to accumulate.

The mean errors within 2% from the fast scanning trials can be likened to the results of the human gait tracking experiments (Yun et al., 2007), where the mean error can be thought of as the total error in end position after 50 motions or 'steps'. The authors obtained a similar result in terms of error after approximately 350 steps, showing that the algorithms are effective for large and small distances providing they are broken up into finite chunks. It would be reasonable to suggest that if the authors individual step displacement were analysed then a similar standard deviation would be obtained to the proposed system results for no load. The key point from this, as explained by (Hampson et al., 2019), is that these MARG displacement algorithms can be effective when used in an appropriate application with their limitations within the application understood.

3.7. Conclusions from Inertial Elasticity Mapping

3.7.1. MARG Based Elasticity Mapping Practicality

With a mean error close to 0%, as in the cases of fast scanning, it could be said that the proposed system would work for tactile mapping (with errors within 2%) providing a sufficient number of similar scans over the same breast area were taken, but the system would not work reliably if a single scan were taken due to the poor standard deviation of displacement measurements. That being said, the application of multiple fast scans to the breast would be highly uncomfortable for the patient and would largely defeat the goal of tactile imaging in breast cancer management, to reduce the need for painful and traumatic procedures like mammography and biopsies.

Similarly, with both a mean error $> 37\%$ and a standard deviation of 58% when loaded, the proposed system would not work for tactile mapping (using the proposed system alone) with a slow stroke rate in any circumstance, as no number of repeated measurements will yield an acceptable average result without exhaustive characterisation of tracking performance over stroke rate and load.

It is clear that MARG based position tracking is not suitable in the location and registration of tactile images within a complete map, although it is effective in material strain measurements for elasticity estimation due to the repeated compression cycles, due to its poor accuracy and reliability in this particular application. The writing is not on the wall for a MARG based elasticity mapping system yet though, as the elasticity measurement aspect is still effective. When integrated with a tactile array, the array can

make differential measurements of lesions and estimate the absolute elasticity of the lesion using the background tissue measurement from the MARG based system. This quantified tactile image can then be stitched using image mosaicking, a process that has been tried in the literature (Egorov and Sarvazyan, 2008) to produce a quantified tactile map of the breast tissue. The issue with creating the tactile map using such a technique is that there is limited information on where on the breast the scan probe is at any point in time, and the information is limited to a quadrant of the breast. This 2D quadrant map is subject to change over time through a combination of operator procedure, patient orientation, and subtle changes in breast position between scans; and can make tracking lesions between scans problematic.

On the point of the clinical validity of the elasticity measurements, further elaboration is required. The device was effective at measuring elastic materials, when the average strain rate matched that of the Instron, however the method will swiftly deteriorate when real tissues are used that exhibit viscous and shear thinning properties. Unlike with a traditional compression elastometer, the strain rate of the proposed system cannot easily be controlled, and is highly variable during compression, and so the device is not expected to give accurate results when used in real biological materials with complex properties. The method of measuring material strain is fundamentally not suitable for the ‘slow’ motion caused by viscous creepage, as highlighted in the mapping experiments and so viscous properties other than viscous drag cannot be measured with this system. The characterisation of properties in the event of shear thinning is expected to be possible, but the number of compressions required to characterise the tissue

response vs load and load rate would make the device even more impractical to use than it already is. The conclusion from this is that, although the developed algorithm is novel and measures strain in the context of elasticity measurement, the method is not well suited to the characterisation of biological materials due to the lack of control over the strain rate, and the assumption of material linearity used to reject ‘bad’ data limiting the usage scope of the technology. By itself, the technology is an interesting academic achievement particularly in the field of dead reckoning, but it is not considered to be useful clinically after initial testing and should not be explored further for that purpose.

3.7.2. Summary and Next Steps

This chapter has developed a novel MARG based displacement estimation algorithm for measuring material strain and applied it to elasticity measurement of soft elastic tissues with an accuracy of $< 4\%$ over a material elasticity range of 9kPa to 90kPa by employing sensor fusion with a tactile pressure sensor. Explanation has been presented on how the single point elasticity measurement system (Hampson et al., 2019) can be integrated with a tactile array to form quantified elasticity images that will aid in breast lesion diagnosis (Egorov et al., 2009). Despite this, the conclusion drawn is that MARG based elasticity measurement, though effective in its own right, is not practical in a clinical context due to the awkwardness in use, and that the method involves continuous palpations of the tissue that can become uncomfortable to the patient.

This chapter has also attempted to develop a method using the same MARG based displacement estimation technique to register tactile images in relation to each other, but through preliminary investigations this was shown to not be a viable solution

currently. This is because the current tactile scanning method, a slow single pass of the tactile sensor over the surface of the breast with the sensor compressing the tissue, is not compatible with MARG based displacement estimation which generally requires fast/sharp motion with little deviation from the intended path.

It is clear that a better method of mapping tactile images is required, one that is capable of locating a lesion precisely on the breast without being subject to scanning procedure, and that a more practical method of determining the breast background elasticity is required to reduce the burden and discomfort of use to the patient. One option for tactile image tracking is to develop a system that can track both the scan probe and the patient in an absolute coordinate frame. This has been attempted before (Wellman, 1999) but fails in tracking the patient movement and so is still dependent on strict patient placement. Utilising the popular and widespread camera-based 3D object tracking may help in that regard now, as it certainly did not exist outside academic circles at the time, but solutions based on external tracking systems involve large infrastructure and costs, not suitable for a GP or a home use case. Developing a system that can locate the tactile images onto natural features of the patient's body will be a much better prospect, as these features can be tracked between scans and are usually stable. Perhaps the easiest method of identifying features on a body is visually, with a camera image, which shall be investigated in the next chapter of this thesis.

Chapter 4

Optical and Tactile Breast Imaging

4.1. Introduction

This chapter explores the development of a handheld breast elasticity mapping technology based on infrared vein imaging and tactile sensors, technologies used in different aspects of breast imaging that are expected to be complementary. The rationale for using vein imaging for mosaicking tactile images into a tactile map is that demarked features are required for image based mosaicking to be effective, and blood vessels are well defined in infrared. This provides both a functional method of mosaicking tactile data to gain a full breast view, but may also give additional information such as invasiveness and relation of lesions w.r.t. blood vessels, as well as monitoring lesion location changes over time.

This chapter serves as the theory, design and initial validation for the developed technology, leading onto further development and testing in later chapters. The chapter concludes with a discussion on the significance of the results, concluding that the developed system is practical in isolation, but must be developed further to be complementary to TI in clinical imaging.

4.2. Opto-Tactile Breast Imaging Systems

Cameras and tactile sensors have only recently begun being used together in breast cancer diagnosis and screening in the academic literature. Authors in the literature (Rana et al., 2020) (Saleheen et al., 2013) (Sahu et al., 2013) have realised that tactile sensing is limited in its scope of use and have turned to fusion with optical and hyperspectral imaging to improve the capabilities of tactile imaging, without significant increase in system cost. Although each author has tackled a separate problem in tactile imaging, these being lesion localisation and lesion elasticity measurement respectively, they have each brought new ideas to the table when considering a final solution in the pursuit of an absolute elasticity map of the breast, with lesions localised and analysed, in a manner that can be tracked between check-up scans.

The advantage of a camera-based imaging system over a fully tactile sensor system is that of spatial resolution, however a camera-based system must be combined with a tactile sensor in order to provide elasticity information. A typical tactile sensor-based cancer screening system consists of a sensing area of 40mm x 50mm split into 12x16 sensor elements, or 192 pixels, whereas a camera system would have at least 500,000 pixels in a similar sensing area (for a 0.5MP camera). This vastly increased spatial resolution makes determining the size of a spherical lesion (Oleksyuk et al., 2015), and producing feature maps of the inspected tissue (Rana et al., 2020), simple. Conversely, a camera-based elasticity imaging system, has low resolution in applied load distribution which makes resolving complex shapes and lesion structures difficult.

Purely tactile imaging systems have attempted to obtain both tactile maps (Wellman et al., 1999b) (Egorov and Sarvazyan, 2008) and absolute elasticity of a lesion, but the methods were never applied together in a meaningful manner in industry. The tactile maps produced were flat planes referenced to a fixed point on the body (Wellman, 1999), specifically the line connecting the supra-sternal notch to the xiphoid, and so any change in breast orientation with respect to this line will be interpreted as a change in lesion position between scans. This was later improved by splitting the breast into quadrants with a strict scanning procedure (Sarvazyan and Egorov, 2009). This helped control deviation between scans, but still required the physician to perform the scan in a repeatable process and did not account for the population variance in breast size and shape (a generic breast map, not patient specific).

Other works presented a camera based tactile imaging system that relies on the lesion deforming a Polydimethylsiloxane (PDMS) optical waveguide in response to an applied measured load (Saleheen et al., 2013). The deformation of the waveguide scatters light as total internal reflection no longer holds which can then be detected by a monitoring camera. A change in observed image size with respect to the applied load is used to calculate the elasticity of the lesion. This method has been shown to work well in determining the elasticity and size of spherical lesions, and to their credit was shown to be robust to interobserver variability (Oleksyuk et al., 2016). The key drawback of a design like this, which is hyperspectral rather than directly optical imaging, is that the ability to resolve complex lesion shapes, lesions with multiple nodules, or separate lesion in very close proximity to each other is that the ability of the design to resolve

lesion shape is determined by the flexibility of the waveguide. A single flexible layer cannot conform to complex geometries without the application of a significant restraining force, from a solid backing for example, resulting in a blurring of nodules into a single mass, shown in Figure 4.1. This is a problem for lesion classification, but not for basic screening, and this is not a problem in purely tactile sensor-based systems, where complex shapes can be easily identified from the independent sensor elements. Additionally, the deformation image of the lesion does not contain information on the background tissue or surrounding structures, therefore it cannot be used to create tactile maps of the breast surface in its current form.

Thermography is currently the most widespread camera-based breast cancer screening method, with multiple commercial manufacturers and a global market. Thermography provides lesion location information on the breast by measuring the infra-red emissions from the breast. Higher emission, or temperature, is indicative of higher cellular activity typical of malignant breast conditions. An example of a thermogram is shown in Figure 4.2. This method does not produce elasticity information as the previously described methods do, as it lacks tactile information, and so its capability is limited to screening only and will require additional methods such as mammography and biopsy for lesion diagnosis. It is important to note how the vascular tree (veins in the breast) shows up brightly in IR thermography.

The benefits of each method: tactile, optical, and thermal; can be combined together to alleviate the downsides of each individual method. Tactile sensor arrays provide both a method of determining lesion elasticity given knowledge of the

background tissue properties and a method of resolving complex lesion relief detail. Camera systems boast increased spatial resolution which can be used to produce accurate surface maps and can be used to measure elasticity when fused with simple tactile sensors. Finally, thermography, specifically IR imaging, provides a continuous trackable structure on the breast for locating tactile maps over time, the vein network.

In this chapter, a fused IR camera and tactile sensor system is proposed and demonstrated for the purpose of providing a patient specific and time trackable map with background tissue elasticity information. An initial prototype shall consist of simple tactile sensors and an IR camera, which will output a map of the vein network and background tissue elasticity, providing a proof of concept leading onto the integration of a full tactile array to provide accurate lesion elasticity in addition to the vein mapping capability. The tactile array is not currently implemented in this system due to the significant commercial investment required to create a modified tactile array for this application. The description of the proposed system shall be split into the two main functional elements in the following sections: elasticity measurement of the background tissue, and vein mapping; each investigated separately.

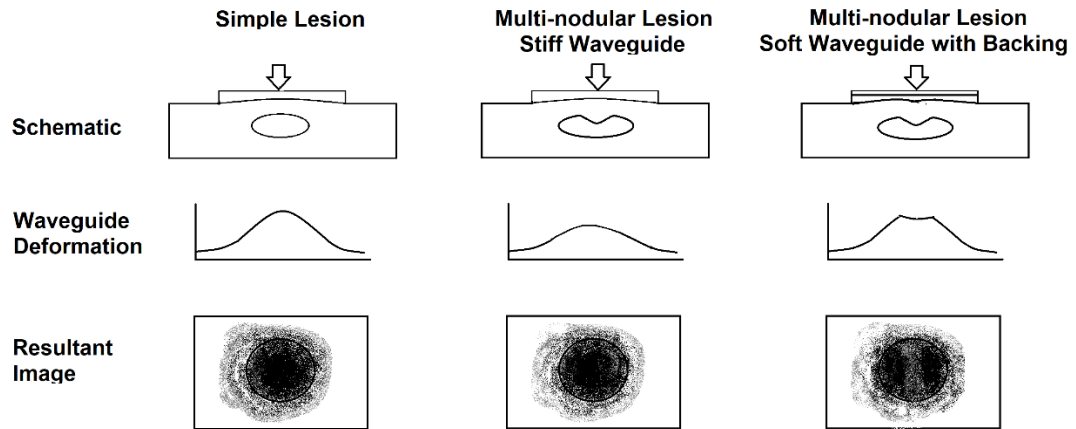


Figure 4.1 - Illustrative example of waveguide deformation not being responsive to multi-nodal lesions due to waveguide stiffness, resultant image tone is inverted for clarity. Tactile imaging does not suffer from this issue as each measurement element is independent of its neighbours.



Figure 4.2 - Example thermogram of breast tissue, showing prominent vein network and, thankfully, no visible breast condition (adapted from Pacific Chiropractic and Research Centre – Breast Thermography)

4.3. Breast Background Elasticity Measurement

The first problem to be solved is the measurement of the background elasticity of the breast. There are currently no commercial solutions available for this using cameras and tactile sensors and so a new hardware setup will be required. A simplified proof of concept design with simple geometry and large camera shall be presented initially for the purpose of validating the proposed elasticity measurement method. This leads onto developing the design into the footprint of commercially available tactile imaging systems using miniature cameras. This provides confidence in each step of the design process and makes it easier for commercial partners to implement the research.

4.3.1. Hardware Description

The proposed system consists of 4 main components: an IR illuminator to illuminate the breast tissue, an IR camera to record images, tactile sensors to measure the applied load distribution, and a domed lens cover to give a known stress distribution on the tissue.

A ring of 850nm IR LEDs sits behind a frosted clear acrylic diffuser, shown in Figure 4.3. In the centre of the LED ring is a 38mm diameter clear lens cap, flush with the IR diffuser, to maintain a simple pressure distribution on the tissue. The LEDs are supplied with 12V from a generic 1A external power supply. Behind the LED ring are 4 S8-10N SingleTact™ capacitive pressure transducers (Pressure Profile Systems Inc., US-CA) secured in place, for a total normal load rating of 40N, at a radial distance of 26mm in a square using 3M 300LSE tape (3M Company, US-MN), between the LED

ring and a rigid acrylic backing on the camera lens assembly. The camera lens is an Azure-0518M10M 2/3", 5mm, F1.8 C mount lens (Azure Photonics – US-MA). The camera used is a FLIR Blackfly BFS-U3-51S5M-C 75FPS 5MP mono camera (FLIR Systems UK, UK) arranged with the lens to focus on a distance of 80mm from the camera sensor to about 3mm in front of the 38mm acrylic lens cap, to ensure that the camera is focused inside the tissue. It is critical to the design that the acrylic lens cap be free from scratches, marks, and dust, as blemishes will be visible in the camera image.

The SingleTact™ sensors have a stated repeatability within 1%, and <2% linearity error, and are connected through their 10-bit I²C interface modules to an ATMEGA32u4 microcontroller (Microchip Technology Inc, US-AZ) running at 16MHz. An InvenSense™ MPU6050 (TDK, JP) accelerometer and gyroscope module is also connected to the microcontroller via I²C, which is used to determine the orientation of the camera and assist in the calibration process. The microcontroller receives data from the SingleTact™ sensors and the MPU6050 at 100Hz, and outputs the data as a serial stream to a PC over USB. 5V is supplied to the electronics via USB, the camera is interfaced using a separate USB connection. The prototype is shown in Figure 4.4 and Figure 4.5. Image capture and load/orientation data capture is performed on the PC by a MATLAB 2017 program. The proposed algorithms are similarly implemented in MATLAB, in post processing for this prototype. Orthogonal lines passing through the centres of opposing SingleTact™ sensors and the scanner centre define a moving right-handed coordinate frame with the scanner centre as the origin, both the MPU6050 and the camera are aligned with these new axes.

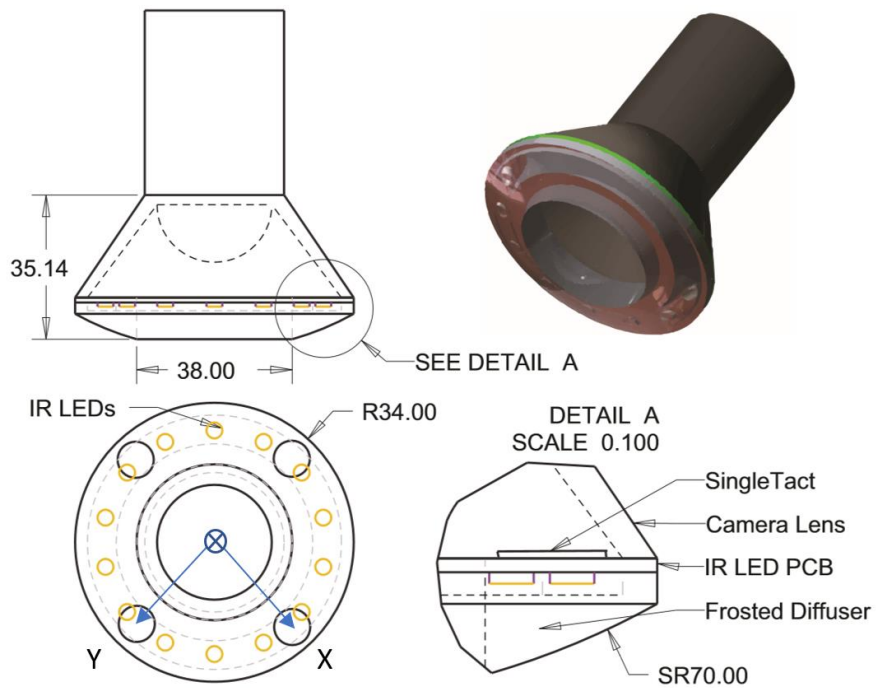


Figure 4.3 - Breast scanner simple prototype design highlighting key points in the mechanical design of the scanner.



Figure 4.4 - Prototype scanner assembly showing electronics interfacing with the mechanical system.

There is an IR opaque layer between the clear view window and the frosted diffuser to stop internal reflection of the LEDs into the lens. The lens is polished and demarked using flame polishing and finished with acrylic polish. Frosting of the diffuser is achieved by roughing the diffuser surface with coarse sandpaper on both sides. The system is held by the camera body; the electronics are sufficiently shielded and coated with lacquer such that this is not of concern in terms of interference.

The MPU6050 is interfaced with the microcontroller via the I²C bus as previously described, however an additional data line is used to allow the MPU6050 to interrupt the processor for data transfer. This interrupt is used to synchronise the data from the MPU6050 with that from the SingleTacts.

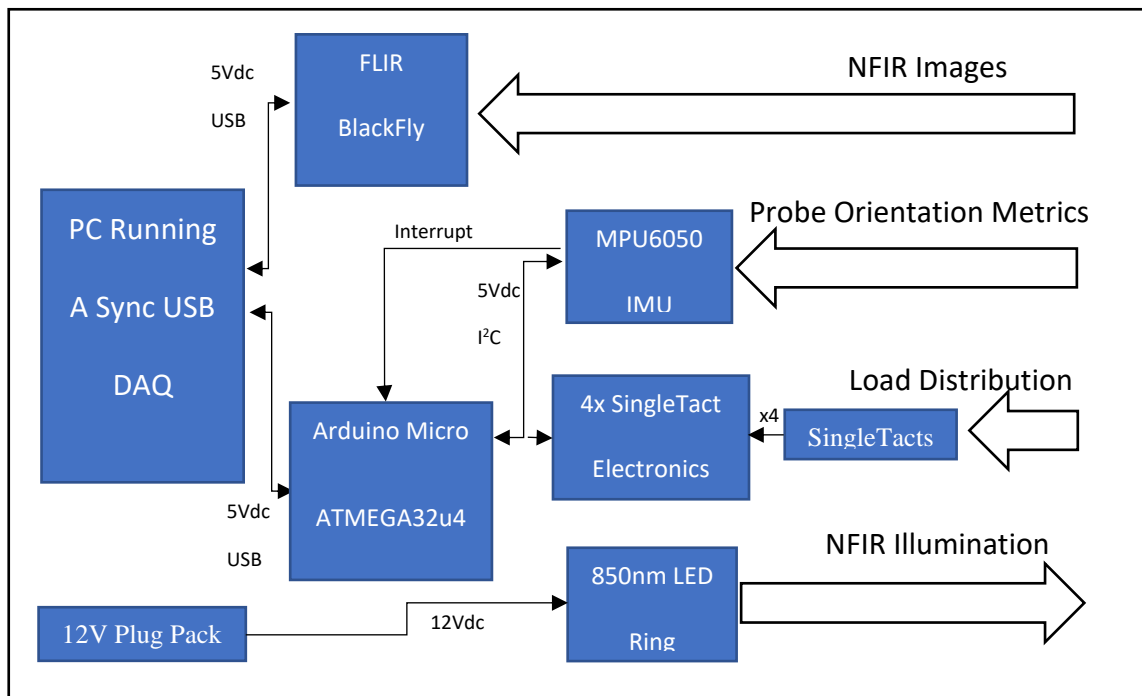


Figure 4.5 - System Block Diagram of proposed system. Each SingleTact sensor is interfaced with a unique electronics module with individually configured I²C addresses. In this system, 4K7 resistors are used on the I²C bus.

4.3.2. Theory of Operation

Previous works have presented innovative ideas when it comes to using the deformation of a waveguide under load to indirectly image and quantify an embedded lesion in terms of shape and elasticity (Saleheen et al., 2013) (Sahu et al., 2014) (Oleksyuk et al., 2015). By observing the change in the apparent size of a lesion, specifically the size of the deformation of the waveguide, with respect to load the stress/strain curve of the lesion can be estimated. This approach is limited by sensitivity to background tissue elasticity, a sensitivity the authors had not investigated, which can skew both the elasticity measurement and the size estimation similar to conventional tactile imaging. The technique is also sensitive to the malleability of the waveguide, which can affect size, elasticity, and shape estimation as illustrated in Figure 4.1.

The idea of observing an apparent change in size (strain) with respect to an applied load (stress) can be applied to the estimation of the background breast elasticity. Instead of indirectly observing the deformation of the embedded tissue through a deforming waveguide, the surrounding tissue can be observed directly by a camera deforming under load. By observing the deformation of the tissue directly, in response to an applied load, the elasticity of the surface tissues can be estimated whilst providing a clear view of the tissue are under inspection for future mapping of tactile images. By imaging the breast in the near field infra-red (NFIR) spectrum, the vascular network within the breast tissue can be observed as shown in Figure 4.2 and used as the basis of a tactile map (Zharov et al., 2004) (Nioka and Chance, 2005).

4.3.2.1. Observing Tissue Deformation in Variable Load Images

Consider a soft inflated rubber balloon. When the balloon is pressed, the surface of the balloon stretches in response to being pressed. Specifically, the balloon is deforming against the applied stress. In the same way someone may watch a balloon stretch when pressed, the deformation of any soft elastic material can be observed in response to stress and recorded using a camera. By quantifying the deformation in response to an applied load, the elastic properties of the material can be determined.

A finger pressing a soft balloon, though anecdotally relevant, is difficult to picture accurately due to the interesting geometry of the human finger and the inability to see through the finger. A simpler example can be applied, where a transparent cylinder is pressed straight into the elastic surface. Viewing through the transparent cylinder, one would observe the uniform stretching of the surface from the centre of the cylinder varying with the amount the cylinder is pressed into the surface. The proposed scanner mimics the transparent cylinder and will produce a response as shown in Figure 4.6, where an increasing stress on the elastic material causes increased deformation of the surface that would be interpreted by a camera observer as a stretch perpendicular to the applied load.

The stretching of the material surface, from the camera viewpoint, can be thought of as zooming in on the surface, where a small original area of material now fills a larger proportion of the image as shown in Figure 4.6. In this situation the material features being observed near the periphery of the images would disappear from view as the load increases.

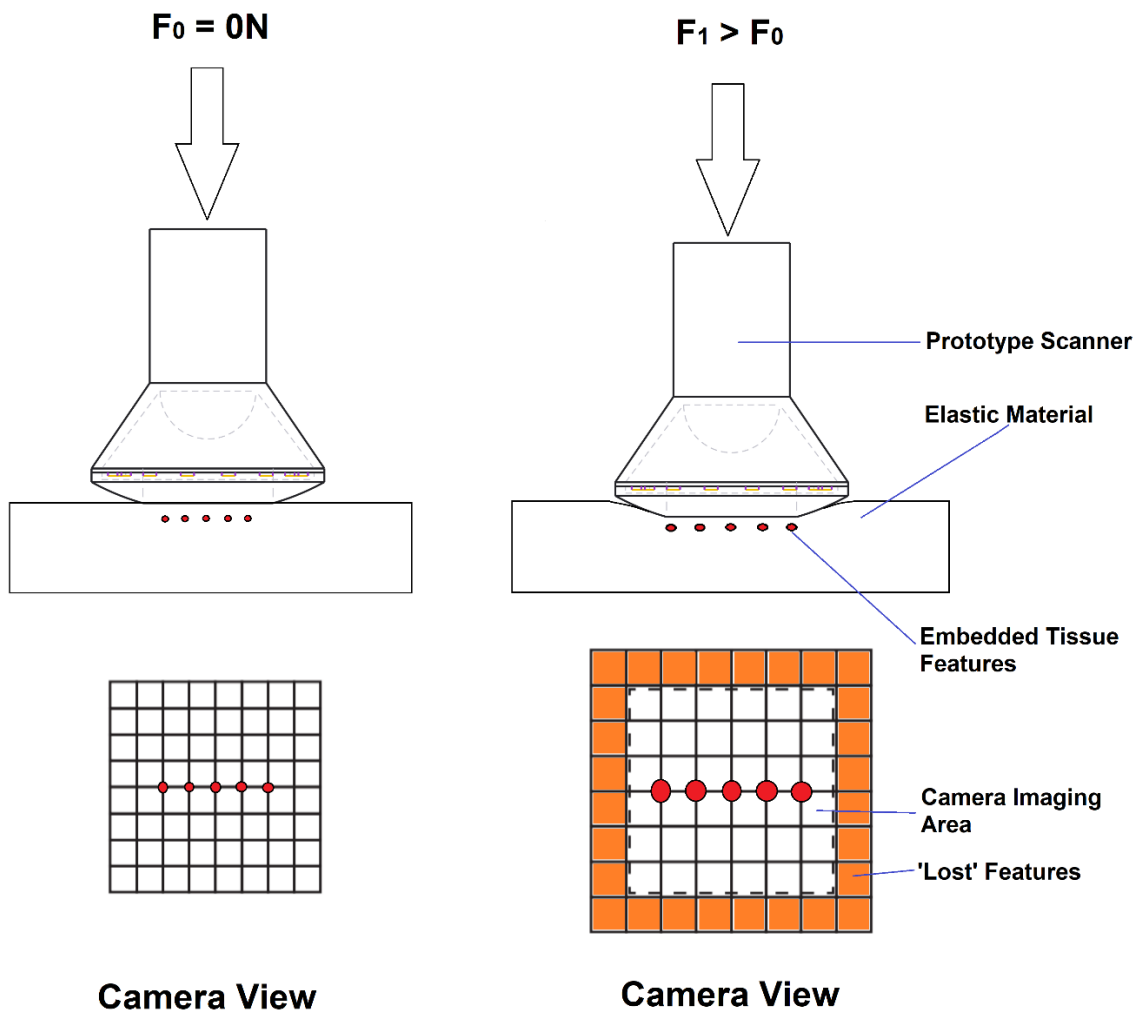


Figure 4.6 – Effect of increased normal load on image view plane. The increase in load increases the deformation of the homogeneous material equally in all directions, causing embedded (uncoupled) features to separate equally in response. This separation, which is a simple stretch in the camera view, can be considered an image scaling effect.

A similar description can be given to the more complex situation, where the applied load is not normal to the material surface. In this situation the applied load is not uniform across the scanner surface, and so it is reasonable to say that the deformation will not be uniform either. The outcome of the normally loaded case, that the stretching and deformation increases with load, and that load usually increases with compression depth into the material, can be applied to this situation to describe what is happening beneath the scanner surface.

As the scanner tilts into the material about the centre of the scanner face, for a constant average applied load, one side of the scanner will press deeper into the material and increase the local load in that area, and the opposing side will retreat and reduce the local load in that area as shown in Figure 4.7. With the load changing across the scanner face, and knowledge that the deformation of the material increases with load, it is clear that the deformation will be changing across the scanner face. The deformation will be greatest at the point of maximum load on the scanner face, and least at the point of minimum load. The load distribution and material deformation across the scanner face is a function of the average applied load, the tilt angle, and the geometry of the scanner face. The material deformation will appear in the camera view, as shown in Figure 4.7, as an increase in zoom on one side of the image, and a reduction in zoom on the opposing side. The effect of shear load and torsional loads on the material will not be considered in this project due to the necessary hardware. The effect of shear can be reduced using low friction lubricant gel and the effect of torsion can be minimised with proper experimental procedure.

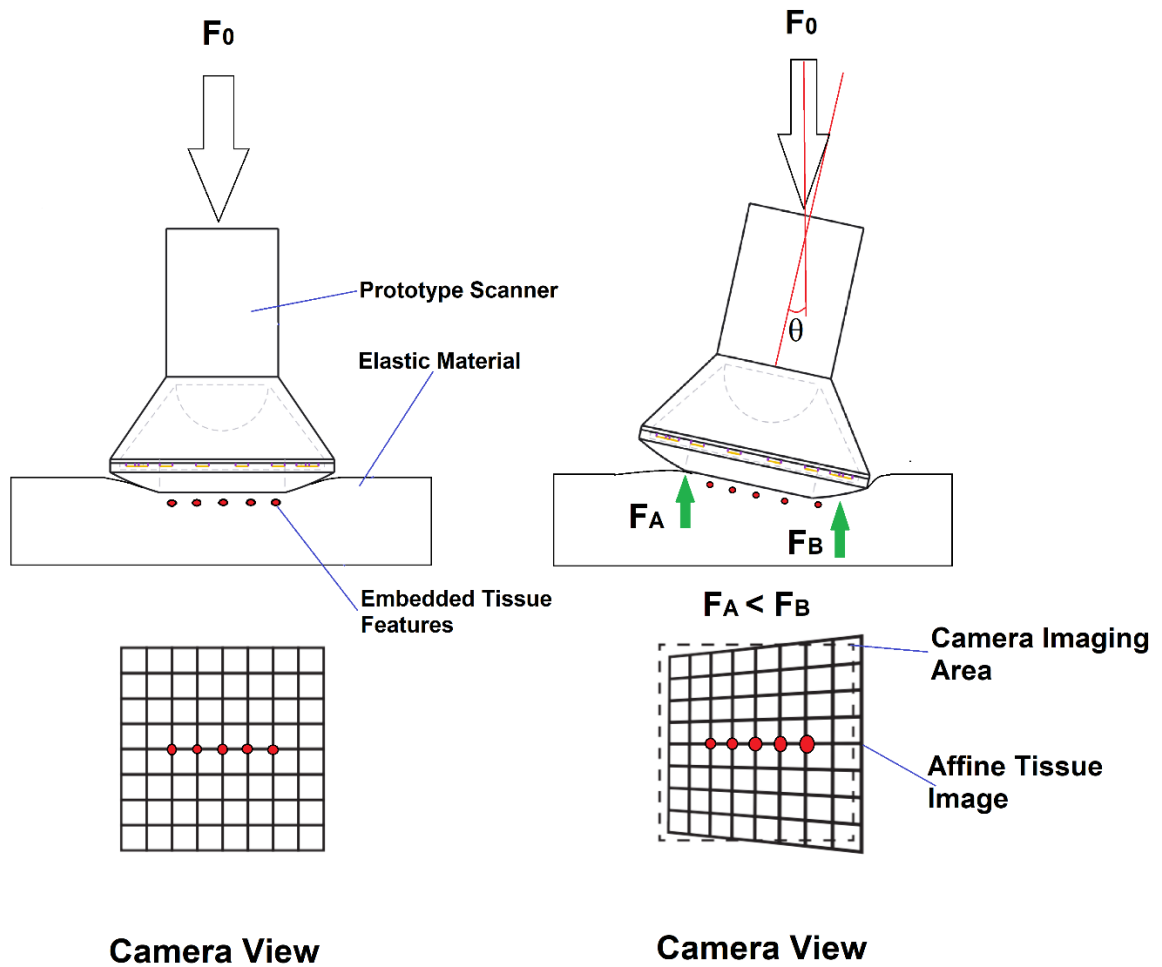


Figure 4.7 – Effect of increasing affine tilt on image view plane. The increase in tilt angle θ , for a fixed average load F_0 , creates a difference between F_A and F_B (the material reaction forces on opposing sides of the scanner) due to the changes in scanner depth along its view surface. This causes the embedded tissue features to separate unequally. This creates a stretching effect that varies across the image plane and can be considered a non-linear image scaling effect.

4.3.2.2. Recording Tissue Deformation in Variable Load Images

Variations in the apparent location of a particular feature in the material, or breast, between images can be tracked using an image feature tracking algorithm such as the scale invariant feature transform (SIFT) algorithm (Lowe, 2004). It is true that there are many other feature identification algorithms out there, such as: MSER, Hessian, A-SIFT, and SURF; which will likely change system performance (Morel and Yu, 2009), however in this application SIFT is appropriate. This project is not about the intricacies of each feature transform method, or detailed comparison of each method as performed by others in the literature (El-gayar et al., 2013) (Karami et al., 2017) (Nuari et al., 2019), it utilises a suitable feature tracking algorithm as a tool for a ‘higher’ purpose. In the simplified case of a normal compression into the tissue, with no camera tilt, the observed deformation is simply a scaling between images with differing loads as shown in Figure 4.6, and so the scale invariance of SIFT is utilised to track this (J.M. Morel, 2011), without the additional unnecessary complexity and functionality available from other algorithms. It is also easy to find well documented open source implementations of SIFT feature tracking in several computing languages, likely improving its suitability in many applications particularly due to its long history in the literature (Brown and Lowe, 2007).

SIFT detects image features, or key points, in an image by finding local maxima/minima of Difference of Gaussians (DoG) functions that are robust across multiple Gaussian blurring scales (Lowe, 2004) (Nuari et al., 2019). This involves blurring the test image with different scales of Gaussian blurring, and then finding significant points in the scale space by taking the difference of the blurred images. Key

points produce strong local maxima and minima in this method but can also be the result of noise and imaging artefacts such as image edges. False or insignificant features, features that are not robust to small changes in noise, are discarded by interpolating the scale space of the DoG functions to firstly determine an accurate position for the feature and secondly to determine the local significance of the feature using the ratio of principal curvatures. This process eliminates edge responses and low contrast features that are not considered robust, as these features will be poorly defined or have severely uneven principal curvatures.

Detected features are then assigned an orientation based on the local image gradient, which allows for invariance to image rotation. The feature locations at various scales and the feature orientation together provide invariance to image location, scale, and rotation. The feature parameters are then concatenated into a key point descriptor, robust to minor affine changes, using histograms of orientation and gradient magnitudes in the surrounding area of a feature. SIFT features are well known to be robust feature descriptors, usually outperforming other methods for low affine distortion where speed is not critical (El-gayar et al., 2013) (Karami et al., 2017).

As mentioned, there are many other feature extraction algorithms that are either: similar to SIFT but run faster such as SURF, RIFT, BRIEF, and ORB (Karami et al., 2017); or outperform SIFT in certain conditions where affine distortion is high such as A-SIFT or A-KAZE (Yu and Morel, 2011) (Alcantarilla et al., 2013). SIFT shall be used for this project due to its ease of implementation and its understandable documentation in the literature and public spheres.

To determine deformation, or the motion of feature positions between frames, the difference in location must be determined for a particular pair of features common in each image. This requires that common feature pairs be found between the images, which is done by matching the feature descriptors of features in each image for agreement within a certain tolerance. Lowe used a probabilistic nearest neighbour search algorithm, which computed the Euclidean distance between a given descriptor vector and a key point (Lowe, 2004). The probability of a correct match was estimated using the distance ratio between the nearest neighbour and the second nearest neighbour. Values with ratios greater than 0.8 were rejected as improbable matches resulting in a 90% rejection of false matches with less than 5% rejection of true matches. From these matched features, changes in position or rotation between images can be determined.

The basic process in this application begins by applying a binary mask to the raw images from the camera system, to eliminate the view of the inside of the scanner and focus only on relevant vein structures as shown in Figure 4.8. The SIFT algorithm described above is then applied to each image sequentially to generate a list of robust feature descriptions in each image. The features are then matched to find connected feature pairs between the images as shown in Figure 4.9. Deformation, or changes, between the images can be determined either: using a homography matrix, which is an estimation of how the camera has moved, computed using Random Sample Consensus (RANSAC) which compares groups of matched features for a common transform; or by simple linear algebra when the deformation regime/type is known, as it is in this application. This shall be further explored in following sections.

Image 1 at $F = F_0$
Raw Image

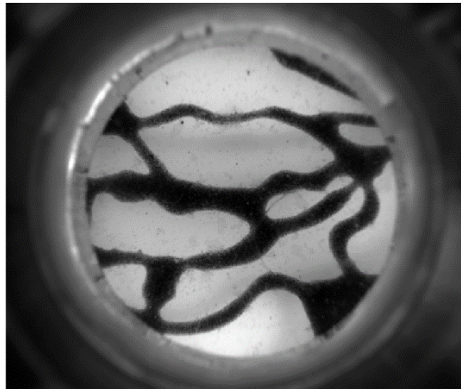


Image 1 at $F = F_0$
Mask Applied

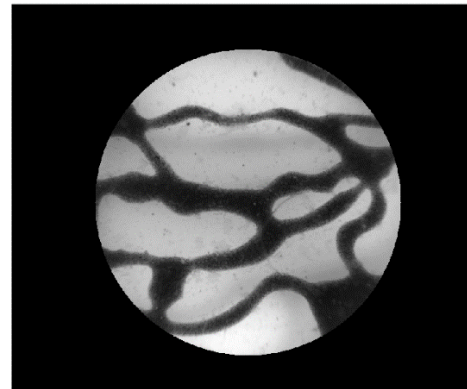


Figure 4.8 – Application of a binary mask to raw images of phantom tissue. The camera view area in the proposed scanner does not match the area of the scanner window and so a binary mask is applied to remove the view of the inside of the scanner assembly. This leaves only the image features of interest, specifically the observed tissue.

Image 1 at $F = F_0$

SIFT Feature Matches

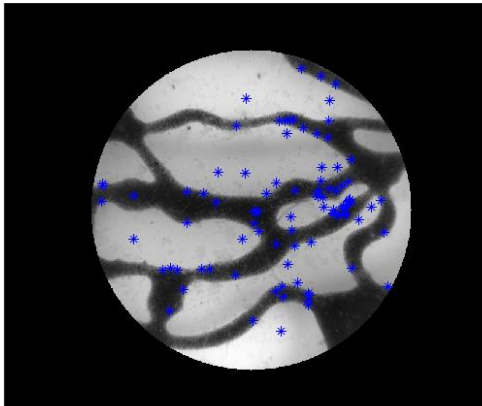


Image 2 at $F \gg F_0$

SIFT Feature Matches

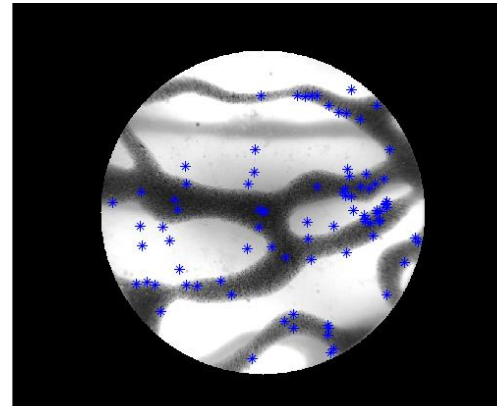


Figure 4.9 – SIFT point matching between normal load variant images. The SIFT points, specifically groups of points indicating key parts of the tissue geometry, spread out in response to the applied load. The location of each feature is recorded for each image and so the variation in feature position between images can be tracked with respect to applied load. As this is a normal loading case, with zero tilt, the features spread equally radially from the mask aperture centre as described in Figure 4.6.

4.3.2.3. Determine Applied Load and Tilt Angle

The total load applied by the scanner to the tissue surface is measured directly by summing the individual loads of each of the 4 SingleTact™ pressure transducers on the proposed scanner. The SingleTact™ sensors present the only points of contact between the scanner face and the main body of the scanner, therefore 100% of the applied load must be transferred through them. This means that the total applied load F_{Total} can be calculated using Equation 4.1, where F_1 and F_2 represent the forces on opposing sides of the y axis; and F_3 and F_4 represent the same on the x axis of the scanner.

$$F_{Total} = F_1 + F_2 + F_3 + F_4 \quad (4.1)$$

This is more generally defined as the surface integral of point forces across the scanner face surface, as defined in Equation 4.2, but as the individual surface stresses are unknown initially and there are 4 known ‘point’ loads coming from the SingleTact™ sensors, Equation 4.1 can be applied instead.

$$F_{Total} = \int_1^{Nx} \int_1^{Ny} F_{[x,y]} dy dx \quad (4.2)$$

As the surface integral is a continuous function which can approach an integration of infinite points, it is more useful to think of it as the summation of ($N_x \times N_y$) discrete point loads that act in the centres of their respective areas. This is a form of finite element problem solving and will make estimation of the applied stress field more intuitive later. An illustrative diagram of the finite load nodes is shown in Figure 4.10.

The total load on the scanner can be transferred to average applied stress, σ , simply by dividing by the scanner face area, A . This can be generalised to say that the stress at any node location, $[x,y]$, is the load at that node divided by the node sample area, as shown in Equation 4.3.

$$\sigma_{[x,y]} = \frac{F_{[x,y]}}{A} \quad (4.3)$$

The SingleTact™ sensors will each read a fractional average value of the total measured force, which will all be equal if the scanner is pressed normally into a homogeneous material. It is this principle that can be used to estimate the applied load at any discrete node location on the scan face.

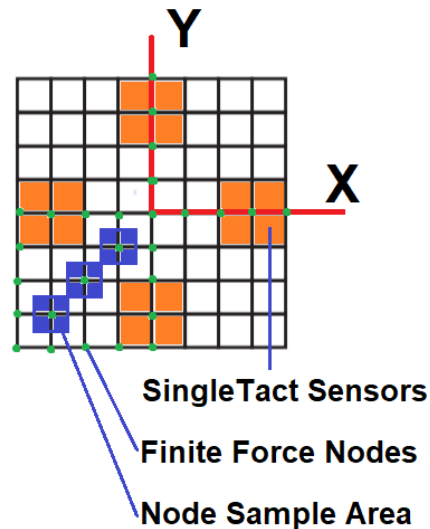


Figure 4.10 -Illustrative example of finite load discretisation. The scan surface is divided into an equidistant grid, the nodes are positions of point loads assumed to be the total load of their respective surrounding area. The 4 SingleTact™ sensors, as they are on a separate layer, can approximate point loads centred at the sensor location. This illustration is not to scale.

The average load measured by the SingleTact™ sensors, for a normally loaded case, is given by Equation 4.4. This can be expanded into a general form that applies to the surface of the scanner by realising that the division of the total load is by the number of force nodes used in the scanner. For the simple case with the SingleTact™ sensors, this value is 4 as the sensor can be considered a node with a separation of 52mm. When discretised into N nodes, the node separation becomes 52/N. For the general normally loaded case, the load at any node location will be the average of all the nodes and can similarly be calculated from Equation 4.4.

$$F_{Average} = \frac{F_{Total}}{4} = \frac{F_{Total}}{N_{Elements}} = \frac{F_{Total}}{N_x N_y} \quad (4.4)$$

This average value applies at all nodes, when the scanner is normally loaded, such that the summation of all nodes still equals the total applied force. When the scanner is tilted into the tissue, this average load will only apply in the centre of the scanner, with the loads at other locations deviating from this value by a function of the change in compression depth across the scanner face. The variation in compression depth across the scanner face is a function of the face geometry and the tilt angle that can be determined by rotating the plane that defines the scanner face by the respective tilt angles about the x and y axes.

The plane of the scanner face can be described using its normal vector, u , defined in Equation 4.5 as it is flat and can then be rotated about the x and y axes of the scanner by angles θ and φ respectively using rotation matrices to yield the new orientation of the

scanner face. This is also described using its normal vector, u' , which is calculated in Equation 4.6. The difference in z coordinates between planes defined by u and u' gives the relative change in compression depth, dz , with respect to the centre of the scanner face for face coordinates x and y . The relative change in compression depth is calculated in Equation 4.7.

$$u = [0 \ 0 \ 1]^T \quad (4.5)$$

$$u' = \begin{bmatrix} 1 & 0 & 0 \\ 0 & \cos \theta & -\sin \theta \\ 0 & \sin \theta & \cos \theta \end{bmatrix} \begin{bmatrix} \cos \varphi & 0 & \sin \varphi \\ 0 & 1 & 0 \\ -\sin \varphi & 0 & \cos \varphi \end{bmatrix} [u] \quad (4.6)$$

$$dz_{[x,y]} = \frac{-1}{u'_3} (u'_1 x + u'_2 y + 0) \quad (4.7)$$

The relative change in compression depth at a location on the scanner face can then be combined with Hooke's law to estimate the new applied load at a point on the scanner surface. Hooke's law defines change in reaction force in response to an applied deformation, or vice versa, as a constant, k , for an elastic material. The application of Hooke's law is shown in Equation 4.8, which allows the point load at any node on the scanner face to be calculated for a given tilt angle. The value of k is scaled by a factor of $N_x N_y$ to account for the area change between the full scanner surface and the node area.

$$F_{[x,y]} = \frac{F_{Total} - kdz_{[x,y]}}{N_x N_y} \quad (4.8)$$

The tilt angles, θ and φ , can be determined easily from the integrated orientation sensor if the initial orientation of the tissue is known, however it is more likely that it will be unknown and will often be changing as the probe moves around a 3D surface. In this case the tilt angles can be calculated with respect to the surface using another application of Hooke's law. By combining the deformation illustration in Figure 4.7 with Equation 4.8, the SingleTact™ readings on a single axis can be used to determine the tilt angle of that axis. For a single axis, with 2 nodes, the expression for $F_{Average}$ becomes Equation 4.9. As there are only 2 nodes, with a known location at distance $\pm S$, the deviation in compression depth can be calculated using trigonometry and translated into a force at each node using Hooke's law as shown in Equation 4.10 and Equation 4.11. By solving these equations simultaneously for θ , an expression for tilt angle can be obtained in terms of the 2 SingleTact™ measurements on each axis as shown in Equation 4.12. A similar process yields an expression for φ as shown in Equation 4.13.

$$F_{Average} = \frac{F_1 + F_2}{2} \quad (4.9)$$

$$F_1 = F_{Average} - kS_y \sin \theta \quad (4.10)$$

$$F_2 = F_{Average} + kS_y \sin \theta \quad (4.11)$$

$$\theta = \sin^{-1} \left(\frac{F_2 - F_1}{2kS_y} \right) \quad (4.12)$$

$$\varphi = \sin^{-1} \left(\frac{F_4 - F_3}{2kS_x} \right) \quad (4.13)$$

4.3.2.4. Estimating Elasticity from Variable Load Images

In the case of normal loading, where $F_{1:4}$ are approximately equal, the value of k can be ignored as it is not required to make a simple elasticity measurement. The estimation and calibration of the constant, k , for an elastic material shall be described in Section 4.3. Recording the change in image feature positions between images with low x and y translation over varying loads is a measure of the material lateral strain in response to a longitudinal compression. Combining this strain with the applied stress yields the Young's modulus, E , or elasticity of the material under test. For elastic materials E is a constant, but it need not be in real tissues as the method is a characterisation of the stress/strain curve of the material.

As the scanner face is flat, and the load is evenly distributed across the scanner face, the lateral strain will be equal in every direction. As such it is convenient to use the change in radial distance from the scanner centre as the measure of lateral strain. This gives a scalar value that is more intuitive to deal with. The radial distance of a feature from the scanner centre is simply the Euclidean distance of the feature from the centre. The change in radial distance, dR , between images with varying load can be estimated from Equation 4.14 where R and R' are the feature distances in the lower loaded and higher loaded images respectively. The change in radial distance is a linear function of the lower loaded image feature distance, meaning that Equation 4.15 is a constant, α , for a fixed change in applied load, which is identical to the lateral strain.

For multiple concentric images taken at varying loads, the value of the lateral strain, $\varepsilon_{Lateral}$, can be measured with respect to the applied load. The gradient of this relationship is a constant for an elastic material and can be used to determine the elasticity of the material using the Poisson ratio, ν , of the elastic material (assumed to be 0.5 for an elastic material) to estimate the longitudinal strain, $\varepsilon_{Longitudinal}$, and Equation 4.16 which relates applied stress, σ , with resultant strain using the elasticity of the material. This results in an expression for the elasticity of the material in terms of the change in applied load and resultant observed change in image feature radial distance, shown in Equation 4.17. The elasticity value calculated is the mean elasticity of the material under the scanner, the background elasticity for tissue without a lesion. In cases with an embedded lesion, the mean is a good facsimile of the background providing the lesion is small with respect to the scanner area (Egorov and Sarvazyan, 2008).

$$dR_i = R'_i - R_i \quad (4.14)$$

$$\frac{dR_i}{R_i} = \alpha = \varepsilon_{Lateral} = -\nu \varepsilon_{Longitudinal} \quad (4.15)$$

$$E = \frac{\sigma_{Longitudinal}}{\varepsilon_{Longitudinal}} \quad (4.16)$$

$$E = -\nu \frac{dF_{Total}}{A_{Scanner} \left(\frac{dR_i}{R_i} \right)} \quad (4.17)$$

4.3.3. Practical Validation

4.3.3.1. Test Material and Method

The use of SIFT feature tracking in estimating lateral strain, and the use of Equation 4.17 in integrating load measurements and lateral strain into an elasticity estimate, is validated by using the proposed system on an elastic test material and comparing the output with a known reference measurement of the material.

The test material used in this validation is made from multiple layers of Ecoflex™, 000-35 and 00-10 rated Polydimethylsiloxane (PDMS) two part elastomer (Smooth-on, Inc., US-PA), as shown in Figure 4.11, with an A:B mixture ratio and additive thinning agents, Silicone Thinner™ (Smooth-on, Inc., US-PA) for each material layer given in Table 4.1. The silicone elastomer samples were cast sequentially into uniform rectangular slabs with dimensions given in Table 4.1. The total dimensions of the sample material are 130mm x 130mm x 20mm. The material has a hand-cut phantom vein structure, made from silicone mixed with K30050 microfine graphite powder (Kasp Security Ltd. UK), to provide representative features for the SIFT algorithm to track in the IR spectrum. This is constructed from a cast flat sheet of doped silicone, manually cut to a representative pattern based on generic images of breast vein patterns, modified to be a single piece for manufacturing reasons. Assessments of the optical properties of the materials have been made for PDMS (Laura Di Sieno et al., 2019) (Vaicekauskaite et al., 2020), and carbon dust (Papoular and Papoular, 2014), where the current phantom will be the superposition of the two although it is out of scope to characterise this.

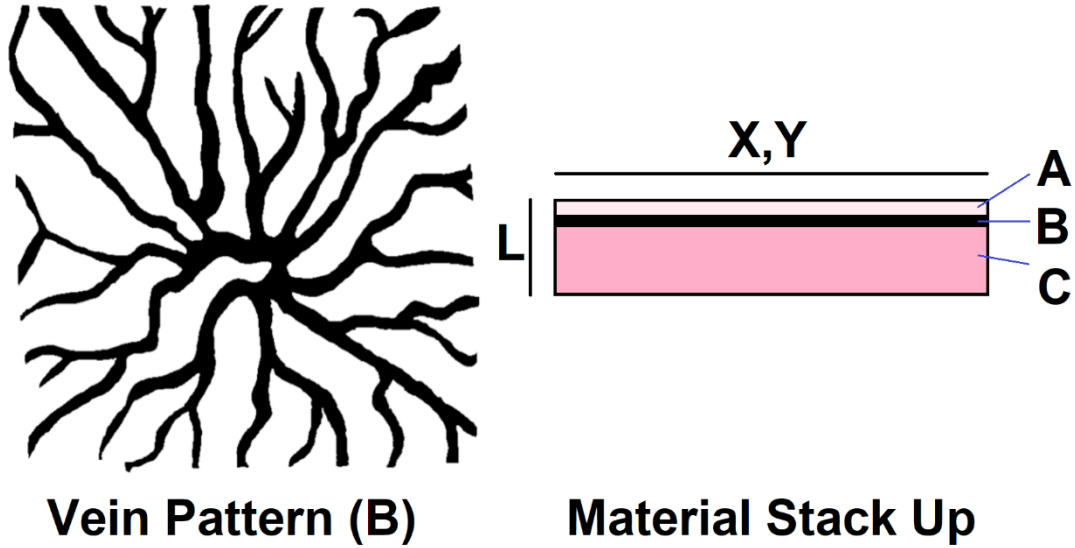


Figure 4.11 - Validation material construction diagram. The vein pattern is a flat structure in layer B. The values of dimensions X, Y, and L are: 130mm, 130mm, and 20mm respectively.

Table 4.1 – Material compositions for the validation sample. The vein layer (B) comprises of two separate materials. B₁ is the vein pattern itself, with the voids filled in with the skin material (A), designated as B₂.

MATERIAL COMPOSITIONS FOR CAMERA ELASTICITY VALIDATION TRIAL				
Sample Layer	Material A:B Ratio	Thinner By Mass	Additives By Mass	Thickness (mm)
A	000-35 1:1	+0%	None	4
B₁	00-10 1:3	+20%	Carbon Dust 1:100	2
B₂	00-10 1:3	+0%	None	2
C	00-10 1:1	+10%	None	14

There is little literature on the properties of PDMS and carbon mixtures, but the carbon in this case is there to provide easily demarked features for initial testing of the system prior to more representative testing with detailed optical properties. In future examples and phantoms, as shown later in this thesis, the mixture of SilcPig PMS488C skin pigment (Smooth-on, Inc., US-PA) provides a more representative phantom for detailed testing of system performance. The method is supported in the recent literature on optical PDMS phantoms for other applications (Regal et al., 2020) as being appropriate for use at 850nm. There is a lack of literature on the effect of these additives on the elasticity and mechanical properties of PDMS mixtures, however low concentrations of dry powder is expected to harden PDMS, and high concentrations will weaken the structure due to cross linker inhibition. The same is true for the liquid pigment except for it always weakens the structure (lowering the elasticity), where the manufacturer recommends concentrations below 3% to maintain mechanical properties. As the assembled structure elasticity is the value of interest, rather than the value of the individual layers, this is of little consequence to the validation of the system.

Validation of the calculated elasticity for the material sample as a whole is performed by comparing the response from the proposed system with the response from an Instron® 3342 universal testing machine (Instron Engineering Corp., UK) with a 2519-102 (50N) loadcell. The Instron® 3342 has a stated accuracy of 0.5% and compresses the sample using the same sensor cap indenter as the handheld camera-based system at a compression rate of 5mm/s. The Instron® reference makes its measurements at the centre of the sample material.

4.3.3.2. Validation Results

The proposed scanner is pressed normally into the centre of the test material by hand, in the same location as the Instron® reference measurement. The maximum load does not exceed 20N, 50% of the total combined rating of the SingleTact™ sensor array. Water based ultrasonic coupling gel is used to reduce the surface friction on the scanner face, to allow the surface to deform properly (this is standard practice in most forms of breast scanning including ultrasound and tactile imaging). The reference value of elasticity from the Instron® is $7.03\text{kPa} \pm 0.22\text{kPa}$, from 4 repeated measurements.

In this trial an initial image of the sample material is taken with the scanner resting on the material surface, where the applied load is the weight of the scanner itself, $F_0 = 5.27\text{N}$. Figure 4.12 shows a typical measurement of the differential lateral strain between two images of the sample material, the first taken at $F_0 = 5.27\text{N}$ and the second taken at $F = 14.1\text{N}$. This gives a differential load, dF_{Total} , of 8.83N . The graph shows the change in location of a feature position between the two images with respect to the measured location on the second image and validates the assertion of Equation 4.15 that a constant value can be determined for the apparent stretching of the material between the two images. The best fit line of dR/R with 159 feature points gives a lateral strain value of 0.133.

This by itself is sufficient to obtain an elasticity measurement, as we have an applied differential load and a measured resultant strain. Assuming the material Poisson's ratio is 0.5, and the contact surface area is 0.0048m^2 , the value of E can be determined as 6.89kPa which is within the Instron® reference window.

By utilising the high frame rate of the camera, many measurements can be made in a short period of time. Calculating the SIFT feature location changes over many images (>100) with respect to the applied load, yields a more stable estimate can be determined as shown in Figure 4.13. The value of elasticity from this method, 7.15kPa, shows that the initial approach using 2 images yielded an appropriate result, however this was subject to the 2nd image being taken in the ‘linear contact’ region of the stress strain curve. At low loads, the measurement of strain is dominated by movement of the scanner laterally as there is not enough load for friction to hold it in place. Beyond a differential stress of $\sim 1250\text{N/m}^2$ (6N), there is sufficient friction to inhibit lateral translation of the scanner and so the material can be measured correctly.

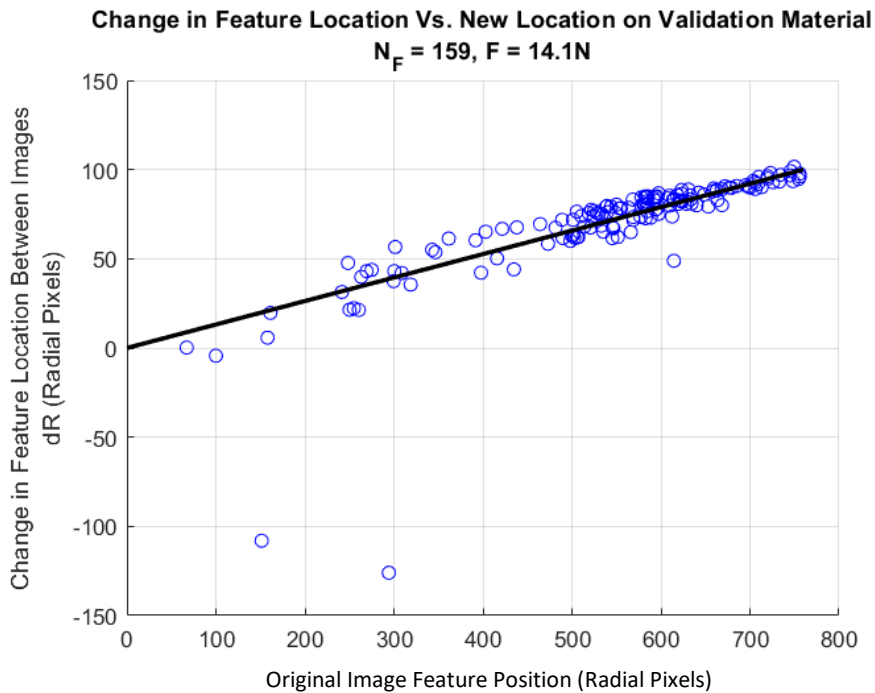


Figure 4.12 – dR shown as a linear function of R . For a constant force, the change in a features radial location between 2 images is a linear function of the measured location of the feature on image 2. This allows a single constant, α , to be determined for the pair which is equivalent to the lateral strain at the applied load.

The applied load, and resultant measured lateral strain from SIFT feature tracking can produce a solution for the material elasticity when taking the mean response over the linear contact region as shown in Figure 4.13. This region is limited on the upper end by viscous creepage of the test material as the load approaches a maximum and is held relatively constant. By selecting any single image from the linear contact region and comparing that with the image at F_0 , the worst-case error is 28% from the mean response. Normally, the estimate from a single image will be the mean response over multiple images with a standard deviation of 5.23%, or 0.37kPa.

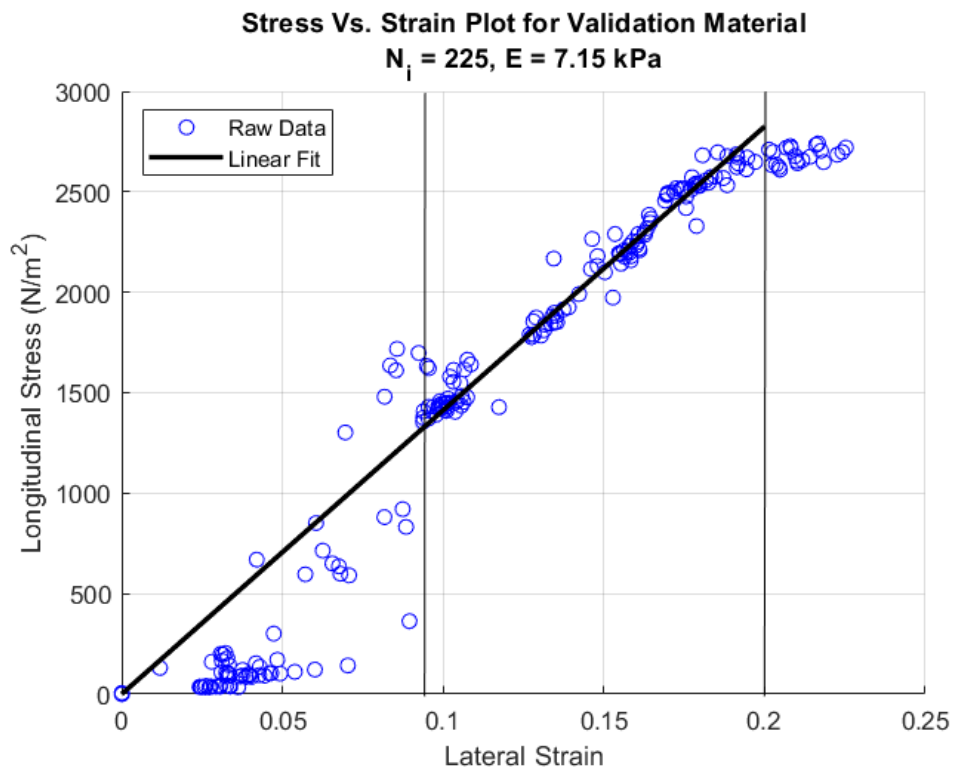


Figure 4.13 – Stress Vs. Strain plot for the validation material as estimated by the proposed system. Each lateral strain value is the best fit gradient of each of 225 images compared with an initial image at F_0 as described in Figure 4.12. These strain values are plotted with the applied differential stress when the second image is taken to produce the stress/strain plot.

The elasticity estimates obtained from each image in the linear region of the material are shown in Figure 4.14. The statistics for all of the camera-based measurements are compared with the Instron® statistics in the right figure frame. This shows that the camera-based system is effective in producing an elasticity estimate when using Equation 4.17 in the linear range of an elastic material, with a mean error of 1.7% when compared with the Instron® reference measurement. The individual measurements made with two images are relatively good, but outliers exist, and so multiple images should be used for an accurate estimate of the material elasticity.

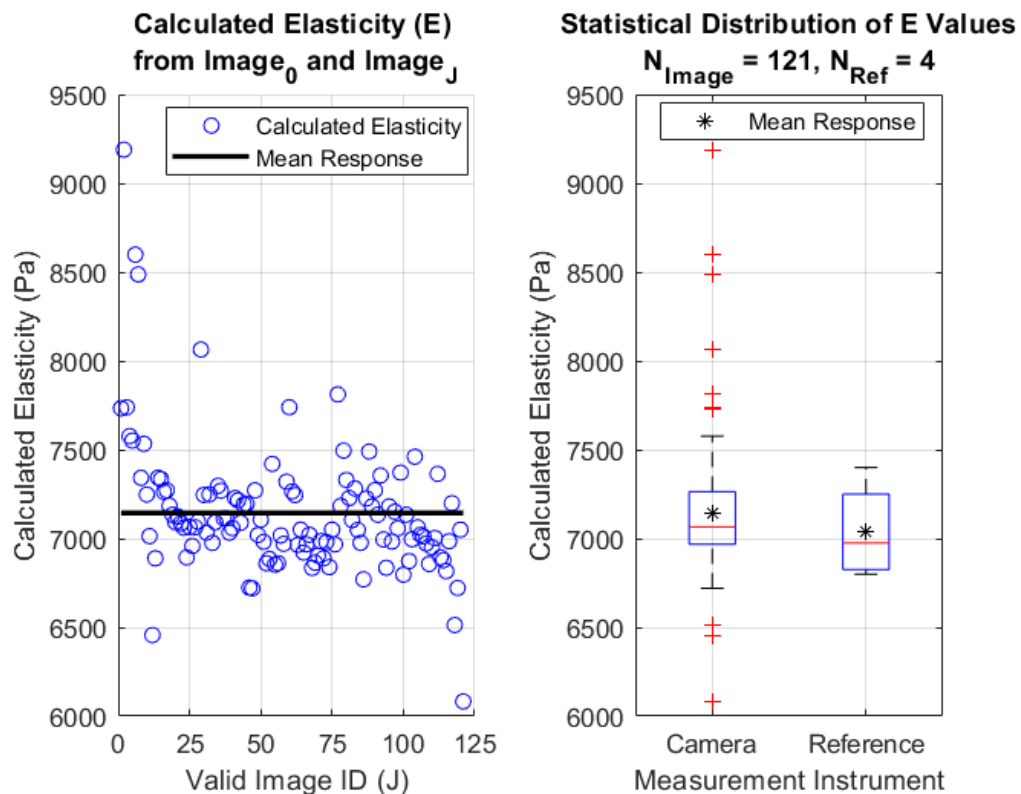


Figure 4.14 – Single compression elasticity measurement statistics. Left) Elasticity estimates using the J^{th} image in the linear region of the material compared with an initial image at F_0 . Right) Statistical distribution of the 121 solutions from a single compression cycle of the proposed camera system compared with a reference measurement taken over 4 separate cycles to estimate confidence.

4.3.4. Discussion

The elasticity results from the camera-based system, for the sample material with a complex, deformable, and observable embedded structure; are compelling when compared with the Instron® reference measurements. This means the use of SIFT in tracking features with respect to applied load can be validated in that it produces appropriate solutions when used in the proposed system.

As the algorithm is able to produce a realistic solution, with mean error and standard deviation within the reference measurement variability, it is safe to say that the application of SIFT in measuring material lateral strain is valid. It should be expected that for an elastic material Equation 4.17 would be valid, which has been shown in this test. However, it is important to note the limitation of applying the elasticity equation to obtain realistic results on practical data.

Making measurements at low loads is not feasible by hand due to the high lateral movement of the scanner across the surface. This makes estimating an average radial location change difficult, particularly if the motion is in both the x and y axes simultaneously. Additionally, SIFT is not totally immune to image noise and imperfections (scratches) on the scanner face and dirt/features on the material surface can introduce fixed artefacts in the image view. The fixed artefacts and image noise will produce SIFT features that are invariant to the applied load and so cannot be used to measure the resultant strain. Finally, there is a limit to the elastic range of most real materials before they begin exhibiting non-linear behaviour, and so only using solutions from the linear portion of the stress/strain curve is vital in calculating the elasticity as a

constant. There are several workarounds to these issues, which can negate their effects when used practically.

Firstly, the issue of high lateral translation at low loads, below 6N but typically around 1N, can be reduced using less surface lubricant. This is not an ideal solution, as the lubricant is required to allow the skin to deform without sticking to the scanner face. A better solution is to simply ignore data at low loads, as has been done in this test. For clarity these 'low loads' are very small indeed and using a larger range of loads, that are still comfortable for a patient, will better utilise the dynamic range of the force sensors.

Secondly, there is little that can be done about image noise other than using higher quality cameras but, the artefacts introduced by image noise rarely carry over from one image to the next and so the effect of this is relatively low. The bigger effect is from fixed artefacts that are invariant to load. Scratched lenses are a common problem in computer imaging, which is exacerbated by the acrylic scanner face used in the prototype system which is prone to scratching during manufacture. Using a glass scanner face would increase the systems resilience to scratching. Naturally, dirt and debris will accumulate on the material/skin surface and stick to the residual lubricant on the scanner. Regular cleaning of the material and scanner surfaces, particularly prior to use will help alleviate this source of error. Despite these basic workarounds, there is a limit to how far the issue on fixed image artefacts can be solved; as there will be naturally occurring fixed artefacts on the patient's skin in live use, particularly hair. The hair follicles will be able to move, as they will deform with the skin, but the hair itself will stick to the scanner face as a result of the lubricant. While this cannot be totally accounted for, the

expected effect can be reduced by focussing the camera several millimetres below the skin; it would be highly impractical to insist on shaving or waxing prior to clinical evaluation using this system. In this situation, the majority of features tracked will be in the embedded vein network and not on the skin; as the number of load invariant features will be small using this measure, there will be a sufficiently large number of mobile features to estimate the material strain.

Finally, most materials do not exhibit linear elastic responses over a wide range of applied loads. This is not necessarily a problem as the primary goal of elasticity measurement is the characterisation of the stress/strain curve of the test material. The general elasticity formula, Equation 4.16, will assume a linear response over the full load range, however Equation 4.17 allows for a non-linear response to be characterised, resulting in an elasticity value for a given strain or stress. This is appropriate when characterising normal highly non-linear materials with high load ranges (Wellman et al., 1999a). In this case, the rule on omitting the ‘low load’ region of the stress/strain curve would still apply as this region is dominated by lateral motion and not necessarily representative of the underlying material properties.

This validation trial does not fully test the capability of the proposed system to measure elasticity over a range of material parameters, which shall be investigated later in this thesis; but proves that SIFT tracking can be used to measure material strain and, when integrated with tactile force sensors, characterise the stress/strain curve of an elastic material. The system has been validated on a simple material and will now be progressed onto mapping applications prior to rigorous testing.

4.4. Application in Improved Tactile Mapping

4.4.1. Introduction

Tactile mapping is the process of spatially referencing sequential tactile images for the purpose of gaining an overall tactile map of a larger structure. This allows for a complete picture of the internal tactile structure of the test material, and allows for the spatial relationship between tactile features, in this case embedded lesions, to be determined and monitored over time w.r.t. each other and w.r.t. other reference locations. Performing a tactile scan of the whole breast at once using a single large sensor (Gentle, 1988) produces a total tactile view without mosaicking smaller images but is impractical and will be equally, if not more, uncomfortable than typical X-ray mammography due to the need to compress the entire breast in a similar manner.

Methods of mosaicking tactile images have been proposed in the past using a magnetic position tracker to track the spatial relationship between images so that they could be superimposed on a flat map (Wellman, 1999), this was effective but limited in that the map was not referenced to the breast and was in fact a flat image referenced to the suprasternal notch of the patient. This made analysis between subsequent scans difficult, as the breast needed to be in exactly the same position/orientation w.r.t. the suprasternal notch, a situation made unlikely by the mobile and pendulous nature of breast tissue. This was followed up a decade later, where sequential tactile images were correlated with one another and overlaid at the point of maximum correlation to produce the mosaic (Egorov and Sarvazyan, 2008). This was effective and more

practical than the previous iteration as it did not require an external position tracking system but was limited in that the images were no longer robustly referenced to anything on the body unless the tactile scan passed over the nipple. Additionally, the method was not robust to rotation in the tactile images, it could only deal with translation, and so was unsuitable for practical implementation (Sarvazyan and Egorov, 2012).

The ideal situation would combine the basic selling points of both previous methods, the body structure referencing and low infrastructure requirement respectively, and this can be achieved using the vein images previously collected for elasticity measurement. The vein images can be mosaicked using image processing techniques, such as the SIFT algorithm previously described, to produce a map of the breast onto which tactile images can be referenced, as shall be shown in this thesis. This is a common method used in other condition monitoring applications including visual pipe inspection (Summan et al., 2018) and robotic guidance (Khan et al., 2020).

The key benefits of using the developed IR vein imaging system for tactile mapping are: firstly, the reuse of developed technology; secondly, the tactile images would be directly referenced to a structure within the breast and so would be relatively robust to orientation changes between scans; thirdly, the superposition of tactile images on the vein network will allow for an indication of the blood inclusion/invasiveness of the lesion; finally, the system would be robust to rotation of the scanner in use during a scan session, which suggests an implementation based on this system will be effective in practical use where rotation and variation is guaranteed by the manual nature of these systems in use.

4.4.2. Image Affine Deformation Reduction

The biggest problem in forming a map of the vein structure from images taken during tactile imaging is from the deformation of the vein structure as a result of the tactile imaging process. It is clear that when the scanning probe is pressed into the tissue to obtain the elasticity estimate, the vein structure and other tissues deform. This is not useful for creating a map of the original breast as all of the structure features would be out of position with respect to each other.

The SIFT algorithm, currently used for material elasticity estimation, is not able to handle relatively large affine tilt angle changes (Morel and Yu, 2009) and Affine SIFT (A-SIFT), a SIFT variant capable of handling view angle changes, is very slow and unsuited to real-time implementation (Yu and Morel, 2011). In order to reduce the affine distortion, and so be able to use SIFT to produce tactile vein maps, the additional sensors implemented into the scanner can be used to estimate the affine tilt directly in real-time. Knowledge of the tilt angle, from the hardware, and the contact mechanics; based on the applied load, scanner geometry, and material properties; allows for the affine deformation to be removed and the image recast into an ‘undeformed’ state with zero tilt angle. This is, in effect, an inverse transform function to invert the deformation of the vein structure caused by the contact during the tactile imaging process.

From Equation 4.12 and Equation 4.13, it has been shown how the tilt angles can be estimated from the load measurement difference, from the tactile sensors, and the stiffness coefficient (k) which is constant related to the material properties and geometry. The tilt angle can now be used to estimate the stress field across the scanner face. The

load, F , at any point on the scanner face is estimated using Equation 4.8. The adapted elasticity equation, Equation 4.17, can be rearranged to estimate the ‘undeformed’ radial location of an image feature (R) based on its location on a deformed image (R'), the applied load (F), and the material properties (E and ν) as shown in Equation 4.18. This expression removes the ‘stretching’ between loaded images with zero tilt angle by taking into account the applied stress and material properties. The elasticity, E , is determined using the originally described process. This process removes visual deformation of the images.

The expression can be generalised to include the tilt angle effect on the stress field, calculated in Equation 4.8, by understanding that the deformation, or stretching, increases with load. The applied load varies across the scanner face, as a function of the tilt angle, and so the deformation across the image will similarly vary. As such, the load distribution across the scanner face can be used to estimate the localised strain at a particular point on an image. Equation 4.19 shows how to ‘undeform’ an individual pixel’s location (P) based on the deformed pixel location (P'), the load at the position of P' , and the material properties as an inverse function of the applied contact. The load (F) is determined as a function of the tilt angle, scanner geometry, and material constant (k).

$$R_i = \frac{R'_i}{1 - \nu \left(F_{Total} / A_{Scanner} E \right)} \quad (4.18)$$

$$P_{[x,y]} = \frac{P'_{[x,y]}}{1 - \nu \left(F_{[x,y]} / A_{Element} E \right)} \quad (4.19)$$

4.4.3. Estimation of Material Constant ‘k’

4.4.3.1. Measuring ‘k’ from IMU/MARG Sensor Fusion

The material stiffness constant ‘k’ is required to determine the affine tilt into the material, and thus estimate the stress distribution on the scanner face for affine deformation reduction. This is calculated using sensor fusion between the pressure sensors and the MPU6050 IMU, using the IMU to provide a reference angle for use in estimating the required ‘k’. Equation 4.12 and Equation 4.13 calculated the tilt angles based on the constant ‘k’ and the measured difference in pressure measurements on each axis, and can be rewritten into Equation 4.20 to estimate ‘k’ based on pressure difference and reference angle from the IMU.

$$k = \frac{F_2 - F_1}{2S_y \sin \theta} = \frac{F_4 - F_3}{2S_x \sin \varphi} \quad (4.20)$$

4.4.3.2. Measuring ‘k’ Practically

To measure ‘k’ practically, the pressure sensors must be calibrated for linearity after being mounted onto the scanner as described in Appendix B. Then the transform between the IMU axes and the pressure sensor axes must be determined, in terms of angle offset to allow for the use of IMU orientation in this application. This offset is determined once during manufacture to give the corrected orientation of the pressure sensor axes. IMU orientation is estimated with respect to the local gravity vector using well documented 6DOF sensor fusion (Madgwick et al., 2011).

With the pressure sensors calibrated for linearity, and axes offset angle determined, an initial orientation estimate can be made using the IMU. When the load difference on the pressure sensor axes is zero, then the current IMU orientation is the orientation of the material surface, θ_0 and φ_0 . Then: a small angle perturbation can be made to a single axis, or both, with the tilt angle being measured as the difference between the initial material orientation and the current orientation, θ_i and φ_i after the tilt perturbation as shown in Equation 4.22. An estimate of ‘k’ can then be made by sweeping across angles in a range ($\pm 10^\circ$) and linearly fitting to the resulting relationship between the axial pressure difference and the sine of the angle.

In an ideal situation the value of ‘k’ measured using x or y axis tilts would be equal however, minor differences in materials and imperfections in the sensor calibration process can lead to small differences in the estimates of ‘k’ from each axis. As such, it is appropriate to use an average of the two as shown in Equation 4.22.

$$\theta = \theta_i - \theta_0, \quad \varphi = \varphi_i - \varphi_0 \quad (4.21)$$

$$k = \frac{k_y + k_x}{2} \quad (4.22)$$

The constant ‘k’, like the material elasticity ‘E’, must be determined for each patient at the start of the scanning process. The process is fast, as there is no image processing to do, taking approximately 4 seconds in total, described in Appendix B.

4.4.4. Producing Vein Maps by Mosaicking

Mosaicking is the process of matching spatially distanced, but overlapping, images and merging the images with the appropriate spatial relationship to form a single larger image. This process is basically the computer equivalent of solving a jigsaw, except that we have knowledge that two images should go together, we must simply find how they go together, analogous to rotating a jigsaw piece and trying each side of the piece for the best fit. In this case, the range of possible image relations in terms of translation and rotation is continuous rather than discrete for the simple jigsaw analogy.

Applying Equation 4.19 to loaded images removes projection distortion from loaded/deformed images. This unwraps the loaded images into a planar projection that can then be mosaicked over one another, as the images will have similar scale throughout the image frame. The SIFT algorithm, previously described and used for estimation of the elasticity required to unwrap the images, can be similarly used in this situation for mosaicking (Brown and Lowe, 2007) (Khan et al., 2020). The SIFT feature descriptors for overlapping images can be matched and a net transform determined using Random Sample Consensus (RANSAC) (M.A.Fischler and R.C. Bolles, 1981). RANSAC is an optimisation technique to find a transform between matching points that rejects outliers and spurious false matches that make it through the SIFT matching function by looking for agreement between random groups of matching points. Although RANSAC is a relatively old algorithm, it is still widely used in image processing specifically in mosaicking and panorama creation (Summan et al., 2018). When RANSAC has found the best fit homography matrix, a transform describing the relation

of one image to another via a change in camera position/orientation, the images can then be overlaid onto a blank map with the proper relationship. Improvements to visual quality can be made upon completion of the imaging process. By appreciating that the errors from image mosaicking in this context integrate linearly with image number and time (Rana et al., 2020), structure reconstruction can be improved by centring the mosaic on the centre-most image which reduces the visual distortion to the overall map.

The 3x3 transformation matrix, T_i , relating unwarped image_{*i*} to unwarped image_{*i+1*} is accumulated by matrix multiplication to find the total equivalent transform, $T_{Equivalent (i)}$, relative to unwarped image_{*i=1*} as shown in Equation 4.23. Once the individual image processing has completed and ‘N’ images have been processed, the centre adjusted transform for each image, $T_{Adj (i)}$, can be computed using the inverse transform for the centre most image as shown in Equation 4.24. In this context T_1 is a simple 3x3 eye matrix, and $N/2$ is the image index of the centre most image in the scan process. The initial unwarping process is illustrated in Figure 4.15.

$$T_{Equivalent (i)} = T_i * T_{i-1} \quad (4.23)$$

$$T_{Adj (i)} = T_{Equivalent (i)} * T_{Equivalent (\frac{N}{2})}^{-1} \quad (4.24)$$

With the transformation matrices of each unwarped image known, the images can be overlaid sequentially on a blank map with relationship T_{Adj} relative to image 1, as shown in Figure 4.16. The structure being imaged in this example is the test material presented in Figure 4.11, for which elasticity values were previously determined.

Image 1 at $F = F_0$

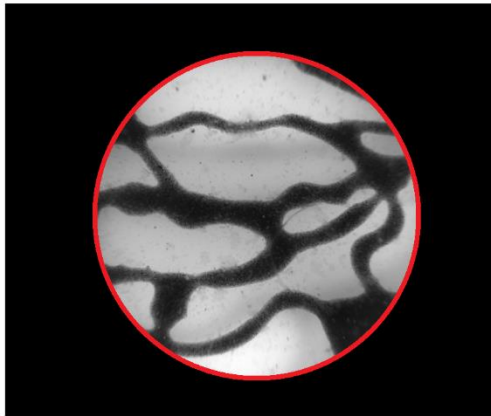


Image 2 at $F \gg F_0$

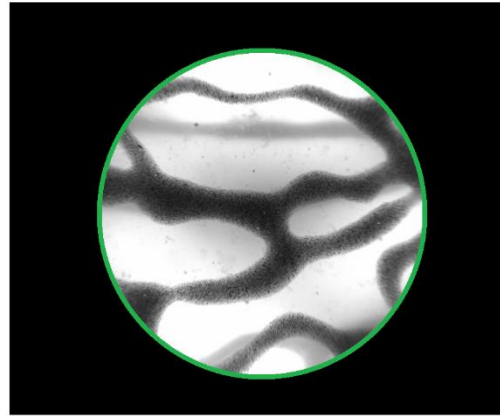


Image 2 from Image 1 Perspective

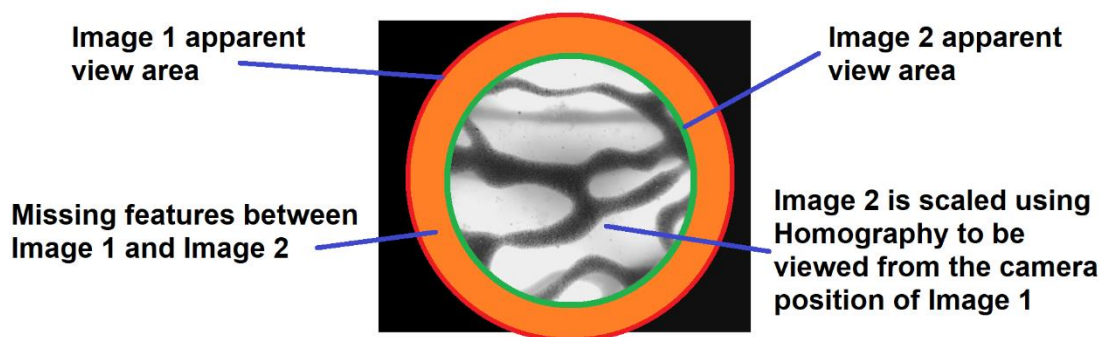


Figure 4.15 - Projection of loaded tissue images to the unloaded viewpoint. The deformed image (Image 2), taken at a high normal load, can be projected onto the viewpoint of the undeformed surface (Image 1) using the homography matrix describing the transform between image 1 and image 2. The two images have a similar centre and so there is only a transform in the z axis (akin to zooming). The difference in observed tissue surface area between load states, caused by increased stretching at higher load, leads to missing features in the periphery of the image when the deformed image is projected into the undeformed view plane as illustrated in Figure 4.6.

The vein image mosaic, shown in Figure 4.16, does show clear banding from the scan direction where some features do not fully line up, however the total error accumulated after the 365 images used here is only 0.3% when compared with reference measurements from a VICON photogrammetry tracking system (Rana et al., 2020) which has approximately 0.5mm positioning accuracy (Summan, 2015). This shows that this method is effective for forming maps of deformable vein structures, the validity of which over a range of materials and feature densities shall be tested further in Chapter 6. Tactile data can then be referenced onto this embedded structure map using the spatial relationship between a future tactile sensor and the vein imaging camera.

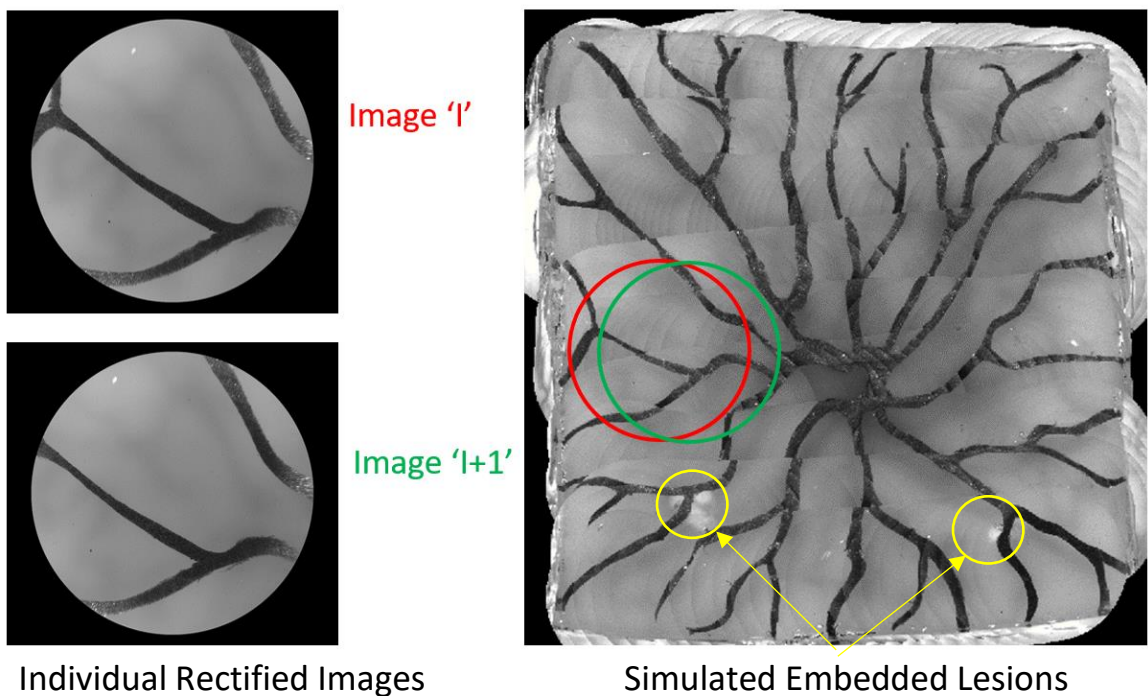


Figure 4.16 – Mosaicking of affine corrected images. Image 'I' and 'I+1' are distortion corrected to remove affine distortion and recast images to their estimated 'undeformed' state. Following distortion correction, the homography matrix between image I and I+1 is calculated using RANSAC on SIFT features. The 2 images are then overlaid using the transformation matrix, $T_{Adj(i)}$, to produce a continuous mosaic of registered images.

4.4.5. Discussion

The image unwarping technique using Equation 4.19 has been shown to be effective in reducing distortion in loaded images, where comparison between image matching features for SIFT alone vs. the proposed image unwarping function and SIFT together showed approximately 2.5 times as many diagonal inliers for the proposed function than for SIFT alone over the 365 images used in the sample trial (Rana et al., 2020). Perhaps more importantly, the standard deviation for diagonal matches for SIFT alone was >2 times higher than for the proposed function and SIFT together. This is summarised in Figure 4.17. This high variability and low average matching feature count leads to unreliable solutions for SIFT alone.

Mosaicking of images deformed in the process of image capture is a difficult problem, with several proposed methods in the literature. Comparing the proposed system against: basic structure from motion (SFM) photogrammetry (Micheletti et al., 2015), Finite Element Modelling (FEM) based SFM (Agudo et al., 2016), and Non-rigid SFM (Haouchine et al., 2014); Rana shows that the total accumulated positioning error of the proposed system is at least 4.1 times less than for the mentioned methods (Rana et al., 2020) as summarised in Table 4.2. This margin increases with variation in the applied load and deformation, but this shall be discussed in more detail in Chapter 6.

Further improvement is possible using bundle adjustment, a global optimisation scheme to optimise the transforms for all overlapping images (Triggs et al., 2000), however the scale of the scanning regime and currently obtained positioning accuracy makes implementing this very complex step not resource effective for this project.

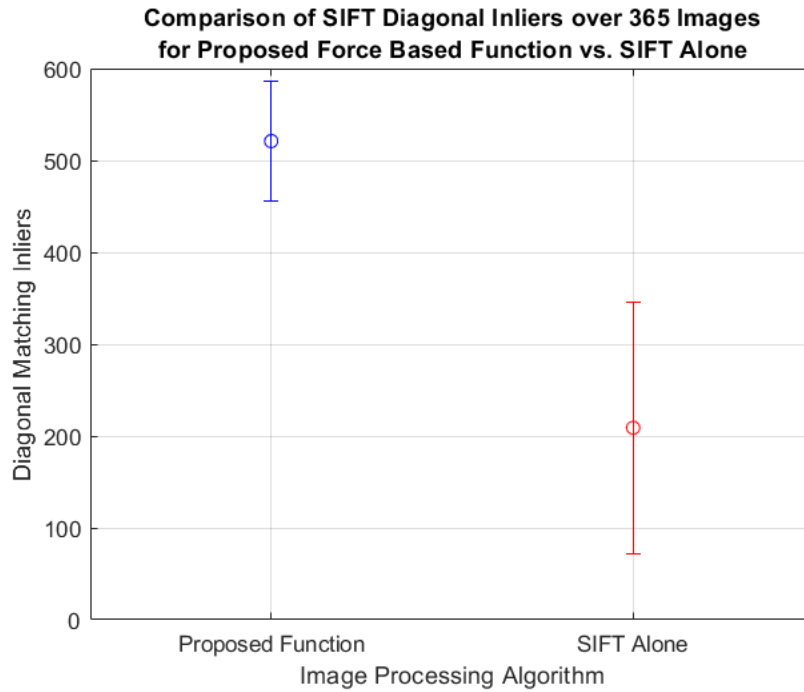


Figure 4.17 - Comparison of the proposed force-based feature matching function vs. SIFT. Note that both methods use SIFT for feature extraction, but the proposed force-based system, using Equation 4.19, produces more matches with adjacent images than SIFT due to reduced image distortion.

Table 4.2 - Total camera position error comparison. The proposed camera system and algorithm is compared with other SFM methods, suitable from similar applications, that do not factor in the applied load or utilise the extended camera hardware. The parameters were 365 images with a total displacement of 764mm.

TOTAL CAMERA POSITION ERROR COMPARING PROPOSED SYSTEM WITH OTHER METHODS				
Method	Proposed Hardware System	SFM (Micheletti et al. 2015)	FEM/SFM (Agudo et al. 2016)	NRSFM (Haouchine et al. 2014)
RMS Error (mm)	2.261	15.263	11.821	12.360
Error (%)	0.296	1.833	1.496	1.221

The initial results shown here, and in the literature (Rana et al., 2020), show that the combined tactile sensor and IR imaging system is effective at reducing distortion on images taken during contact tactile scanning, which has the effect of producing higher accuracy structures and image registration than other methods that do not utilise the additional hardware. Applied to tactile imaging, this well-defined base structure will provide the basis for accurate registration of tactile images with respect to one another and with respect to the vein structure, when a tactile image is taken simultaneously with the IR vein image. If a tactile imaging array were fused with this technology, the implied registration accuracy of tactile features would be 0.296% as the two imaging techniques would be rigidly spatially related.

The use of this type of system in tactile mapping, and registration of tactile images, has several key benefits over previous tactile image registration techniques. These are mainly: There is no need for external tracking systems for tracking probe position with respect to the body (Wellman, 1999), the system is referenced to mobile structures within the body that are robust to motion of the patient (Quieregatto et al., 2014), and the system is robust to rotation of the imaging system using the rotation invariance of SIFT which is a must for a manually controlled hand held scanner (Egorov and Sarvazyan, 2008).

It is believed that this technology is scalable, allowing the system to be implemented in a smaller configuration, for implementation in commercial TI systems such as SureTouch™, which will mean the impact of the technology will be greater than designing the tactile imaging system around this relatively large camera prototype.

4.5. Conclusion from Optical Tactile Mapping

4.5.1. Prototype Optical Based System Practicality

The optical system has been shown to be capable of producing an estimate of elasticity for an elastic material within the range of typical breast tissues by observing the deformation of vein structures under load. The system has also been shown to be able to produce accurate global depictions of the vein structure by non-rigid mosaicking of local overlapping images (Rana et al., 2020).

The method of operation, specifically the way the operator collects data using the system, is very similar to currently used clinical TI devices (SureTouch™) in that the system is scanned gently across the breast to form the mosaic, with a gentle normal compression to perform the elasticity measurement. The practicality can thus be described as ‘good’ as it is no more awkward than current TI in terms of operator use and likely patient experience, especially compared with the MARG based system (Hampson et al., 2019) proposed in Chapter 3.

On the note of public perception: although this system is non-invasive, in that it is not harmful nor penetrates the body, the use of a camera can be described as invasive in terms of privacy. The camera and lens combination used is capable of resolving the vein structure and the patients simultaneously (although they are out of focus), and so adoption of this technology in its current form may be hindered by privacy concerns. Although this issue is not generally applicable to the population in general, recent trends in the media surrounding surveillance and data collection by private entities have shown

that there is a subset of the population at large that may find issue with such imaging systems. It is well known that such people have a disproportionately loud voice when it comes to lobbying and policy making, and so future designs of this technology should take this into account.

4.5.2. Summary and Next Steps

This chapter has developed a novel handheld breast mapping technology based on the fusion of tactile sensors, orientation sensors, and IR cameras capable of forming a composite image of the vein structure within 0.3% spatial error that tactile data can be referenced to in future (Rana et al., 2020). This chapter has also developed a novel implementation and variation of A-SIFT based on physical measurement of contact stresses, allowing for reduction in affine and projective distortion. This allows SIFT to produce 2.5 times as many feature matches on average over 365 images than it would be able to produce otherwise. This chapter has also demonstrated a novel elasticity measurement technique based on the tracking of SIFT features with respect to load for measuring the background elasticity of a tissue or material within 2% of a reference standard with a standard deviation of 5.23%. This provides both a stable structure for tactile data to be referenced to, and the background elasticity required for differential measurement of lesion elasticity.

The main limitation of this system, and the implementation of the algorithms, is that it has been tested on flat elastic phantoms. It is common to begin on simple examples first and validate the response before moving onto complex structures. Similarly, it is easy to obtain reference measurements for elasticity and position for flat

structures, it is very difficult to obtain reference values for complex geometries and so this problem will not be considered for this thesis. On that note, however, the method of measuring the tilt angle of the probe into the tissue is robust to surface orientation changes from Equation 4.21. Tracking the surface orientation using the difference between probe and compression angles will allow for the formation of 3D structures in the absence of significant shear on the structure. This simplified test system, using initially planar surfaces, does not test the device performance using 3D stacked structures, nor features that are less demarked than blood vessels. This limitation is not expected to significantly effect performance when applied to such structures/features or clinical trials. The SIFT algorithm that forms the basis of the proposed algorithm is suitable for 3D objects and additional features, even ones that may not be visible in adjacent images, will have a net positive effect on the performance of the system when compared to this simplified test example.

As this system worked and was practical, the initial validation results were shortened to simply show the device working and what it would output in context. Expansive exploration into elasticity measurement accuracy over a broad range of material elasticities must be performed. Similarly, testing over a range of feature densities must also be done to estimate the practicality of this system on patients with varying levels of visible vascular structure without requiring clinical assessment. In the current implementation, there is no space for a tactile array to identify tactile lesions in situ, and so the system shall be miniaturised to be compatible with current TI technology.

Chapter 5

Prototype System Development and Testing

5.1. Introduction

This chapter covers continued development of the proof-of-concept system demonstrated in Chapter 4 into a practical, handheld, hybrid tactile imaging prototype capable of estimating the background elasticity of breast tissue and forming compound tactile images. This prototype will be designed to match the geometry of the SureTouch™ tactile breast screening system, to accelerate commercial adoption of these research outputs and increase the impact of research by working with industry partners. The additional developments, beyond the miniaturisation of the technology, involves the implementation of continuously updating material properties, adjusting the calculation of the applied load distribution to take into account the new probe geometry, the registration of tactile sensor data onto the IR vein map, and the analysis of tactile sensor data error sources. The developed system will be tested in terms of positioning accuracy for tactile mapping and elasticity measurement capability, over a range of simulated phantom breast tissue with varying elasticity and vein structures. This will show that the proposed technology and algorithms are effective in both regards. This chapter outputs a functional and practical tactile mapping prototype that is demonstrated on phantoms.

5.2. Integration into Commercial Footprints

5.2.1. System Design

The developed system is designed to be easily implementable in the existing commercial TI systems, specifically SureTouch™, by condensing the required technology and utilising the empty space inside the TI system. This mainly involves designing the camera system and optics to fit into a small form factor, around a contact surface similar to the SureTouch™ tactile array. An internal view of the developed prototype, shown in Figure 5.1, highlights how this is achieved.

The developed system is based on an Edmund Optics EO-1312M USB board level camera (Edmund Optics Inc., US-NJ) which is a 1.3MP, 25FPS monochrome camera with a global shutter. This camera is secured to a rigid plastic mounting plate, with the appropriate generic M12 size lens protruding through the mounting plate and into a simulated SureTouch™ sensor backing. This sensor backing is designed to have the same dimensions as the SureTouch™ system, allowing for a tactile array to be mounted directly to it in future design iterations. The SureTouch™ backing features a hollow centre, containing a 17 x 15mm (OD) 850nm LED ring, and a flush acrylic view port with a 12mm x 10mm viewing area. Between the sensor backing and the rigid mounting plate are 4 SingleTact™ S8-10N capacitive pressure sensors (PPS Inc., US-CA) bonded onto each respective surface using 3M 300LSE double sided tape (3M Company, US-MN) at known distances from the scanner centre as shown in Figure 5.2. These sensors are read using a custom I²C SingleTact electronics controller.

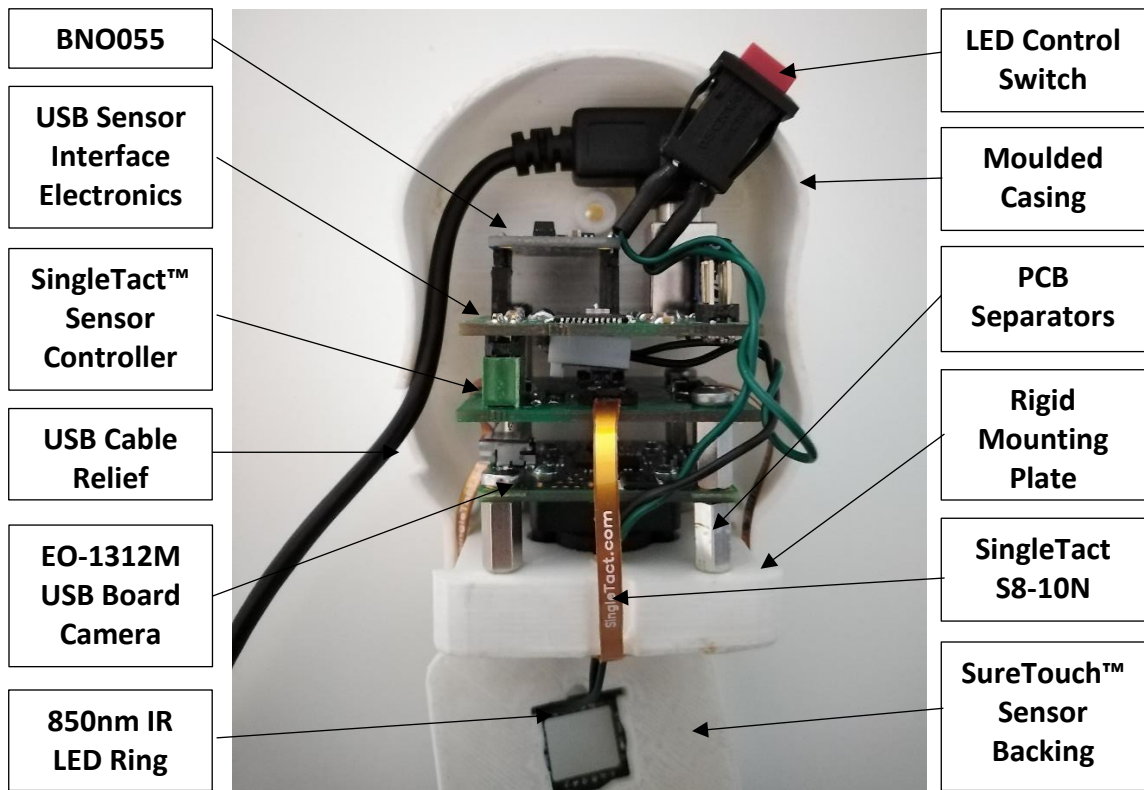


Figure 5.1 - Developed prototype system internal view. The system hardware components are highlighted in the image. See Figure 5.2 and Figure 5.4 for more details.

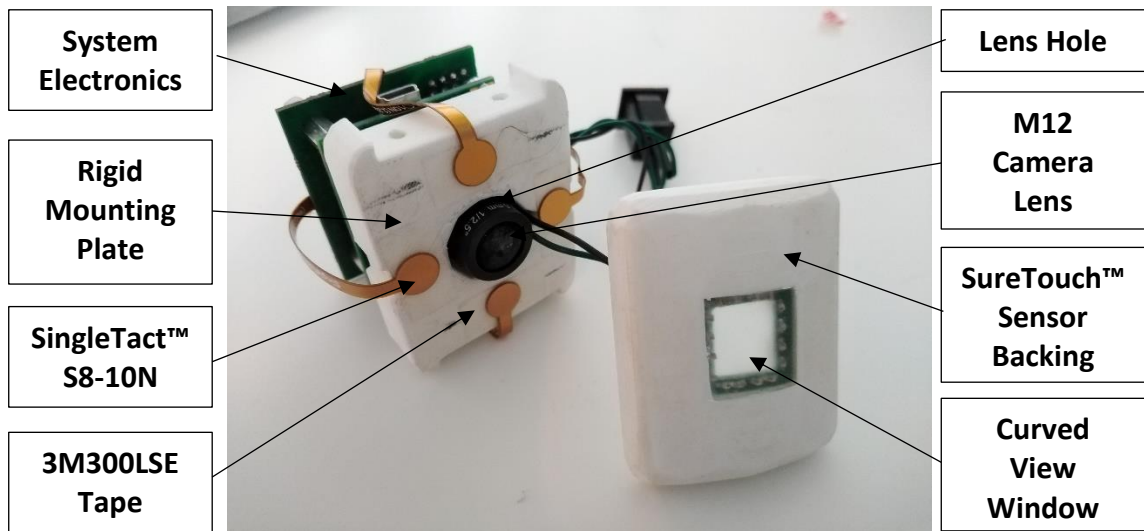


Figure 5.2 - Developed prototype system underside view. The positioning of the SingleTact™ pressure sensors is shown behind the curved tactile array mould with a transparent window. Double-sided tape bonds the SingleTact™ sensors to both surfaces.

The SingleTact™ sensor controller is polled at 100 Hz via I²C by the governing sensor interface electronics board, which provides 5V to the system peripherals and converts the sensor data into a USB data stream using an ATmega32U4 microcontroller (Microchip Technology Inc., US-AZ) clocked at 16 MHz. The interface electronics also reads orientation data via I²C from a Bosch BNO055 9 DOF MARG absolute orientation sensor (Robert Bosch GmbH, DE), implemented as an Adafruit 2472 breakout board (Adafruit Industries LLC., US) at 20 Hz. Data is streamed out from the sensor system via a USB cable to a PC for use with a MATLAB based serial port reader DAQ program. This is shown as a block diagram in Figure 5.3.

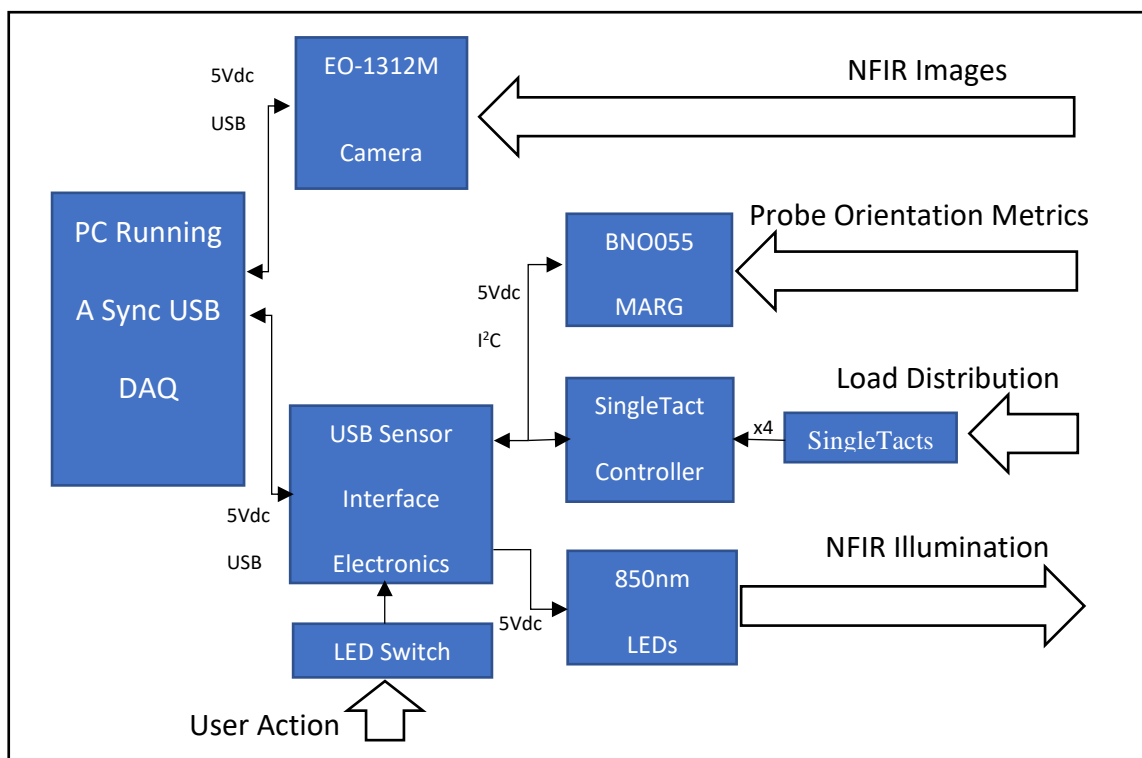


Figure 5.3 - Prototype System Block Diagram. The separate electronics modules are highlighted, and their purposes clarified. The SingleTact controller is a custom proprietary system, for replication 4x SingleTact Electronics modules can be used in parallel, as used in the precursor system from Chapter 4.

Each electronics module is secured to the rigid mounting plate using standard steel PCB spacers, to maintain component alignment in the event of a casing bend. The casing is an ergonomically moulded PLA material, secured to the rigid mounting plate as shown in Figure 5.4 and not in contact with the internal electronics to maintain sensor alignment. The LEDs are controlled using a push button switch on the outer case, so that they are not running continuously. This is to limit the heat dissipated by the LED module which, if left running continuously, can lead to ‘fogging’ of the view window and camera lens. The total power dissipation from the LED ring is limited to 200mW. The LED window is sealed from the front to stop liquid ingress. The sensor gap is intended to be sealed/covered using the tactile array protective sleeve.

Alignment between the BNO055 sensor axes, the SingleTact™ sensor axes, and the camera [x,y] axes is critical to system operation. Deviations in alignment are tolerable, and can be compensated for by rotation matrices, providing they are found during manufacture and the calibration process shown in Appendix B.

The system is completed using a SureTouch™ tactile array disposable sheath, a transparent low friction sheet to eliminate shear forces from the contact face. This allows for some protection to the SingleTact™ sensors from lubrication gel, and stops the system from sticking to test materials. The sheath is pulled tight over the view window, such that no creases or bubbles are visible in the camera image. This is a critical step, as these artefacts can obscure test features in the relatively small viewing area, leading to unreliable results. The final system prototype is shown in Figure 5.4.

The geometry of the faceplate does not hold any special academic significance, in that the shape does not award performance benefits over any other besides perhaps comfort, and was selected as a pragmatic engineering decision to accelerate future impact and academic output through the utilisation of existing technology, specifically the SureTouch tactile array. This is deemed important to future clinical research into breast tactile imaging using this technology, where long development times limit the impact of new technology on the clinical landscape.



Figure 5.4 – Prototype system completed view in use. The system fits comfortably in the hand, with an easy-to-use push button on the surface to activate the IR LEDs. The hand is kept clear of the SingleTact™ pressure sensors, eliminating interference through contact.

5.2.2. Minor Algorithm Changes for New Geometry

The geometry of the contact surface is different to that of the initial prototype developed in Chapter 4, and so the applied stress can no longer be assumed to be uniformly distributed over the scanner face when normally loaded. Due to the curvature of the contact surface in the new prototype system, the applied stress at a particular location will be function of the geometry and will be maximum at the point of maximum compression as expected. Recalling Equation 4.8, describing the point load at a particular position on the scanner surface given some material property, k , and the change in compression depth from the centre of the scanner, dz , simplified in Equation 5.1. In this case, the change in compression depth was estimated as the rotation of a flat plane by orthogonal tilt angles θ and ϕ respectively. For the new prototype, dz cannot be described as a flat 2D plane rotated and must be defined as the rotation of a 3D surface. This 3D surface is defined in Equation 5.2 and Equation 5.3. Here, z is the change in height of the scanner face as a function of the scanner radius, r , and the given location on the x axis in the direction of curvature. The scanner is flat in the y axis, and so is not used to calculate z . In this system r is 40mm.

$$F_{[x,y]} = F_{Average} - kdz_{[x,y]} \quad (5.1)$$

$$z = -r + \sqrt{r^2 - x^2} \quad (5.2)$$

$$3D_{Position} = [x, y, z]^T, \quad |x| < \frac{r}{2}, \quad |y| < 25mm \quad (5.3)$$

In a similar manner to the method of Chapter 4 this surface can be rotated by tilt angles θ and φ respectively, to determine the change in compression depth from the centre of the scanner face as a function of the tilt angles, the x and y location on the face, and the curvature of the scanner. Although the scanner face is large, and so the total curvature 'z' is large, the image view port is small in comparison and so the total curvature of the view window is very small, less than 5% of the view port dimensions. This is a result of small angle approximations and Equation 5.2. The very small curvature of the view window means that the deformation of the tissue visible in the view port can be approximated to that of the flat plate described in Chapter 4. However, if the view port were larger or the tilt angles are very large ($>20^\circ$), then the effect of lateral stress must be considered. This is not a testable condition, as the SingleTact™ sensors used to estimate the stress field are not suitable for the level of shear stress obtained at these angles (Hampson et al., 2019).

The estimation of elasticity, and reduction in image distortion, are similar to the method for the flat plate from Chapter 4, with the adjustment of the geometry as described. This results in deformation being measured at a cartesian location on the array rather than at a radial location. In a similar theme, the single value of k averaged from axial estimations cannot be used in this new configuration. The value of k is now axis dependant, which means that more measurements are required to ensure stability of this value in use.

5.3. Automatic Calibration in Use

5.3.1. Normalisation of Tactile Array

Prior to use, the tactile array must be normalised to account for slight changes in sensor properties since the last calibration. The tactile arrays used come calibrated for linearity from the manufacturer, however changes in temperature, initial/previous loading conditions, and humidity can affect the linearity and output offset of the sensors on an individual element basis. This normalisation is required every time the system is used, or when the system is moved to a new location, as described in the SureTouch™ training documentation (not publicly available). The normalisation linearises the output over a specified range and is only valid for a short period of time, sufficient to perform a single scan, but no longer.

The normalisation technique used for the SureTouch™ array is shown in Figure 5.5. The SureTouch™ system is entered into its ‘calibration’ mode via the GUI. The sensor system is then held still, unloaded, for a short time to get a stable reading of the sensor offset for each element. The sensor system is then pressed normally by hand into a calibration block of soft, homogeneous, and elastic material on top of a reference scale to a target load of 1.5kgf. The internal gain of each element is then adjusted to obtain a nominally flat response across the array, with a linear relationship. This method of normalisation does not prepare the system for changes in operating temperature, or creepage, during operation. These have always been assumed to be small, and their effects negligible, for a simple indicator of lesion location (Egorov et al., 2009).

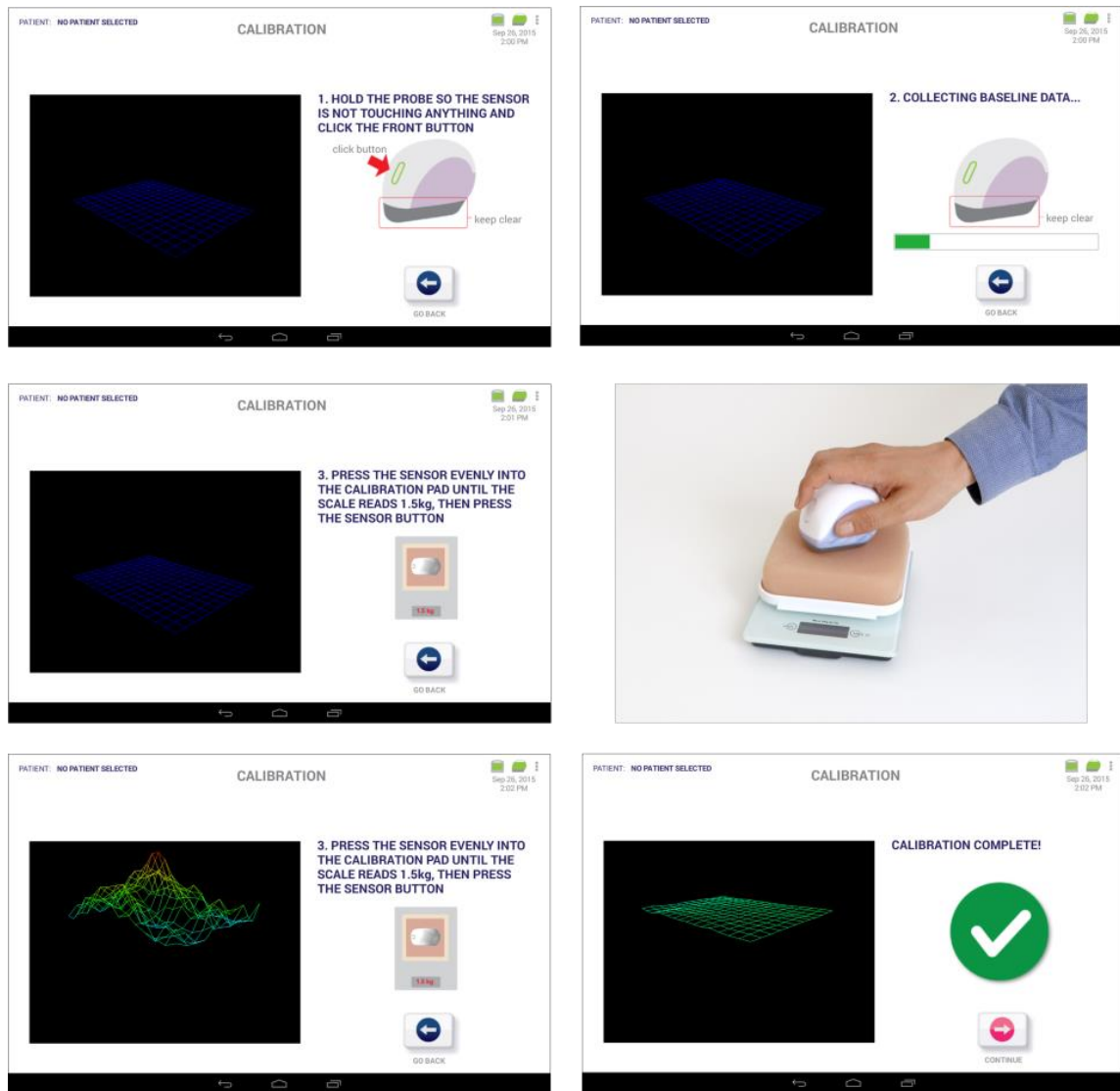


Figure 5.5 - Method of normalisation of the SureTouch™ tactile array (adapted from SureTouch™ training documentation 2015). The tactile array is normalised in the same way as it is done in the SureTouch™ clinical system. An unloaded measurement is taken of the current sensor baseline. The array is then pressed firmly, and normally, into an elastic soft material to a known load. This allows for a linearisation of the stress output for that range, unique for each sensor element, resulting in a flat response for simple homogeneous materials.

5.3.2. Initial Load and Orientation Sensor Calibration

The post manufacture calibration of the SingleTact™ load sensors, and the BNO055 MARG sensor, to determine the initial axes offset and account for manufacturing irregularities is performed as described in Appendix B. The SingleTacts are available calibrated from the manufacturer, however once they are mounted in place they must be recalibrated to account for the mounting conditions. This is a onetime calibration process, and would not be performed by the system operator, or clinician.

Prior to use, the orientation sensor must be calibrated first, as it is later used to normalise the SingleTact™ sensors. This is done following the process outlined in the BNO055 datasheet (Sensortec, 2020), and illustrated in Figure 5.6. The integrated accelerometers and gyroscopes are calibrated by placing the prototype in the 3 cardinal orientations, and their negatives, moving slowly between each and lingering in each for >4 seconds. The prototype holder has been designed to achieve the orthogonality required. The magnetometers are then calibrated by waving the prototype in a figure 8 motion. Once the BNO055 signals that calibration is complete, the calibration parameters are stored for later use, meaning calibration does not need to be done on every use, except when the system is moved to a location with a different magnetic field.

Following the orientation sensor calibration, the prototype is pressed normally into a homogeneous block of soft elastic material up to 1.5kgf, measured with a reference scale, similar to the procedure for the SureTouch™ array. The orientation sensor is used to confirm normal loading or compensated for slight tilt. A measurement is made of each sensor offset, and adjustment is made to the internal gain to achieve a

nominally flat response. This process is done each time the system is used to compensate for creepage and temperature changes and is valid for only a short time similar to the SureTouch™ normalisation process.

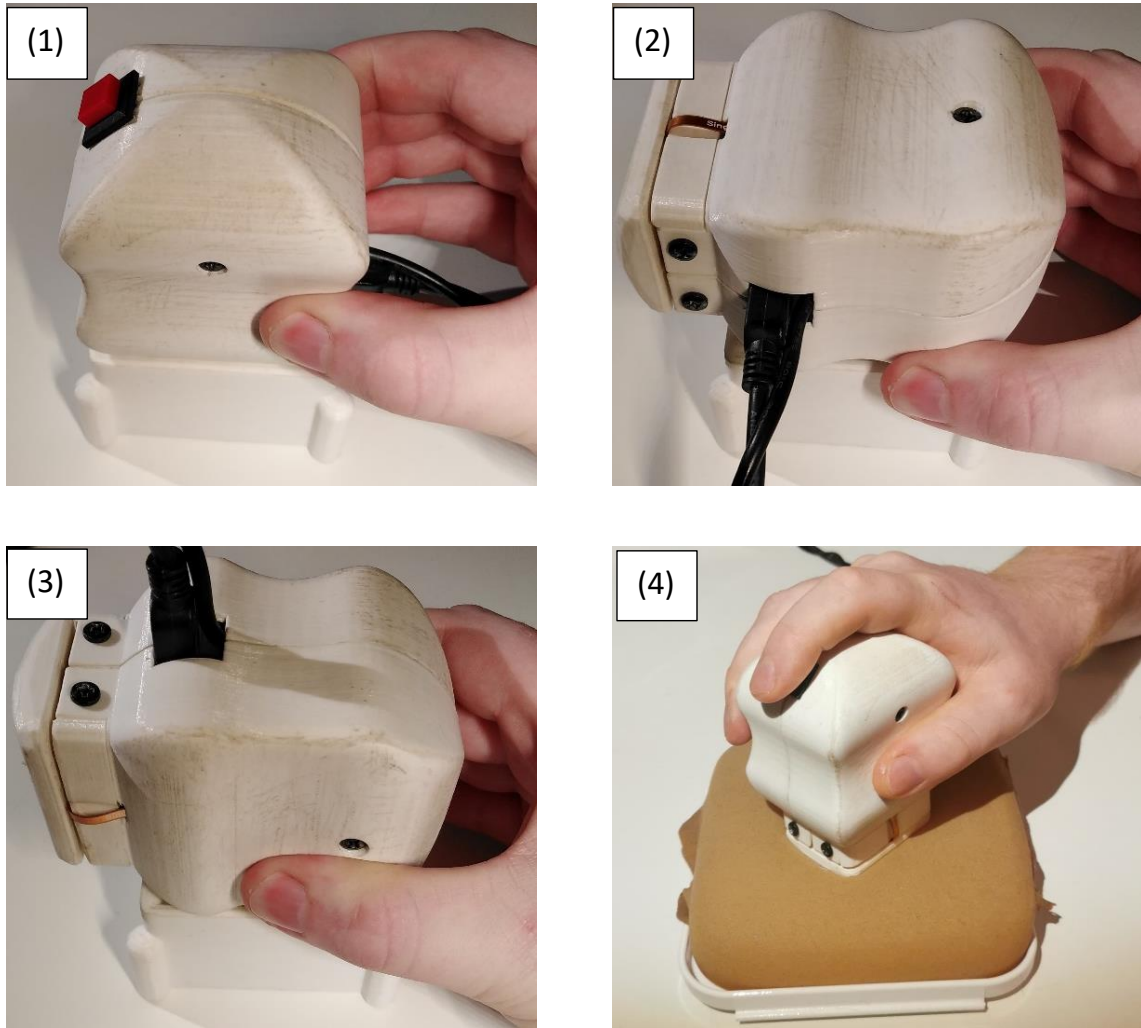


Figure 5.6 - Illustrative prototype calibration/normalisation process. The sensor system is placed in the 3 orthogonal cardinal directions (insets 1-3) and their negatives, moving slowly between them to calibrate both the accelerometers and gyroscopes. The magnetometers are calibrated by slowly waving the scanner about in a figure 8 motion. Once done, the system can have the SingleTacts normalised in the same process as the SureTouch™ array (inset 4) by pressing normally into a calibration block. The calibrated MARG sensor is used to confirm the compression angle.

5.3.3. Dynamic Material Property Estimation

The initial estimation of material properties, required for background elasticity and for image registration, is performed as described in Chapter 4. The validity of this value is limited in practice to the location where the measurement was taken, as biological materials and breast tissues are rarely homogeneous even at the largest scales. In order to make the system practical in a general sense, by not using a single value as a generalisation of the full test area, a method of re-evaluating the material properties during the scanning process is required.

The base image mosaicking algorithm, utilising the initial material property estimates (Rana et al., 2020), is augmented with 2 additional parallel steps, as shown on the right of Figure 5.7. As each image is parsed through the physics-based image rectification function, processed using SIFT, and compared with the previous image to determine the spatial relationship, the displacement is monitored for a near zero condition. If this condition is false, then there is a significant spatial separation between 2 images, and the image is then cached for mosaicking. If the condition is true, then the images have very little displacement between them, and so they can be considered to be concentric. Sequential images that meet this criterion are added to a separate caches, depending on the measured load distribution on the scanner.

In the case of normal loading, within a small threshold, the images are loaded into a cache. When 5 images are accumulated in a small area, with the displacement condition still true, a new evaluation of the material elasticity 'E' is made, which updates the value used for image rectification until a new value can be determined.

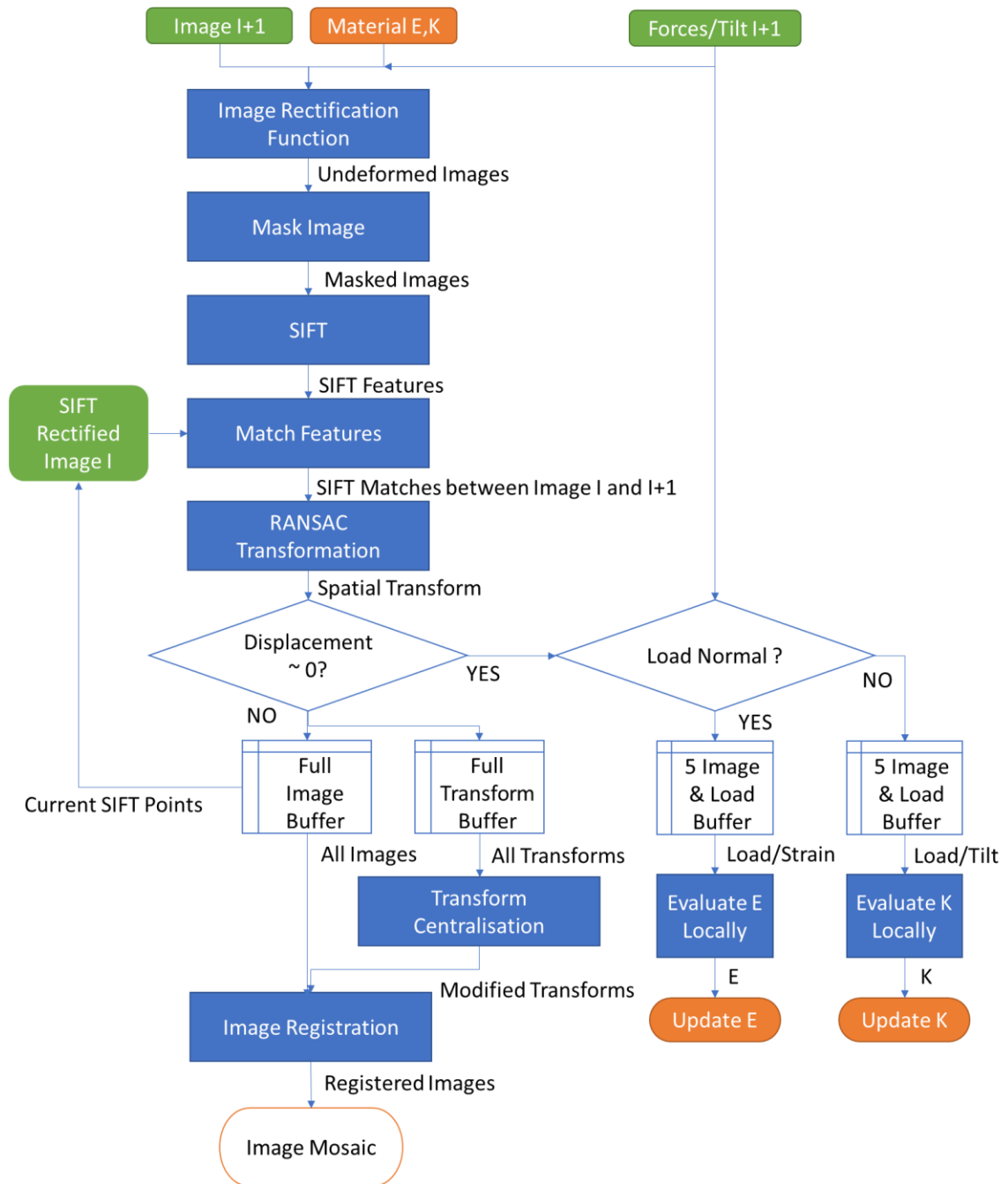


Figure 5.7 - General flowchart of automatic material property estimation. The vein images are rectified, matched, and spatially registered as described in Chapter 4. The addition is the processes on the right of the flowchart, where sequential images that have very low relative displacement will be separated into a buffer. If 5 images exist within a low displacement threshold, then they will be considered concentric and will be used to re-evaluate the material properties E , and k , as previously specified in Chapter 4 providing the images span a suitably large load range.

In the case of tilted loading, outside the normal loading threshold, images are loaded into a separate cache from the normally loaded static images. When 5 images are accumulated in a small area a new evaluation of 'k' is made, updating the value used for image rectification until a new value can be determined.

The new estimates require the load and tilt values to span an appreciable range for the results to be valid, as shown in Figure 4.13. This can be guaranteed by defining the scanning process to include a regular 'kneading' motion, with the scanner being pressed gently into the tissue and rocked from side to side whilst being passed over the breast. This is similar to how SureTouch™ is used in clinical practice, particularly in the detailed scan mode, and so is not a major deviation in procedure. If the load/tilt does not span a sufficient range, determined from the initial material property estimation, then the value will not be updated.

The values of E and k are spatially related using the IR vein image mosaic, allowing for an interpolated surface of values to be created. This surface can be used in post processing, as a second pass to further improve the output image, although this is not necessary for the current proof of concept trials. The elasticity surface can also be used to estimate local areas of background elasticity change. The resources required to fully validate and test the efficiency of this practical algorithm change robustly, by scanning a fully calibrated test material and verifying system response, are unavailable for this project. However, the individual methods of measuring E and k work, and so it can reasonably be claimed that this will also work, as it is simply a continuous execution of the pre-existing algorithms.

5.4. Registration of Tactile Images onto Vein Structure

5.4.1. Interfacing Tactile and IR Images

Tactile images are interfaced with IR images practically by equating the apparent pixel density of the tactile image with that of the IR images, so that they each cover a representative physical area. The tactile images are in fact a 12x16 stress array, but this can be interpreted as a 2D colour map or grayscale image. A 12x16 image is not directly compatible with a 1.3MP image, so the pixel density is used to enlarge the tactile image until there is a similar number of pixels in a given physical area. Figure 5.8 shows the types and size of the two imaging technologies being fused. The 12x16 tactile image has a scale of 0.4 pixels/mm, with a coverage area of 30mm x 40mm. The IR vein image has a scale of 74.2 pixels/mm with a coverage area of 10mm x 12mm. The tactile image is up sampled to have the same pixel scale as the IR vein images, by a factor of 180.5 using cubic interpolation. This allows the images to be integrated together using pixel indexes, which is a convenient value to use.

Continuing the issue of the differences in coverage area between the IR and tactile images, the difference in physical location between the imaging media must be taken into account. This is done by defining the offset in position and orientation of the tactile image w.r.t the IR images as a rigid transform matrix. This allows the different media to be overlaid and referenced with the proper spatial relationship as shown in Figure 5.9. The rigid transform, consisting of a designed translational offset and a rotational alignment is known from system design and manufacture.

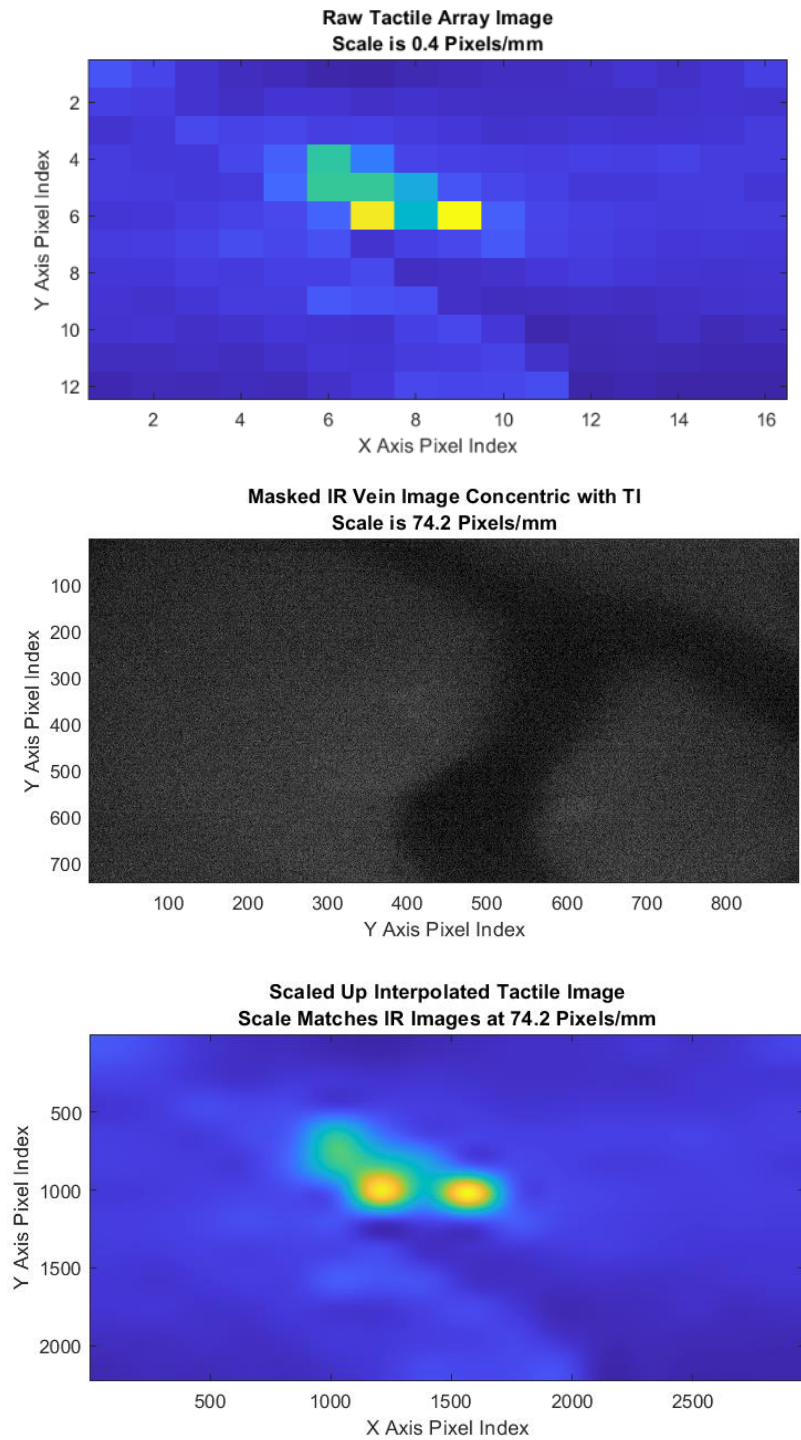


Figure 5.8 - Tactile and IR Image Re-scaling Stages. Top) A 12x16 (30mm x 40mm) Tactile Image is taken of an area of the breast. Middle) A concentric, simultaneous 742 x 891 IR image is taken (10mm x 12mm). Bottom) The Tactile Image is rescaled with interpolation to match the IR image pixel physical scale of 74.2 pixels/mm for plotting.

As the tactile images are rigidly coupled to the IR vein images, the image mosaicking quality and accuracy will be equivalent to that of the IR images alone. The expected output can be gleaned from Figure 5.9, where a tactile scan showing lesions is overlaid on the surrounding vein structure for registration and later inclusion/invasiveness analysis. The tactile inclusions would not be visible in the region of the IR viewport from a single image, however this area would be filled in using sequential overlapping images as described in the following section.

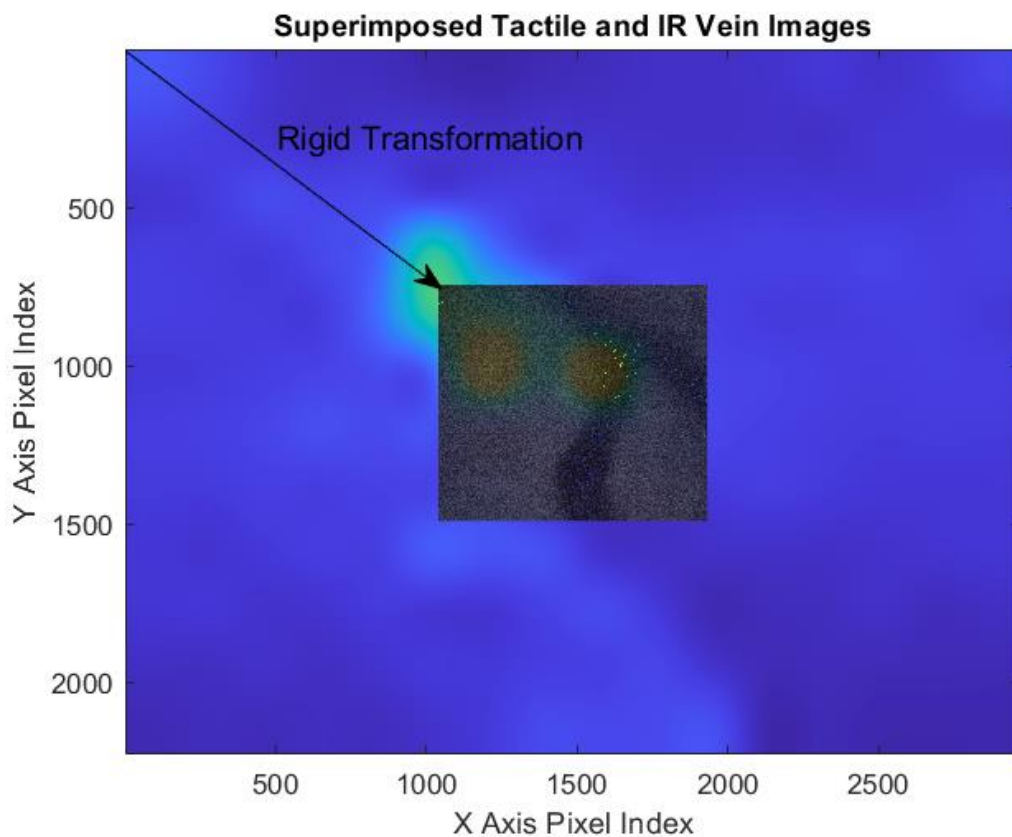


Figure 5.9 - Superimposed Tactile and IR Vein Images. The vein image is related to the tactile image using a rigid transform, known from system design. This offset includes the physical offset between the tactile array and the camera, as well as any misalignment between the two during manufacture. Transparency of the IR image is set to 0.85 for illustrative purposes.

5.4.2. Tactile Image Registration Method

A key objective of this thesis has been to register tactile images onto the vein structure of the breast, to remove subjectivity in lesion location, and allow locations to be tracked accurately over time. This can be done during one of two phases in the breast scanning process, either: concurrently with the vein image mapping, using the relationship between the tactile image and vein image to superimpose the two; or retrospectively, registering a vein image and coincident tactile image onto a pre-existing vein map. The former method is akin to the current ‘general scan’ from SureTouch™, where a scan is made of the entire breast and ‘hotspots’ are identified. The latter method is akin to the ‘detailed scan’ from SureTouch™, where an examiner would return to a ‘hotspot’ for a closer examination, in this case a high-resolution tactile image would be obtained for further analysis and diagnosis.

The homography matrix between two vein images, calculated during the vein mapping process, can be used to register tactile images by the same method. The relationship between tactile images and the vein images can be described using another transformation matrix, detailing the difference in origin position and orientation between the two media. This fixed transformation can then be applied to the existing homography matrix between the two vein images to register the tactile images onto the vein map. This process is shown illustratively in Figure 5.10, where tactile data is mosaicked using the IR vein images, filling in areas covered by the IR camera port, independent of load. This is the important technological step forward, as the tactile image correlation method (Egorov and Sarvazyan, 2008) fails when varying load reduces the ‘visibility’ of lesions.

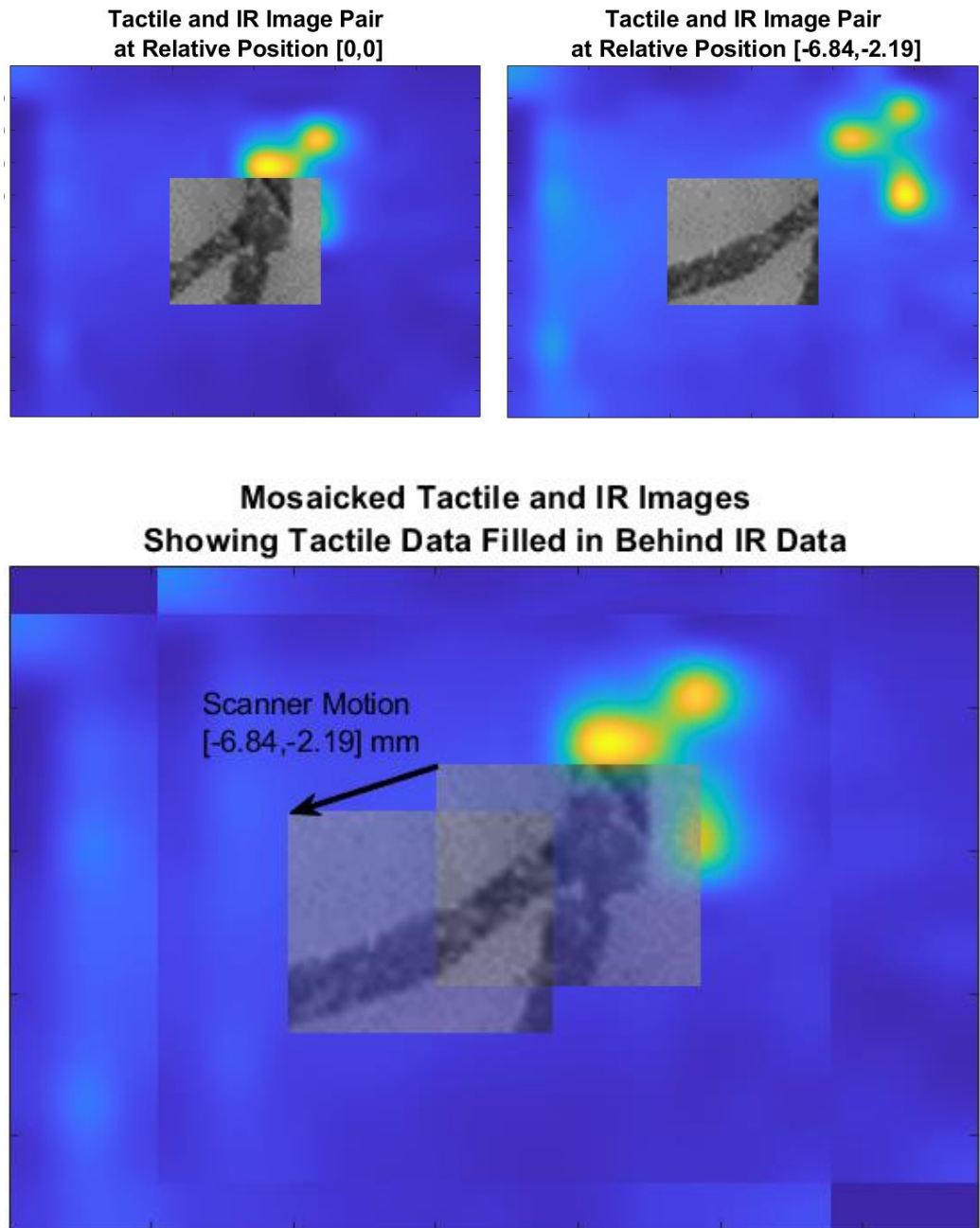


Figure 5.10 - Mosaicked Tactile Data using IR Vein Images on silicone phantoms. The IR vein images are used to track the motion between frames, which is independent of load, and the tactile images are referenced onto the IR image mosaic. This allows for tactile data from the IR camera port to be filled in.

In order to mosaic the tactile images in a coherent and meaningful manner, overlapping images taken at different loads must be normalised to a common background level. This is akin to the IR vein image rectification from Chapter 4, where the images are rectified to their equivalent unloaded state. Tactile images cannot be normalised to their unloaded state, as the content of tactile images depends on load, and so they are rectified to the background elasticity surface at the location of the tactile image using background subtraction. Background subtraction reduces the baseline of the tactile images to a common value, typically zero, by fitting a second order surface to the tactile array data and then subtracting this surface from the tactile image. This method does not reduce the measured relative stress of an embedded lesion, and is the standard method in the literature and commercial implementations (Egorov and Sarvazyan, 2008).

The background imaging process is further improved for the purpose of elasticity imaging, as opposed to tactile imaging, by adding the interpolated elasticity surface, generated by dynamic material property estimation, to the mosaicked, background subtracted, tactile data. This results in a coherent tactile mosaic, overlaid on an embedded vein structure, with its local baseline set to the background elasticity of the underlying tissue at a given location. Although the addition of the background elasticity is not important for a simple search for embedded objects, it will be very important for the determination of embedded object properties and later classification of lesions (Egorov et al., 2009) (Oleksyuk et al., 2016).

5.4.3. Deviation in Project Hardware

The extreme cost and commercial investment required to modify the SureTouch™ pressure sensor array to accommodate the imaging system, specifically rearranging the electrical connections around the camera hole, necessitates the use of a simpler sensor array as a proof of concept before modifications will be made by commercial partners. The change in hardware does not make any difference to the image registration algorithm as the image registration is performed using the vein images, rather than the tactile images.

The prototype system will be validated, in terms of its ability to register a tactile image onto a body structure, using a PN5420 strip sensor (Pressure Profile Systems, US). This is a 1x12 element array covering a 5mm x 80mm area, with elements of 5mm x 6.7mm sampled at 100 Hz. This is secured to the scanner using 3M 300LSE tape. This is a large reduction in resolution from the SureTouch™ array, which will inhibit further analysis of the tactile images after registration, however this will be suitable for proving that tactile images can be registered using vein imaging. The change in physical size of the sensors used in the prototype, shown in Figure 5.11, means that the scan speed must be controlled to ensure tactile image overlap between acquired frames. The integrated prototype output image is shown in Figure 5.12 which illustrates the rigid transform between the tactile images and the IR images. Note that the rigid transform describing the relationship between the IR camera images and the tactile array will be different for different hardware. Similarly, the required scaling to make the TI pixel size match the IR image pixel size will change proportionally to the change in element size.

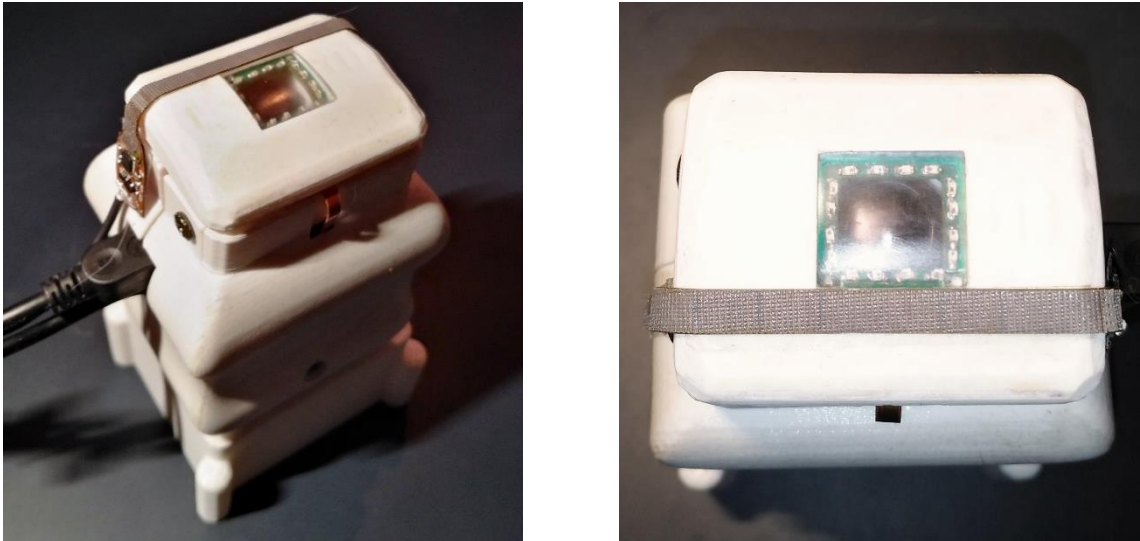


Figure 5.11 - Positioning of PN5420 Tactile Array. The Tactile strip is secured to the long axis of the contact plate, adjacent and parallel to the view port. The sensor electronics are secured to the rear with adhesives for strain relief. The unused portion of the sensor array is folded on the opposite side of the scanner and secured with adhesive.

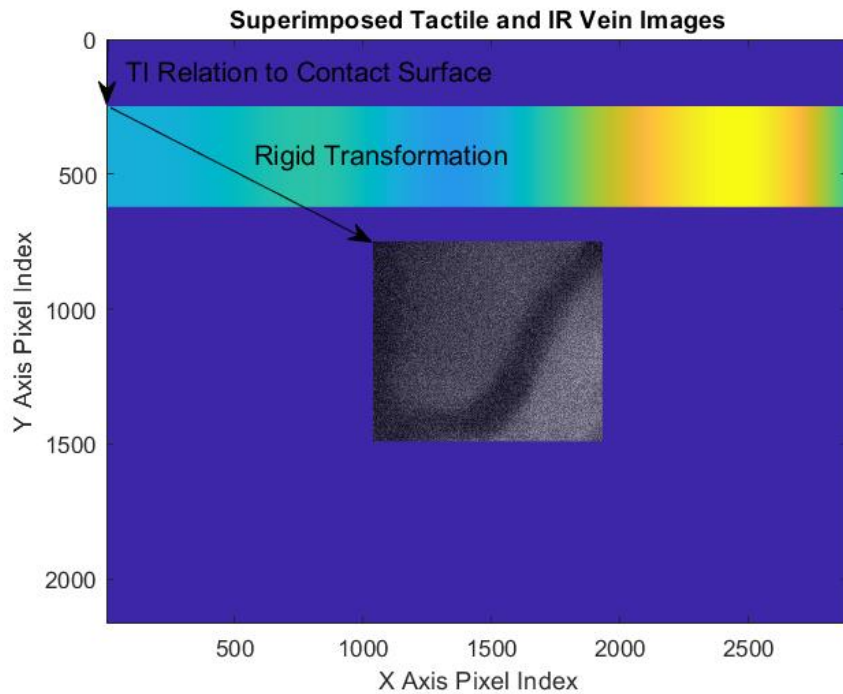


Figure 5.12 - Superimposed Tactile and IR Vein Images. The vein image is related to the tactile image using a rigid transform, known from system design. The rescaling is similar in process to that shown in Figure 5.9.

The PN5420 sensor strip does not have square elements and so the scaling of the tactile image, in terms of the pixel scale, is not uniform in order to match the scale of the IR images. This scaling follows the same basic process from Figure 5.8, except a separate factor is applied to the x and y dimensions respectively. This factor is 556.5 and 371 for the x and y axes respectively, fixing the pixel scale at 74.2 pixels/mm to match the IR vein images.

The PN5420 is a 1 x 12 element array, however only 6 are utilised for the system, fitting well into the contact surface as shown in Figure 5.11. The remaining sensor elements are folded gently out of the way and secured with adhesive tape. Similarly, the integrated electronics for the array is folded and secured to the rear of the scanner with adhesive tape. The sensor array is not configured for OEM applications, and so additional interface electronics are required to read data out to a USB terminal. The additional system components are shown in Figure 5.13. The integrated array electronics are connected to a D710 Bluetooth DAQ (Pressure Profile Systems Inc., US-CA), which communicates wirelessly with a Parani® SD1000U USB Bluetooth adapter (Sena Technologies Inc., US). Data is recorded by PPS Chameleon DAQ software and exported as a .csv file for analysis and post processing in MATLAB.

Data from the multiple sensor systems in use within this prototype scanner are synchronised using a brief compression event, that allows for a common point to be identified in the tactile data, the camera data, and the load/orientation sensors. In future clinical implementation, all sensor media would be handled by a single controller and so would be automatically and implicitly synchronised.

Comparing Figure 5.12 with Figure 5.9, clearly the use of the strip sensor will have a detrimental effect on the quality of the tactile mosaic in terms of spatial resolution and coverage, however this is simply a demonstration that tactile images can be registered to non-rigid structures. The information available from the tactile mosaic will be better realised with the 2D array. Postproduction interpolation of the tactile mosaic can assist in filling in minor holes in coverage, but as stated previously, project limitations stop the use of ideal components for further analysis of the tactile data.

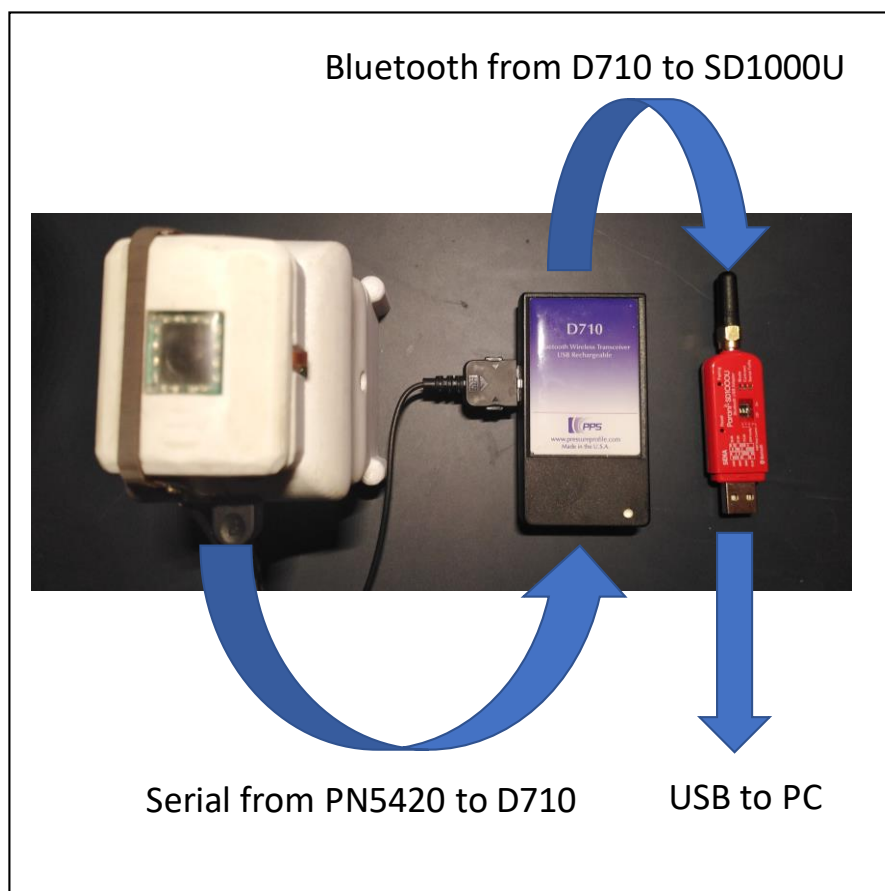


Figure 5.13 - Implementation of PN5420 in the Prototype Scanner. The PN5420 array is connected to the D710 Bluetooth module, which powers the sensors. This communicates wirelessly to the Bluetooth adapter, relaying the data to a PC. The rest of the system, shown in Figure 5.3, is unaffected by this additional technology.

5.4.4. Registered Tactile Images using Proposed Prototype

Verifying and demonstrating that the proposed system is capable of registering tactile images is done by scanning the test phantom described in Chapter 4. As it is not possible to register 1D tactile images without an external translation estimator, registration is purely from the IR image mosaicking as previously described. A typical scan pattern is shown in Figure 5.14, which clearly shows that the sequence of tactile images have been spatially related and registered onto the underlying vein structure. It is similarly clear that the spatial relations and post processing steps allow observation of complex lesion shapes representative of their true form, allowing lesions to be observed when they are not visible in the IR images. The tactile element size limits the resolution in the x dimension however the proposed system function is compellingly demonstrated with elasticity measurement and lesion contour corresponding well to reality.

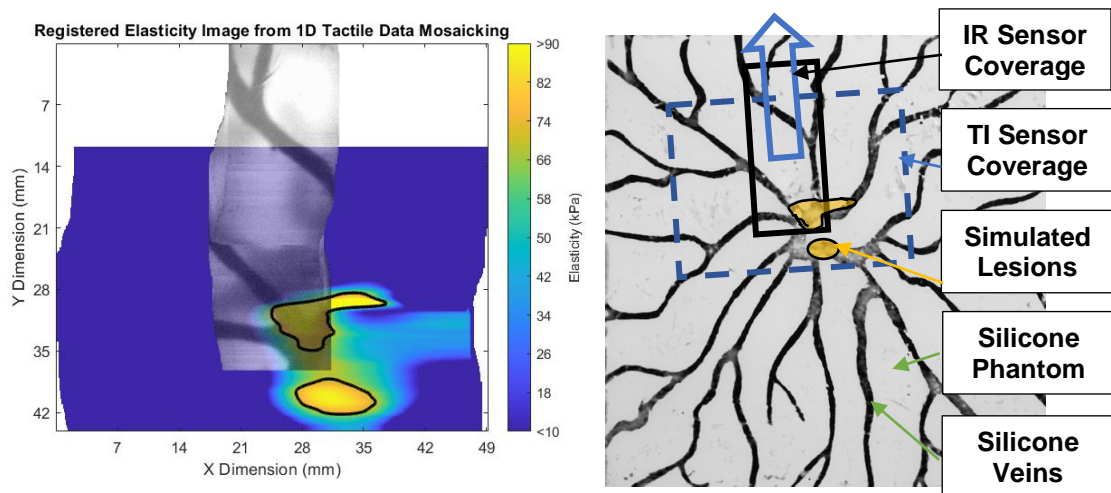


Figure 5.14 - Registered Tactile Images from Prototype System. Left) 1D tactile images mosaicked using IR vein images to form compound 2D tactile images. Filtration and background subtraction allows for complex geometry to be viewed. Right) Diagram of the test phantom used for context, with sensor coverage and true lesion areas shown.

Figure 5.14 showed that the proposed system and image registration method is effective at spatially relating tactile images, particularly as the tactile correlation technique proposed in early literature is not possible in this 1D case (Egorov and Sarvazyan, 2008). The scan was performed at a typical scan load of 1.5kgf (14.5N), with tilt controlled within $\pm 5^\circ$ at a scan rate of approximately 0.02m/s. The probe is covered in a disposable sheath and lubricated with 3-IN-ONE® multipurpose oil (WD-40 Co. Ltd., UK) to reduce shear stress. In a general use case, the limited coverage area of the IR camera is of little consequence, as the mosaicked tactile image with a large coverage area is what is really used for basic medical decision making. Although it is useful to have a fully populated vein map for the purpose of locating detailed scans in future, this will require many passes with the probe in order to get sufficient overlap. For the 130x130mm area discussed here, a total of 10 back and forth passes are required to fully populate the area with vein images, but only 3 are needed to fully populate the area with tactile images with 50% overlap to increase the apparent resolution.

The tactile array used here is not ideal, the large element size reduces the resolution, and the array protrusion reduces the validity of pressure measurements such that detailed material analysis cannot be done on this tactile mosaic without additional work. The result presented here can be compared to Figure 5.10, where the larger array is used to give higher resolution results, allowing extrapolation of how well the system will work when implemented with high quality, purpose designed, components. This serves as a proof of concept for the generation of new commercial and clinical prototypes, the registration accuracy of which shall be investigated in the next sections.

5.5. Test Strategy and Methodology

The developed prototype developed and demonstrated in this chapter is intended as a practical solution to elasticity mapping, and so comprehensive testing is required to complement the initial validations previously presented. Testing is constrained to silicone phantoms with a range of realistic properties to act as proof-of-concept in order to build commercial support for future technological developments. It is not feasible to test every condition and use case, due to material and control limitations however, testing encompasses a representative range of scan motions observed in clinical TI in terms of scan speeds, applied load, and tilt angles.

In this testing the ability of the prototype to measure background tissue elasticity and construct IR vein maps, in terms of positional accuracy, shall be determined against variations in both background elasticity and vein density on silicone phantoms in order to estimate the expected system efficacy in future clinical trials. Additional testing on the image matching accuracy vs. the applied load and tilt angle shall prove that the image deformation reduction function developed in Chapter 4 is effective for tactile mapping. The tactile mapping accuracy of the developed prototype is coupled to that of the IR mapping accuracy, and so the developed prototype shall be tested without the affixed tactile array. This is not an ideal state of affairs and is necessitated by limitations imposed on this project, particularly in terms of available materials, however from the testing presented here and the tactile map formed in Section 5.4 the system is suitably compelling and rigorously tested within scope to make fully integrated testing unnecessary for this proof-of-concept prototype.

5.5.1. Test Materials

The phantom materials used for this testing are similar to those used in the validation tests of Chapter 4, in that they are made from layered silicone with an embedded IR visible vein pattern. For the purpose of parametric testing, 3 values of background elasticity with 3 values of vein density each have been made to represent the breadth of real-world conditions.

The phantoms used in this testing are made from multiple layers of Ecoflex™, 000-35, 00-10, and 00-30 rated Polydimethylsiloxane (PDMS) two part elastomer (Smooth-on, Inc., US-PA), as shown in Figure 5.15, with an A:B mixture ratio, additive thinning agent Silicone Thinner™, and pigment Silc-Pig™ (Smooth-on, Inc., US-PA) for each material layer given in Table 5.1. The silicone elastomer samples were cast sequentially into uniform rectangular slabs with dimensions given in Table 5.1. The total dimensions of the sample material are 130mm x 130mm x 20mm. The material has a phantom vein structure, made from silicone mixed with carbon dust, to provide representative features for the SIFT algorithm to track in the IR spectrum. The use of Silc-Pig™ PMS488C light skin pigment on the skin layer is to obscure the vein structure partially and increase the realism of the whole system in the visible spectrum.

The silicone elastomer was mixed according to the manufacturer recommendation, with vacuum degassing before and after pouring into the mould. Layer C was cast first, with the vein layer cast separately into another similar mould, so as to better facilitate the cutting of the vein structures. The cut vein layer was then layered over the set layer C, still in its mould, to form layer B₁. More of the layer C material,

minus the thinner but including pigments, was then poured over the existing layers filling in the voids in layer B₁ and bringing the overall thickness to the desired level, forming layers B₂ and A. Although the manufacturer recommends baking the set elastomers at a low temperature to fully cure them, this was not done in this case as doing so increases the elasticity of the samples. The long-term stability of the prepared phantoms is reduced as a result; however, the samples are calibrated before testing.

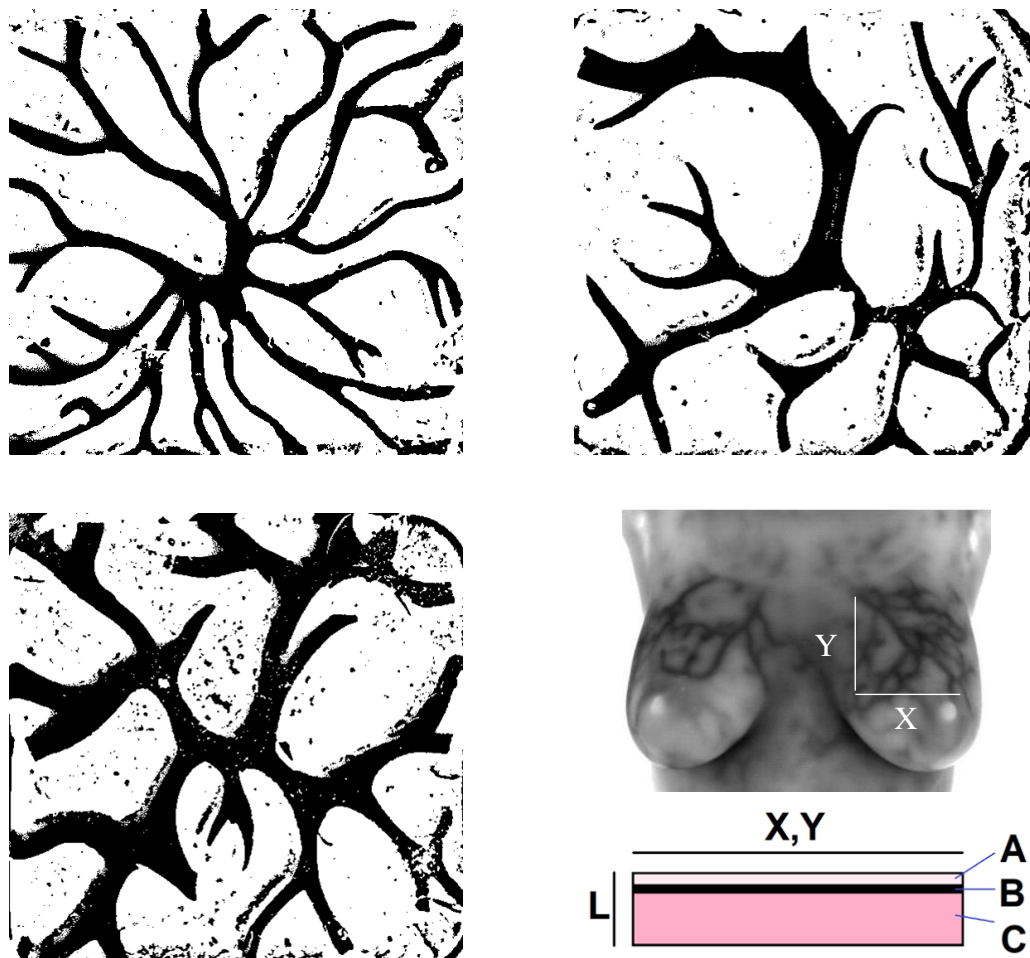


Figure 5.15 - Silicone phantom material construction. Top Left) Thin veins with high feature density. Top Right) Medium veins with medium feature density. Bottom Left) Thick veins with low feature density. Bottom Right) Phantom layer material stack-up and representative breast vein image (adapted from Pacific Chiropractic and Research Centre – Breast Thermography)

Table 5.1 - Material compositions for silicone phantom testing. The vein layer (B) comprises of two separate materials. B₁ is the vein pattern itself, with the voids filled in with the skin material (A), designated as B₂. Sample numbers of 1-3, etc. represent the 3 different vein layer structures denoted in Figure . Lengths X and Y are 130mm.

MATERIAL COMPOSITIONS FOR PARAMETRIC TESTING OF PROPOSED PROTOTYPE ON SILICONE PHANTOMS					
Sample Number	Sample Layer	Material A:B Ratio	Thinner By Mass	Additives By Mass	Thickness (mm)
1-3	A	000-35 1:1	+0%	PMS488C +1%	4
	B ₁	00-10 1:3	+20%	Carbon Dust 1:100	2
	B ₂	000-35 1:1	+0%	PMS488C +1%	2
	C	000-35 1:1	+10%	None	14
4-6	A	00-10 1:1	+0%	PMS488C +1%	4
	B ₁	00-10 1:3	+20%	Carbon Dust 1:100	2
	B ₂	00-10 1:1	+0%	PMS488C +1%	2
	C	00-10 1:1	+10%	None	14
7-9	A	00-30 1:1	+10%	PMS488C +1%	4
	B ₁	00-10 1:3	+20%	Carbon Dust 1:100	2
	B ₂	00-30 1:1	+0%	PMS488C +1%	2
	C	00-30 1:1	+10%	None	14

5.5.2. Test Strategy and Validation

The aim of this limited testing is to provide a proof-of-concept and build commercial confidence slowly, in order to secure additional invaluable commercial support in the form of custom tactile arrays for integration into the developed prototype in future works. Without the support of commercial entities to handle the reliable implementation of tactile sensors, TI cannot develop far beyond its state from the 1990's.

Testing of the prototype is performed in 3 key stages, each building confidence and understanding on the previous stages. Firstly, the performance in term of image feature matching is tested against variation in load and tilt angle, with correlation between SIFT matches and load/tilt angle being shown. This will prove whether the image deformation reduction technique presented in Chapter 4, is effective compared to a test using SIFT alone. This is done using an axial compression of the test materials, with no lateral translation, varying the load and probe angle continuously.

Secondly, the performance in terms of positional accuracy of the reconstructed probe path is tested against the applied load and tilt angle, with correlation between relative position error between frames and the applied load/tilt angle being shown. This will show how effective the whole system is at registering images when the probe is moving in a natural manner. This is done using a scan of phantom 5 (medium veins, medium elasticity) for illustrative purposes, with an oscillating probe pattern. The positional reference comes from a VICON photogrammetry tracking system as used in previous literature for this task (Rana et al., 2020) which has approximately 0.5mm positioning accuracy (Summan, 2015).

Thirdly, the overall effectiveness of the system in registration of images and background elasticity estimation respectively is determined vs. the elasticity and vein density of the test material. This is required as the changing elasticity alters the total vein structure deformation in response to an applied load, and the changing vein density alters the number of available image features. The testing for image registration is done by scanning each of the 9 samples in a representative manner and measuring the difference in end locations of the probe compared with a VICON reference measurement. This will show the effectiveness of the prototype system in registering images and measuring background elasticity over a simulated range of realistic conditions prior to further development and clinical testing outside the scope of this work. The testing for the elasticity measurement is done by taking multiple compressive readings with the proposed prototype in the centre of each of the 9 samples and comparing them with a reference measurement from an Instron® 3342 universal testing machine (Instron Engineering Corp., UK) which has a stated accuracy of 0.5% and compresses the sample using the same sensor cap indenter as the handheld camera-based system.

5.5.3. Test Controls

The testing detailed above has certain control variables that are recorded for repeatability and representative comparison between tests. For the purposes of this thesis, all testing in this chapter is performed at $22 \pm 1^\circ\text{C}$, humidity is not recorded although is implicitly controlled by the constant temperature. Humidity is known to affect tactile sensors; however, it is a constant effect like temperature that can be calibrated out and is not expected to change during the course of the testing. Calibration for all test cases is

performed for accurate steady state response at 22°C, with the normalisation routine detailed in Section 5.3 performed before each scan to account for any unexpected drift, from creep, hysteresis, or temperature change between scans of the test materials.

Testing of the image matching and probe tracking vs load and tilt angle has additional controls, particularly: the applied load range was restricted to a range of 0-15N, and the tilt angle restricted to $\pm 20^\circ$ in order to protect the sensor and probe assembly for future testing. Testing of the system ability to measure background elasticity has a controlled load range of 0-15N with angle control within $\pm 5^\circ$. Testing of the system ability to register images, in the general case, has a controlled load of 10 ± 2 N, with tilt angle controlled at $\pm 5^\circ$. These controls are not expected to negatively affect the conclusion of the tests, as clinical use of TI is typically in this range.

5.5.4. Testing Limitations

All testing has limitations in one form or another, and it is important to establish both the cause of a limitation and its expected effect on results when considering the efficacy of any system for a particular task. There are several important limitations to the scope of the testing of the prototype system that must be considered when drawing conclusions. The first is that the tactile array is not used for the tests. This is a result of the desired tactile array, the SureTouch™ array, not being available for implementation, however the accuracy is not related to the tactile array in use and so this will not affect the end result but must be considered when discussing the system ability to register tactile images. As the tactile array used in the prototype is not optimal, further testing with the reduced array described in Section 5.4 is not appropriate and so the tactile

mosaicking results from Section 5.4 must be considered along with the accuracy presented by this testing when determining the effectiveness of the system.

Secondly, testing is performed at a single nominal temperature of 22°C. This is due to the need to calibrate the elasticity of the test materials at each temperature of interest. This is of particular difficulty as the temperature cannot be controlled at values other than the ambient background when in the Instron® testing machine, and the uncertainty in the elasticity change with temperature will be unacceptable when assessing the elasticity measurement accuracy at anything other than the calibration temperature. Due to an appropriate sensor error model, which will be developed in Chapter 6, this limitation is not expected to affect the results, however a limitation it remains as it cannot be reliably tested with the resources available.

Finally, the testing is performed on flat silicone samples. This is a limitation in 2 regards: the creation and calibration of 3D silicone breast phantoms was impractical and out of scope for this project, and the novel nature of the technology and logistical difficulties during the project inhibited clinical testing on truly realistic materials. This limitation is common practice in the literature, particularly for early stages of technological development (Wellman, 1999) (Ayyildiz, 2011) (Oleksyuk et al., 2015) (Rana et al., 2020). This limitation does affect the conclusion, as the validity of the system is not tested on realistically shaped 3D samples, however it is common practice to begin with a flat system as a proof of concept before developing onto more complex samples and testing and so this testing scope is not considered problematic.

5.6. Imaging Matching Vs. Load and Tilt Angle

Following calibration of the prototype as described in Appendix B, and subsequent normalisation, each sample phantom was compressively imaged axially with the control measures stated previously remaining centred in a consistent position. The scan of each sample was lubricated using 3-IN-ONE® multipurpose oil (WD-40 Co. Ltd., UK) and assisted using a SureTouch™ disposable sheath to reduce friction. Both materials are transparent, and do not affect the captured images.

Knowing that the proposed image mosaicking algorithm is effective in forming representative images (Rana et al., 2020), the sensitivities to operational parameters will be focussed on here. A typical response is shown in Figure 5.16, showing the correlation between the number of matching SIFT features between concentric images in a scan as a function of applied load and tilt angle for SIFT and the proposed algorithm respectively. For the SIFT implementation, there is high sensitivity to applied load and tilt angle, which is significantly reduced using the proposed algorithm. The sensitivity is expected, as increased load reduces the overlap between adjacent images and increasing tilt increases the affine distortion which SIFT struggles to deal with. The proposed algorithm still exhibits sensitivity to applied load, expected due to the reduction in image overlap, however this is smaller than that for SIFT alone due to the algorithm being unaffected by slight focal changes under load. Generalising the testing to observe the response over multiple samples, the first order surface fits are normalised and combined to form an average sensitivity response as shown in Figure 5.17 which accounts for base differences in sample feature density.

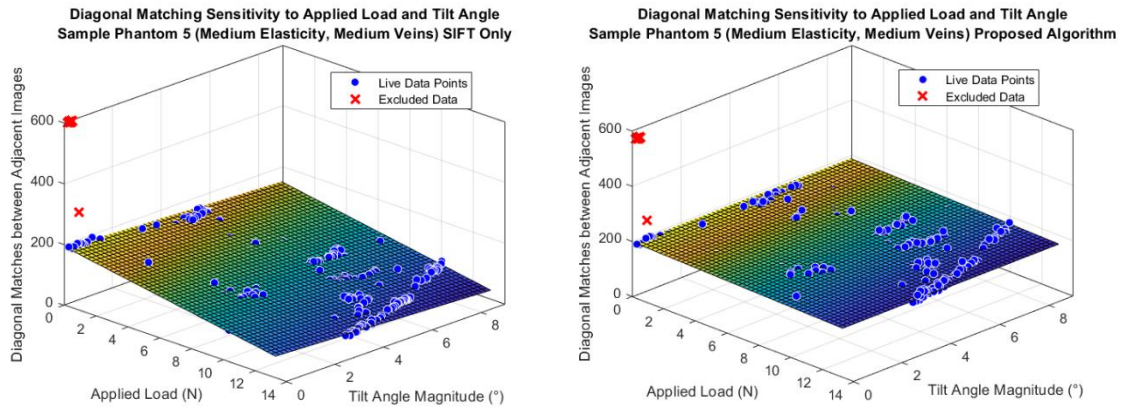
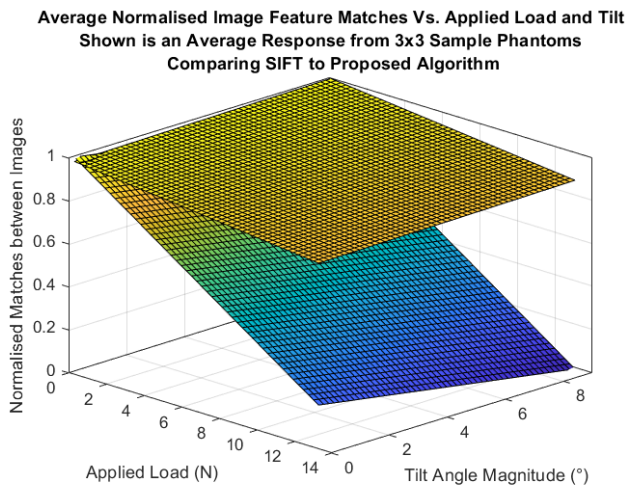


Figure 5.16 - Image Matching Vs. Load and Tilt Angle using SIFT (Left) and the proposed algorithm (Right). The sensitivity of image matching to load and tilt angle can be expressed by a 1st order surface with $R^2=0.93$ and $R^2 = 0.30$ respectively. Excluded data is from when the probe was stationary, where high matching is naturally expected. This illustrates the effectiveness of the proposed algorithm in reducing sensitivity to load and tilt.



AVERAGE SURFACE FIT PARAMETERS AND 95% CONFIDENCE INTERVAL			
PARAMETER	P00	P10	P01
SURFACE			
PROPOSED	0.9862	-0.009782	0.001734
	±0.022	±0.0018	±0.0041
SIFT	1.017	-0.06218	-0.02285
	±0.034	±0.0021	±0.0045

Figure 5.17 - Normalised Feature Matching Vs. Applied Load and Tilt Angle. Normalisation is used to account for variation in typical image matching between the 9 samples as a result of differing feature geometry, allowing an average response to be computed. The ‘flat’ surface (proposed algorithm) shows little sensitivity to load, or tilt, compared with SIFT alone. Error in surface fit is indicated in the inset table.

Normalisation of the sample scans, consisting of 220 to 373 images each, is done by scaling the largest range from the SIFT/Proposed Algorithm matched features from 0 to 1, and applying the same transfer function to the smaller of the ranges. Normalised results for each sample are then averaged, producing the resultant representative surface fits shown in Figure 5.17Figure , denoted by Equation 5.4 where P is a fit paramter, F is the applied force, and ψ is the tilt (elevation) angle magnitude in spherical coordinates.

$$z = P_{00} + P_{10}F + P_{01}\psi \quad (5.4)$$

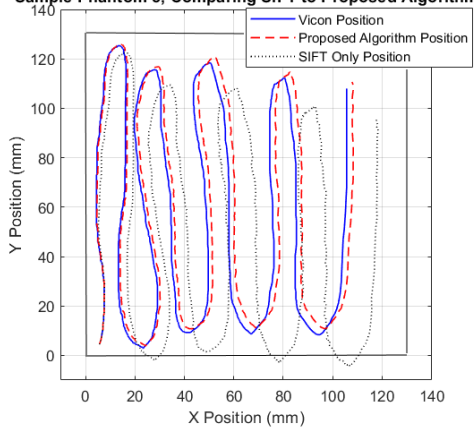
The testing for image feature matching sensitivity shows that the performance of SIFT reduces with both applied load and tilt angle as expected, and while sensitivity still remains in the proposed algorithm the sensitivity magnitude to load and tilt is typically reduced by a factor of 6.36 and 13.18 respectively when processed in parallel on the same data. Additionally, the 95% confidence intervals from the sensitivity surface fit shows reduced variability in sensitivities between samples for the proposed algorithm compared with SIFT, although this reduction is small. The sensitivity variation between samples, indicated by the surface fit 95% confidence interval, is a result of the physical differences between the samples and is entirely expected. The results of this testing shows that the proposed physics based image rectification algorithm is effective in increasing the number of SIFT feature matches between adjacent images when compared with SIFT alone, building upon earlier works to the same effect (Rana et al., 2020). The number of features is correlated with the registration accuracy (Nuari et al., 2019) and so this positive result leads into further testing of probe tracking accuracy.

5.7. Probe Tracking Vs. Load and Tilt Angle

Following initial calibration of the prototype as described in Appendix B, and subsequent normalisation, each sample phantom was scanned in full with the control measures stated previously. The scan of each sample was lubricated as previously specified and conducted at an average stroke speed of 0.03m/s in line with typical TI clinical use. A typical representative position estimation response is shown in Figure 5.18, showing the position estimates generated by the proposed algorithm and by SIFT compared with a reference measurement from the Vicon system. It should be noted that although the results of the proposed algorithm shown are typical of wider testing, the results for SIFT alone are not, as SIFT can often produce unreliable results or none at high loads and tilt angles. Due to this, the SIFT results are illustrative of a ‘best case’ scenario, and so will not be considered in further testing.

Error in odometry systems are typically cumulative over time, and the proposed system is no different as shown in Figure 5.18. Over a typical simple scan pattern, scanning backwards and forwards over the sample surface, small errors in image matching and translations add up. This usually means that the overall position error increases, however it is possible for the total error to reduce should the image matching underestimate the translation between images after consistently overestimating. The total error is a function of time, however the rate of error accumulation is a function of the applied load and tilt angle as shown in Figure 5.19, which makes sense from Figure 5.18. It is also clear that the proposed algorithm is a significant improvement over SIFT, although this comes as no surprise from earlier testing and research (Rana et al., 2020).

**Position Estimation Using Prototype System Vs. Reference
Sample Phantom 5, Comparing SIFT to Proposed Algorithm**



**Total Position Errors During Scan of Sample Phantom 5
Shown with Applied Load and Tilt Angle**

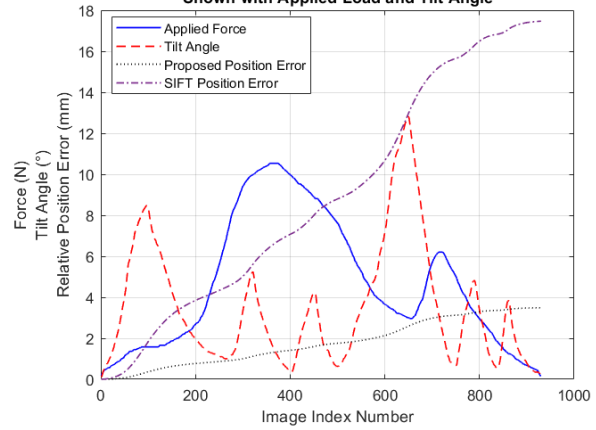


Figure 5.18 – Typical sample scan position estimation. Left) Position estimation of SIFT and proposed algorithm compared with Vicor reference. The scan passes do not overlap, but this is not of relevance. Right) Error accumulation over scan duration, shown with applied load and tilt. Clearly the error is linked with the load/tilt variation over the scan.

**Position Error Accumulation Sensitivity to Applied Load and Tilt Angle
Sample Phantom 5 Comparing SIFT to Proposed Algorithm**

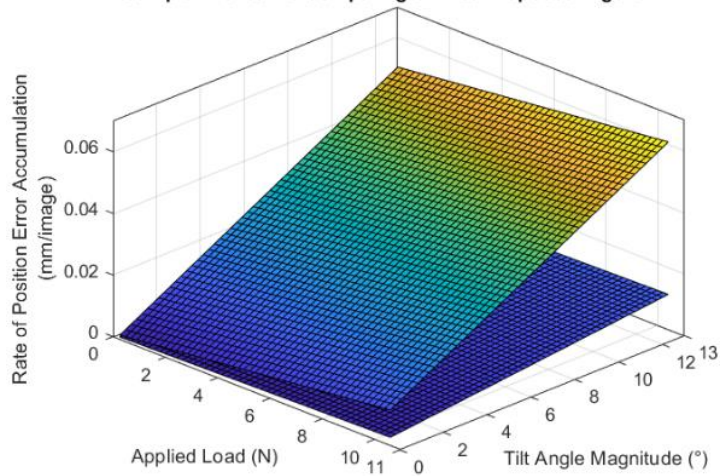


Figure 5.19 – Rate of error accumulation sensitivity to load and tilt angle. The results are for the same scan detailed in Figure 5.18. The sensitivity to tilt angle is greater than for applied load, with SIFT sensitivity (the steeper surface) being significantly larger than the proposed algorithm as expected from SIFT failing under high tilts.

The typical result shown here aligns favourably with testing performed by other researchers (Rana et al., 2020), with the critical difference being that the rate of error accumulation is highly variable in this testing whereas earlier research showed a relatively linear increase in error as a result of the constant controlled scan load and tilt used in that initial research. The mean loads were similar, allowing for comparison, although caution must be exercised when drawing detailed conclusions as only orders of magnitude can be compared with confidence due to experimental differences.

It is convenient to use an error ratio metric when evaluating the position accuracy, which describes the total position error as a percentage of the total distance travelled. For this scan, a value of 0.34% is obtained, which is favourable compared with testing of the larger and higher resolution system from Chapter 4 with had 0.29% over a total path distance of 1.6m. This suggests that the reduction in camera size not affected the accuracy significantly, and the accuracy is improved compared with existing registration methods with error ratios typically >1.2% (Rana et al., 2020) as shown in Table 5.2.

Table 5.2 – Comparison of positioning error obtained on a single scan of similar phantom materials with different technologies and algorithms. Testing of three additional methods was performed by Dr. Rana (Rana et al., 2020), with implementations unavailable for testing on current prototypes.

COMPARISON OF POSITIONING ERROR TO EXISTING METHODS AND PROTOTYPES						
System Metric	Chapter 5 Prototype Proposed	Chapter 5 Prototype SIFT	Chapter 4 Prototype Proposed	SFM CH4 Prototype	FEM CH4 Prototype	NRSEFM CH4 Prototype
ERROR RATIO (%)	0.337	1.686	0.296	1.833	1.496	1.221
RMS ERROR (mm)	2.091	10.467	2.261	15.263	11.821	12.360

Generalising the testing to observe the response over multiple samples with similar loading regimes, the first order surface fits are normalised and combined to form an average sensitivity response as shown in Figure 5.20. The fit surface parameters are noted, and defined in Equation 5.4. As this testing focusses on the changes in rate of error accumulation, rather than total error, there is little variation between samples as indicated by the narrow 95% confidence intervals on the fit surfaces. Compared with SIFT alone, the proposed algorithm offers a typical improvement in sensitivity to load and tilt angle by a factor of 4.99 and 5.01 respectively. The results of this testing shows that the proposed algorithm is effective in decreasing the rate of position error accumulation when compared with SIFT alone and existing methods in the literature, building upon and expanding earlier works to the same effect (Rana et al., 2020). This is a positive result that leads into testing of total error in a general use case.

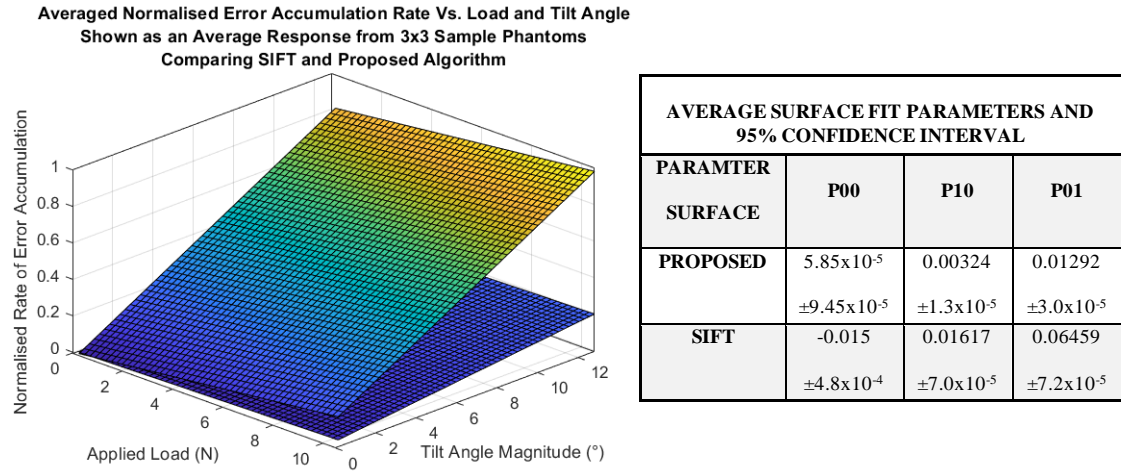


Figure 5.20 - Normalised Error Rate Vs. Applied Load and Tilt Angle. Normalisation is used to account for any variation in typical base error between the 9 samples as a result of differing feature geometry, allowing an average response to be computed. The 'flat' surface (proposed algorithm) shows little sensitivity to load, and tilt, compared with SIFT alone. Error in surface fit is indicated in the inset table.

5.8. Performance Vs. Elasticity Vs. Feature Density

5.8.1. Elasticity Measurement

Compressing the centre of each sample in turn through a load range of 0-15N yields elasticity estimates using the method described in Chapter 4 section 4.2.3, that is compared with a reference measurement from an Instron® 3342 universal testing machine. The testing involves 5 compressions using the proposed system on each sample, with each compression consisting of > 100 images over the specified load range. These values are then compared against the mean of 4 reference measurements for each sample. The results of parametric testing across the 3 hardness classes and 3 vein structure classes are shown in Figure 5.21. The first order surface fit to the results describes the elasticity absolute error, as a percentage of the reference elasticity measurement, as a function of the feature density and reference elasticity. The surface fit is defined in Equation 5.5, where P is a fit parameter, E_0 is the reference elasticity in kPa, and n is the feature density class.

$$z = P_{00} + P_{10}E_0 + P_{01}n, \quad n = [1,2,3] \quad (5.5)$$

The results, summarised in Table 5.3, show typical elasticity absolute errors of $2.36\% \pm 0.93\%$ with worst case error < 4.5% over an elasticity range of 9kPa – 60kPa with insignificant sensitivity to both feature density and elasticity. There is no observed correlation between either variable and the total spread of elasticity estimates for a given sample. This shows that the system is effective over the range of test materials.

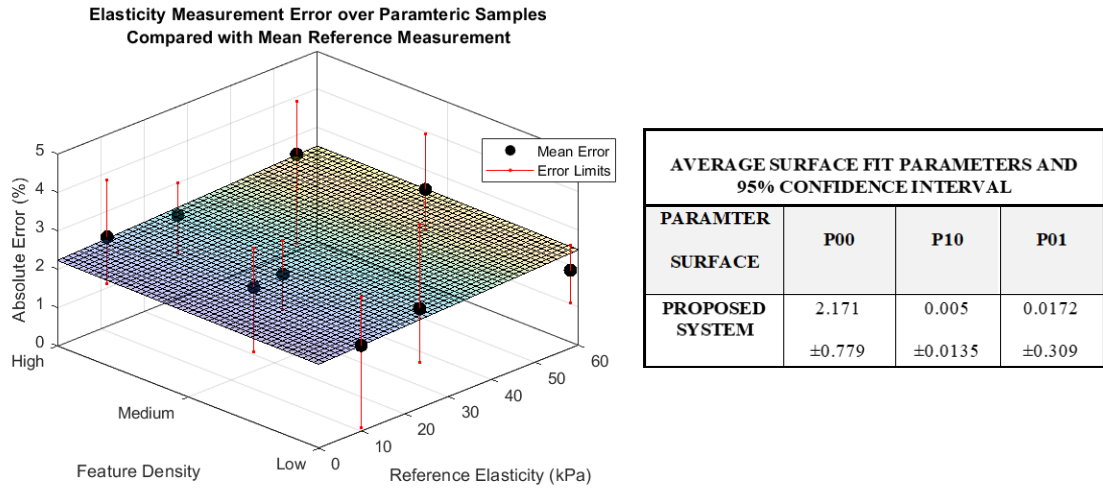


Figure 5.21 - Elasticity measurement error sensitivity to sample parameters. The results show little sensitivity to feature density and true elasticity as indicated in the inset table. The total spread for an individual sample varies, but the mean absolute error is relatively constant, with $R^2 = 0.12$.

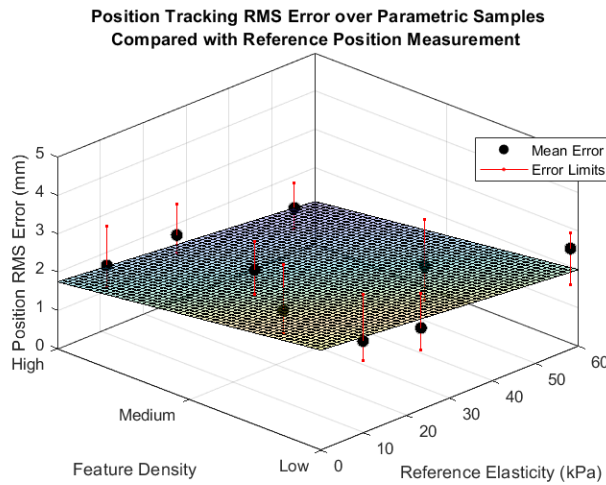
Table 5.3 – Proposed system elasticity measurement results. The results of repeated reference measurements are shown to complement Figure 5.21. The minor natural variation in elasticity for each of the hardness classes gives additional coverage over the total range. Error values show max/min of testing results range.

ELASTICITY MEASUREMENT RESULTS FOR PROPOSED SYSTEM ON PARAMETRIC SAMPLES COMPARED WITH REFERENCE MEASUREMENTS						
SAMPLE FEATURE DENSITY PARAMETER	SAMPLE ELASTICITY PARAMETER					
	SOFT		MEDIUM		HARD	
	Measured (kPa)	Reference (kPa)	Measured (kPa)	Reference (kPa)	Measured (kPa)	Reference (kPa)
LOW	10.0	9.8	22.7	23.3	56.9	58.1
	+0.12	+0.2	+0.33	+0.2	+0.49	+0.1
	-0.21	-0.1	-0.51	-0.2	-0.38	-0.4
MEDIUM	15.5	15.2	22.4	21.9	56.4	54.8
	+0.15	+0.1	+0.19	+0.1	+0.79	+0.2
	-0.26	-0.1	-0.20	-0.2	-0.58	-0.1
HIGH	11.2	11.5	27.2	27.8	56.6	55.2
	+0.14	+0.2	+0.27	+0.3	+0.76	+0.2
	-0.17	-0.1	-0.23	-0.1	-1.27	-0.3

5.8.2. Probe Position Tracking

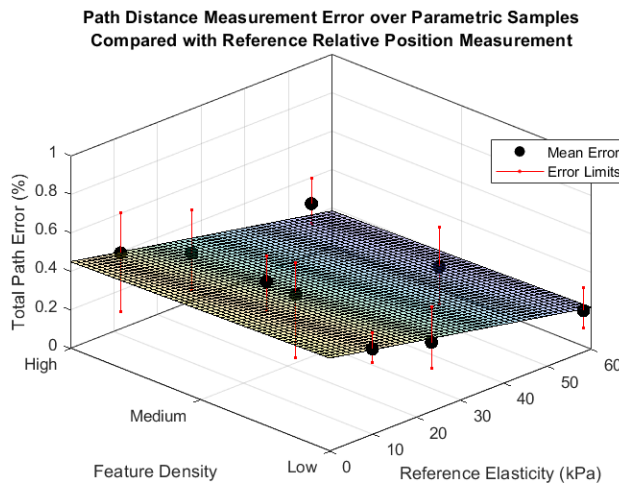
Performing repeated representative scan patterns over the 9 phantom samples, lubricated and with load/tilt controls of $10\pm 2\text{N}$ and $0\pm 5^\circ$ allows the probe position estimation accuracy to be determined. The results of 5 repeated overlapping scans with a total path length $> 1200\text{mm}$ (> 10 passes) are shown in Figure 5.22. where the RMS position error describes the conservative typical absolute differences between the estimated probe position and the corresponding coincident reference measurement from the VICON. The results clearly show that over the range of materials tested, the typical position error is within 2mm of the reference with a standard deviation of 0.86mm across all results. This means that over the $120\times 120\text{mm}$ scannable area, the device is typically accurate to 2mm when compared with the 0.5mm accurate VICON reference. The 1st order surface fit to the data indicates slight sensitivity to both elasticity and feature density, with the RMS error typically decreasing for increasing material elasticity and feature densities. The surface fit is defined in Equation 5.5, with fit parameters detailed in Figure 5.22.

The typical RMS error result of 2mm is a good result as accuracy is within 1 SureTouch™ array sensor element which gives this number some context. In terms of path reconstruction, the absolute path length error is another measure of the displacement measurement accuracy focussing in 1D which allows for conceptualisation of image registration accuracy in a typical scan pass. The results from the previous tests are shown using this metric in Figure 5.23. In this situation, the total path length error can be used as a measure of the registration accuracy of one image to another.



AVERAGE SURFACE FIT PARAMETERS AND 95% CONFIDENCE INTERVAL			
PARAMETER	P00	P10	P01
SURFACE			
PROPOSED SYSTEM	3.05 ±1.347	-0.01 ±0.0234	-0.437 ±0.533

Figure 5.22 - Position tracking RMS error sensitivity to sample parameters. The results show sensitivity to feature density and true elasticity, as indicated in the inset table. The results show that as feature density and elasticity increase, the position error reduces with $R^2 = 0.47$.



AVERAGE SURFACE FIT PARAMETERS AND 95% CONFIDENCE INTERVAL			
PARAMETER	P00	P10	P01
SURFACE			
PROPOSED SYSTEM	0.499 ±0.1348	-0.0044 ±0.0023	-0.0165 ±0.0534

Figure 5.23 - Path distance measurement sensitivity to sample parameters. The results show limited sensitivity to feature density, with larger sensitivity to elasticity as indicated in the inset table. The total path error decreases as feature density and elasticity increase, with $R^2 = 0.78$.

The results from analysis of path error shows that the path reconstruction error is typically $< 0.5\%$, over path lengths in the range of 1.2-1.8m (10-15 passes over the material). The results show a mean path error of 0.33% with a standard deviation of 0.17% when compared with the VICON reference measurement. The worst case observed error was 0.62% , which is an excellent result compared with expected performance from similar image registration methods that had errors $> 1\%$ (Rana et al., 2020). The results show similar sensitivity to elasticity and feature density as the RMS error, in that the path error decreases as material elasticity and feature density increases. The relative sensitivities to these parameters are different from the RMS position error plot, with the RMS error having greater sensitivity to feature density than to elasticity, and the path error having greater sensitivity to elasticity than to feature density. The sensitivities cannot be compared quantitatively as they are measures of different physical concepts, but it is important to note that the sensitivities to both feature density and elasticity are small for either metric making deviations in error caused by sensitivity to these parameters small in comparison to their mean value.

In summary, considering the surface fit extents as an approximation of the continuous variation in probe performance over the test parameters, the proposed system has a typical RMS position error of $1.8\text{mm} \pm 0.65\text{mm}$ over the range of 45 tests, and a typical image registration accuracy of $0.33\% \pm 0.15\%$ over the same test sets. This shows that the system is capable of stable operation over the range of simulated breast tissues, with positioning errors within the size of a SureTouch™ tactile element. This is a positive result that demonstrates the system accuracy and practicality in use.

5.9. Discussion

The results show that the proposed system is effective in measuring both the background elasticity of the sample and in registering IR vein images as detailed in the previous testing section. This effectiveness was indicated in initial validation testing of the core method in Chapter 4, but was comprehensively tested once integrated into a practical footprint. The minimal change in error between the proposed methods implemented on the Chapter 4 prototype and that implemented on the current prototype, highlighted in Table 5.2, shows that the performance has not been significantly impacted by the miniaturisation of the system components.

The background elasticity measurement accuracy of the system is high and is in line with other compression based, static desktop, soft tissue elastometers (Egorov et al., 2008) across the range of available test materials. The very low sensitivity to both the elasticity and feature density of the sample materials shows that a relatively flat response is expected over the continuous parameter space. The test materials were made to span the largest range of normal breast tissues (Wellman et al., 1999a), with sufficient spacing to support parametric testing. The choice of purely silicone phantoms for this testing was appropriate as the tissue mimicking viscous properties of other materials such as agar (Manickam et al., 2014) were not required for the static mechanical tests, and the long shelf life of silicone phantoms was considered practically important for testing (Cao et al., 2013). Due to material calibration constraints the materials could not be tested with the probe immediately after calibration, however the low variability in reference measurements for a given sample indicates that this is not a problem.

The positioning error presented here, although small, is slightly exaggerated by minor differences in motion detected by the VICON and true motion of the probe w.r.t. the material surface. The reference measurement is an absolute measurement in 3D space, whereas the probe position is relative to the material upper surface. Adhesion between the test material and the probe will cause motion observed by the VICON to not be visible by the probe to the same extent, with subsequent slippage being seen by the probe but not by the VICON. The phantom test materials are large in comparison to their thickness and well lubricated so the effect of this will be small, however this limitation tends to lead to an overestimation of the positioning errors. This is a better result, as it means the performance witnessed in this testing is an upper bound on the positioning error. The probe path error is a better metric to look at in this case, as the direction of the slip/adhesion does not affect the total path length as it does the 2D position estimation. The results shown for both cases are positive, with the positioning error and path error being within one tactile element of the intended SureTouch™ array, meaning the tactile registration error will not be detrimental to current screening TI.

The positive IR image registration results coupled with the tactile array registration demonstration in Figure 5.14 proves that tactile frames can be mosaicked using IR vein images to form comprehensive tactile maps of tissues. When tactile map pixel averaging is used, the effect of the minor registration errors on tactile images will be reduced when adjacent scan passes overlap. It is known that further accuracy improvements can be achieved using bundle adjustment (Triggs et al., 2000), but is not necessary due to the small scan area and relatively high base registration accuracy.

5.10. Conclusion to Prototype System Development

5.10.1. Developed Prototype System Practicality

The developed system, being a handheld device, is inherently more practical than any static piece of equipment. Considering the impracticality of the handheld system from Chapter 3, this does not necessarily mean the system is truly practical just because it is handheld, but in this case it is. The system is easily scanned across the phantom surface with the help of lubrication, as is the case in current TI. The system presented here has the same tissue scanning process, other than the additional calibration step for the MARG sensor, as SureTouch™ which is known for ease of use.

The proposed system does not use external components such as reference position trackers, other than a PC/Laptop, which makes the system a great improvement over previous tactile mapping works that required such devices (Wellman, 1999). Additionally, the proposed system does not rely on features on the tactile image to mosaic the tactile frames, and so the ability to track motion is independent of the applied load which controls visible tactile features. This makes this work a significant improvement in practicality over previous works that used tactile image correlation (Egorov and Sarvazyan, 2008) as the proposed system works with no tactile features.

5.10.2. Suitability for Purpose and Engineering Limitations

The purpose of this prototype was to demonstrate that tactile mapping is feasible using tactile image mosaicking, to provide a stable platform for future embedded lesion analysis and clinical testing. The proposed prototype has met this objective as

demonstrated throughout this chapter and in doing so has met another major project objective in measuring the background elasticity of a soft material. The limited integration with a tactile array has shown that the proposed system can display elasticity differences over a material referenced to the underlying patient specific vein structure in simulated phantoms. These outputs: background elasticity, large scale tactile images, and tissue differentiation; meet the project objectives in providing a practical proof-of-concept prototype that can easily be developed further into an integrated system for clinical testing. The system developed and tested in this chapter will allow future works to focus on tissue differentiation and clinical validation, as measuring background elasticity and forming repeatable tactile maps is critical to accurate measurements of embedded objects from surface compressions (Sarvazyan and Egorov, 2009).

As the 1x6 tactile array used is not optimal, and was not designed for this type of application, further analysis of the tactile maps for the purpose of accurate embedded lesion measurements was not feasible in this project. The prototype has been properly demonstrated, with descriptions of how the system would operate using the SureTouch™ array, and so it can be safely stated that the proposed prototype is suitable for its purpose. In the current implementation, tactile image mosaicking was not possible in real-time due to tactile, camera, and auxiliary data not being able to be combined into a single data stream, and the subsequent need for a data synchronisation event. This does not affect the outcome of the system in any way, and it is well known that image processing of this type can be performed in real-time (Summan et al., 2018), so the

system is suitable for its purpose and can deliver tactile maps quickly with future commercial dedicated sensor integration.

5.10.3. Summary and Next Steps

This chapter has presented a novel handheld tactile mapping and elasticity measurement system with registration errors of $0.33\% \pm 0.17\%$ and elasticity measurement errors of $2.36\% \pm 0.93\%$ validated over a wide range of simulated breast phantoms. This work has built upon previously published works (Rana et al., 2020) and work from Chapter 4 of this thesis, and represents a significant improvement over earlier works in this field in terms of practicality and accessibility in a clinical setting (Wellman, 1999) (Egorov and Sarvazyan, 2008).

The potential impact of the proposed system is maximised by developing the system within the confines of a commercial TI system, allowing the developments presented here to be easily adopted in industry. Similarly, the tiered proof-of-concept style testing of the core methods and integrated system provides confidence and detail on system functionality, adding to the impact as less effort is required by other researchers or developers to further this work. The scope of this work has been limited by material availability and so its clinical impact cannot be fully assessed. From the research presented in Chapter 2 the key metrics for cancer differentiation have been delivered and so a resulting improvement in diagnostic and differential accuracy is expected when the system is combined with existing tactile analysis methods (Egorov et al., 2009). In the mean-time, this chapter has shown that the proposed system is effective

in tactile mapping in its own right and demonstrates functionality that can be applied into other applications of TI and further afield.

The next steps, generally, for this research is further component integration and implementation with the SureTouch™ tactile array, and subsequent evaluation of absolute elasticity measurements of embedded lesions. This is out of scope for this thesis due to material availability and so a different trajectory towards the same goal shall be taken. In order to perform accurate measurements of embedded lesions, on a fully integrated system, there must be confidence in the pressure readings from the tactile array. To achieve this, the error sources applicable to TI must be analysed, particularly when use conditions differ between phantom and clinical trials. Error sources such as temperature sensitivity, amongst others, are known to affect the response of other medical imaging technologies (Mulvana et al., 2011) and so it is reasonable to suggest that they will affect performance in TI. As there is a lack of error modelling, or references to the same, in the medical TI literature the next step of this project is to investigate and document applicable error sources, and implement suitable methods to mitigate them in a practical use case. This shall be done in Chapter 6.

The outcome of this analysis will further the commercial impact of this thesis, as the error sources and mitigation strategies can be directly implemented into current clinical TI. This will provide a stable TI platform allowing for future analysis of compound tactile images, for the purpose of detailed lesion characterisation, following further commercial system implementation of the proof-of-concept prototype demonstrated in this thesis.

Chapter 6

Tactile Sensor Error Modelling

6.1. Introduction

This chapter explores the analysis, mitigation, and effect of TI sensor error sources affecting practical reliability of clinical TI. Following project limitations on further clinical testing of the prototype system from Chapter 5, this chapter aims to improve the practical reliability of the sensor system itself, addressing key gaps in the literature whilst solving a practical problem limiting future development of clinical TI.

The chapter begins with a review of the relevant literature and illustration of the dominant error sources affecting capacitive tactile sensors. Each error source is then addressed individually and the effect of each on the output of a tactile breast image is shown on phantom tissue. The error effect is modelled and measured for a commercially available TI system, leading onto the development of a simple error correction model.

The error correction model is validated parametrically and is shown to be effective in controlling sensor error over a wide range of realistic operating parameters expected to be generally applicable in future clinical testing. This will be able to control the variability of TI in the literature in future clinical tests beyond the scope of this thesis.

6.2. Tactile Sensor Error Analysis and Modelling

This thesis has focused thus far on practical tactile image registration and background elasticity estimation, towards the goal of accurate diagnosis and reporting of breast conditions. This functionality was demonstrated and tested in Chapter 5. The next stage of the tactile imaging tissue characterisation process, the estimation of embedded lesion elasticity, requires both a good estimation of the background elasticity (Egorov and Sarvazyan, 2008), and either a representative measurement of the differential stress between the background and the lesion (Egorov et al., 2009) or an estimation of the lesion deformation (Oleksyuk et al., 2016). Although several methods of measuring embedded lesion elasticity using tactile imaging have been presented in the literature, with each one being effective in their own right, they have all lacked an acknowledgement of tactile imaging error sources and subsequent implementation of a suitable reverse error model to keep the results valid over a range of practical use cases.

The analysis of the accuracy of the tactile sensors, particularly the creep and temperature sensitivity, is critical to the goal of measuring the absolute elasticity of an embedded lesion in situ from a differential stress image with a background elasticity estimate. The lack of an appropriate error model, or acknowledgement of practical error sources in the literature relating to clinical TI, limits the usefulness of existing systems and their impact in future clinical development. Although a change in sensor properties is not likely to affect a system simply searching for where ‘something’ is in the breast or not, when it comes to making definitive measurements of the lesion properties in terms of size and elasticity, the accuracy of the sensors over a range of practical use conditions

must be investigated to provide confidence in any decisions made. This analysis and development shall be performed in this chapter, following an introduction on significant sensor and environmental error sources in tactile imaging.

The analysis and testing performed in this chapter focusses on the SureTouch™ tactile array, with measurements being valid for that type of sensor system, however the applicable error sources are common to all capacitive tactile sensors to varying degrees. This means that the importance of detailing the error sources, defining their causes, and developing mitigation strategies, is not limited to the current breast cancer imaging topic. The error sources presented here affect all medical tactile applications, with magnitudes dependent on the particular sensor system and architecture used, and so careful analysis of sensor error must be performed in each application using realistic operating conditions and system use cases in order to ensure proper accuracy. This type of analysis is common in other advanced medical imaging techniques such as ultrasound (Liao et al., 2015) (Mulvana et al., 2011) as well as in general tactile sensing (Sánchez-Durán et al., 2015), so it is important to understand these errors to improve general TI reliability.

6.3. Tactile Imaging Sensor Error Sensitivities

The basic parallel plate capacitor force/pressure sensor description, given in the project introduction, although true, is a great over-simplification of a complicated system prone to error from a wide pool of sources including but not limited to the list below. The majority of these effects are governed by the electrical and mechanical properties of the dielectric material, although the plate assembly does factor into the analysis. A diagrammatic illustration of these effects is shown as referenced, where the effect is exaggerated for illustrative purposes:

- Thermal Baseline sensitivity (Figure 6.1)
- Thermal Scale Factor (sensitivity) sensitivity (Figure 6.1)
- Viscoelastic Creep (Figure 6.2)
- Hysteresis (Figure 6.3)
- Cross Coupling between adjacent sensor array elements (Figure 6.4)
- Dielectric changes under load and temperature (Figure 6.1)
- Manufacturing changes to dielectric material (Figure 6.5)
- Manufacturing errors in plate/electrode alignment (Figure 6.6)

Depending on how the plate capacitance is measured, they can also be affected by dielectric charge leakage, capacitive fringing, and the equivalent series resistance (ESR) of the sensor to varying degrees of severity. Many of these effects should come as no surprise, as they are common to all force sensors (Kalinin, 2014) (Jewell Instruments LLC., 2020), or are prevalent in traditional capacitors.

Consider the general equation for a capacitive plate force sensor, recalled in Equation 6.1, calculating the capacitance of a parallel plate capacitor in response to an applied load. In this case: C is capacitance, ϵ_0 is the permittivity of free space, ϵ_R is the relative permittivity of the dielectric, d_0 is the initial plate separation, F is the applied force, A is the plate area, and E is the elasticity of the dielectric. The capacitive fringing effect is not included here, keeping the equation simple, as the size of the tactile elements in comparison to the separation makes this negligible (Chen et al., 2019).

$$C = \frac{\epsilon_0 \epsilon_R A}{d_0 \left(1 - \frac{(F/A)}{E}\right)} \quad (6.1)$$

The most variable, and thus greatest source of error, term in this expression is d_0 . As a capacitive force sensor is fundamentally a displacement sensor, with the displacement related to the applied load, the plate separation and change thereof has a large effect on the capacitance. The majority of the listed error sources affect d_0 in some way, with thermal expansion of the dielectric, hysteresis, cross coupling, and viscoelastic creep; each having significant effects. In practical calibration, the individual effects can often be inseparable and have unknown coefficients. However, the effects of some error sources such as: thermal expansion of the dielectric and electrodes, thermal softening of the dielectric, changes in dielectric constituents; can be combined into a higher-level term that is measurable and controllable, such as baseline temperature sensitivity and scale factor temperature sensitivity.

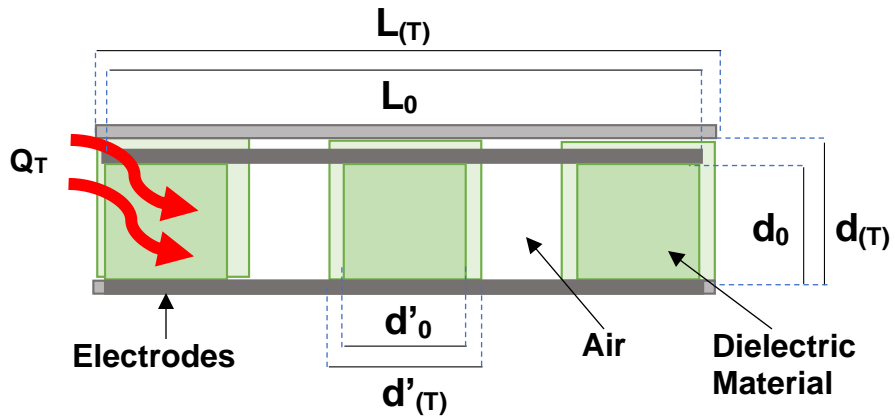


Figure 6.1 - Effect of thermal expansion on capacitive plate pressure sensors. Many materials expand when heated, but some can contract. This has the effect of varying the plate area through L , the plate separation through d , and the average dielectric constant through d' changing the ratio of material to air in vented air mixture dielectric sensors. Temperature also changes the stiffness and viscosity of the materials in the dielectric.

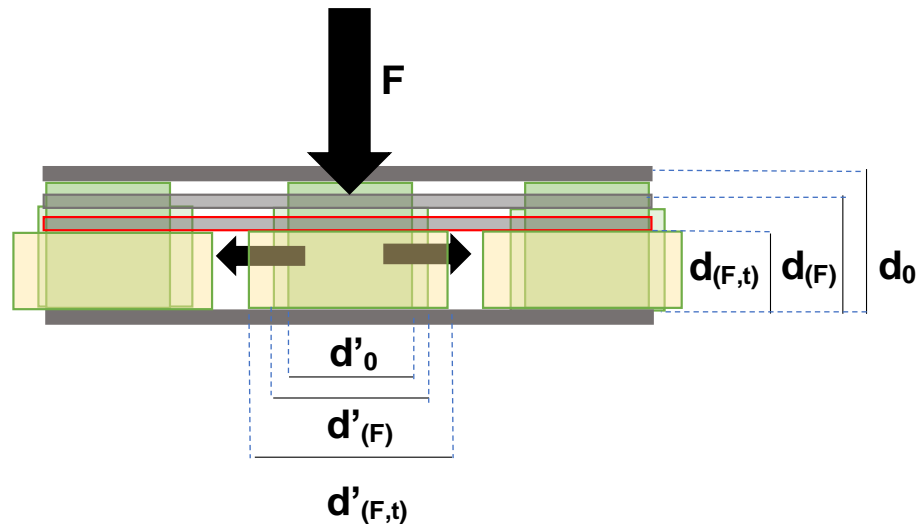


Figure 6.2 - Effect of viscoelastic creep on capacitive plate pressure sensors. The sensor will respond to an applied force as expected, but will then sink further over time with no change in load, F . This is due to the dielectric material 'flowing' viscously. When the load is removed, the sensors return to their original state viscously, with a time dependency of the plate separation d on t .

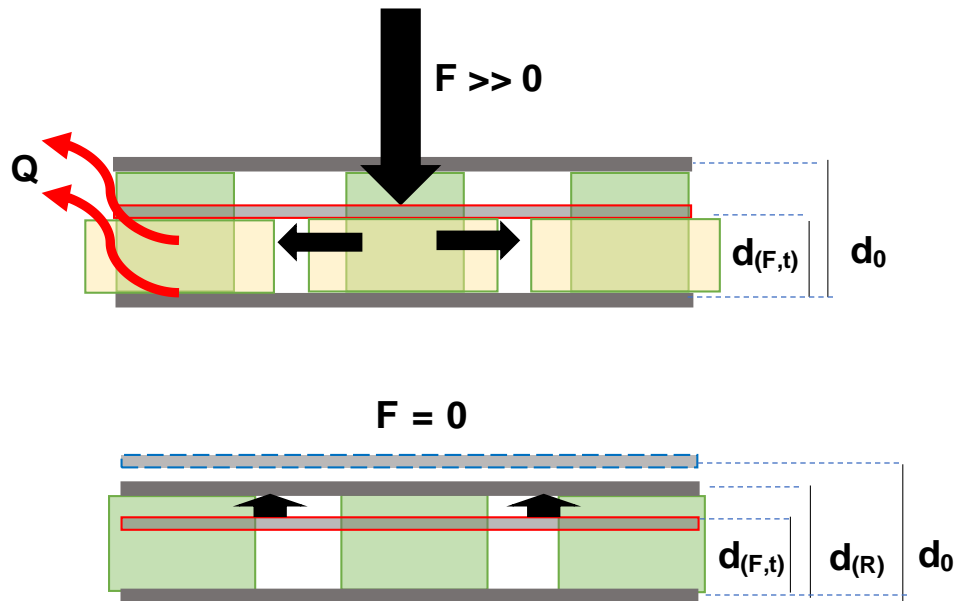


Figure 6.3 - Effect of hysteresis on capacitive plate pressure sensors. This is related to creep, in that when the material creeps there is an associated energy loss from the system as heat. This reduces the elastic potential energy in the springy dielectric and thus when the force is removed, the sensor plates do not recover to their original state.

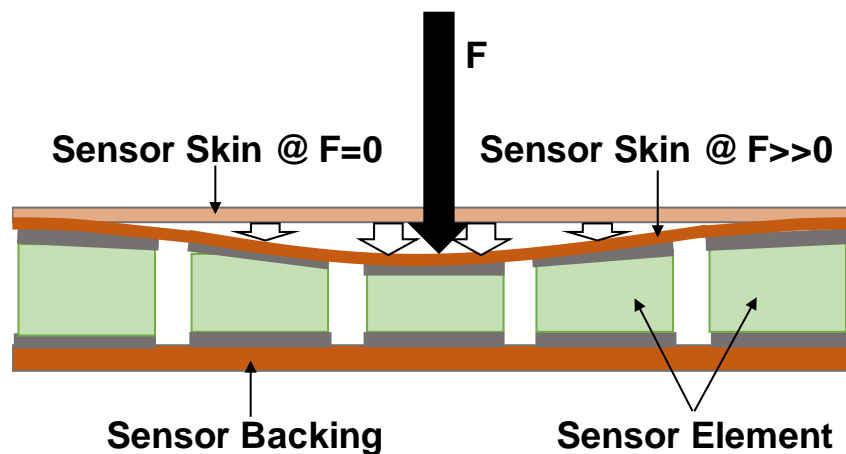


Figure 6.4 - Effect of cross coupling on capacitive pressure sensor arrays. The sensor array covering, or skin, which is required to maintain the structural integrity of the array cannot deform ideally. As the skin couples the elements together, stimulation of one element with a load will couple into adjacent elements. This is a 2D effect, for 2D arrays, although only 1D is shown in the image.

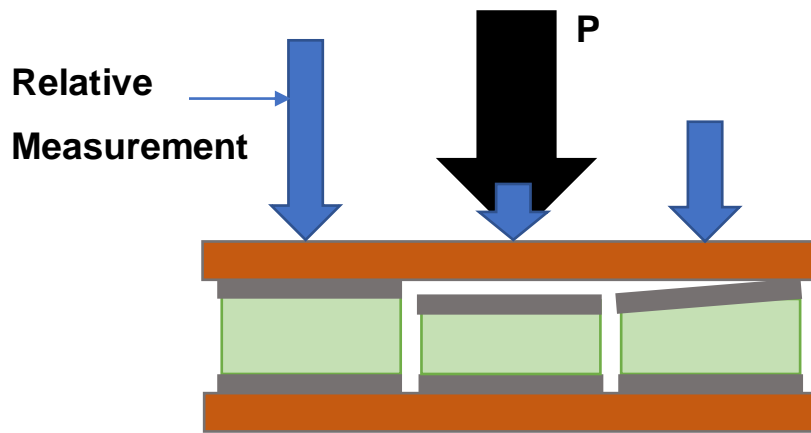


Figure 6.5 - Effect of error in the dielectric distribution on capacitive sensor arrays. Small manufacturing variations in the deposition of the dielectric material can change how each element responds to an applied pressure. This effect will be amplified by cross coupling in this example with a rigid skin. Without the skin, each sensor element receives the same pressure, but due to differences in d_0 they have different sensitivities.

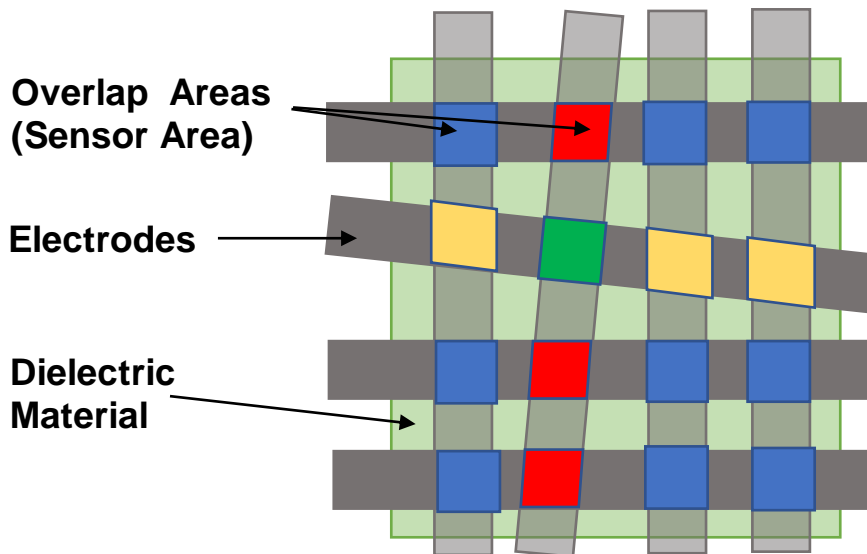


Figure 6.6 - Effect of electrode misalignment on capacitive sensor arrays. Electrode misalignment, from manufacture or wear, causes variation in the nominal value of the sensor area, A . This changes the sensitivity of the affected elements. The changing proximity of elements also changes the effect of cross coupling.

6.3.1. Thermal Analysis

The thermal expansion of the dielectric material, and electrodes affects the terms: d_0 , ϵ_R , and A . This has the effect of changing the baseline capacitance in an unloaded state, and subsequently changes the scale factor with an opposing sign. The thermal expansion expression is given in Equation 6.2 where: L is the length of a component in a particular dimension, L_0 is the length of the object at an initial temperature T_0 , T is the temperature, and K_{TE} is the coefficient of thermal expansion for the material.

$$L = L_0(1 + K_{TE}(T - T_0)) \quad (6.2)$$

For a common tactile sensor architecture with copper electrodes and a silicone bubble dielectric, which have widely spaced balls of silicone rubber with air in the remaining space, coefficients of linear expansion can be found in the literature for each material. $K_{TE(\text{Copper})} = 16.7\text{ppm}/^\circ\text{C}$ (Walt Boyes, 2010), and $K_{TE(\text{Silicone})} = 300\text{ppm}/^\circ\text{C}$ (Albright Technologies, 2020) for the purpose of this discussion. These values are variable, however it is the order of magnitude difference that is important here. From these values the expansion of the dielectric, which increases d_0 thus decreasing C , dominates the effect of the electrode expansion, increasing A thus increasing C .

The increase in d_0 and A has the net effect of lowering the zero-load capacitance offset of the sensor, which has the secondary effect of lowering the sensitivity to applied load. However this effect is countered by the thermal softening of the silicone dielectric, estimated as $K_S(\text{Silicone}) = -0.05\text{MPa}/^\circ\text{C}$ (Shin-Etsu Chemical Co, 2016), reducing the

elasticity (E) of the dielectric as shown in Equation 6.3. This results in increasing the deflection range of the sensor in response to an applied load, and thus increasing the capacitance sensitivity to applied load.

$$E = E_0 + K_S(T - T_0) \quad (6.3)$$

The effect of these temperature sensitivities combined can be modelled, using a parallel plate model based on Equation 6.1 with appropriate temperature terms substituted as shown in Figure 6.7. The values the model outputs are subject to approximation on how the sensor behaves, however the trend between temperature and baseline/sensitivity is the important output, to verify the error discussion in this section.

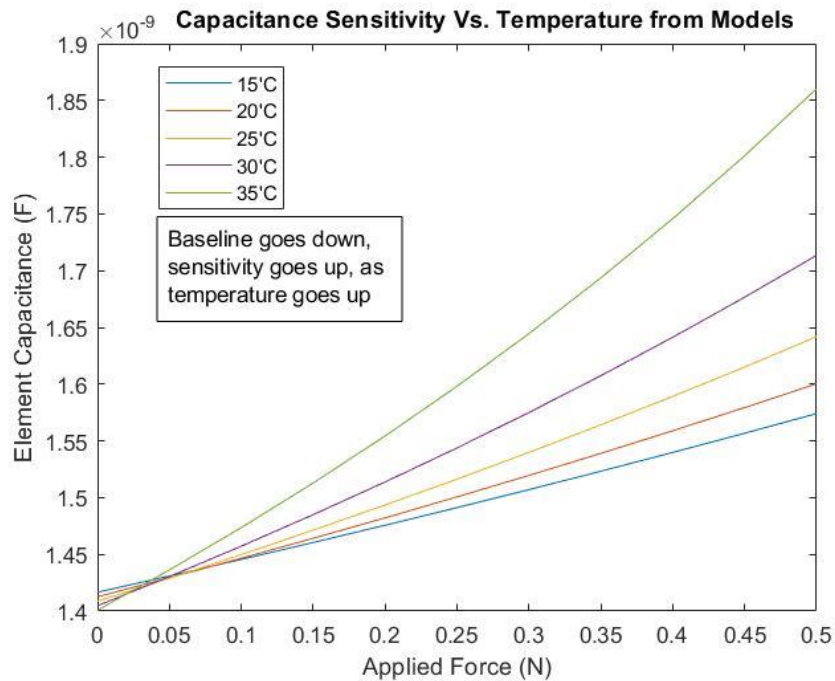


Figure 6.7 - Modelling of capacitive force sensors. The results show that the superposition of the mentioned temperature effects cause a reduction in sensor output zero offset, whilst increasing sensitivity to an applied load.

Although the values given by the model may not be totally accurate, as there are many assumptions made on the sensor architecture, the description of effects is clearly shown with increasing sensitivity and reducing offset with temperature increase. It is often inconvenient to know and calibrate these sensors at this lowest level, and so it is common to simply ignore the base physical causes and simply address the symptoms directly at the sensor output. This is particularly relevant as other sensor topologies are known to have different sensitivities, and even polarities to the sensitivity.

By applying a known pressure to the sensors, as described in Appendix C1, and calibrating the sensor to output that value at a fixed temperature, the previous physical analysis steps can be skipped. The calibration equation for simple sensors, relating a measured pressure P to a reference pressure P_0 in terms of the initial calibration sensitivity S_0 (typically 1) and temperature coefficients for offset and sensitivity respectively, is shown in Equation 6.4. The sensor output is calculated from Equation 6.5, where α and β are calibration constants for sensitivity and offset respectively, which can be verified by rearranging Equation 6.1, highlighting that these constants are based on physical parameters of the sensors. This is an automatic process handled by the PPS Chameleon™ software. With this form of calibration, it is not important to know what materials a sensor contains, it is only important to observe the sensor in operation.

$$P_0 = P(S_0(1 + K_{Sensitivity}(T - T_0)) + K_{Offset}(T - T_0)) \quad (6.4)$$

$$P = \frac{\alpha}{C} + \beta \quad (6.5)$$

Looking at the SureTouch™ tactile array specifically, the temperature coefficients, $K_{\text{Sensitivity}}$ and K_{Offset} , have been determined and are shown below in Figure 6.8. The temperature sweep used was from 18°C to 38°C, to fully encompass the range of expected operational temperatures from room temperature to above the breast temperatures (de Souza et al., 2015) (Lubkowska and Chudecka, 2021), with linear results allowing the temperature coefficients to be described as a constant for each metric. It is clear that an element-by-element calibration is required from the variation measured between elements and based on the variation between elements it is reasonable to say that each sensor array will need this analysis done in future. For this tactile array $K_{\text{Sensitivity}}$ and K_{Offset} are 0.0176 ± 0.0014 /°C and -0.0601 ± 0.0009 PSI/°C respectively.

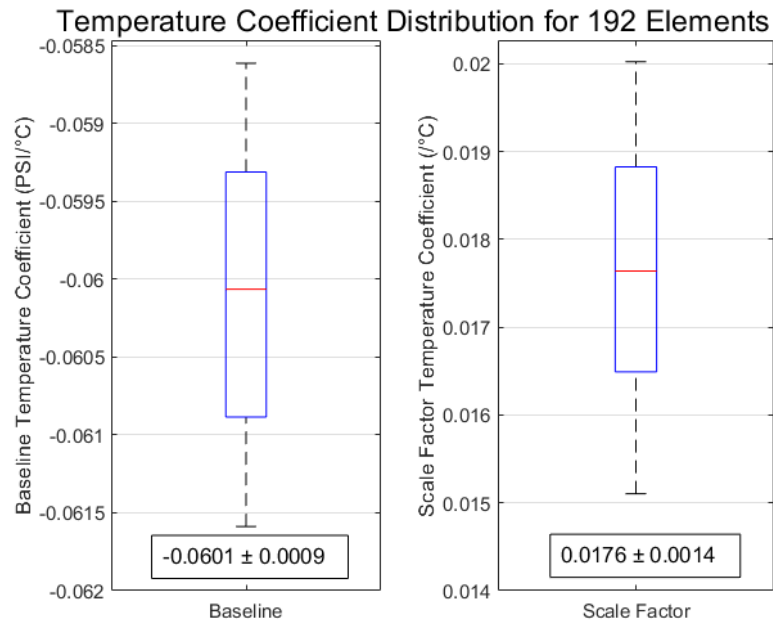


Figure 6.8 – Results of temperature sensitivity analysis. The results for each element are averaged from 3 temperature sweeps. The variation between elements is normally distributed about the mean values indicated as expected. The sensitivity of the sensors to changes in d_0 is apparent in both the baseline and scale factor temperature coefficients.

6.3.2. Effect of Thermal Sensitivity on Tactile Images

The acknowledgement and analysis of the temperature sensitivity of tactile sensors is particularly important in medical applications where the sensors are in contact with the patient. In typical phantom based validation studies, the temperature is well controlled in laboratory settings, with authors commonly stating their control temperature at either 20°C or 25°C. Live clinical testing features large temperature differences between the normalisation cycle, performed at ambient temperatures of 18°C to 25°C depending on location, and the tactile scan, performed on a patient with breast skin temperatures of typically 34°C (de Souza et al., 2015). Even with an insulating jacket or skin over the sensors to slow the temperature change, through the thermal impedance of the jacket/skin, the sensors will still exhibit a significant temperature change and subsequent error over the scan duration as illustrated in Figure 6.9. There are 2 modes of operation to consider when determining the size/hardness error from temperature change, which are: constant strain, and constant stress (Real use condition). Each of these cases has a different response and physical interpretation.

The constant strain mode is perhaps misleading and is more accurately described as a constant reference stress mode, where the measured TI array baseline shifts but the true applied stress does not. In this mode, the temperature coefficients cause a reduction in the background stress and an increase in the measured lesion stress, as described by thermal drift data in Figure 6.9. Over a temperature change between 22°C to 34°C, the prominence, or relative hardness, of the lesion has increased by 44.1% which is interpreted as an increase in the severity of the lesion and the background estimate has

reduced. Interestingly the measured size of the lesion is unchanged in this mode, due to the ratiometric method of calculating lesion diameter (Egorov and Sarvazyan, 2008) being unaffected by the change in baseline, and linear scaling of the tactile image.

In this situation the lesion prominence and measured diameter are used to visualise the effect of the error under test as they have low sensitivity to scan procedure differences in comparison to other lesion parameters such as mobility and elasticity. This means that they can be used to easily visualise the effect of the error sources, without significant variability from other factors during measurement.

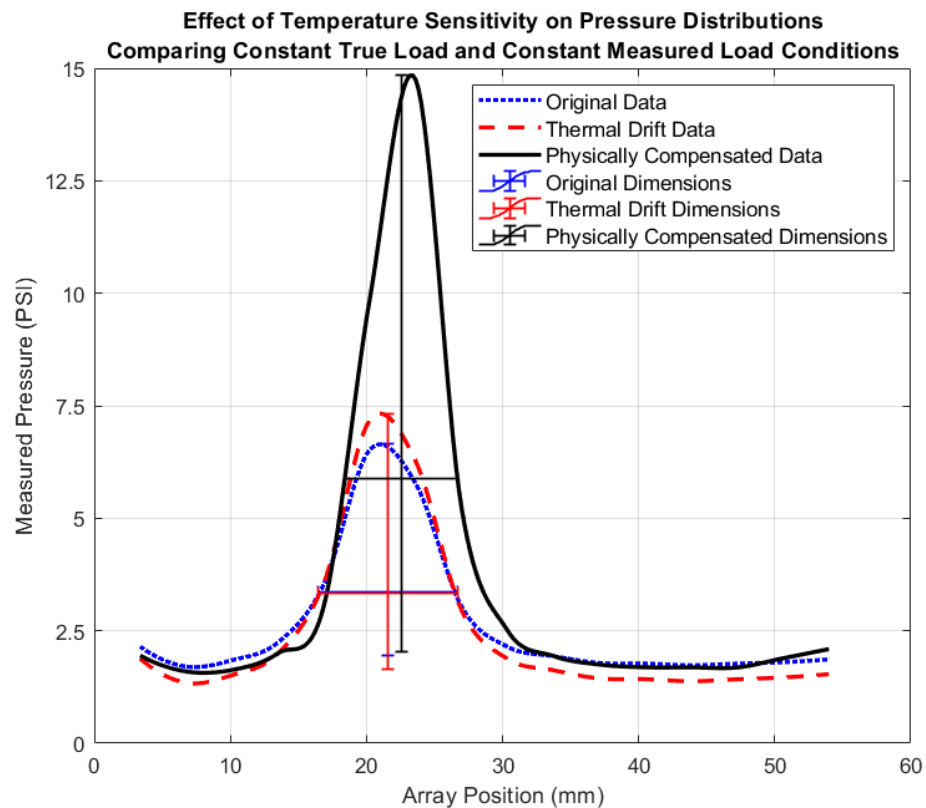


Figure 6.9 - Effect of temperature on tactile pressure distributions of a 10mm phantom lesion. The temperature sensitivity causes an increase in lesion severity and reduction in measured background pressure, this precipitates a servo-controlled increase in true load to maintain this value which increases the severity of the lesion again.

The compressions at differing temperatures were made into equivalent systems, with a ‘stiff’ 10mm ball bearing ($E > 500$ kPa) embedded halfway into a 25mm block of silicone breast phantom (Sure Inc., US-CA) with $E \approx 12$ kPa. The scan load was maintained at 2.5kg, increasing to 3.1kg to maintain the baseline. This setup can lead to highly non-linear behaviour at high strains, representative of some natural tissues.

The lesion prominence and diameter are measured using similar features on the tactile images particularly: the peak load, the load distribution standard deviation, and the approximation of the baseline load. These metrics are described in Equation 6.6 and Equation 6.7 respectively. In this case the peak is the maximum pressure value at the centre of a lesion, and the background is the value of the second order surface fit of the tactile image at the location of the peak load. The diameter is calculated as the extrema of a contour line of the pressure distribution (Pd) in the x and y dimensions, with the contour ‘ C ’ defined in Equation 6.8. The value for the contour was determined through empirical testing by early researchers in the field to give the best results on phantom and clinical samples.

$$prominence = \frac{peak - background}{background} \quad (6.6)$$

$$diameter = mean(\max(Cy) - \min(Cy), \max(Cx) - \min(Cx)) \quad (6.7)$$

$$0.3 = \frac{Pd - background}{peak - background} \quad (6.8)$$

The constant measured stress mode is an operator feedback-controlled system to change the true applied stress such that the output of the TI reports a constant scan pressure. This is the most likely operation mode for this error to manifest in. In this situation there is no apparent baseline shift, despite the actual applied load increasing from 2.5kg to 3.1kg as shown by the physically compensated data in Figure 6.9. Due to the nonlinearity of the materials, the dynamics of the coupled components, and the increase in sensitivity of the tactile array, the prominence of the lesion is increased by 159% and the size of the lesion has decreased by 17.6% when compared with the original measurement due to the stress distribution changing in response to the increase in true applied load. The vast change in dimensions and prominences are primarily governed by temperature sensitivity, but also by the interaction between the lesion, tissue, and scanner. As such it is not possible to generate a general empirical equation to describe the change in measured lesion properties vs. temperature. It is clear however, that careful temperature characterisation at the sensor level is required to control these errors when making detailed measurements of lesions.

The results presented here are relatively crude and represent an exaggeration of the current use case of TI. To use TI as an accurate piece of metrology equipment, the temperature response would need to be carefully calibrated, or the device needs to be calibrated at its operating temperature. In the current screening role of TI, the errors witnessed here are not going to be as severe, as TI is only used to detect the presence of a lesion and characterisation is not relied upon, and over time it is simply a comparison between scans with the same background load but with perhaps different temperatures

following natural variation in the order of 4°C, limiting the error that can accumulate as shown in Figure 6.10. In this situation, the apparent change in a lesions size and prominence is limited to 1.94% and 5.06% respectively for a temperature change of 31°C to 35°C, a range selected to span the expected range of realistic breast temperatures (Lubkowska and Chudecka, 2021) (Lozano et al., 2020) although the maximum can exceed 36.5°C. The scans were taken to maintain a constant baseline after the temperature drift, and the true applied load is detailed in the figure. The error in this case is unlikely to cause problems in current screening TI, as the lesion is still detected, and the change is relatively small, however as we transition to detailed characterisation these errors must be controlled.

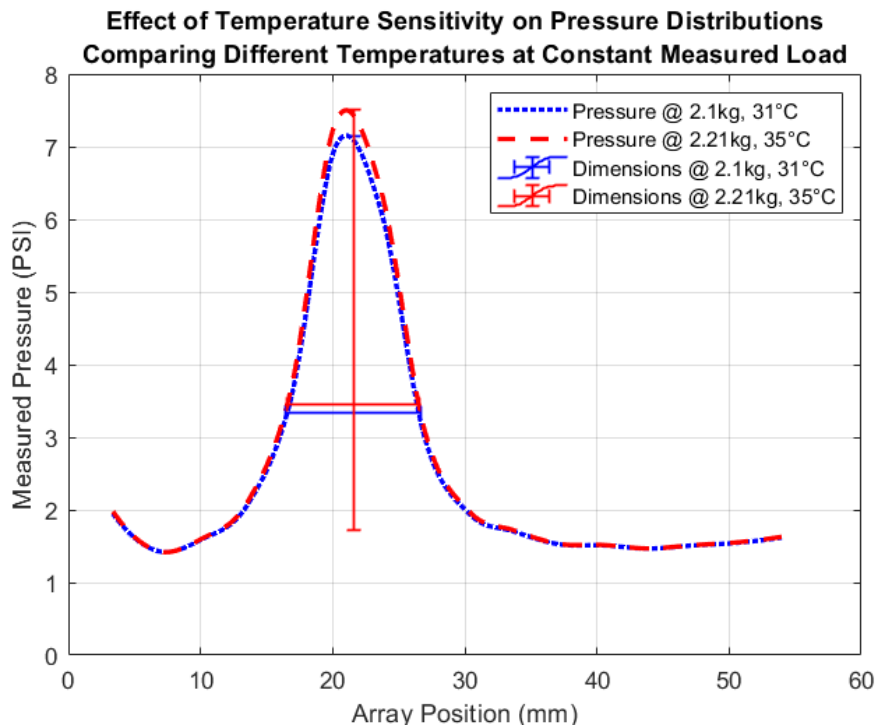


Figure 6.10 - Effect of realistic temperature changes between scans. As subsequent scans are compared for changes, the temperature difference between scans must be accounted for as this effect can lead to a conclusion of lesion change when there is none.

6.3.3. Short Term Creep Analysis

Short term creep of tactile sensors is caused by the viscoelasticity of the dielectric material, as opposed to long term creep which is a form of aging of the sensor. Creep is the input dependent rate of output change in response to a fixed constant input. Ideal elastic materials do not exhibit this phenomenon, but most real soft materials such as silicone and hard foams do. This is where, for the example of the silicone bubble dielectric, the material cannot instantly deform and so ‘flows’ much like a liquid until it settles at a fixed value. As viscous effects are governed by load rate, this is naturally going to be logarithmic with time, specifically that is the creep rate will start at some initial value determined by the applied load and drop to zero logarithmically over time. This phenomenon is dependent both on the dielectric material, and the architecture of the sensor, and so there is no suitable value to pull from the literature.

As creep leads to lateral expansion and subsequent further axial compression of the dielectric in response to a compressive applied load. This means that, in response to an applied compressive load, the output will jump to some value before creep will cause the output to increase logarithmically with time, as described by the Kelvin-Voigt representation of the standard linear solid model, or Zener model, for viscoelastic materials (Roynance, 2001) detailed in Equation 6.9. Here: σ is the applied stress, ε is the resultant strain, η is the viscosity of the dielectric, and E_1 and E_2 are characteristic elasticities of the dielectric.

$$\sigma + \frac{\eta}{E_1 + E_2} \dot{\sigma} = \frac{E_1 E_2}{E_1 + E_2} \varepsilon + \frac{E_1 \eta}{E_1 + E_2} \dot{\varepsilon} \quad (6.9)$$

The key takeaway from the 3-element solid model, is that the initial elastic reaction, in terms of strain, will be σ/E_1 ; the sensor will then creep towards a value denoted by $\sigma(E_1 + E_2)/E_1E_2$; with a time-constant of η/E_2 . Relating the equation to the capacitor expression in Equation 6.1, the part describing the response to force, $(F/A)/E$, would be substituted with Equation 6.9 rearranged to solve for the strain ϵ in response to an applied stress σ . Depending on whether dynamic or static response is preferred, the array can be calibrated using either response condition as shown in Figure 6.11.

The complex differential equations required to analytically describe this behaviour based on dielectric physical properties can be skipped, again by calibration, through observation of the retardation time of the sensors in response to applied loads. By observing the change in sensor output in response to a fixed input, the characteristic elasticities and viscosity can be determined providing accurate values for the other capacitive sensor terms are known. This is not often known, and so the initial viscoelastic response can be described as shown in Equation 6.10 (Ryan Roeder, 2013), in the absence of other error sources. In this equation: γ is a constant related to the magnitude of overshoot, τ is a time constant, and t is the time in seconds.

$$P = P_0 \left(1 + (\gamma - 1)e^{-\frac{t}{\tau}} \right) \quad (6.10)$$

The creep characteristics for the SureTouch™ array can be determined using the method described in Appendix C2. The results of this analysis is shown in Figure 6.12. Elasticity and viscosity change with temperature, so calibration is performed at the operating temperature of 34°C, based on the mean breast temperature from the literature.

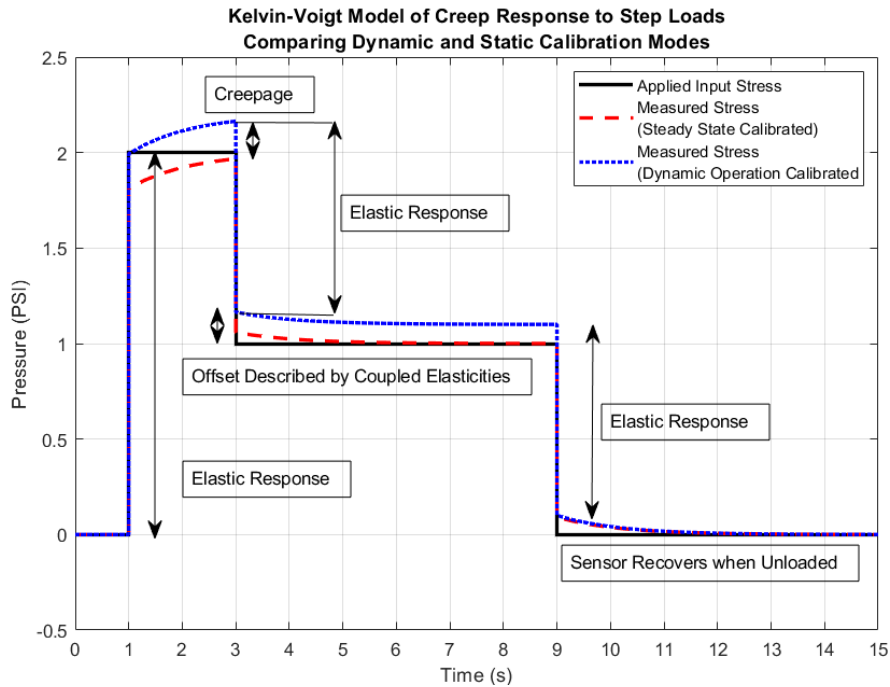


Figure 6.11 - Illustration of creepage in capacitive pressure sensors. The dynamic mode gives correct values instantaneously but drift out over time with a steady state response governed by coupled elasticities. Steady state mode gives the wrong value immediately but converges to the correct solution.

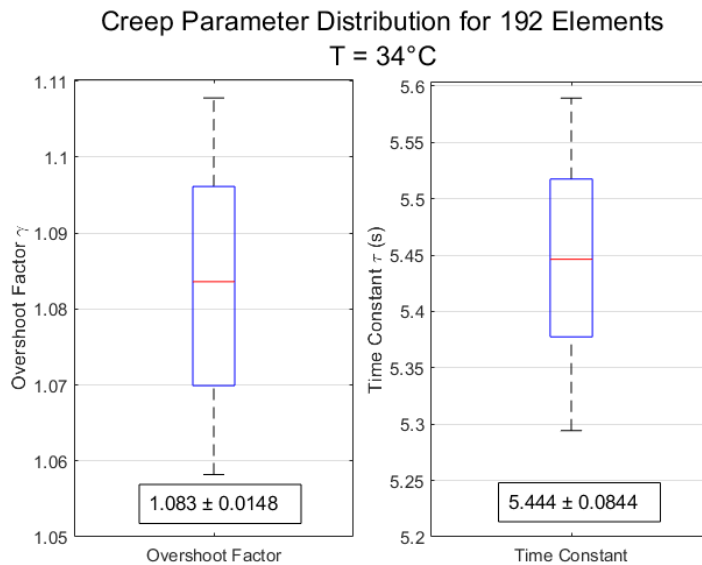


Figure 6.12 - Results of creep parameter analysis. The overshoot factor, when the sensors are calibrated for dynamic response is based on the temperature sensitivities previously discussed. The small SDs indicate that the elements are fairly homogeneous.

6.3.4. Effect of Short-Term Creep on Tactile Images

Viscoelastic creep at relatively low loads does not affect the prominence or measured dimensions of a lesion, in constant true load mode, as both of these quantities are measured using a ratio of the peak value to the baseline on a tactile image. The sensor overshoot after a sufficiently long amount of time, typically 5τ or greater, settles to a constant factor of the applied load denoted by γ , 1.083 ± 0.0148 , and so the ratio of peak to baseline is unchanged. In the more common constant measured load mode the increase in the baseline over time, shown in Figure 6.13, results in a controlled reduction in true stress to maintain the sensor baseline. This decrease in contact stress lowers both the lesion prominence and measured diameter by 3.69% and 2.12% respectively after 5τ , for a scan of a 10mm spherical inclusion at an initial scan force of 2.5kg and control scan force of 2.31kg.

The relatively short time constant of 5.444 ± 0.0844 s, compared with the overall scan duration, means that the sensor will quickly settle to a steady state value in real use. When the tactile scan is performed quickly such that creep cannot accumulate ($<0.1\tau$) the error can be kept in check, however it is impractical to perform measurements at this speed. The time constant also means that separate scans, or reapplication of the scanner must have a 'wait' period of at least 30s so that the creep residuals do not accumulate and lead to an overestimation of applied stress.

The sensors can be calibrated to give proper dynamic response where the elastic portion will be equivalent to the applied load and will overshoot to γ times the load or can be calibrated to exhibit steady state response where the sensor will initially

undershoot to $1/\gamma$ of the applied load before settling at the applied load. For tactile breast imaging the latter is more appropriate as it is a static measurement, however in other applications where dynamic response is preferred the steady state response will be adversely affected. As the estimation of hardness and diameter is ratiometric, the overshoot/undershoot does not affect the response in constant true load mode, however in the common case of baseline control the creep must be accounted for when making detailed measurements.

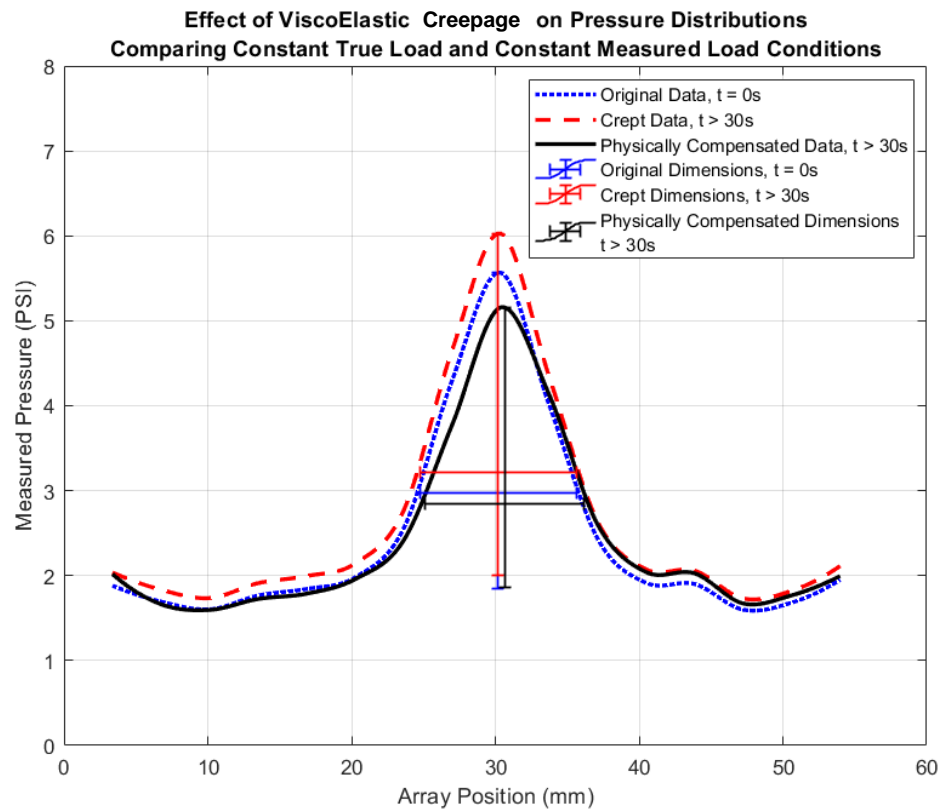


Figure 6.13 - Effect of creep on tactile pressure distributions. The creep in constant true load scanning does not affect either the lesion prominence or the diameter, however in the realistic constant measured load system, the servo action to maintain the baseline reduces both the prominence and the diameter over time.

6.3.5. Hysteresis

Hysteresis is a measure of the energy loss in, or efficiency of, a sensor or material in general and is caused by internal friction (Hara et al., 2020). Relating specifically to sensors, hysteresis is the non-time-dependant residual offset on a sensor output when the input has returned to zero after a non-zero stimulus. The energy loss is typically proportional to the energy input, and so the residual offset after a stimulus event will be proportional to that stimulus event. This is similar to the overshoot caused by viscoelastic creep, which is also proportional to the applied stimulus after some time, leading to many authors and engineers to confuse the two. The reason for this can be seen in Figure 6.14, where the sensor response to a step load has very high residual offset immediately after the load event. Comparing this to the slow response, the excessive offset diminishes over time as viscous creep is recoverable, however some residual offset remains after a long time, which is the sensor hysteresis. The hysteresis loop can be closed with negative pressure inputs, returning the sensor to its starting state.

Hysteresis in this context is measured using the same apparatus as the viscoelastic creep described in Appendix C2, with the result of $1.801 \pm 0.118\%$ being illustrated in Figure 6.15. Similar to measurements of the other mechanical properties of the tactile sensors this is done at the operating temperature of 34°C , as the hysteresis is related to the viscous properties of the dielectric. This value is in line with expectations from the literature (Sánchez-Durán et al., 2015) for tactile sensors, with the variation between elements attributed to the variations in d_0 as the sensor dielectric thickness has a significant effect on the hysteresis (Hara et al., 2020).

**Separation of Viscoelastic Creep and Hysteresis
In Steady State Calibrated Sensors**

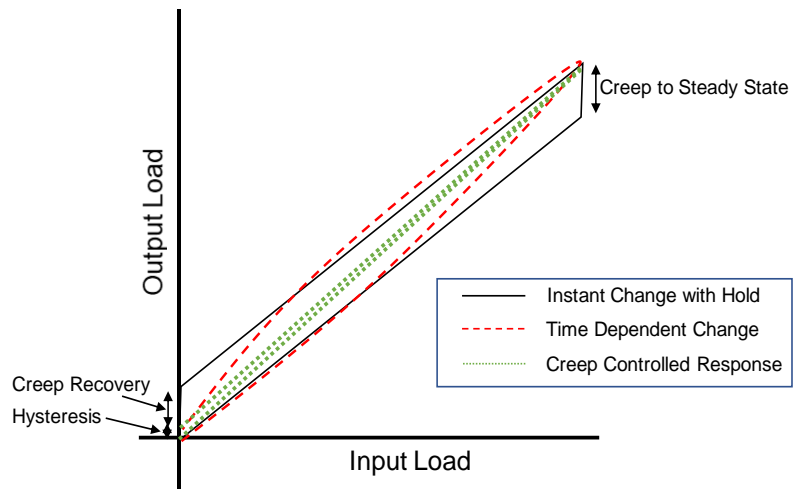


Figure 6.14 - Illustration of the coupling between creep and hysteresis. When creep is accounted for, either through calibration or waiting for creep to settle, the small residual offset when the input is zero is the hysteresis.

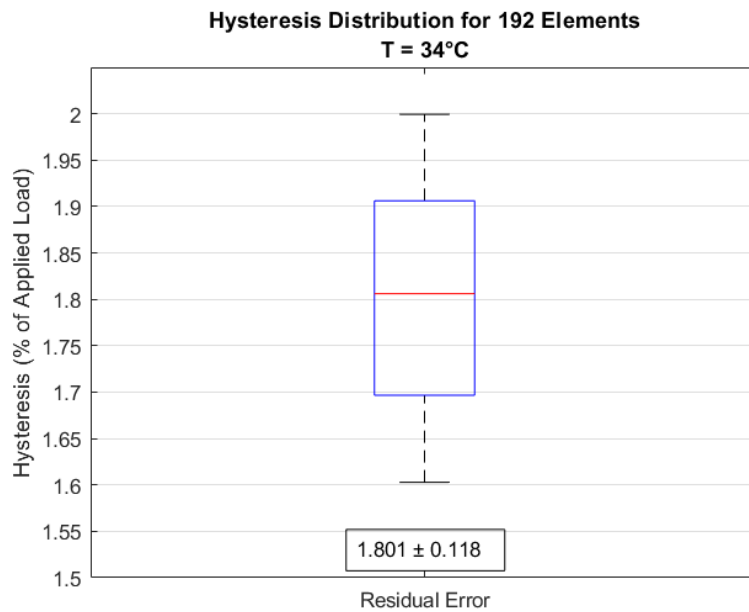


Figure 6.15 - Results of hysteresis analysis. The value of hysteresis represents the 'efficiency' of the dielectric in recovery of elastic potential energy and is a result of the friction within the dielectric.

6.3.6. Effect of Hysteresis on Tactile Images

Hysteresis, in this context, does not affect the tactile images in a variable manner like creep and temperature does as a result of the calibration method used for the tactile array. The effect of hysteresis, based on steady state calibration, is cumulative over a number of loading cycles rather than time, and accumulates at a rate given by the hysteresis and the maximum applied load during the cycle.

The typical hysteresis value of 1.801% does not have a measurable effect on the pressure distributions on the tactile array that can be differentiated from the measurement uncertainty after 1 repeated loading cycle. The manual control of the tactile array during the imaging process cannot reliably achieve a decrease in the baseline small enough to compensated for the hysteresis after 1 cycle at 2.5kg scan force. By observing the tactile array response over 10 cycles, in both constant true load and constant measured load modes, the effect of hysteresis drift can begin to be seen as shown in Figure 6.16. The testing involved 10 repeat measurements of a 10mm phantom lesion, described previously, each taking > 30s for creep to stabilise with > 60s recovery time between trials, without resetting the sensor baseline between trials. The target scan force on the reference sensor was 2.5kgf, dropping to 2.36kgf in constant measured load mode as a result of manual servo control.

The testing showed that after 10 independent and aligned measurements, without resetting the sensor baseline, the lesion diameter and prominence increased 1.14% and 1.56% respectively for constant true load and changed 2.24% and -3.11% respectively

for constant measured load. It is implied that the change caused by 1 cycle is approximately 1/10 of this value, and so is insignificant compared to other error sources.

This error is not likely to affect clinical TI in a breast cancer screening context as this type of extreme load variation is not realistic and the sensor is renormalised between independent measurements. This means that the effect of this error can be considered negligible over a scan session, however it serves as a reminder that renormalisation of the array is important between scans in order to maintain accuracy.

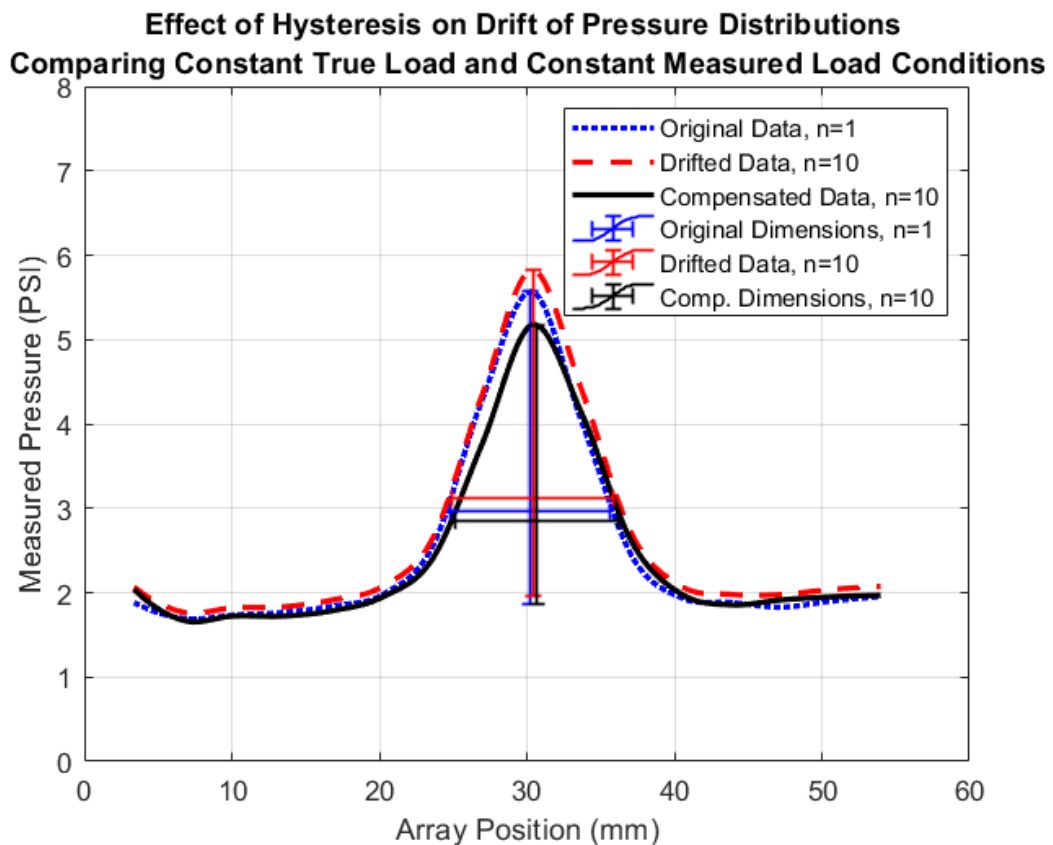


Figure 6.16 - Effect of hysteresis on tactile pressure distributions. The hysteresis does not affect the first measurement, but subsequent independent measurements begin to drift upwards at a rate prescribed by the hysteresis and the applied load in each cycle. The increasing sensor baseline triggers a servo response from the user to maintain the baseline that reduces the true contact stress.

6.3.7. Element Cross Coupling

Cross coupling between sensor elements is a phenomenon inherent with closely spaced elements on a tactile array, where stimulation of a particular individual element causes an unwanted change in adjacent elements. This is mainly caused by the stiffness of the sensor array skin, which is unable to ideally deform in response to a point load. Consider the analogy of a balloon skin. When an inflated balloon is pressed, the surface of the balloon does not conform perfectly around the finger, instead it arches towards the fingertip. Lightly inflated balloons conform better than fully inflated balloons, as the surface is not so stiff. Similarly, in the case of the capacitive sensor array, compression of a single element does not typically result in an ideal deformation of the sensor coating in response to the applied load. It bends from its initial position to its deformed state gradually, and if that transition region crosses another sensor element then the adjacent sensor shall experience a cross coupled compressive load. This was previously illustrated in Figure 6.4.

This phenomenon is governed by several factors, including skin thickness, skin stiffness, layer adhesion, and friction; so, it is not trivial to model this behaviour in terms of measurable, or inferable quantities and so it shall be measured directly. Using the method described in Appendix C3, the cross coupling between elements can be determined by loading a single element and observing coupling with adjacent elements as a function of applied load. As with other mechanical tests, this is performed at a nominal temperature of 34°C. It can be seen from the collated results of all elements, shown in Figure 6.17, that the inclusion of the protective silicone skin increases the

effect of cross coupling compared with the bare sensors from $0.82 \pm 0.36\%$ to $2.88 \pm 0.22\%$. This is expected due to the increased skin stiffness (Shore 70A) and resultant physical coupling between elements. An interesting outcome is the reduction in the interelement variation in cross coupling when the skin is introduced, this is likely due to the adhesion to the skin reducing the range of motion of adjacent elements. For the sensor array used in this analysis, there was no detectable sensor response 2 elements away from the actuated element over the sensor calibrated range (0 – 5 PSI), as such there is no need to model the cross coupling as a continuous function of displacement.

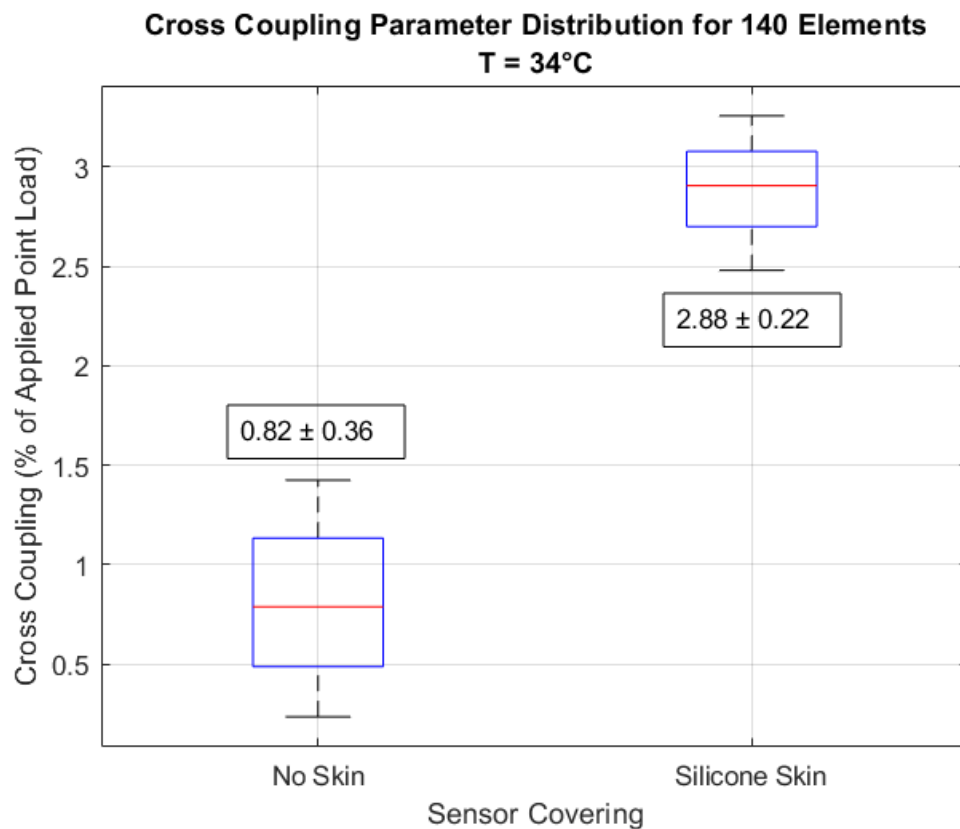


Figure 6.17 - Results of cross coupling analysis. This shows the signal measured on an element adjacent to a stimulated element over the sensors operating range. The addition of the silicone skin to the SureTouch™ array has increased the effect of cross coupling; however it has significantly reduced the variation between elements.

6.3.8. Effect of Element Cross Coupling

Performing a tactile scan of the same 10mm lesion as before at a scan force of 2.5kg shows the effect of additional cross coupling. This scan was performed at 22°C with the silicone skin on. The typically 2.88% cross coupling causes a decrease in the prominence of the lesion of 3.63% with a subsequent increase in measured lesion diameter of 1.72% by sharing peak loads across adjacent elements. There is no appreciable change in the baseline as a result of cross coupling for this lesion size, and so no user servo control was required, maintaining the interaction between the scanner/lesion/tissue which limits the effect of cross coupling on tactile distributions as shown in Figure 6.18.

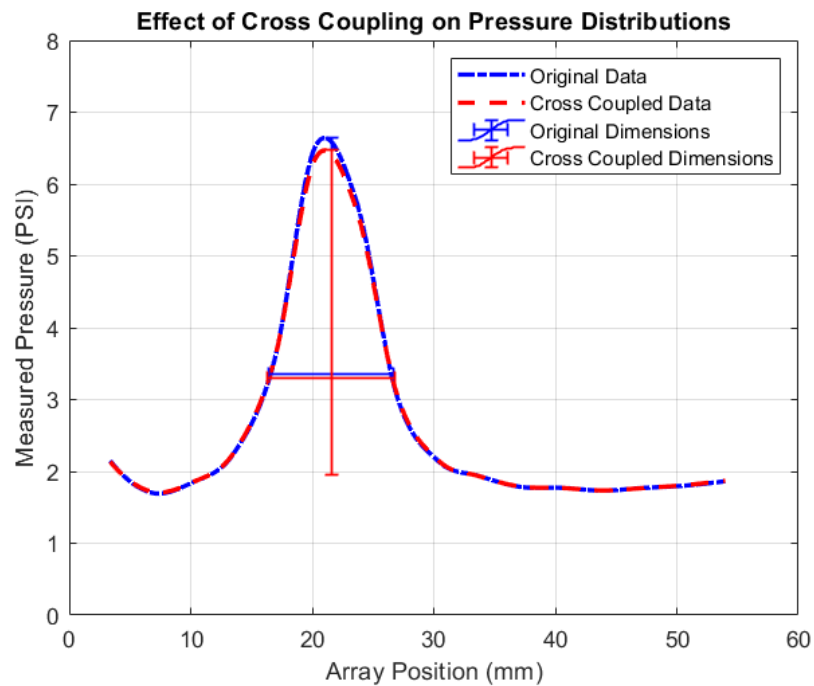


Figure 6.18 - Effect of cross coupling on tactile pressure distributions. The 2.88% cross coupling reduces the prominence of the lesion and increases the diameter by sharing load amongst adjacent elements. The effect is not significant compared with other errors.

6.4. Error Summary and Relative Effect Discussion

The error sources discussed in this chapter and their values are summarised in Table 6.1. The relative effect of each error source on the measured lesion properties is also noted using (+) for an increase, (0) for no/minimal effect, (0*) for no initial effect, and (-) for decrease. The number of notes indicates the severity of the error effect on the stated measurement. Only a relative description can be given at this point as the magnitude of the effect is dependent on the system dynamics, where nonlinearities in material interaction cause large changes in measurements for small condition changes.

Table 6.1 - Summary of tactile array error terms. The different error values for the SureTouch™ array are noted in the table along with the relative effect of the error source on the measured size and hardness (prominence) of the simulated lesion.

SUMMARY OF ERROR TERMS AND THEIR RELATIVE EFFECT ON MEASURED LESION PROMINENCE AND DIAMETER							
Variables				Affects Lesion Prominence?		Affects Lesion Diameter?	
Name	Symbol	Value	Unit	Constant True Load	Constant Measured Load	Constant True Load	Constant Measured Load
Sensitivity Temperature Coefficient	K_s	0.0176	/°C	++	+++	0	-
Baseline Temperature Coefficient	K_z	-0.0601	PSI/°C				
Overshoot (Dynamic Calibration)	$\gamma(ss)$	108.3	% of Applied Load	0	-	0	-
Undershoot (Steady Calibration)	$1/\gamma$ (dyn)	92.3	% of Applied Load	0	+	0	+
Time Constant	τ	5.444	s	0	0	0	0
Hysteresis	SS	1.801	% of Applied Load	0*	0*	0*	0*
Cross Coupling	CC	2.88	% of Applied Load	-	-	+	+

The results for the error parameters are definitive and accurately describe the behaviour of the sensor under certain conditions, however the effect of these sensor errors on measurements of complex material structures is not trivial to determine as shown throughout Section 6.2. Changes to the baseline of the sensors are intuitive for some error sources, but the effect on measurement of an embedded lesion is complicated and governed by the initial load and the initial geometry of the test material (Egorov and Sarvazyan, 2008). Simply allowing the error to accumulate is not realistic, due to the typical TI scanning method where a constant baseline is maintained. This baseline is measured using the tactile array, which is undergoing variation from error sources, and so triggers a manually controlled servo response in order to maintain the value at a steady state. In this situation, not only is the baseline and sensitivity of the sensor changing in response to the error source, but also the material interaction with the sensor is changing as a result of the manual control. This change in the material interaction, in constant measured load mode, causes a change in measured lesion prominence and diameter that cannot be corrected using a sensor element error model in post processing, unlike the case of constant true load which can be corrected in post processing.

As a consequence of this, the error model proposed in the next section can only be tested on direct sensor errors, with detailed testing on embedded lesions outside of the scope for general testing owing to the need to calibrate and model the pressure distribution response as a function of applied load for a range of phantom samples. This is a process that can be done in future works, following real time implementation of the inverse error model on a commercially integrated tactile array.

6.5. Reverse Error Model

It is clear from the illustrative testing of the error effects that detailed measurements of material properties, whether it be the lesion diameter or the relative hardness, cannot be made without addressing the error terms inherent in tactile sensors. This section proposes a basic error control model that helps to mitigate the error from the 4 sources covered in this chapter. The basic hierarchy block diagram of this model is shown in Figure 6.19. Each sub-model inverts their respective error effect on raw sensor data by inverting the governing principles discussed in their respective subsections.

The addition to the prototype design in terms of technology is a calibrated ‘K’ type thermocouple (Electrocomponents plc, UK) required for the thermal compensation model, which is read through a NI-DAQ6009 (National Instruments Corp., US-TX) integrated with PPS Chameleon™ software. For the proposed model, the sensors are calibrated for steady state accuracy, with the thermocouple connected directly adjacent to the centre of the tactile array to ensure representative temperature measurements.

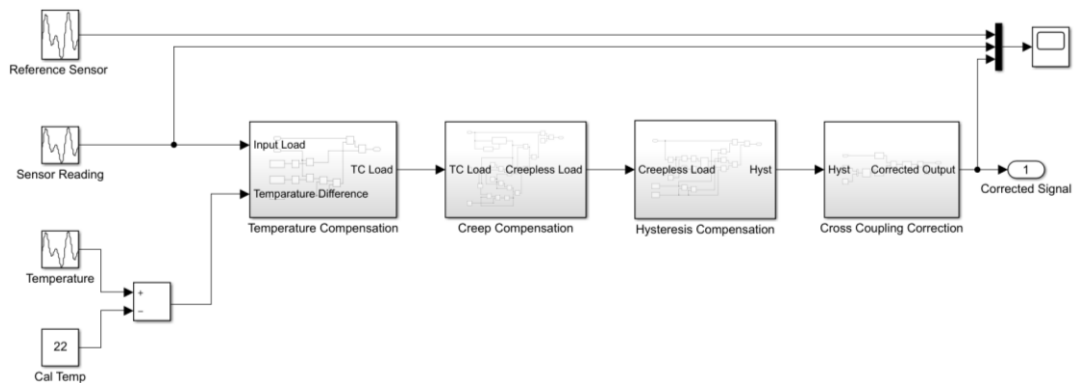


Figure 6.19 - Reverse error model hierarchy diagram. The basic system consists of 4 error inversion functions, one for each variable error source. The model accepts the sensor output and peripheral sensors and outputs an ‘ideal’ sensor response.

The first error source to be addressed is the temperature sensitivity, as it is the most dominant. The error correction model is shown in Figure 6.20. This is a very basic model that negates the baseline shift and sensitivity shift from nominal using the measured temperature coefficients from Table 6.1. This simple corrective model is appropriate, as complex thermal errors such as thermal hysteresis (separate to mechanical hysteresis) do not apply in the typical TI use case as the temperatures are not oscillating. When temperatures do oscillate, in the case of the device being removed from the breast, the system is re-normalised which resets the error to zero. The model accepts calibrated pressure and temperature data, outputting compensated pressure.

The creep compensation model is shown in Figure 6.21, accepting temperature compensated pressure data and outputting creep corrected pressure. This is done by inverting the 3 element Kelvin-Voigt model (Royle, 2001) used to define the elastic and viscous behaviour of the sensors. Using the known elastic undershoot factor the applied load can be predicted from the initial response of the sensor. The model then generates an opposing overshooting creep model, based on a first order exponential decay function for a step response using the measured creep parameters from Table 6.1. The average of the input pressure and opposing creep response results in the original applied input pressure being approximated. Although a step response is discussed here, as the effect of the error compensation and creep is the most pronounced, this is similarly effective for non-step inputs. This type of model is for steady state calibrated sensors, where this is the common operating mode for breast scanning TI and handles time dependent errors, ignoring mechanical hysteresis as this is handled separately.

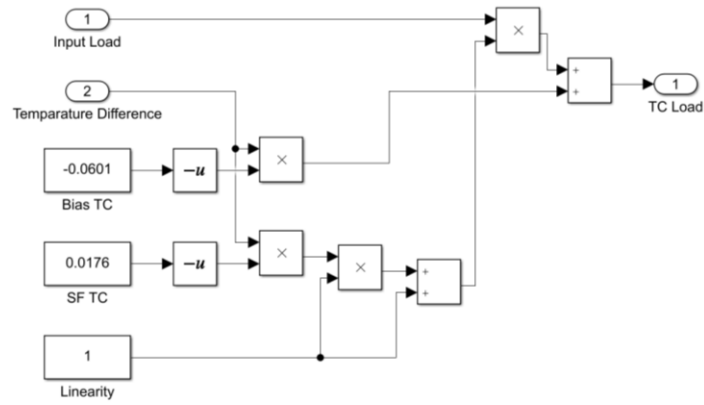


Figure 6.20 - Thermal compensation model. The temperature coefficients are negated to allow for their effects to be subtracted out from the sensitivity and baseline of the sensor readings. The model accepts raw sensor readings and temperature measurements and outputs temperature compensated results.

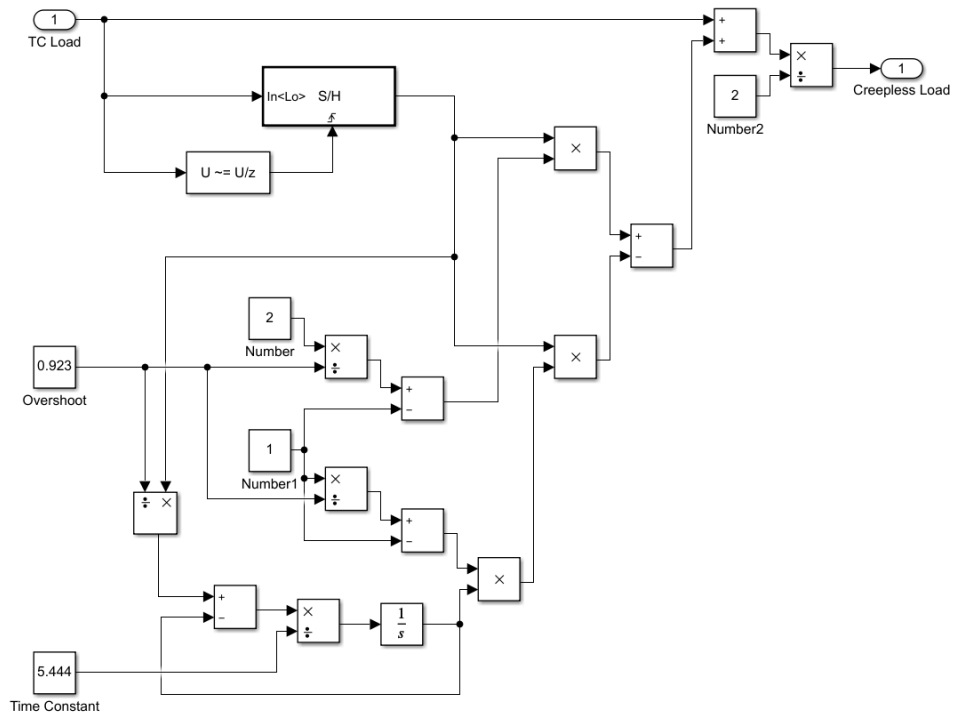


Figure 6.21 - Viscous creep compensation model. The model takes the immediate impulse response from the temperature compensation system and uses that, the time constant, and the expected undershoot to generate a control signal that cancels out the time domain creep response.

The hysteresis correction model is shown in Figure 6.22. This simple model accepts the creep compensated pressure reading and corrects for the energy loss in the system. This is done by assuming that the hysteresis effect is only applied on the decreasing portion of the sensor response, shown in Figure 6.14. This is not universally valid but is applicable to these sensors as they are calibrated to have the correct output after creep using increasing loads. The model works by adjusting the sensitivity and baseline of the sensor dynamically, such that the sensor maintains the calibrated and temperature compensated baseline and sensitivity when the input is increasing but switches the baseline and sensitivity on decreasing inputs to account for hysteresis. The application specific conditions, where creep is known, sensors are calibrated for rising steady state response, and the loads are not continuously cycling, allows a simple model like this to be used, foregoing complex general creep/hysteresis models such as the common Prandtl-Ishlinskii or general Preisach models (Sanchez et al., 2018).

Cross coupling correction, unlike the other error terms, requires data from all elements to be combined into a tactile frame. As the effect of cross coupling can be thought of as a Gaussian blur in imaging terms, the corrective function is an image sharpening technique to invert the effect of the Gaussian blur as shown in Figure 6.23. In this case a 5x5 Gaussian kernel with a standard deviation of 0.365 is used to define the cross coupling. This kernel is then used as a frequency domain filter to amplify high frequency content in the tactile images, narrowing the peak diameter and increasing peak prominence if one is present in the image as desired from Figure 6.18. The large kernel size in comparison to the standard deviation limits the amplification of image noise.

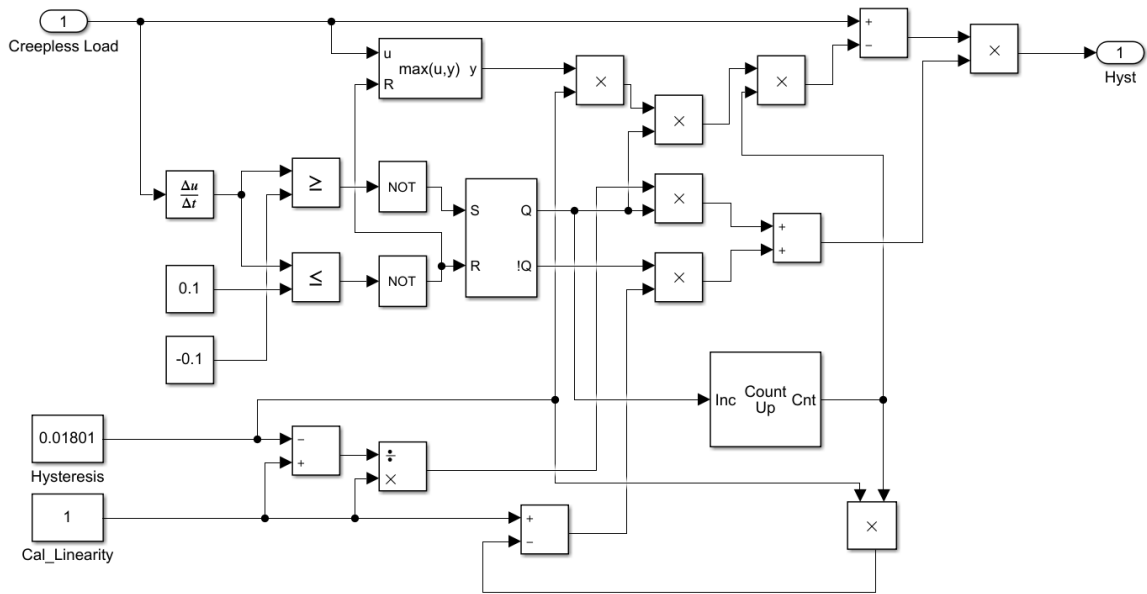


Figure 6.22 - Linearised hysteresis compensation model. The model accepts the creep compensated input and uses the load direction (ascending or descending) to adjust the sensitivity and baseline of the sensor output to compensate for hysteresis in steady state. The effect of this is continuously accumulating until the sensor is tared (reset).

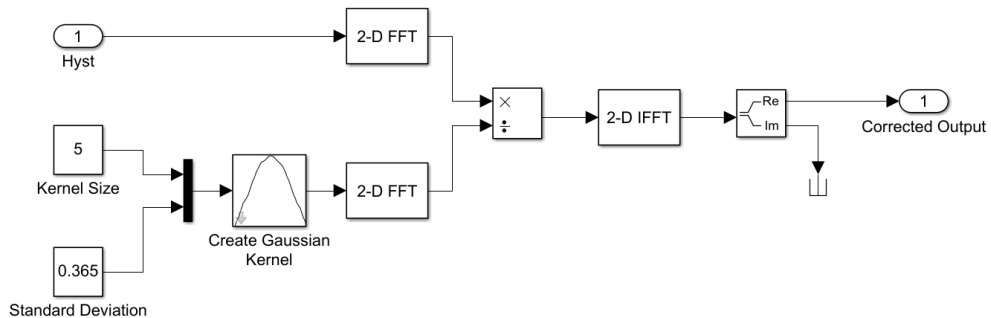


Figure 6.23 - Cross Coupling correction model. The model acts as an image sharpening function, undoing the cross coupling which is modelled as a Gaussian filter. The reverse process requires transition into the tactile image frequency domain for the filters to be effective, followed by transfer back into spatial domain. This process is particular to tactile arrays and requires data from all sensors simultaneously to form a tactile frame.

6.6. Error Model Validation

Model validation is performed in 2 parts. Firstly the temperature model is tested to observe temperature stability of the proposed system in terms of baseline and scale factor tolerance to temperature changes. Secondly, the combined creep and hysteresis mechanical model is tested using cyclical loading at the operational temperature of 34°C to verify correction of time and load dependant drift. General testing of the error inverse model is performed using controlled compressions of the SureTouch™ calibration pad, with reference measurement from the D660 load cell as described in Appendix C.

6.6.1. Thermal Model Validation

Thermal model validation is performed using repeated independent compressions of the SureTouch™ calibration pad at a nominal pressure of 2.5PSI measured using a PPS D660 reference load cell (PPS Inc., US-CA). The sensor is calibrated at 26°C and tested over 18°C-38°C, to encompass the full range of expected breast temperatures and the room temperature state (Lubkowska and Chudecka, 2021) to show performance with both positive and negative dT. Further temperature ranges are not practical with the current test apparatus. The sensor is thermally cycled back to the calibration temperature and tared between compressions. Each compression is 30s with 30s baseline stabilisation at the test temperature as shown in Figure 6.24. It can be seen that the sensor baseline is reducing with increasing temperature, with the loaded value decreasing. The effectiveness of the thermal error compensation model is shown in more detail in Figure 6.25, showing the model is effective.

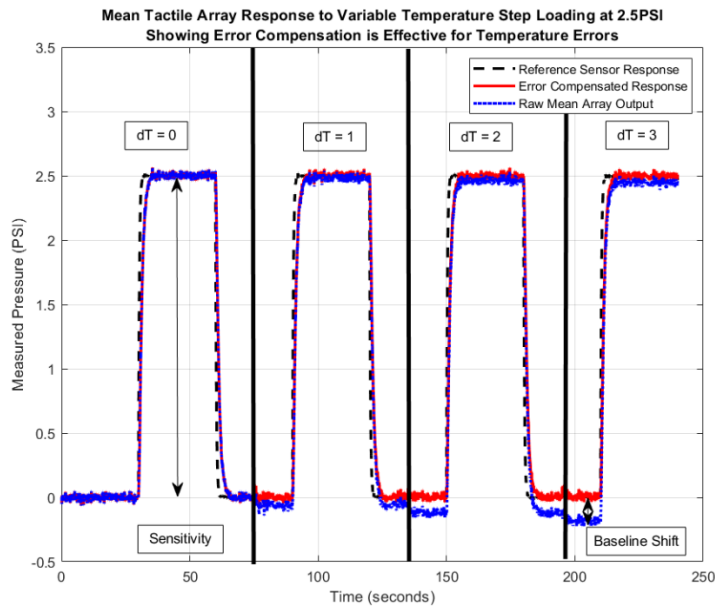


Figure 6.24 - Temperature model time series plot. The sensor zero value decreases with increasing temperature difference from the calibration temperature. The sensor loaded response is less affected due to the sensitivity increasing with temperature, which acts to counter the baseline shift in this situation.

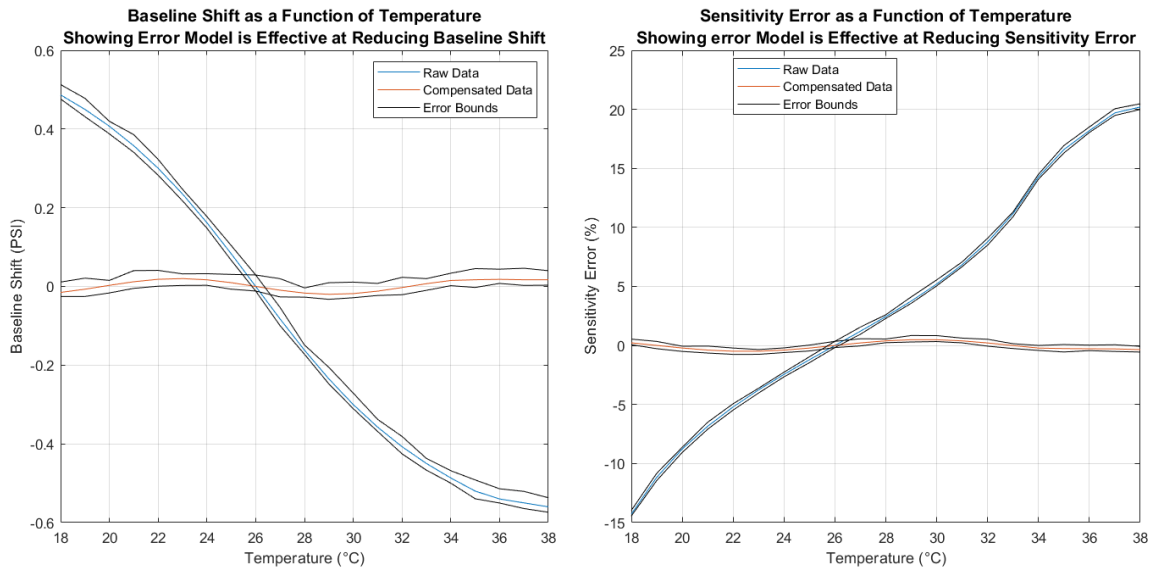


Figure 6.25 – Thermal model error vs. temperature. Left) baseline shift vs. temperature showing 92% reduction in maximum baseline shift over the test range with maximum baseline shift < 0.04PSI. Right) sensitivity error vs. temperature showing absolute maximum compensated sensitivity errors < 0.85% over the test range.

The detailed results from Figure 6.25 show the raw sensor response following the typically expected baseline and scale factor (sensitivity) temperature sensitivity described in Table 6.1. The thermal inverse model is clearly effective at reducing system errors. Considering baseline shift, the absolute maximum baseline shift for the error compensation model is < 0.04 PSI compared with 0.51 PSI for the raw sensor. The typical maximum shift is < 0.02 PSI over the full test range. Considering sensitivity change, the absolute maximum sensitivity error is $< 0.85\%$ compared with 14.6% for the raw sensor. The typical maximum sensitivity error is $< 0.49\%$ over the full test range. There is no net sensitivity to temperature for either baseline shift or sensitivity error over the test range for the proposed error model that can be differentiated from experimental error indicated by the error bounds. The combined effect of baseline shift and sensitivity error result in a worst case total steady state error of 2.4% with a typical maximum error of 1.24% from repeated testing over the full test range. This shows that the proposed thermal error model is effective at controlling thermal sensitivities in tactile arrays.

6.6.2. Mechanical Model Validation

Mechanical error model validation is performed with repetitive loading cycles of 2.5 PSI, equivalent to an extreme scan force of 3.4 kgf, with 50% duty cycle and period of 60s using weights as described in Appendix C. These values are selected to test the mechanical properties over the broadest realistic range of scan pressures, with sufficient time ($>5\tau$) for creep to settle for making hysteresis measurements. The low period is in line with TI quick scan times. The unloading of the sensor to zero simulates the removal of the sensor from the patient, without zeroing the sensor baseline between scans.

A close-up view of the cyclical testing response is shown in Figure 6.26. The D660 reference sensor shows that the applied load is remaining constant, and that the raw sensor response is settling to its steady state value within several seconds. It can be seen that the raw sensor output is gradually drifting upwards every cycle as a result of the hysteresis. The figure indicates that the mechanical compensation model is effective at reducing the sensor error by improving the settling time of the sensor and greatly reducing the hysteresis drift. Expanding this testing over 100 repeated cycles, the improvement in error from the compensation model can be clearly seen in Figure 6.27.

The results show that the maximum time domain error is reduced by approximately 60% from 10% to 4%, and the 1% settling time is reduced from 6.7s to 1.48s typically. This shows that the creep model is effective in reducing time domain errors. This is built upon looking at the error change with cycle number, which shows the error model can settle to 1% error for $n < 41$, compared with $n < 3$ for raw data. This shows the hysteresis model is effective in stabilising response between measurements. Focussing on the region of $n < 5$, the expected worst-case number of cycles without renormalisation of the tactile array in clinical TI, the sensor is not capable of settling to within 1% of the applied load without the hysteresis model. The gradient of error increase is maximum for the raw data in this region and minimum for the proposed error model, showing that the error model is designed to absorb the worst of the errors. In this region, the steady state error after compensation is typically 0.15% after 5τ . This confirms that the error model is effective in reducing accumulating errors when cyclical loads are applied.

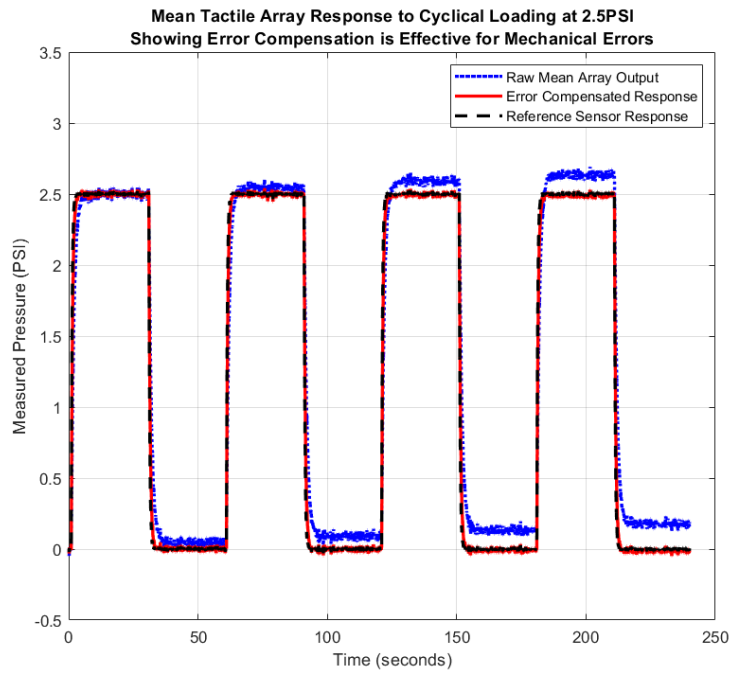


Figure 6.26 - Mechanical model time series plot. The cyclical compressions of 2.5PSI present time domain errors that accumulate every cycle. The inverse model reduces the cyclic error and creep error, but does not completely remove them.

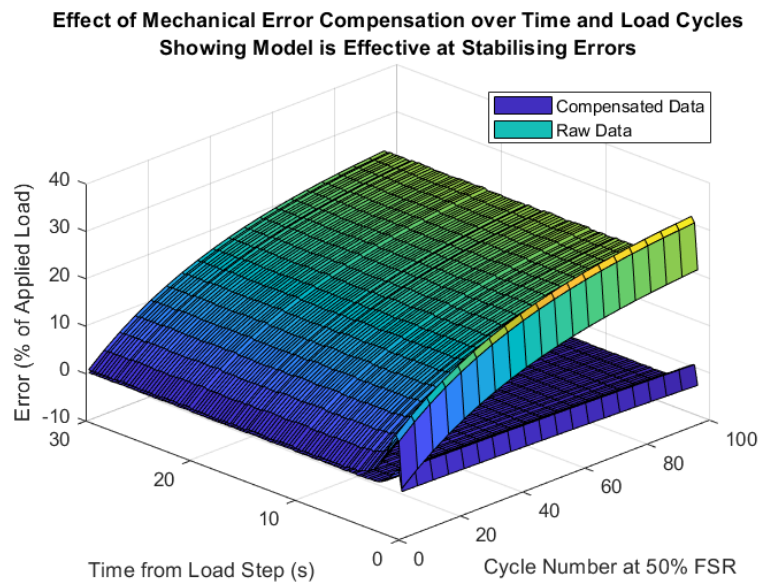


Figure 6.27 – Mechanical model error vs. time and cycles. The model stabilises the error at low cycle numbers where the raw data is unstable before deteriorating. The model improves the time domain response by reducing settling times.

6.7. Discussion

6.7.1. Results

The results of the error model validation testing presented in Section 6.5 have shown that it is possible by properly characterising tactile sensors to achieve a typical worst-case accuracy of 1.24% over the range 18°C-38°C when calibrated for zero steady state error at 26°C. It is separately shown that steady state error < 1% is possible for large numbers of repeated cycles, with worst case time domain errors of 4% settling to <1% within 1.5s at the calibration temperature. This has been shown to be a significant improvement over raw sensor data for the range of conditions tested.

Due to limitations in testing, a full parametric sweep of time, temperature, cycles, and load is not feasible in this work, as whole theses are dedicated to this type of testing in other fields (Agogo, 2016) (Morgan, 2018). Considering the errors presented in this thesis, it is possible to estimate the total system error over a realistically constrained range of test parameters. Considering the reduced realistic operating temperature range described in Section 6.2.2 of 31°C-35°C with a calibration temperature of 34°C, and assuming the hysteresis and creep response will not change significantly in this range, the expected steady state error varies is from 0.23% to -0.18% over this range. This is in contrast to the total errors from 6% to -2% for uncompensated sensor data over the same range for very low cycle numbers. Whilst the proposed error model does not completely remove error sensitivities, it is effective in reducing sensor errors, allowing accuracy < 1% in the tactile sensor response near the calibration and normalisation points.

6.7.2. Limitations in Testing

It was not feasible to parametrically test mechanical error over a range of temperatures due to the difficulty in obtaining reliable measurements with the equipment available. Additionally, it was not feasible to test the error model over a wide range of applied loads, and so an extreme but realistic value of 2.5PSI was selected to give an estimate of the worst-case results. While these limitations do affect the characterisation and validity of the error model over the full parameter space, the testing presented here is useful in defining the bounds of the possible error compensation.

Finally, no measurements of tactile lesions have been done, as it is known that stabilisation of the sensor output will lead to stabilisation of lesion measurements. This does not affect the validity of the error model, as the purpose was to stabilise tactile sensor readings rather than directly controlling tactile lesion measurements. The need for detailed calibration of test materials inhibits further testing on embedded tactile objects.

6.7.3. Implementation Practicality

Implementation of the error model can be performed in real time, as there are no buffered signals used in the model and the model is not computationally expensive. This means that the error model can be applied directly to clinical TI with commercial support with the only additional requirement being a thermocouple. The positioning of the thermocouple is important, as it must be thermally coupled to the sensor elements such that the measurement is representative of the element temperature whilst being spatially separated so as to not interfere with the tactile response.

The calibration of the error sources is not trivial, requiring significant investment in terms of time and equipment in order to characterise the sensors fully. Further testing on multiple units is required to determine the acceptability of using the proposed model and characterised parameters generally for a particular TI implementation such as SureTouch™ in balancing accuracy with calibration costs, however this is not feasible in this thesis.

6.8. Conclusion from Sensor Error Modelling

6.8.1. Applications and Significance

The error sources presented in this chapter are applicable to every application of TI, as well as other sensor architectures, and so the usefulness of this work is not limited to tactile breast imaging. Other medical applications of TI such as prostate imaging (Egorov et al., 2006) and transvaginal imaging (Brandt et al., 2020) operate at similar operating temperatures and scan conditions as those tested here, and so these applications would benefit from a tactile array error model similar to the proposed model. Application specific error parameters will need to be determined for these additional applications, as the tactile arrays used are physically different. These types of errors are inherent in other forms of tactile imaging using other sensor types and physical methods (Ayyildiz, 2011) (Oleksyuk et al., 2016) for breast imaging, without being acknowledged in the literature. This presents doubt on their accuracy when transitioning from phantom to clinical studies, and this work helps to explain some of the variability

in performance observed in testing of such systems. The acknowledgement and mitigation of these sensor errors is critical in reducing experimental variability and providing confidence in measurements made using TI systems.

Documentation of the physical causes of error in tactile sensors is important for informing operators of tactile imaging or sensing equipment generally on the realistic expectation of system performance in their particular application. This is a point that is often overlooked as operators of TI equipment are physicians and product designers rather than measurement scientists, and so by documenting the significant sources of error and their physical causes in a clear and intuitive manner, as presented in sections 6.1 and 6.2, operators can achieve better results even without an inverse model using properly informed experimental design.

6.8.2. Summary and Next Steps

This chapter has addressed a critical hole in the TI literature by exploring the major error sources that affect TI generally before focussing on breast TI, investigating the values of error sensitivities to a variety of factors for commercial TI systems. Basic testing of the effect of the error sources on measurements of embedded lesions using a SureTouch™ tactile array has shown that error sources such as temperature, viscous creep, and hysteresis each have a significant effect on measurements of lesion size and hardness using standard methods (Egorov and Sarvazyan, 2008). In order to stabilise the measurement of tactile features an inverse error model was proposed to directly stabilise sensor element pressure readings and thus indirectly stabilising tactile images of embedded lesions.

Limited validation of the proposed inverse model, using measured sensor error parameters described in Table 6.1, showed significant improvement in terms of sensor error and error sensitivity compared with raw sensor data. The inverse model was demonstrated to produce sensor steady state errors $< 1\%$ with settling times $< 1.5\text{s}$ across a large range of temperatures and loading cycles. When the sensor is used close to the calibration point, in terms of temperature and number of loading cycles, the estimated steady state error drops to $< 0.24\%$ over a realistically constrained range of conditions. The typical use case of breast TI means that low steady state error is important, rather than low dynamic error, and so this is a very positive result that can be applied to commercial TI systems with minimal modifications.

This error modelling work is presented to supplement the tactile mapping prototype system developed in previous chapters, pushing forward the research into practical clinical TI in preparation for the integration of the SureTouch™ tactile array into the developed prototype by commercial partners. Further testing of error sources is limited by the test materials and equipment available during this project. Further testing of the effect of error sources and inverse model on the measurement of lesion size requires further development and integration of the SureTouch™ array into the developed system which is out of scope for this project.

This error modelling and documentation concludes the work possible within the scope of this project and provides a stable platform for future work on tactile lesion measurements that can be applied directly to clinical TI independently to other works, or integrated into the proposed prototype in future works. This work presented a concise

and simple error model that provides a stable sensor platform applicable to clinical TI, that helps to explain the variability in tactile measurements observed in early works (Sarvazyan and Egorov, 2009) as well as providing an expectation on the change in performance when transferring from phantom to clinical testing.

Chapter 7

Conclusion

7.1. General Summary

This thesis has explored clinical applications of TI, and the requirements for development of TI in breast cancer imaging from a simple screening tool to a stand-alone tissue differentiation and discrimination system for in-situ early diagnosis of breast cancer. This functionality was predicted in early clinical works on the subject (Egorov et al., 2009). Analysis of literature on automated cancer diagnosis using machine learning and the important metrics used, cross referenced with the capabilities of academic and commercial breast TI led to the conclusion from Chapter 2 that the required additional metrics were: background elasticity of the breast, a large scale view of the whole breast, and spatial registration of lesions within the breast structure. These metrics are expected to supplement existing TI capabilities and enable discrimination of tissues with the accuracies observed for machine learning using modalities such as X-ray mammography.

Two methods of achieving these metrics were developed in largely blue-sky research based on the fusion of tactile sensors with orientation/inertial sensors and IR cameras respectively. The use of MARG sensor-based displacement estimation was

found to be effective in measurement of material elasticity within 4% MAE, but was not found to be practical for tactile mapping of large structures. The use of an IR camera integrated with tactile and orientation sensors was found to be effective for both elasticity measurement and image mosaicking and was considered to be a practical solution suitable for further development. Both technologies developed through Chapters 3 and 4 led to high quality publications and collaborations (Hampson et al., 2019) (Rana et al., 2020).

The practical IR camera based tactile mapping and elasticity method developed in Chapter 4 was developed into a proof-of-concept, hand-held, tactile mapping prototype by demonstrating that the technology could be integrated into the footprint of clinical TI systems. This integrated prototype was demonstrated in Chapter 5 to be able to mosaic tactile array data into a composite tactile map with location accuracies of $0.33\% \pm 0.17\%$ and background elasticity measurement errors of $2.36\% \pm 0.93\%$ over a realistic range of phantom tissues. Limitations in the integration of appropriate tactile arrays into the prototype inhibited further testing of the prototype system towards accurate clinical lesion measurements.

Thinking ahead to a fully integrated clinical prototype, using a purpose built modified SureTouch™ tactile array, error sources affecting the measurement of embedded lesion hardness and diameter in current TI were explored and documented. Through characterisation of error sensitivity to temperature change, viscous creep, and hysteresis, and subsequent limited testing on the relative effect of these on phantom lesion measurements, it was determined that these error sources were significant and

needed to be addressed in order to advance TI further. A simple reverse error model was developed for future real time implementation on a SureTouch™ array. This was validated over an extreme range of operating conditions, resulting in stability < 1.25% over a temperature range of 18°C to 38°C, and settling to <1% error within 1.5s at the calibration temperature. Limitations to testing stopped full parametric testing of operating conditions and testing on embedded lesion measurement, however it is well understood that providing stable sensor outputs will result in stable lesion measurements.

This thesis has delivered a practical hand-held tactile mapping prototype based on current clinical TI, capable of measuring the background elasticity of soft tissues and spatially registering tactile array data, designed for accelerated integration into commercial systems for maximum impact. The prototype, and associated error modelling, presents a stable tactile mapping platform for future works in embedded lesion characterisation by addressing the limitations of early and state-of-the-art breast TI (Wellman, 1999) (Egorov and Sarvazyan, 2008) (Sarvazyan and Egorov, 2012).

The consideration of usefulness driving the generation of the proposed systems has led to effective and practical solutions to industrial problems, marrying academic novelty with practical solutions for the clinical environment. Critical gaps in the academic literature on TI have been addressed in this thesis through the implementation of utilitarian solutions, and problems in clinical usage of TI have been solved using novel blue-sky research backed up with appropriate and detailed testing. This type of development strategy is increasingly important in a world where the requirements for academic success rely more and more on commercial impact and support.

7.2. Thesis Impact

The potential impact of this thesis has been maximised through the ethos of appropriate technology, conforming to what is already accepted rather than branching out onto something completely new. This means that impact can be built upon, whereas completely new technology resets the clock on the route to impact with other new technologies not advancing clinical performance beyond the earliest stages of TI. (Wellman, 1999) (Ayyildiz, 2011) (Oleksyuk et al., 2015). This design strategy allows the integrated prototype, with novel adaptations, to progress directly into clinical evaluation with the justified expectation that it will be superior to previous TI implementations, where it is not guaranteed that a completely novel system architecture will be superior to equivalent systems.

The scope of this thesis limits direct evaluation of the clinical impact of this work, however the predictions made during early clinical TI studies (Egorov et al., 2009) (Tasoulis et al., 2014) and the analysis of diagnostic metrics from Chapter 2 allows for estimation of the clinical impact that can be evaluated in future works. It is estimated that the metrics delivered by the proposed system, background elasticity and lesion location on a whole breast view, coupled with increased sensor stability shall improve the clinical sensitivity of TI from its current level ~85% to > 95%, with a corresponding increase in specificity, in line with studies performed on other imaging modalities. This will result in further reductions in the benign condition referral rate from the primary screening process, reducing the burden on the secondary care system and reducing the unnecessary stress and risk to patients with benign conditions.

7.3. Future Development and Work

Continuation of this work shall focus on further integration of tactile array technology into the prototype system, which will involve the design and implementation of a custom tactile array based on the SureTouch™ array modified for the addition of a camera viewport. This requires close commercial support and collaboration due to the difficulty in producing tactile arrays, with DIY solutions being no better than the earliest TI implementations, and the expense of designing custom hardware of this kind. The proposals in this thesis provide a compelling case for this support in future works.

Following integration with appropriate tactile arrays, future work will progress onto detailed evaluation of lesion properties from the tactile maps created by the developed prototype in terms of elasticity and diameter in phantom studies, with the goal being to prove accuracy and reliability is improved compared with existing TI methods in the literature. The error model can be progressed separately onto clinical TI systems to validate that accuracy and stability of existing metrics are improved.

Finally, after successful implementation of this work into clinical TI repeated clinical testing is required to duplicate previous TI studies in terms of measurement accuracy vs. current ultrasound (Wellman et al., 1999b) and lesion classification accuracy (Egorov et al., 2009) (Tasoulis et al., 2014). This will accurately assess the current standing of TI in breast screening in comparison to competing technologies and gauge the incremental improvement to diagnostic accuracy delivered by technology developed in this thesis.

7.4. Additional Applications of This Work

The work presented in this thesis is not restricted to breast TI, and parts of the developed prototype can be applied to a variety of applications in medical imaging and further afield with three key areas of ultrasound, deformable material odometry, and clinical needle guidance described below. These additional areas for the application of work developed in this thesis increases the overall impact of this work, and present exploitable opportunities for future work and collaboration beyond the core research path of breast cancer diagnosis.

Firstly the elasticity measurement and tactile mapping functionality can be applied to other exterior medical imaging applications such as abdominal imaging. As the image registration method uses IR vein images rather than tactile data, it can be applied to assist in registration of other measurement media such as ultrasound. This will allow for 2D slices from sonograms to be mosaicked into 3D images of the internal material structure. This represents an exciting development, by providing competing technologies for complex phased array 3D ultrasound. Additionally, the developed system for measuring the probe angle with respect to the surface can be applied to general ultrasonic inspection of soft materials providing context to the ultrasound images.

Secondly, the image mosaicking method using force sensors to correct for the deformation of the contact surface has applications in general robotic odometry. If the elasticity measurement function is not required, the method can be shrunk further to operate on an optical mouse sensor which will allow for accurate robotic positioning on

soft or deformable structures. This is of particular interest in contact NDT of large composite material structures, where proper probe contact can deform the surface of the structure under test.

This work has an application in clinical needle guidance where knowledge of the needle assembly force and tilt angle on the skin can help to localise the tip of the needle in 3D space for targeted cancer drug delivery (Frazier et al., 2019) amongst other applications including needle core biopsies, anaesthesia injection, and arterial line insertion. These precision clinical needle insertion tasks are typically performed with the assistance of ultrasound imaging (Zhang et al., 2020a), however the high imaging resolution needed makes this difficult when precision application is required. Force sensors have already been applied to targeted needle insertion to help with this (Zhang et al., 2020b), and so the work presented in this thesis can be applied to further this line of research to improve needle localisation accuracy in these applications.

Finally, the error modelling performed here applies to any form of TI or simple tactile sensing and so is of interest in both academic and commercial developments of TI. Application of the error correction strategy presented in this thesis can be applied to any other research project carried out using tactile sensors. As this is often industrially/clinically focussed commercial research, the route to impact of this work is short, and represents a valuable tool for commercial partners.

References

- Agogo, G.O., 2016. Statistical modelling for exposure measurement error with application to epidemiological data (PhD Thesis). Wageningen University.
- Agudo, A., Moreno-Noguer, F., Calvo, B., Montiel, J.M.M., 2016. Sequential Non-Rigid Structure from Motion Using Physical Priors. *IEEE Trans. Pattern Anal. Mach. Intell.* 38, 979–994. <https://doi.org/10.1109/TPAMI.2015.2469293>
- Akay, M.F., 2009. Support vector machines combined with feature selection for breast cancer diagnosis. *Expert Systems with Applications* 36, 3240–3247. <https://doi.org/10.1016/j.eswa.2008.01.009>
- Albright Technologies, 2020. Coefficient of Thermal Expansion. Part Design. URL [albrightsilicone](http://albrightsilicone.com) (accessed 1.27.21).
- Alcantarilla, P., Nuevo, J., Bartoli, A., 2013. Fast Explicit Diffusion for Accelerated Features in Nonlinear Scale Spaces, in: *Proceedings of the British Machine Vision Conference 2013*. Presented at the British Machine Vision Conference 2013, British Machine Vision Association, Bristol, p. 13.1-13.11. <https://doi.org/10.5244/C.27.13>
- American Cancer Society, 2019a. Breast MRI. Breast Cancer Early Detection and Diagnosis. URL <https://www.cancer.org/cancer/breast-cancer/screening-tests-and-early-detection/breast-mri-scans.html> (accessed 1.24.21).
- American Cancer Society, 2019b. Newer and Experimental Breast Imaging Tests. Breast Cancer Early Detection and Diagnosis. URL <https://www.cancer.org/cancer/breast-cancer/screening-tests-and-early-detection/experimental-breast-imaging.html> (accessed 1.25.21).
- American College of Radiology, 2013. ACR BI-RADS ATLAS - Mammography.
- Anderson, B.O., Shyyan, R., Eniu, A., Smith, A., Yip, C.-H., Bese, N.S., Chow, L.W.C., Masood, S., Ramsey, S.D., Carlson, R.W., 2006. Breast Cancer in Limited-Resource Countries: An Overview of the Breast Health Global Initiative 2005 Guidelines. *The Breast Journal* 13. <https://doi.org/10.1111/j.1075-122X.2006.00199.x>.
- Ayyildiz, M., 2011. A NOVEL OPTO-ELECTRO-MECHANICAL TACTILE SENSOR FOR BREAST CANCER IMAGING (Masters Thesis). Koc University.
- Barr, R.G., Nakashima, K., Amy, D., Cosgrove, D., Farrokh, A., Schafer, F., Bamber, J.C., Castera, L., Choi, B.I., Chou, Y.-H., Dietrich, C.F., Ding, H., Ferraioli, G., Filice, C., Friedrich-Rust, M., Hall, T.J., Nightingale, K.R., Palmeri, M.L., Shiina, T., Suzuki, S., Sporea, I., Wilson, S., Kudo, M., 2015. WFUMB Guidelines and Recommendations for Clinical Use of Ultrasound Elastography: Part 2: Breast. *Ultrasound in Medicine & Biology* 41, 1148–1160. <https://doi.org/10.1016/j.ultrasmedbio.2015.03.008>
- Bhardwaj, A., Tiwari, A., 2015. Breast cancer diagnosis using Genetically Optimized Neural Network model. *Expert Systems with Applications* 42, 4611–4620. <https://doi.org/10.1016/j.eswa.2015.01.065>

- BHI Houston, 2020. MAMMOGRAM. Breast Health Institute Houston. URL <https://www.breastinstitutehouston.com/mammogram/> (accessed 12.23.20).
- Bian, J., Zhang, J., Hou, X., 2021. Diagnostic accuracy of ultrasound shear wave elastography combined with superb microvascular imaging for breast tumors: A protocol for systematic review and meta-analysis. *Medicine* 100, e26262. <https://doi.org/10.1097/MD.00000000000026262>
- Brandt, J.S., Rosen, T., Raalte, H.V., Kurtenos, V., Egorov, V., 2020. Characterization of Perineum Elasticity and Pubic Bone-Perineal Critical Distance with a Novel Tactile Probe: Results of an Intraobserver Reproducibility Study. *OJOG* 10, 493–503. <https://doi.org/10.4236/ojog.2020.1040044>
- Broach, R.B., Geha, R., Englander, B.S., DeLaCruz, L., Thrash, H., Brooks, A.D., 2016. A cost-effective handheld breast scanner for use in low-resource environments: a validation study. *World Journal of Surgical Oncology* 14. <https://doi.org/10.1186/s12957-016-1022-2>
- Brown, M., Lowe, D.G., 2007. Automatic Panoramic Image Stitching using Invariant Features. *Int J Comput Vision* 74, 59–73. <https://doi.org/10.1007/s11263-006-0002-3>
- Brusseau, E., Detti, V., Coulon, A., Maissiat, E., Boublay, N., Berthezene, Y., Fromageau, J., Bush, N., Bamber, J.C., 2013. In Vivo Response to Compression of 35 Breast Lesions Observed with a Two-Dimensional Locally Regularized Strain Estimation Method. *Ultrasound in Medicine and Biology* 40, 300–312. <https://doi.org/10.1016/j.ultrasmedbio.2013.02.017>
- Cao, R., Huang, Z., Varghese, T., Nabi, G., 2013. Tissue mimicking materials for the detection of prostate cancer using shear wave elastography: A validation study: Tissue mimicking materials for prostate cancer. *Med. Phys.* 40, 022903. <https://doi.org/10.1118/1.4773315>
- C.D Haagensen, 1986. *Diseases of the Breast*, 3rd ed. Saunders, Philadelphia.
- CDC, 2020. What Is a Mammogram? Breast Cancer. URL https://www.cdc.gov/cancer/breast/basic_info/mammograms.htm (accessed 12.23.20).
- Chen, X., Zhang, Z., Yu, S., Zsurzsan, T.-G., 2019. Fringing Effect Analysis of Parallel Plate Capacitors for Capacitive Power Transfer Application, in: 2019 IEEE 4th International Future Energy Electronics Conference (IFEEC). Presented at the 2019 IEEE 4th International Future Energy Electronics Conference (IFEEC), IEEE, Singapore, Singapore, pp. 1–5. <https://doi.org/10.1109/IFEEC47410.2019.9015111>
- Chino, K., Takahashi, H., 2018. Influence of pennation angle on measurement of shear wave elastography: in vivo observation of shear wave propagation in human pennate muscle. *Physiological Measurement* 39.
- Cleveland Clinic, 2019. Magnetic Resonance Imaging (MRI) and Breast Cancer: Test Details. Cleveland Clinic. URL <https://my.clevelandclinic.org/health/diagnostics/8332-mri--breast-cancer/test-details> (accessed 12.23.20).

- Coutts, L.V., Miller, N.R., Mortimer, P.S., Bamber, J.C., 2016. Investigation of In Vivo skin stiffness anisotropy in breast cancer related lymphoedema. *Journal of Biomechanics* 49, 94–99. <https://doi.org/10.1016/j.jbiomech.2015.11.043>
- de Campos, C.P., Corani, G., Scanagatta, M., Cuccu, M., Zaffalon, M., 2016. Learning extended tree augmented naive structures. *International Journal of Approximate Reasoning* 68, 153–163. <https://doi.org/10.1016/j.ijar.2015.04.006>
- de Souza, G.A.G.R., Brioschi, M.L., Vargas, J.V.C., Morais, K.C.C., Dalmaso Neto, C., Neves, E.B., 2015. Reference breast temperature: proposal of an equation. *Einstein (São Paulo)* 13, 518–524. <https://doi.org/10.1590/S1679-45082015AO3392>
- Dietrich, C., Barr, R., Farrokh, A., Dighe, M., Hocke, M., Jenssen, C., Dong, Y., Saftoiu, A., Havre, R., 2017. Strain Elastography - How To Do It? *Ultrasound Int Open* 03, E137–E149. <https://doi.org/10.1055/s-0043-119412>
- Egorov, V., Ayrapetyan, S., Sarvazyan, A.P., 2006. Prostate mechanical imaging: 3-D image composition and feature calculations. *IEEE Transactions on Medical Imaging* 25, 1329–1340. <https://doi.org/10.1109/TMI.2006.880667>
- Egorov, V., Kearney, T., Pollak, S.B., Rohatgi, C., Sarvazyan, N., Airapetian, S., Browning, S., Sarvazyan, A., 2009. Differentiation of benign and malignant breast lesions by mechanical imaging. *Breast Cancer Research and Treatment* 118, 67–80. <https://doi.org/10.1007/s10549-009-0369-2>
- Egorov, V., Lucente, V., Shobeiri, S.A., Takacs, P., Hoyte, L., 2019. Biomechanical Mapping of the Female Pelvic Floor: Uterine Prolapse Versus Normal Conditions 25.
- Egorov, V., Sarvazyan, A.P., 2008. Mechanical Imaging of the Breast. *IEEE Transactions on Medical Imaging* 27, 1275–1287. <https://doi.org/10.1109/TMI.2008.922192>
- Egorov, V., Tsyuryupa, S., Kanilo, S., Kogit, M., Sarvazyan, A., 2008. Soft tissue elastometer. *Medical Engineering & Physics* 30, 206–212. <https://doi.org/10.1016/j.medengphy.2007.02.007>
- Egorov, V., van Raalte, H., Sarvazyan, A.P., 2010. Vaginal Tactile Imaging. *IEEE Transactions on Biomedical Engineering* 57, 1736–1744. <https://doi.org/10.1109/TBME.2010.2045757>
- El-gayar, M.M., Soliman, H., meky, N., 2013. A comparative study of image low level feature extraction algorithms. *Egyptian Informatics Journal* 14, 175–181. <https://doi.org/10.1016/j.eij.2013.06.003>
- Elmesidy, D.S., Eissa, M.A.G.A.M., Hamed, S.T., Youssef, O.Z., Nada, O.M., Hashem, L.M.B., 2021. Axillary lymph node status in BIRADS 4-5 female patients: can shear wave and strain ultrasound elastography help? *Egypt J Radiol Nucl Med* 52, 176. <https://doi.org/10.1186/s43055-021-00560-8>
- Elyas, E., Papaevangelou, E., Alles, E.J., Erler, J.T., Cox, T.R., Robinson, S.P., Bamber, J.C., 2017. Correlation of Ultrasound Shear Wave Elastography with Pathological Analysis in a Xenografic Tumour Model. *Sci Rep* 7, 165. <https://doi.org/10.1038/s41598-017-00144-5>
- Ettelaie, A., Layeghi, M., Zarea Hosseinabadi, H., Ebrahimi, G., 2019. Prediction of modulus of elasticity of poplar wood using ultrasonic technique by applying

- empirical correction factors. *Measurement* 135, 392–399. <https://doi.org/10.1016/j.measurement.2018.11.076>
- Fan, B., Li, Q., Wang, C., Liu, T., 2017. An Adaptive Orientation Estimation Method for Magnetic and Inertial Sensors in the Presence of Magnetic Disturbances. *Sensors* 17, 1161. <https://doi.org/10.3390/s17051161>
- Farrugia, D.J., Fischer, T.D., Delitto, D., Spiguel, L.R., Shaw, C.M., 2015. Improved breast cancer care quality metrics after implementation of a standardized tumor board documentation template. *Journal of Oncology Practice* 11, 421–423.
- Frazier, S., Morgan, H., McBride, M., Angela, B., Mulvana, H., Graham, Delyth, 2019. Ultrasound and Microbubble Gene Delivery for Targeting Altered Placental MicroRNAs in Preeclampsia. *IEEE International Ultrasonics Symposium (IUS)* 1551–1555.
- Gentle, C.R., 1988. Mammobarography: a possible method of mass breast screening. *Journal of Biomedical Engineering* 10, 124–126. [https://doi.org/10.1016/0141-5425\(88\)90086-6](https://doi.org/10.1016/0141-5425(88)90086-6)
- Gu, J., Polley, E.C., Boughey, J.C., Fazzio, R.T., Fatemi, M., Alizad, A., 2021. Prediction of Invasive Breast Cancer Using Mass Characteristic Frequency and Elasticity in Correlation with Prognostic Histologic Features and Immunohistochemical Biomarkers. *Ultrasound in Medicine & Biology* 47, 2193–2201. <https://doi.org/10.1016/j.ultrasmedbio.2021.03.039>
- Guray, M., Sahin, A.A., 2006. Benign breast diseases: classification, diagnosis, and management. *The oncologist* 11, 435–449.
- Hampson, R., Dobie, G., West, G., 2019. Elasticity Measurement of Soft Tissues Using Hybrid Tactile and MARG-Based Displacement Sensor Systems. *IEEE Sensors J.* 19, 10262–10270. <https://doi.org/10.1109/JSEN.2019.2930207>
- Hansson, E., Manjer, J., Ringberg, A., 2014. Inter-observer reliability of clinical measurement of suprasternal notch-nipple distance and breast ptosis. *Indian Journal of Plastic Surgery* 47, 61. <https://doi.org/10.4103/0970-0358.129625>
- Haouchine, N., Dequidt, J., Berger, M.-O., Cotin, S., 2014. Single view augmentation of 3D elastic objects, in: 2014 IEEE International Symposium on Mixed and Augmented Reality (ISMAR). Presented at the 2014 IEEE International Symposium on Mixed and Augmented Reality (ISMAR), IEEE, Munich, Germany, pp. 229–236. <https://doi.org/10.1109/ISMAR.2014.6948432>
- Hara, Y., Yoshida, K., Khosla, A., Kawakami, M., Hosoda, K., Furukawa, H., 2020. Very Wide Sensing Range and Hysteresis Behaviors of Tactile Sensor Developed by Embedding Soft Ionic Gels in Soft Silicone Elastomers. *ECS J. Solid State Sci. Technol.* 9, 061024. <https://doi.org/10.1149/2162-8777/aba913>
- Hu, Q., Whitney, H.M., Giger, M.L., 2020. A deep learning methodology for improved breast cancer diagnosis using multiparametric MRI. *Sci Rep* 10, 10536. <https://doi.org/10.1038/s41598-020-67441-4>
- Jerison, D., Burgiel, H., 2010. Quadratic Approximation at 0 for Several Examples. MIT Press 18.01SC, 3.
- Jewell Instruments LLC., 2020. Tiltmeter Temperature Coefficients: Source, Definition and Use to Improve Accuracy.

- Jia, W., Luo, T., Dong, Y., Zhang, X., Zhan, W., Zhou, J., 2021. Breast Elasticity Imaging Techniques: Comparison of Strain Elastography and Shear-Wave Elastography in the Same Population. *Ultrasound in Medicine & Biology* 47, 104–113. <https://doi.org/10.1016/j.ultrasmedbio.2020.09.022>
- Jiang, L., Cai, Z., Wang, D., Zhang, H., 2012. Improving Tree augmented Naive Bayes for class probability estimation. *Knowledge-Based Systems* 26, 239–245. <https://doi.org/10.1016/j.knosys.2011.08.010>
- J.M. Morel, 2011. Is SIFT scale invariant? *Inverse Problems and Imaging* 5, 115–136. <https://doi.org/10.3934/ipi.2011.5.115>
- Kalinin, V., 2014. Modelling of hysteresis and creep in SAW strain sensors, in: 2014 IEEE International Frequency Control Symposium (FCS). Presented at the 2014 IEEE International Frequency Control Symposium (FCS), IEEE, Taipei, Taiwan, pp. 1–4. <https://doi.org/10.1109/FCS.2014.6859976>
- Karabatak, M., Ince, M.C., 2009. An expert system for detection of breast cancer based on association rules and neural network. *Expert Systems with Applications* 36, 3465–3469. <https://doi.org/10.1016/j.eswa.2008.02.064>
- Karami, E., Prasad, S., Shehata, M., 2017. Image Matching Using SIFT, SURF, BRIEF and ORB: Performance Comparison for Distorted Images 5.
- Khan, A., Mineo, C., Dobie, G., Macleod, C., Pierce, G., 2020. Vision guided robotic inspection for parts in manufacturing and remanufacturing industry. *Jnl Remanufactur.* <https://doi.org/10.1007/s13243-020-00091-x>
- Krogh, M.R., Nghiem, G.M., Halvorsen, P.S., Elle, O.J., Grymyr, O.-J., Hoff, L., Remme, E.W., 2017. Gravity Compensation Method for Combined Accelerometer and Gyro Sensors Used in Cardiac Motion Measurements. *Annals of Biomedical Engineering* 45, 1292–1304. <https://doi.org/10.1007/s10439-017-1798-4>
- Kuhl, C.K., Keulers, A., Strobel, K., Schneider, H., Gaisa, N., Schradung, S., 2018. Not all false positive diagnoses are equal: On the prognostic implications of false-positive diagnoses made in breast MRI versus in mammography / digital tomosynthesis screening. *Breast Cancer Res* 20, 13. <https://doi.org/10.1186/s13058-018-0937-7>
- Laura Di Sieno, Hélène Sportouche, David Savéry, Sanathana Konugolu Venkata Sekara, Bogdan Rosinski, Andrea Farina, Edoardo Ferocino, Pranav Lanka, Paola Taroni, Antonio Pifferi, Alberto Dalla Mor, Rinaldo Cubeddu, 2019. Solid heterogeneous phantoms for multimodal ultrasound and diffuse optical imaging: an outcome of the SOLUS project for standardization, in: *Novel Biophonics Techniques and Applications V*. Presented at the European Conferences on Biomedical Optics, Munich, Germany. <https://doi.org/10.1117/12.2526645>
- Laxminarayan, R., Chow, J., Shahid-Salles, S.A., 2006. *Intervention Cost-Effectiveness: Overview of Main Messages. Disease Control Priorities in Developing Countries.* 2nd edition. 52.
- Lee, J.M., Arao, R.F., Sprague, B.L., Kerlikowske, K., Lehman, C.D., Smith, R.A., Henderson, L.M., Rauscher, G.H., Miglioretti, D.L., 2019. Performance of Screening Ultrasonography as an Adjunct to Screening Mammography in

- Women Across the Spectrum of Breast Cancer Risk. *JAMA Intern Med* 179, 658. <https://doi.org/10.1001/jamainternmed.2018.8372>
- Lefemine, V., Osborn, G., Mainwaring, A., Goyal, S., 2012. Have Standardised Referral Forms Reduced the Number of Inappropriate Referrals to Breast Clinic? *Bulletin* 94, 1–3. <https://doi.org/10.1308/147363512X13189526438954>
- Levkovich, I., Cohen, M., Pollack, S., Drumea, K., Fried, G., 2015. Cancer-related fatigue and depression in breast cancer patients postchemotherapy: Different associations with optimism and stress appraisals. *Palliative and Supportive Care* 13, 1141–1151. <https://doi.org/10.1017/S147895151400087X>
- Liang, W., Lawrence, W.F., Burnett, C.B., Hwang, Y.-T., Freedman, M., Trock, B.J., Mandelblatt, J.S., Lippman, M.E., 2003. Acceptability of Diagnostic Tests for Breast Cancer. *Breast Cancer Res Treat* 79, 199–206. <https://doi.org/10.1023/A:1023914612152>
- Liao, X., Qiu, Z., Jiang, T., Sadiq, M., Huang, Z., Demore, C., Cochran, S., 2015. Functional Piezocrystal Characterisation under Varying Conditions. *Materials* 8, 8304–8326. <https://doi.org/10.3390/ma8125456>
- Liu, G., Zhang, M.-K., He, Y., Li, X.-R., Wang, Z.-L., 2019. Shear wave elasticity of breast lesions: would it be correlated with the extracellular matrix components? *Gland Surg.* 8, 399–406. <https://doi.org/10.21037/gs.2019.04.09>
- Lowe, D.G., 2004. Distinctive Image Features from Scale-Invariant Keypoints. *International Journal of Computer Vision* 60, 91–110. <https://doi.org/10.1023/B:VISI.0000029664.99615.94>
- Lozano, A., Hayes, J.C., Compton, L.M., Azarnoosh, J., Hassanipour, F., 2020. Determining the thermal characteristics of breast cancer based on high-resolution infrared imaging, 3D breast scans, and magnetic resonance imaging. *Sci Rep* 10, 10105. <https://doi.org/10.1038/s41598-020-66926-6>
- Lubkowska, A., Chudecka, M., 2021. Thermal Characteristics of Breast Surface Temperature in Healthy Women. *IJERPH* 18, 1097. <https://doi.org/10.3390/ijerph18031097>
- Madgwick, S.O., Harrison, A.J., Vaidyanathan, R., 2011. Estimation of IMU and MARG orientation using a gradient descent algorithm, in: *Rehabilitation Robotics (ICORR), 2011 IEEE International Conference On.* IEEE, pp. 1–7.
- M.A.Fischler, R.C. Bolles, 1981. Random Sample Consensus: A Paradigm for Model Fitting with Applications to Image Analysis and Automated Cartography. *Comm. of the ACM* 24, 381–395.
- Mandrik, O., Ekwunife, O.I., Meheus, F., Severens, J.L. (Hans), Lhachimi, S., Uyl-de Groot, C.A., Murillo, R., 2019. Systematic reviews as a “lens of evidence”: Determinants of cost-effectiveness of breast cancer screening. *Cancer Med* 8, 7846–7858. <https://doi.org/10.1002/cam4.2498>
- Manickam, K., Machireddy, R.R., Seshadri, S., 2014. Characterization of biomechanical properties of agar based tissue mimicking phantoms for ultrasound stiffness imaging techniques. *Journal of the Mechanical Behavior of Biomedical Materials* 35, 132–143. <https://doi.org/10.1016/j.jmbbm.2014.03.017>
- Matsumura, T., Umemoto, T., Fujihara, Y., Ueno, E., Yamakawa, M., Shiina, T., Mitake, T., 2009. Measurement of elastic property of breast tissue for elasticity imaging,

- in: 2009 IEEE International Ultrasonics Symposium. Presented at the 2009 IEEE International Ultrasonics Symposium, IEEE, Rome, Italy, pp. 1451–1454. <https://doi.org/10.1109/ULTSYM.2009.5442044>
- McCain, S., Newell, J., Badger, S., Kennedy, R., Kirk, S., 2011. Referral patterns, clinical examination and the two-week-rule for breast cancer: a cohort study. *Ulster Medical Journal* 80, 4.
- Memorial Sloan Kettering Cancer Centre, 2021. Anatomy of the Breast. URL <https://www.mskcc.org/cancer-care/types/breast/anatomy-breast> (accessed 8.22.21).
- Micheletti, N., Chandler, J.H., Lane, S.N., 2015. Structure from Motion (SfM) Photogrammetry. *Geomorphological Techniques* 13.
- Morel, J.-M., Yu, G., 2009. ASIFT: A New Framework for Fully Affine Invariant Image Comparison. *SIAM J. Imaging Sci.* 2, 438–469. <https://doi.org/10.1137/080732730>
- Morgan, L.E., 2018. *Quantifying and Reducing Input Modelling Error in Simulation*. Lancaster.
- Mulvana, H., Stride, E., Tang, M.-X., Hajnal, J.V., Eckersley, R.J., 2011. Temperature-dependent differences in the nonlinear acoustic behavior of ultrasound contrast agents revealed by high-speed imaging and bulk acoustics. *Ultrasound in Medicine and Biology* 37, 1509–1517.
- Nahid, A.-A., Kong, Y., 2017. Involvement of Machine Learning for Breast Cancer Image Classification: A Survey. *Computational and Mathematical Methods in Medicine* 2017, 1–29. <https://doi.org/10.1155/2017/3781951>
- NASA, 2012. Technology Readiness Level. URL https://www.nasa.gov/directorates/heo/scan/engineering/technology/txt_accordio_n1.html (accessed 3.22.21).
- Neto, P., Pires, J.N., Moreira, A.P., 2013. 3-D position estimation from inertial sensing: minimizing the error from the process of double integration of accelerations, in: *Industrial Electronics Society, IECON 2013-39th Annual Conference of the IEEE*. IEEE, pp. 4026–4031.
- NHS, 2018. Why it's offered. Breast Cancer Screening. URL <https://www.nhs.uk/conditions/breast-cancer-screening/why-its-offered/> (accessed 10.29.20).
- NICE, 2020a. Suspected cancer recognition and referral: site or type of cancer.
- NICE, 2020b. Suspected cancer: recognition and referral. NG12 86.
- NICE, 2018. Early and locally advanced breast cancer: diagnosis and management. NG101 61.
- Nioka, S., Chance, B., 2005. NIR Spectroscopic Detection of Breast Cancer. *Technol Cancer Res Treat* 4, 497–512. <https://doi.org/10.1177/153303460500400504>
- Nuari, M.R., Utami, E., Raharjo, D.S., 2019. Comparison of Scale Invariant Feature Transform and Speed Up Robust Feature for Image Forgery Detection Copy Move 6.
- Oleksyuk, V., Saleheen, F., Caroline, D.F., Pascarella, S.A., Won, C.-H., 2016. Classification of breast masses using Tactile Imaging System and machine learning algorithms. *IEEE*, pp. 1–4. <https://doi.org/10.1109/SPMB.2016.7846857>

- Oleksyuk, V., Saleheen, F., Yi Chen, Won, C.-H., 2015. Tactile Imaging System for inclusion size and stiffness characterization. *IEEE*, pp. 1–6. <https://doi.org/10.1109/SPMB.2015.7405472>
- Onan, A., 2015. A fuzzy-rough nearest neighbor classifier combined with consistency-based subset evaluation and instance selection for automated diagnosis of breast cancer. *Expert Systems with Applications* 42, 6844–6852. <https://doi.org/10.1016/j.eswa.2015.05.006>
- Ozdemir, M., Ozdemir, G., Eroglu, O., 2018. Investigating Ballistic Gelatin Based Phantom Properties for Ultrasound Training, in: IFMBE. Presented at the World Congress on Medical Physics and Biomedical Engineering 2018, Singapore, pp. 789–793. https://doi.org/10.1007/978-981-10-9035-6_145
- Papoular, R.J., Papoular, R., 2014. Some optical properties of graphite from IR to millimetric wavelengths. *Monthly Notices of the Royal Astronomical Society* 443, 2974–2982. <https://doi.org/10.1093/mnras/stu1348>
- Park, S., Kang, B.J., 2021. Combination of shear-wave elastography with ultrasonography for detection of breast cancer and reduction of unnecessary biopsies: a systematic review and meta-analysis. *Ultrasonography* 40, 318–332. <https://doi.org/10.14366/usg.20058>
- Pierleoni, P., Belli, A., Palma, L., Mercuri, M., Verdini, F., Fioretti, S., Madgwick, S., Pinti, F., 2019. Validation of a Gait Analysis Algorithm for Wearable Sensors, in: 2019 International Conference on Sensing and Instrumentation in IoT Era (ISSI). Presented at the 2019 International Conference on Sensing and Instrumentation in IoT Era (ISSI), IEEE, Lisbon, Portugal, pp. 1–6. <https://doi.org/10.1109/ISSI47111.2019.9043647>
- Public Health England, 2018. Easy Guide to Breast Screening.
- Quieregatto, P.R., Hochman, B., Furtado, F., Machado, A.F.P., Sabino Neto, M., Ferreira, L.M., 2014. Image analysis software versus direct anthropometry for breast measurements. *Acta Cirurgica Brasileira* 29, 688–695. <https://doi.org/10.1590/S0102-8650201400160010>
- Rahni, A.A.A., Yahya, I., 2007. Obtaining translation from a 6-DOF MEMS IMU—an overview, in: Applied Electromagnetics, 2007. APACE 2007. Asia-Pacific Conference On. IEEE, pp. 1–5.
- Rana, S., Hampson, R., Dobie, G., 2020. Breast Cancer: Model Reconstruction and Image Registration From Segmented Deformed Image Using Visual and Force Based Analysis. *IEEE Trans. Med. Imaging* 39, 1295–1305. <https://doi.org/10.1109/TMI.2019.2946629>
- Rangayyan, R.M., El-Faramawy, N.M., Desautels, J.L., Alim, O.A., 1997. Measures of acutance and shape for classification of breast tumors. *IEEE Transactions on medical imaging* 16, 799–810.
- Regal, S., Troughton, J., Delattre, R., Djenizian, T., Ramuz, M., 2020. Changes in temperature inside an optomechanical model of the human eye during emulated transscleral cyclophotocoagulation. *Biomed. Opt. Express* 11, 4548. <https://doi.org/10.1364/BOE.385016>
- Richard H. Gold, Lawrence W, Bassett, Bobbi E. Widoff, 1990. Highlights from the history of mammography.

- Robert J Miller, 2020a. BREAST MAGNETIC RESONANCE IMAGING. About Cancer. URL http://www.aboutcancer.com/breast_mri_textbook.htm (accessed 12.23.20).
- Robert J Miller, 2020b. Breast Cancer Imaging Studies. About Cancer. URL http://www.aboutcancer.com/breast_cancer_imaging_misc.htm (accessed 12.23.20).
- Roylance, D., 2001. ENGINEERING VISCOELASTICITY. 3-11 mechanics of materials, Materials Science and Engineering 38.
- Rudin, C., 2019. Stop Explaining Black Box Machine Learning Models for High Stakes Decisions and Use Interpretable Models Instead. arXiv:1811.10154 [cs, stat].
- Ryan Roeder, 2013. Mechanical Characterization of Biomaterials, in: Characterization of Biomaterials. Academic Press.
- Rzymyski, P., Skórzewska, A., Skibińska-Zielińska, M., Opala, T., 2011. Factors influencing breast elasticity measured by the ultrasound Shear Wave elastography – preliminary results. *aoms* 1, 127–133. <https://doi.org/10.5114/aoms.2011.20617>
- Sahu, A., Saleheen, F., Oleksyuk, V., Chen, Y., Won, C.-H., 2013. Tactile and hyperspectral imaging sensors for mammary tumor characterization. *IEEE*, pp. 1–4. <https://doi.org/10.1109/ICSENS.2013.6688136>
- Sahu, A., Saleheen, F., Oleksyuk, V., McGoverin, C., Pleshko, N., Torbati, A.H.H.N., Picone, J., Sorenmo, K., Won, C.-H., 2014. Characterization of Mammary Tumors Using Noninvasive Tactile and Hyperspectral Sensors. *IEEE Sensors Journal* 14, 3337–3344. <https://doi.org/10.1109/JSEN.2014.2323215>
- Saleheen, F., Oleksyuk, V., Sahu, A., Won, C.-H., 2013. Non-invasive mechanical properties estimation of embedded objects using tactile imaging sensor, in: Cullum, B.M., McLamore, E.S. (Eds.), . p. 87190K. <https://doi.org/10.1117/12.2015803>
- Samani, A., Zubovits, J., Plewes, D., 2007. Elastic moduli of normal and pathological human breast tissues: an inversion-technique-based investigation of 169 samples. *Phys. Med. Biol.* 52, 1565–1576. <https://doi.org/10.1088/0031-9155/52/6/002>
- Sanchez, J., Mateo, C.M., Corrales, J.A., Bouzgarrou, B.-C., Mezouar, Y., 2018. Online Shape Estimation based on Tactile Sensing and Deformation Modeling for Robot Manipulation, in: 2018 IEEE/RSJ International Conference on Intelligent Robots and Systems (IROS). Presented at the 2018 IEEE/RSJ International Conference on Intelligent Robots and Systems (IROS), IEEE, Madrid, pp. 504–511. <https://doi.org/10.1109/IROS.2018.8594314>
- Sánchez-Durán, J., Vidal-Verdú, F., Oballe-Peinado, Ó., Castellanos-Ramos, J., Hidalgo-López, J., 2015. A New Model Based on Adaptation of the External Loop to Compensate the Hysteresis of Tactile Sensors. *Sensors* 15, 26170–26197. <https://doi.org/10.3390/s151026170>
- Sarvazyan, A., 1998. Mechanical imaging:: A new technology for medical diagnostics. *International journal of medical informatics* 49, 195–216.
- Sarvazyan, A., Egorov, V., 2012. Mechanical imaging-a technology for 3-D visualization and characterization of soft tissue abnormalities: a review. *Current medical imaging reviews* 8, 64–73.

- Sarvazyan, A., Egorov, V., Son, J.S., Kaufman, C.S., 2008. Cost-effective screening for breast cancer worldwide: current state and future directions. *Breast cancer: basic and clinical research* 1, 91.
- Sarvazyan, A.P., 1997. Knowledge-based mechanical imaging, in: *Computer-Based Medical Systems*, 1997. Proceedings., Tenth IEEE Symposium On. IEEE, pp. 120–125.
- Sarvazyan, A.P., Egorov, V., 2009. Mechanical imaging in medical applications, in: *Engineering in Medicine and Biology Society*, 2009. EMBC 2009. Annual International Conference of the IEEE. IEEE, pp. 1975–1978.
- Sensortec, B., 2020. BNO055 Intelligent 9-axis absolute orientation sensor Datasheet.
- Shen, L., Margolies, L.R., Rothstein, J.H., Fluder, E., McBride, R., Sieh, W., 2019. Deep Learning to Improve Breast Cancer Detection on Screening Mammography. *Sci Rep* 9, 12495. <https://doi.org/10.1038/s41598-019-48995-4>
- Shin-Etsu Chemical Co, 2016. Characteristic properties of Silicone Rubber Compounds [WWW Document]. Meeting the increasingly diverse and sophisticated needs of industry with the unique properties of silicone rubbers. URL https://www.shinetsusilicone-global.com/catalog/pdf/rubber_e.pdf (accessed 1.27.21).
- Summan, R., 2015. Spatial calibration of large volume photogrammetry based metrology systems 12.
- Summan, R., Jackson, W., Dobie, G., MacLeod, C., Mineo, C., West, G., Offin, D., Bolton, G., Marshall, S., Lille, A., 2018. A novel visual pipework inspection system. Presented at the 44TH ANNUAL REVIEW OF PROGRESS IN QUANTITATIVE NONDESTRUCTIVE EVALUATION, VOLUME 37, Provo, Utah, USA, p. 220001. <https://doi.org/10.1063/1.5031647>
- Tao, J., Dong, M., Li, L., Wang, C., Li, J., Liu, Y., Bao, R., Pan, C., 2020. Real-time pressure mapping smart insole system based on a controllable vertical pore dielectric layer. *Microsyst Nanoeng* 6, 62. <https://doi.org/10.1038/s41378-020-0171-1>
- Tasoulis, M.-K., Zacharioudakis, K.E., Dimopoulos, N.G., Hadjiminias, D.J., 2014. Diagnostic accuracy of tactile imaging in selecting patients with palpable breast abnormalities: a prospective comparative study. *Breast Cancer Res Treat* 147, 589–598. <https://doi.org/10.1007/s10549-014-3123-3>
- Tian, J., Liu, Q., Wang, X., Xing, P., Yang, Z., Wu, C., 2017. Application of 3D and 2D quantitative shear wave elastography (SWE) to differentiate between benign and malignant breast masses. *Sci Rep* 7, 41216. <https://doi.org/10.1038/srep41216>
- Triggs, B., McLauchlan, P.F., Hartley, R.I., Fitzgibbon, A.W., 2000. Bundle Adjustment — A Modern Synthesis, in: Triggs, B., Zisserman, A., Szeliski, R. (Eds.), *Vision Algorithms: Theory and Practice*, Lecture Notes in Computer Science. Springer Berlin Heidelberg, Berlin, Heidelberg, pp. 298–372. https://doi.org/10.1007/3-540-44480-7_21
- UC Davies Health, 2020. Dedicated Breast CT Research. UCDavies Health Department of Radiology. URL <https://health.ucdavis.edu/radiology/research/bcti.html> (accessed 12.23.20).

- Vaicekauskaite, J., Mazurek, P., Vudayagiri, S., Skov, A.L., 2020. Mapping the mechanical and electrical properties of commercial silicone elastomer formulations for stretchable transducers. *J. Mater. Chem. C* 8, 1273–1279. <https://doi.org/10.1039/C9TC05072H>
- Valenti, R., Dryanovski, I., Xiao, J., 2015. Keeping a Good Attitude: A Quaternion-Based Orientation Filter for IMUs and MARGs. *Sensors* 15, 19302–19330. <https://doi.org/10.3390/s150819302>
- Verma, B., McLeod, P., Klevansky, A., 2010. Classification of benign and malignant patterns in digital mammograms for the diagnosis of breast cancer. *Expert Systems with Applications* 37, 3344–3351. <https://doi.org/10.1016/j.eswa.2009.10.016>
- Walt Boyes, 2010. *Instrumentation Reference Book - Chapter 21*, 4th ed. Elsevier.
- Wellman, P., Howe, R.D., Dalton, E., Kern, K.A., 1999a. Breast tissue stiffness in compression is correlated to histological diagnosis. *Harvard BioRobotics Laboratory Technical Report* 1–15.
- Wellman, P., Howe, R.D., Dewagan, N., Cundari, M.A., Dalton, E., Kern, K.A., 1999b. Tactile imaging: a method for documenting breast masses, in: [Engineering in Medicine and Biology, 1999. 21st Annual Conference and the 1999 Annual Fall Meeting of the Biomedical Engineering Society] *BMES/EMBS Conference, 1999. Proceedings of the First Joint. IEEE*, pp. 1131-vol.
- Wellman, P.S., 1999. *Tactile Imaging - PhD Thesis*. Harvard University Press.
- Woods, R.W., Sisney, G.S., Salkowski, L.R., Shinki, K., Lin, Y., Burnside, E.S., 2011. The mammographic density of a mass is a significant predictor of breast cancer. *Radiology* 258, 417–425.
- Yang, H., Xu, Y., Zhao, Y., Yin, J., Chen, Z., Huang, P., 2020. The role of tissue elasticity in the differential diagnosis of benign and malignant breast lesions using shear wave elastography. *BMC Cancer* 20, 930. <https://doi.org/10.1186/s12885-020-07423-x>
- Yip, M., He, D.D., Winokur, E., Balderrama, A.G., Sheridan, R., Hongshen Ma, 2009. A flexible pressure monitoring system for pressure ulcer prevention, in: 2009 Annual International Conference of the IEEE Engineering in Medicine and Biology Society. Presented at the 2009 Annual International Conference of the IEEE Engineering in Medicine and Biology Society, IEEE, Minneapolis, MN, pp. 1212–1215. <https://doi.org/10.1109/IEMBS.2009.5333964>
- Youk, J.H., Gweon, H.M., Son, E.J., 2017. Shear-wave elastography in breast ultrasonography: the state of the art. *Ultrasonography* 36, 300–309. <https://doi.org/10.14366/usg.17024>
- Yu, G., Morel, J.-M., 2011. ASIFT: An Algorithm for Fully Affine Invariant Comparison. *Image Processing On Line* 1. <https://doi.org/10.5201/ipol.2011.my-asift>
- Yun, X., Bachmann, E.R., Moore, H., Calusdian, J., 2007. Self-contained position tracking of human movement using small inertial/magnetic sensor modules, in: *Robotics and Automation, 2007 IEEE International Conference On. IEEE*, pp. 2526–2533.

- Zhang, S., Graeme, George, Qiao, P., Huang, Z., Xia, C., 2020a. Needle-tissue interaction force study during simulated regional anaesthesia. *J. Phys.: Conf. Ser.* 1544, 012064. <https://doi.org/10.1088/1742-6596/1544/1/012064>
- Zhang, S., Graeme, George, Qiao, P., Huang, Z., Xia, C., 2020b. Ultrasound-guided Needle nerve contact positions detection in Regional Anaesthesia using Needle tip force and Opening injection pressure. *J. Phys.: Conf. Ser.* 1544, 012126. <https://doi.org/10.1088/1742-6596/1544/1/012126>
- Zharov, V.P., Ferguson, S., Eidt, J.F., Howard, P.C., Fink, L.M., Waner, M., 2004. Infrared imaging of subcutaneous veins. *Lasers Surg. Med.* 34, 56–61. <https://doi.org/10.1002/lsm.10248>
- Zheng, B., Yoon, S.W., Lam, S.S., 2014. Breast cancer diagnosis based on feature extraction using a hybrid of K-means and support vector machine algorithms. *Expert Systems with Applications* 41, 1476–1482. <https://doi.org/10.1016/j.eswa.2013.08.044>

Appendix A

Example Referral Forms

A.1. Description of Referral Forms


Section A.2 contains examples of current UK NHS breast cancer referral forms from 3 NHS trusts in England. The forms contain basically the same information; however, it is clear from a cursory glance that these forms offer significantly different levels of detail and are arranged in ascending order of detail. An example of this is in form 1 there is no field for whether breast cancer is suspected, which is present in forms 2 and 3, but it is hidden in the request for symptoms. From looking at the forms, form 2 from NHS Heart of England has the best balance between length and detail, being compressed onto a single page whilst detailing the particulars of the patient and the breast condition that can be determined during the CBE. Additionally, the employment of a high quality and representative diagram for lesion location is felt to improve the reception of the form to physicians and reduces confusion in further tests (Lefemine et al., 2012). The forms, although basically containing the same things such as patient particulars, symptoms, and a location of the condition; often ask different questions not present in other forms such as whether the patient has had a mammogram/radiology/pathology recently.

A.2. Referral Forms from Various NHS Trusts

Southampton NHS University Hospitals NHS Trust	Fax: (023) 8082 5586 If you experience any problem sending this information, please telephone: Tel: (023) 8082 5587
---	--

URGENT SUSPECTED BREAST CANCER REFERRAL FORM

Name: Address: Tel no. Home: Work:	Sex: Date of birth: Hospital number NHS number:	Registered GP Name: Surgery address: Tel. no: Fax: e mail:
Date of referral: New referral <input type="checkbox"/> Re-referral <input type="checkbox"/>	Referring GP name (if different)	

Signs/symptoms: Discrete lump > 30 years <input type="checkbox"/> Asymmetry or puckering <input type="checkbox"/> Bloody nipple discharge <input type="checkbox"/> Recurrence of cancer <input type="checkbox"/>	Examination: 
Past history: Mammogram in last 12 months <input type="checkbox"/> Where:	Family history <input type="checkbox"/>
Radiology in last 6 months <input type="checkbox"/> Where:	Previous history of breast disease <input type="checkbox"/>
Pathology in last 6 months <input type="checkbox"/> Where:	HRT <input type="checkbox"/>
GP SIGNATURE ESSENTIAL PLEASE SUHT to complete imaging as required	

Is this patient aware that they are being referred on a suspected cancer pathway yes/no

Is the patient available to attend within the next 14 days yes/no

If no, from what date is the patient available.....

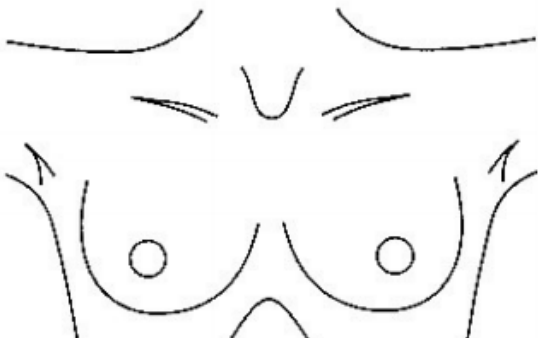
Dear Doctor:

The information contained in this facsimile is intended for the named recipients only.
 It may contain privileged and confidential information and if you are not an intended recipient, you must not copy or distribute it.
 If you have received this facsimile in error, please notify us immediately by telephone on (023) 8082 5587
 Version 7 01/10/2004

REFERRAL FORM FOR PATIENTS WITH BREAST SYMPTOMS (Version 4.0)
If you wish to include an accompanying letter, please do so. **On completion please FAX to the number below.**

ALL PATIENTS WILL BE OFFERED AN APPOINTMENT WITHIN TWO WEEKS OF RECEIPT OF THIS FORM

Please complete all of the fields below as accurately as possible:

Patient Details		GP Details (inc. Fax Number)	
Surname:	NHS No:		
Forename:	Hospital No:		
Address:			
Postcode:		Tel No:	Fax No:
Telephone:		Date of decision to refer:	
Interpreter required? Yes/No	Language:	Date referral made:	
Please indicate whether or not you feel this patient is likely to have breast cancer: Yes <input type="checkbox"/> (Please complete only Section A below) No <input type="checkbox"/> (Please complete only Section B below) NB. Patients will be offered an appointment within 2 weeks regardless of whether or not cancer is initially suspected.		GP signature	
Section A – Suspected breast cancer <ul style="list-style-type: none"> • >30 with discrete mass post period/ menopause <input type="checkbox"/> • <30 with persistent fixed, hard or enlarging lump <input type="checkbox"/> • Lump/ suspicious symptoms in patient with previous carcinoma-in-situ of breast or breast cancer, any age <input type="checkbox"/> • Eczematous nipple change or nipple retraction of recent onset <input type="checkbox"/> • Blood stained nipple discharge <input type="checkbox"/> • Man >50 with unilateral firm subareolar mass <input type="checkbox"/> 		Please indicate the site of the problem: Right: Left: 	
Section B – Breast cancer not initially suspected <ul style="list-style-type: none"> • Breast pain <input type="checkbox"/> • Non blood stained nipple discharge <input type="checkbox"/> • Family history <input type="checkbox"/> • Other breast lump in women < 30 years <input type="checkbox"/> 		Clinical Details: Date/place of last mammogram: _____	
Relevant medical history: _____			
Current medications: _____			
For office use: Was the referral appropriate? Yes / No (if no please give reason) _____			
BREAST CLINICS WITH RAPID ACCESS FACILITIES			
Hospital	Tel	Method of Referral	
Heart of England	0121 424 5000	Choose & Book or bhs-tr.2ww-referrals@nhs.net	

GP Declaration

- I have informed the patient they have suspected Breast cancer or symptoms which may be caused by cancer and that they are being referred to the rapid access suspected cancer clinic.
- I have provided the patient with a 2 week wait information leaflet.
- My patient has confirmed they are available to attend within 2 weeks.

1)

SUSPECT BREAST CANCER REFERRAL (2 week wait)
SYMPTOMATIC BREAST REFERRAL (2 week wait)
FAMILY HISTORY REFERRAL (not 2 week wait)
RECONSTRUCTIVE REFERRAL (not 2 week wait)

Please note that all **2 week wait referrals** (suspected cancer and symptomatic referrals) should now come through the **Referral Assessment Service (RAS)** on eRS.

BaNES CCG have asked that all non 2 week wait referrals (family history and reconstructive) should go via the eRS RSS.

This form should be used for patients who meet the NICE referral criteria for suspect cancer (June 2015) and any other Breast problem.

NHS BANES & WILTSHIRE REFERRAL PROCESS

PLEASE ONLY REFER PATIENTS WHO ARE AVAILABLE TO BE SEEN IN THE
NEXT 14 DAYS
(EXCEPT Family History and other asymptomatic referrals non 2 week wait)

Section 1 PATIENT INFORMATION		<i>(Please complete form in BLOCK CAPITALS)</i>	
Date of Referral		Patient available from	
Surname		First Name	
Male ()	Female ()	Mr Mrs Miss Other	Date of Birth
ADDRESS		NHS number	
POST CODE		RUH Reg No	
EXPLICIT PERMISSION to contact patient		YES () NO ()	
Via Mobile Number () _____		via Day number () _____	
Transport YES () NO ()		Interpreter YES () NO () Language	

Section 2 PRACTICE INFORMATION		<i>(Please use practice stamp if available)</i>	
Referring GP		Telephone	
Practice Name		Fax	
Address		Email	
Post Code			

Section 3: CLINICAL INFORMATION (please tick all applicable entries) please enclose print outs of CURRENT medications and PAST MEDICAL HISTORY

PMH BREAST DISEASE YES () NO () WHEN _____
 CONSULTANT SEEN _____ WHERE _____

PLEASE INDICATE BY TICKING ONE BOX BELOW

- | | |
|---|--|
| <input type="checkbox"/> URGENT REFERRAL SUSPECTS BREAST CANCER
Seen within 2 weeks | <input type="checkbox"/> FAMILY HISTORY
not seen within 2 weeks |
| <input type="checkbox"/> ROUTINE BREAST REFERRAL
Seen within 2 weeks | <input type="checkbox"/> RECONSTRUCTIVE REFERRAL
not seen within 2 weeks |

ALL SYMPTOMATIC PATIENTS SEEN WITHIN 2 WEEKS

Please continue to indicate clinical suspicion to help assign most appropriate appointment.

URGENT REFERRAL ADVISED

- Age 30 and over, have an unexplained / discrete breast lump with or without pain
- Have skin changes that suggest breast cancer
Tether / contour change
- Age 50 and over with any of the following symptoms in one nipple only
 - blood stain / other discharge
 - inversion / retraction / ulceration
 - other changes or concern
- Age 30 and over with unexplained lump in the axilla

NON - URGENT REFERRAL ADVISED

- Age 30 and under unexplained / discrete breast lump
- Breast pain *if initial treatment fails* and / or with unexplained persistent symptoms
- Persistent nipple discharge
- Abscess / mastitis
- Recurrent cyst

CLINICAL EXAMINATION



Comments

INVESTIGATIONS

MEDICAL HISTORY KNOWN ALLERGIES AND MEDICATION

Section 4: REFERRAL MONITORING INFORMATION

Decision to refer date:

Referral received date:

Has this urgent suspected cancer referral been discussed with the patient?	Y	N
Does the patient understand that this referral is being made for a suspected cancer?	Y	N
Has the patient been given the relevant patient information literature?	Y	N

Section 5: CRITERIA FOR URGENT SUSPECTED CANCER REFERRAL

This section provides a link to the NICE GUIDANCE in respect of Breast Cancer and supplies contact details of the provider and department

<https://www.nice.org.uk/guidance/ng12>

To access information about suspect breast cancer, follow the above link and click on section 1.4

For breast pain:

http://www.ruh.nhs.uk/patients/services/breast_unit/common_problems/mastalgia.asp?menu_id=12

For symptomatic breast problems:

http://www.associationofbreastsurgery.org.uk/media/4585/best_practice_diagnostic_guidelines_for_patients_presenting_with_breast_symptoms.pdf

For Family History breast cancer guidance:

<http://www.nice.org.uk/guidance/CG164>

Queries about The breast Unit Service at The Royal United Hospital can be addressed by:

THE BREAST UNIT
ROYAL UNITED HOSPITAL NHS TRUST
ZONE B DEPT B3
COOMBE PARK
BATH
BA1 2NG

01225 825881/2

General queries about the two week wait process for suspected breast cancers should be addressed to the Cancer Manager, Edward Nicolle on Edward.nicolle@nhs.net
Or 01225 824042.

The link to the RUH website for breast cancer is :
www.ruh.nhs.uk/breastunit

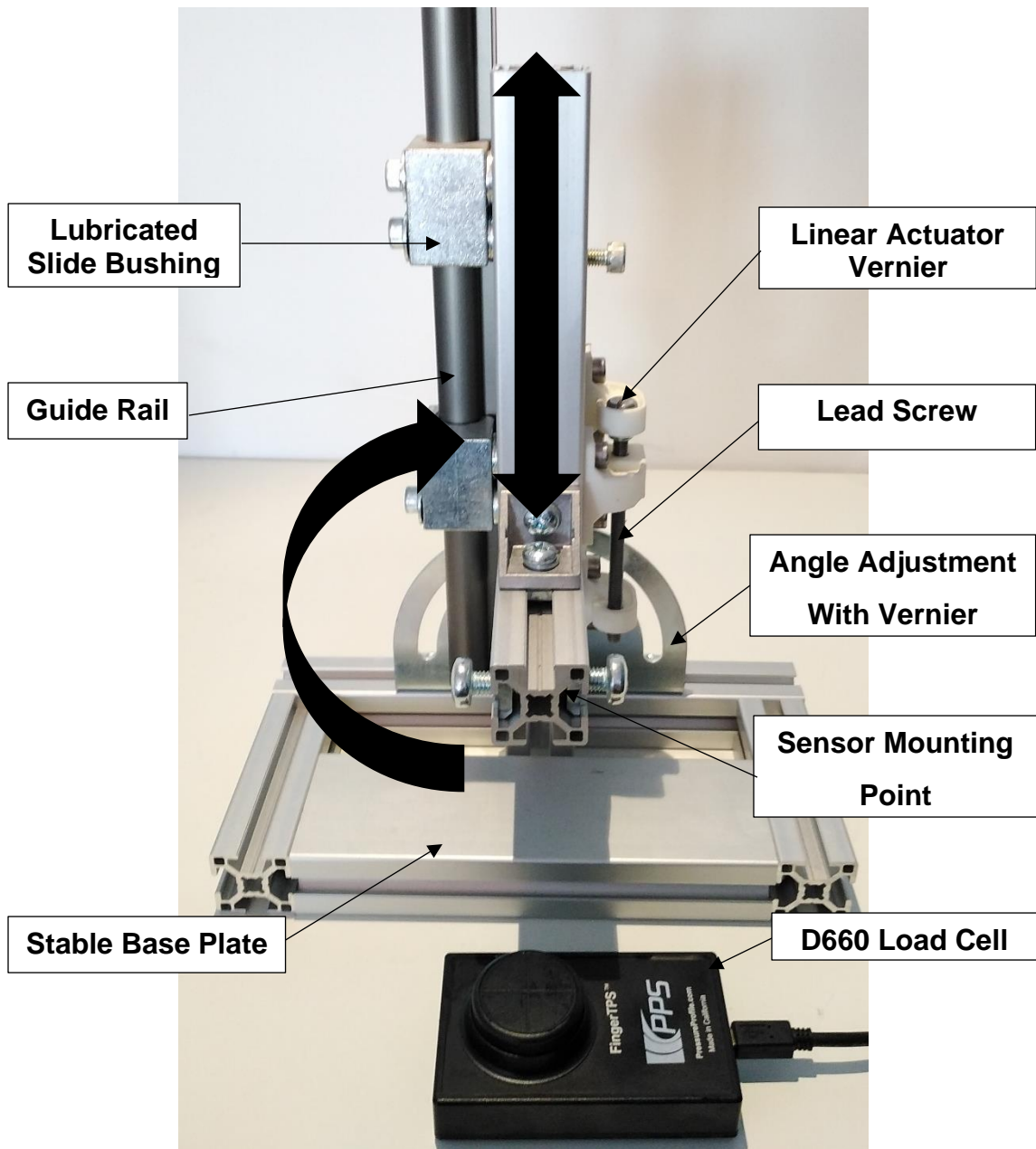
Appendix B

Scanner Sensor Calibration

B.1. Calibration Apparatus

The general purpose calibration apparatus is shown in Appendix Figure B.1, which is used for the calibration of the prototype systems from Chapter 4 and 5 as well as testing on the tactile array from Chapter 6. The apparatus consists of a linear guide rail that the sensor system is attached to using machine screws, which is able to be moved in or out using a leadscrew in order to vary the load applied to the sensor system. The linear guide rail is also tiltable using a vernier and clamp on the back of the apparatus, which allows the sensor under test to be angled into a calibration pad mounted to the base plate. A PPS D660 load cell (PPS Inc., US-CA) is used to provide a measurement of the total load applied to the sensor under test by the apparatus.

The linear actuation and angle adjustment are performed manually, with the values incremented until the angle vernier is correct and the D660 load measurement is at the correct value for the test. The D660 is a force sensor, and so must be converted to equivalent pressure, for calibrating the pressure sensors on the tactile array of the developed system, by dividing the output by the test sensor contact surface area.



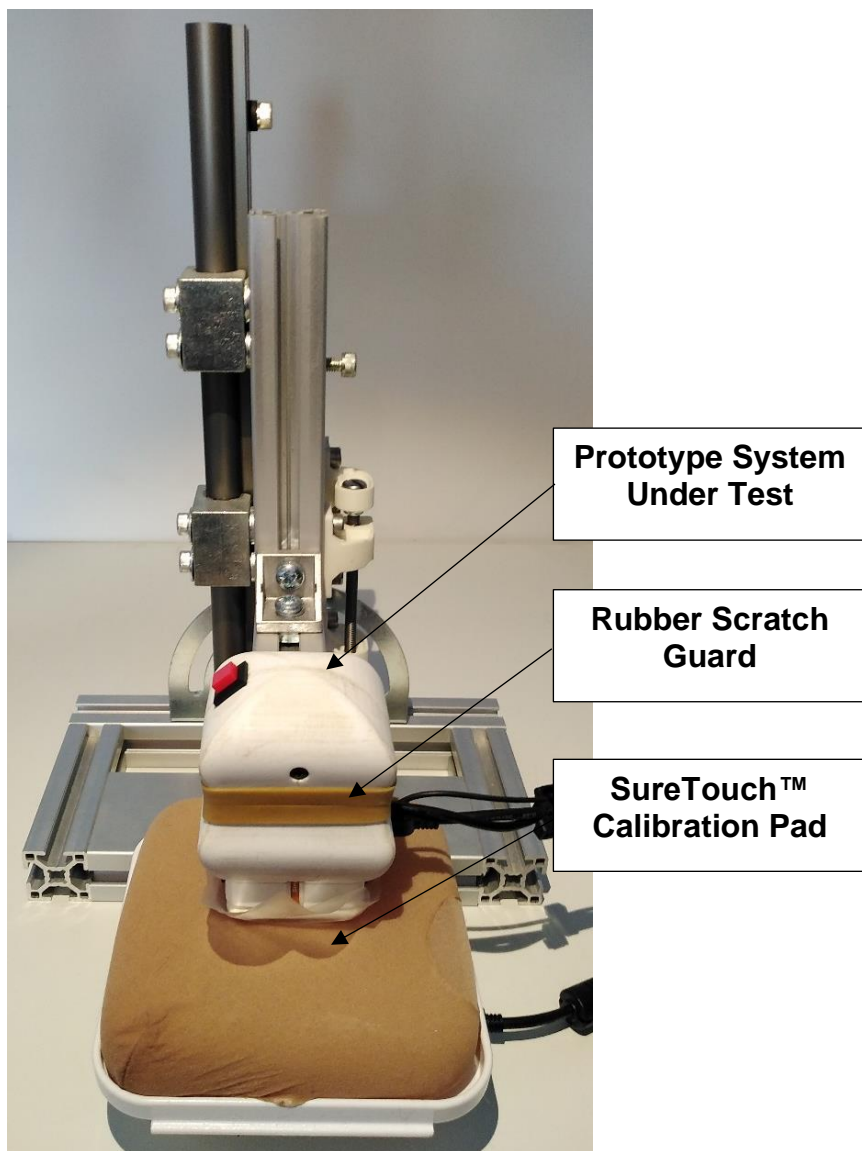
Appendix Figure B.1 - Calibration and test apparatus. The mechanism holds the sensor system under test and allows it to be inserted and held at a defined depth and angle in a SureTouch™ calibration pad on the base plate. A reference load cell is used to measure the total load applied to the sensor under test. The calibration pad can be placed over the reference load cell when this is required.

B.2. Pressure Sensor Normal Calibration

Initial calibration of the 2x2 SingleTact™ array used in the Chapter 4 and 5 prototype systems is performed using the setup shown in Appendix Figure B.2. In this situation the system under test is bolted to the compression apparatus, and a SureTouch™ calibration pad is placed over the D660 load cell. The prototype system is turned on and pressed steadily into the calibration pad, controlling the total applied force using the D660, over the range 0-20N. The SingleTact™ readings are then calibrated in their mounted positions using the D660 measurement.

The loading is not tilted, and so the total force measured by the D660 is expected to be shared equally between the array sensors, but slight manufacturing differences and irregularities in the sensor backing will cause the load to be unevenly shared between sensor elements. As we know that each measurement should be $F_{\text{Total}}/4$, each element output can be forced to this value by a piecewise linear function over the full test range. This type of function allows for changes in the load sharing between elements to be accounted for, resulting in a typical calibrated linearity error of 2% which is sufficient for this purpose.

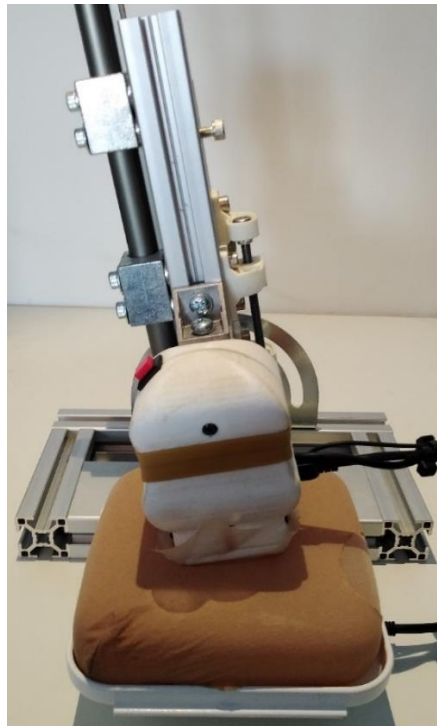
It is clear that each element in the 2x2 array would have a different set of calibration function as they are functions to account for differences between elements. It is also clear, from the fact that the differences are caused by manufacturing tolerances, that other units made to this design will have different sets of calibration functions and so new calibration of this type is required for duplication of this work.



Appendix Figure B.2 – SingleTact™ array normal loading calibration setup. The sensor prototype is bolted to the test apparatus with a rubber scratch guard. The prototype is then pressed normally to the calibration pad surface, with the SingleTact™ readings compared with the D660 reference measurements.

B.3. Scanner Tilt Angle Calibration

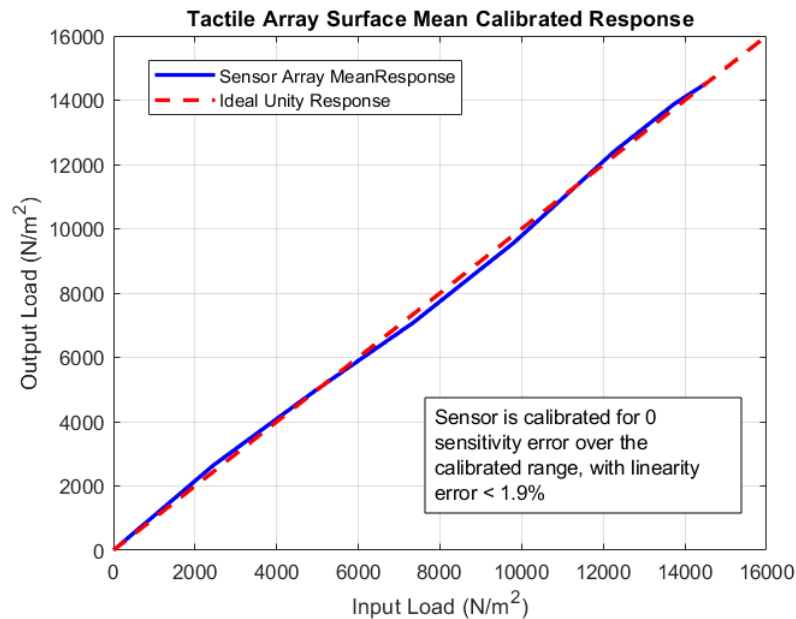
The axis offset between the BNO055 MARG sensor used in the system prototype and the probe axes is determined using the setup shown in Appendix Figure B.3. The prototype is bolted to the apparatus as before and tilted over the desired range using a vernier readout. The rotation measured by the BNO055 is expected to be about a single axis, but manufacturing tolerance and installation variability will mean that the MARG sensor axes are not aligned with the rest of the system. The difference between the reference angle and MARG estimation is measured and accounted for using a rotation matrix to virtually align the two media.



Appendix Figure B.3 - Tilt angle calibration setup. The prototype is tilted left and right over the range -15° to 15° using the vernier angle readout, to calibrate the orientation of the MARG sensor to the prototype axes. This is performed in each axis to average out measurement error from probe alignment with the tilt apparatus.

B.4. Tactile Array Normalisation

Tactile array calibration and normalisation is performed by pressing the tactile array into the calibration pad with zero tilt angle, with discretely incrementing load measured using the D660 reference sensor. A second order surface is fit to the tactile frame, and the surface is scaled linearly such that the surface mean is calibrated to the reference sensor. This allows for a nominally flat array response over the calibration range, minimising the error from the curvature of the array. A typical calibrated response is shown in Appendix Figure B.4, where a linearity error $< 1.9\%$ is achieved over the full calibrated range. The sensors are calibrated to have no sensitivity error at 100% FSR and no baseline shift at 0% FSR at the calibration temperature.



Appendix Figure B.4 – Example SureTouch™ surface calibrated response. The mean of the second order surface fit to the array data is calibrated to the reference sensor using piecewise linear functions between test points. This allows linearity $< 1.9\%$.

Appendix C

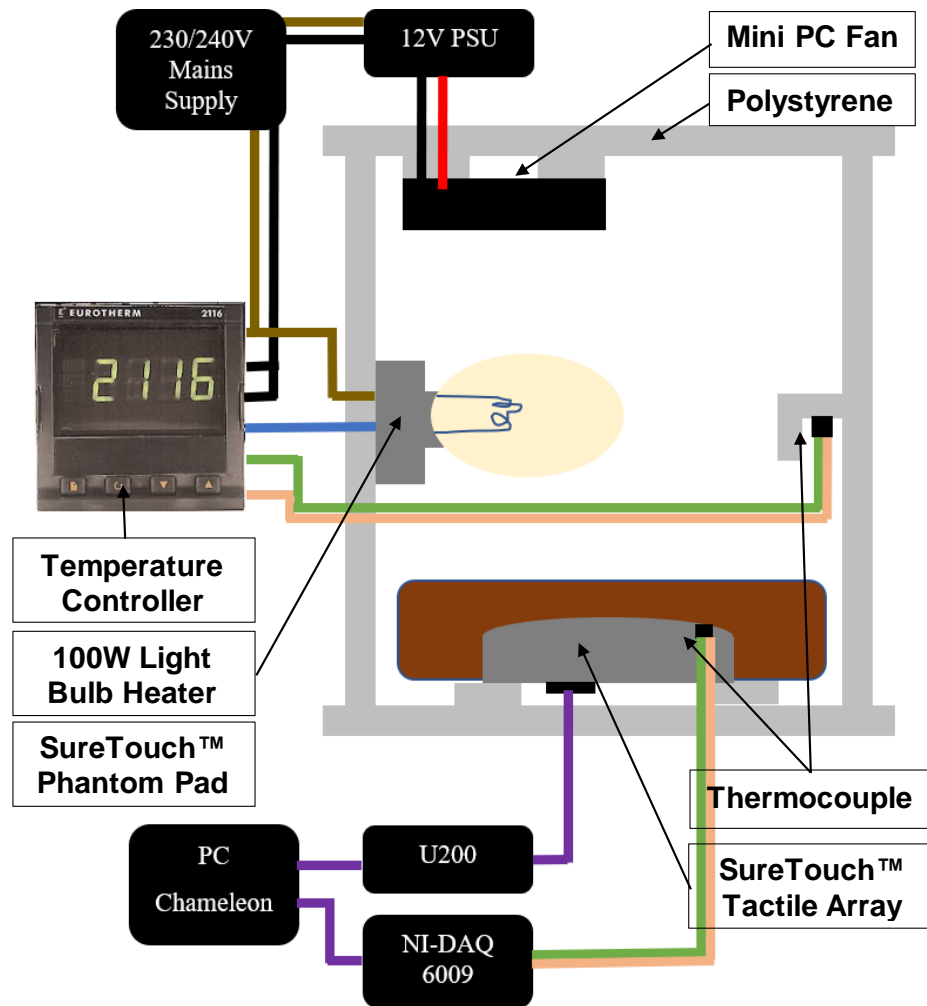
Temperature and Mechanical Analysis

C.1. Temperature Analysis and Apparatus

Measurement of thermal sensitivity of the sensors is done using a thermal control oven as shown in Appendix Figure C.1. The measurement of baseline sensitivity is done by incrementing the temperature of the oven by discrete steps and recording the sensor baseline when the integrated thermocouple measurement is stable and equal to the oven temperature. Measurement of the scale factor thermal sensitivity is performed by similarly heating the sensor and the calibration pad. When the materials have reached thermal equilibrium, they are removed from the oven and a compression test is performed using a reference D660 thermally isolated load cell, to determine the change in sensor sensitivity to load. The large thermal mass of the materials and short test times maintains temperature stability within 0.2° during the compression test.

The thermal oven is a box made from sheets of polystyrene enclosing the sensor array and calibration pad. The oven is fan assisted with a 100W incandescent lightbulb as the heating element. A 'K' type thermocouple of the same type as used for the sensor array provides feedback for a Eurotherm 2116 thermostatic controller (Eurotherm Controls Ltd. UK). The thermocouple is out of the convection path to give conservative

measurements of oven temperature. Thermal control is typically within 5%, however measurements are taken when the sensor is at the correct temperature, and so the measurements are not affected by the oven control tolerance. Cables for internal components are fed through narrow holes in the door that also stop pressure changes inside the oven. The heated materials are raised above the oven bed using spacers to allow air flow under them for even heating.

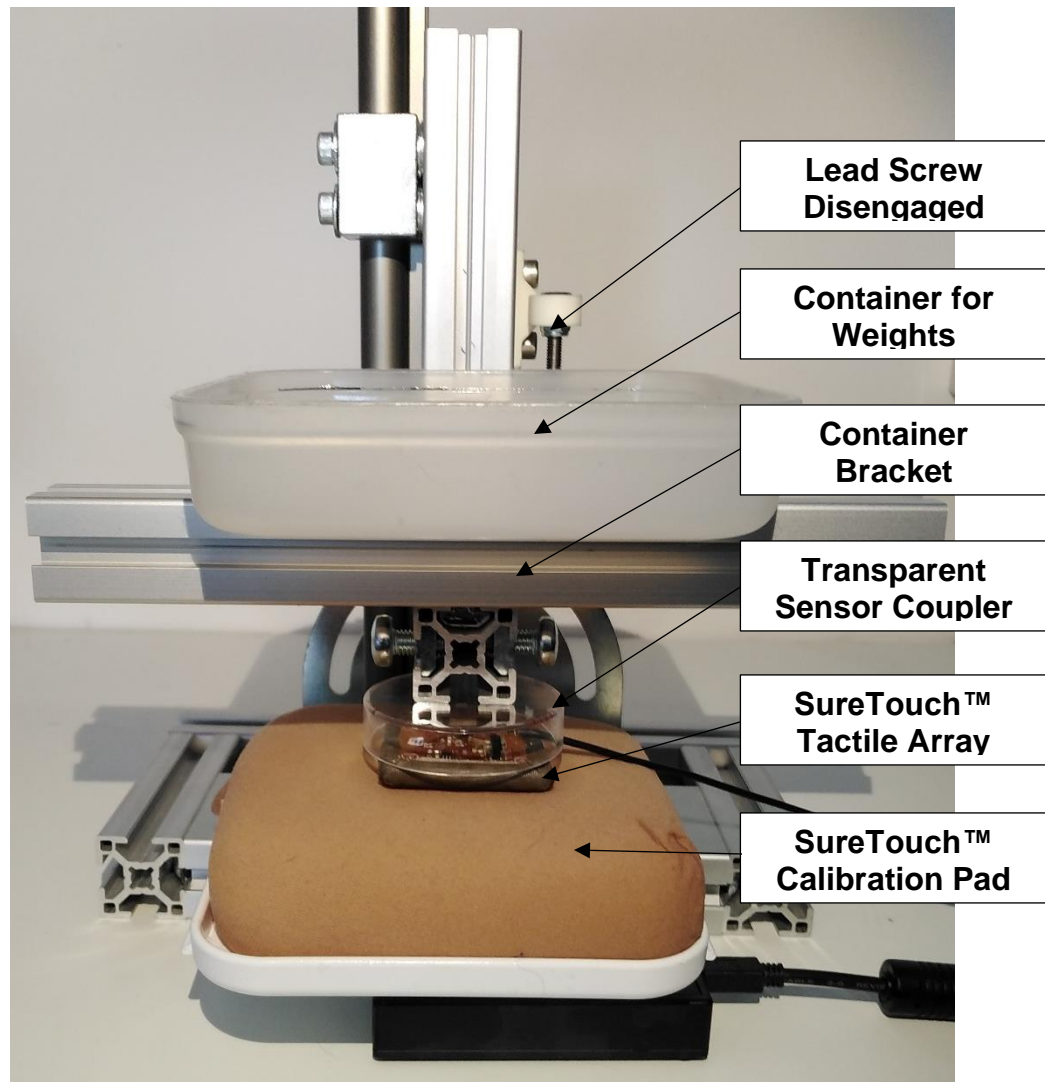


Appendix Figure C.1 – General schematic for a thermal control chamber. The polystyrene insulated chamber can gently warm the tactile array and test material together using the heater and fan to bring all materials to the same temperature evenly.

C.2. Creep/Hysteresis Analysis and Apparatus

The apparatus for mechanical testing of sensor creep and hysteresis is shown in Appendix Figure C.2, and is practically identical to the apparatus from Appendix B. The lead screw is disengaged and replaced with a container for holding small weights. The SureTouch™ tactile array is fixed to the test apparatus using a transparent coupler to insulate the electrical components from the test apparatus and allow the cables to pass out of the system. Using weights, rather than the lead screw, to press the tactile array into the calibration pad allows for the load to be held at a constant value for long periods of time. The weights allow the apparatus to compensate for the creepage of the calibration pad in response to continuous applied load, maintaining a constant load by allowing the tactile array to sink down into the calibration pad to maintain a nominal stress. This is a fundamental physical process, and is better than closed loop control of the leadscrew. The D660 reference is still used to verify the weights added and to record the weights for automated analysis. This process allows the creepage of the calibration pad to be separated from the creepage of the tactile array. The zero load condition is measured with the tactile array separated from the calibration pad surface.

Creep and hysteresis are measured in a similar manner, with weights applied and continuous measurements taken until the sensor output is stable or 5 minutes, whichever is greater, before removing the weights and disengaging the sensor from the surface. Readings are taken in the zero load state, following a loading event, for 5 minutes or until the sensor is stable at some value related to the hysteresis.

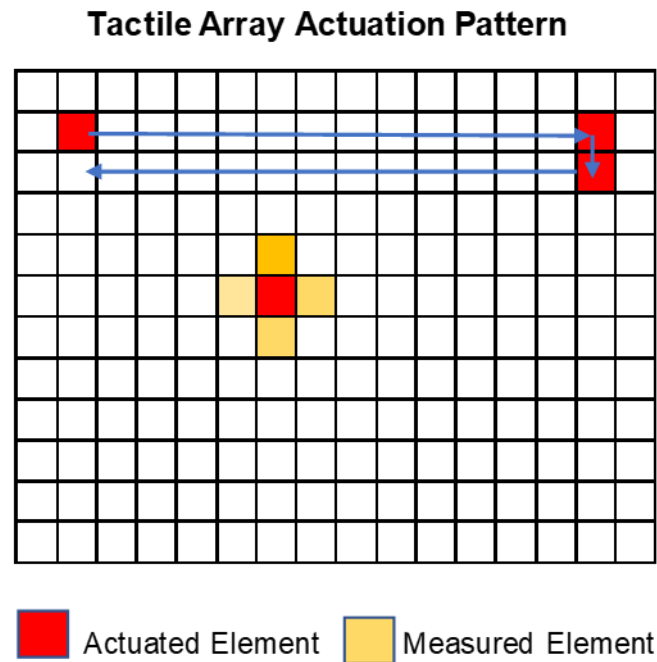


Appendix Figure C.2 – Mechanical Creep/Hysteresis test apparatus. The basic equipment is identical to the setup from Appendix B, with the lead screw disengaged and replaced with a cup for adding weights. Using weights means the creepage of the calibration pad will be continuously corrected for, which is verified by the load cell.

C.3. Cross Coupling Analysis and Apparatus

Cross coupling between elements is determined by compressing an individual element of a pre-calibrated sensor array and observing the typical response of the 4 most adjacent elements as shown in Appendix Figure C.3. This process is repeated for all internal elements, allowing for a typical response to be determined.

The actuated element is compressed using a 1mm diameter cylindrical indenter, centred on the element of interest. Position is adjusted to attempt to keep the surrounding elements approximately equal with each other. The mean output of the 4 peripheral elements is divided by the applied load to determine the cross coupling for that element. The values for each element are then averaged to give a typical array response.



Appendix Figure C.3 - Method for measuring interelement cross coupling. Each internal element is compressed sequentially with a near point load, and the 4 adjacent elements are averaged to determine the coupling between elements.